Theranostic Multibranched Gold Nanoantennas for Cancer Diagnostics via Surface Enhanced Raman Spectroscopy and Photothermal Therapeutics

By

Joseph A. Weinstein-Webb

Dissertation
Submitted to the Faculty of the
Graduate School of Vanderbilt University
in partial fulfillment of the requirements
for the degree of

DOCTOR OF PHILOSOPHY
in
Chemical Engineering

May 31, 2017
Nashville, Tennessee

Approved:

Rizia Bardhan, Ph.D.

Leon M. Bellan, Ph.D.

Matthew J. Lang, Ph.D.

John T. Wilson, Ph.D.

TABLE OF CONTENTS

Page

LIST OF TABLES vi

LIST OF FIGURES vii

Chapter

1 Introduction 1
1.1 Motivation 1
1.2 Cancer Biology 2
1.2.1 Overall Physiology 2
1.2.2 Receptor and Biomarker Targeting 3
1.3 Plasmonic Nanoparticles 4
1.3.1 Fundamentals of Plasmonics 4
1.3.2 Variations in Synthesis, Size, and Shape 5
1.3.3 Biological Applications 7
1.4 Surface Enhanced Raman Spectroscopy (SERS) 8
1.4.1 Raman Spectroscopy 8
1.4.2 Surface Enhanced Raman Scattering 9
1.4.3 Plasmonic Enhancement Mechanisms 11
1.4.4 SERS Biological Applications 12
1.5 Plasmonic SERS Substrates for Biomolecular Detection 13
1.5.1 Paper-Based 13
1.5.2 Planar Substrates 15
1.6 Theranostic Nanoparticles for Cancer Medicine 16
1.6.1 Multi-Modal Imaging 16
1.6.2 Multi-Modal Therapeutics 18
1.6.3 Cancer Theranostics 20
1.6.4 Immunoimaging and Immunotherapy 23
1.7 Bibliography 25

2 Investigating the Synthesis, Geometry-Dependent Plasmonic Tunability, and Photothermal Properties of Multibranched Gold Nanoantennas 32
2.1 Summary 32
2.2 Introduction 33
2.3 Results and Discussion 35
2.4 Conclusions 56

2.5 Methods 57
2.6 Bibliography 61

3 Branched Nanoantenna-Integrated Substrates for Ultrasensitive Biomolecular SERS Detection 66
3.1 Summary 66
3.2 Introduction 67
3.3 Results and Discussion 70
3.4 Conclusions 91
3.5 Methods 92
3.6 Bibliography 97

4 Theranostic Gold Nanoantennas for Simultaneous Multiplexed Raman Imaging and Photothermal Therapy *in vitro* and *in vivo* via Human Xenograft Studies 101
4.1 Summary 101
4.2 Introduction 102
4.3 Results and Discussion 105
4.4 Conclusions 124
4.5 Methods 125
4.6 Bibliography 142

5 Summary and Outlook 147

Appendix A Procedures for MGN-glass SERS Biodiagnostic Assay for Ultrasensitive Detection of Prostate Specific Antigen (PSA) 149
A.1 MGN-glass Preparation 149
A.1.1 Synthesis 149
A.1.2 Characterization 151
A.2 Synthesis of antiPSA-pMBA-MGNs for Sandwich Assay Top Probe 152
A.2.1 Reagents and Materials 152
A.2.2 Buffer Preparation 153
A.2.3 Protein Resuspension 155
A.2.4 Functionalization Chemistry 157
A.3 SERS Biodiagnostic MGN Sandwich Assay: Experimental Design 159
A.3.1 Timeline and Overview of Biodiagnostic SERS Assay 159
A.3.2 Experimental Procedure of Sandwich Assay 159
A.3.3 Raman Measurements of Sandwich Assay 163
A.3.4 Biodiagnostic Control Assays: Testing Specificity and No Antigen Present 164

Appendix B Procedures for *in vivo* SERS Imaging and *ex vivo* Tumor Studies 165
B.1 Mammary Fat Pad Tumor Growth 165
B.2 Synthesis of Actively Targeted MGNs Cocktail for *in vivo* Experiments 166
B.2.1 Reagents and Materials 166
B.2.2 Buffer Preparation 166
B.2.3 Protein Resuspension 168
B.2.4 Functionalization Chemistry 169
B.3 SERS Longitudinal Assays with Portable Raman and Athymic Mice for Both Experimental and Receptor-Blocked Groups 171
B.4 Histology (H and E) and Silver Staining of *ex vivo* Tumor Sections 173
B.5 *Ex vivo* SERS Mapping of Tumor Sections 174

LIST OF TABLES

Table Page

1.1 Examples of theranostic plasmonic nanostructures and their corresponding diagnostic and therapeutic modalities 22

2.1 Effect of core size and branch length on plasmon resonance.....37
2.2 Comparison of refractive index sensitivity of gold nanostructures of various shapes.....52

3.1 Ratio of 1258 to 1294 cm^{-1} peak intensities for varying concentrations of complexed human serum albumin (HSA)/indocyanine green (ICG) probes.....78

LIST OF FIGURES

Figure Page

1.1 Cancer mortality rates across the globe as provided by WHO 2
1.2 Schematic of Hallmarks of Cancer 3
1.3 Diagram of charge oscillations resulting in plasmons for metal nanoparticle 5
1.4 Synthesis of plasmonic nanostructures and tuning resonance to first NIR window for biological applications 7
1.5 Fundamentals of Raman spectroscopy and SERS enhancement 9
1.6 Plasmonic enhancement mechanisms of gold nanostructures 12
1.7 Applications of plasmonic SERS substrates for biomolecular detection 14
1.8 Dual-Modal PT-OCT/SERS imaging *in vivo* with single MGN platform 18
1.9 Multifunctional and combinational therapeutic approach offered by gold nanoplatforms 20

2.1 Electron micrographs of Multibranched Gold Nanoantennas (MGNs) 36
2.2 Supplemental TEMs of MGNs to determine branch distribution for 100 mM HEPES synthesis 38
2.3 Supplemental TEMs of MGNs to determine branch distribution for 300 mM HEPES synthesis 39
2.4 Tunability of MGNs modulated via HEPES-mediated synthesis 41
2.5 Studying growth dynamics of MGN formation through UV-vis spectroscopy 43
2.6 Modifying HEPES/Au^{+3} and the resulting MGN morphologies and resonances....45
2.7 Effect of pH on MGN formation and plasmon resonance....47
2.8 LSPR sensing with MGNs synthesized at various HEPES concentrations....50
2.9 Thermogravimetric analysis of solid state MGNs prepared with 300 mM HEPES....53
2.10 Measuring photothermal capacity of MGNs using Infrared imaging 54

3.1 MGN-paper characterization....71
3.2 SERS liquid detection of 1,4 Benzenedithiol (BDT) with MGN-paper....72
3.3 MGN-paper for protein (Human Serum Albumin) detection via SERS tag (Indocyanine Green) complex....76
3.4 Control MGN-paper studies comparing SERS footprint for different binding conformations of HSA and ICG....77
3.5 Control studies testing non-specific interactions between ICG and MGN-paper....79
3.6 SERS solid swab detection of 4-Aminothiphenol (4-ATP) and Methyl Parathion with MGN-paper 81
3.7 Finite difference time domain (FDTD) simulations of MGN monomers with varying spherical core diameters....83

3.8 Additional FDTD simulations of 25 nm core MGN monomers and dimers to study junction effects 85
3.9 MGN-glass sandwich architecture for Prostate Specific Antigen (PSA) detection 87
3.10 SERS Biodiagnostic assay for ultrasensitive PSA detection via MGN junction geometry 89

4.1 Characterization of antibody labeled MGNs 106
4.2 Fluorescent secondary antibody assay confirming Epidermal Growth Factor Receptor (EGFR) overexpression in MDA MB 231 cells 108
4.3 Cellular TEM micrographs showing binding and uptake of antibody-coated MGNs by MDA-MB-231 cells 109
4.4 SERS singleplex mapping of MDA-MB-231 cells with antiEGFR-pMBA-MGNs 110
4.5 SERS singleplex mapping of MDA-MB-231 cells with pMBA-MGNs 112
4.6 SERS multiplex mapping of MDA-MB-231cells with (1:1) mixture of antiEGFR-pMBA-MGNs to antiPDL1-DTNB-MGNs 113
4.7 SERS multiplex mapping of MDA MB 231 cells with (1:1) mixture of antiEGFR-pMBA-MGNs to antiPDL1-DTNB-MGNs, additional plots 114
4.8 Blocking PD-L1 SERS multiplex mapping of MDA MB 231 cells with (1:1) mixture of antiEGFR-pMBA-MGNs to antiPDL1-DTNB-MGNs 116
4.9 Live phase contrast imaging of MDA MB 231 and MCF7 cells incubated with actively and passively targeted MGNs 117
4.10 Live/Dead confocal fluorescence imaging of MDA MB 231 and MCF7 cells demonstrating photothermal capability of actively targeted MGNs 119
4.11 Photothermal therapy control assays, laser alone and antiEGFR-pMBA-MGNs alone for MDA MB 231 cells 120
4.12 Longitudinal multiplex SERS imaging *in vivo* with actively targeted MGNs, and the effect of receptor blockage 121
4.13 Ex vivo analysis and SERS spatial mapping of MDA MB 231 tumors after excision from mice injected with actively targeted MGNs 124

CHAPTER 1

INTRODUCTION

1.1 Motivation

Cancer is the second leading cause of death globally according to the World Health Organization. Especially dangerous and lethal are the breast cancers that have genetic mutations for surface receptors utilized in drug therapy.[1] This resistance calls for new and innovative treatments that be optimized for cancers based on an individual patient basis/cancer phenotype.[2] Nanoparticle based diagnostics and therapeutics have recently emerged as a novel platform for management and mitigation of cancer at all stages. Gold nanostructures, specifically, have multiple characteristics that make them ideal for cancer theranostics including: (i) high biocompatibility, (ii) ease of bioconjugation, (iii) ability to tune their plasmon resonance to absorb tissue penetrating near infrared light, (iv) their use as contrast agents, and (v) ability to convert light to heat when excited at the plasmon resonance for photothermal ablation of cancer cells. Further, due to their adaptability as a platform, the nanoparticles affect the battle against cancer in multiple different strategies. These theranostic gold nanoprobes can be incorporated into point of care diagnostic (POCD) systems for biomarker detection, used as theranostic probes to delivery multiplex SERS receptor imaging and photothermal therapy or be involved in future immunotherapy[3] treatments.

In this work we demonstrate the use of near-infrared light absorbing multibranched gold nanoantennas (MGNs) to simultaneously deliver diagnostic and therapeutic (theranostic) capabilities in cancer models. More aggressive cancer cell lines require approaches that are

versatile and multifunctional, and the possibilities for the usage in diagnostics or therapeutics for these theranostic MGNs are abundant.

1.2 Cancer Biology

1.2.1 Overall Physiology

According to the WHO, there were 14.1 million new cancer cases, and the disease accounted for 8.2 million deaths. Cancer is the second leading cause of non-communicable disease death behind only cardio vascular disease. As viewed by Figure 1.1, the disease is worldwide and will thus require a global effort in treatment.

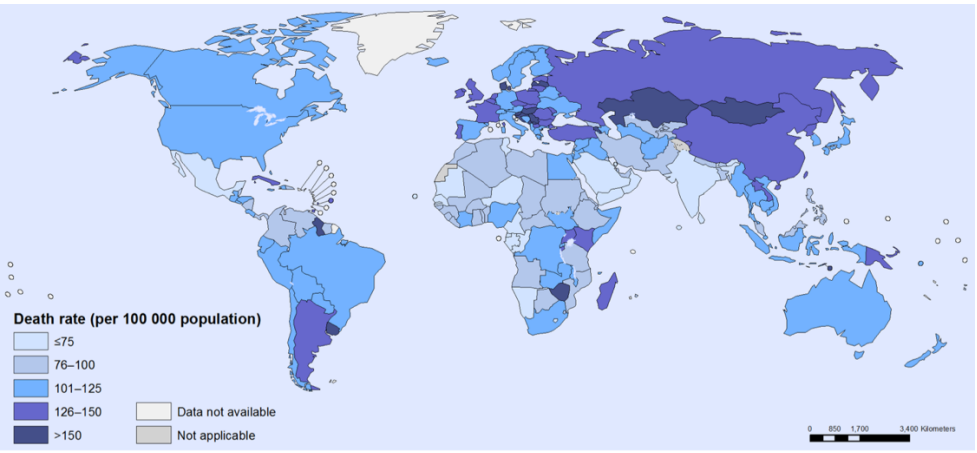

Figure 1.1: Cancer mortality rates across the globe as provided by WHO. Rates are per 100000 population and age standardized for both sexes. Data courtesy of World Health Organization (WHO) for cancer statistics in 2012.

Cancer is the uncontrollable, unadulterated, and immortal capability of the cells to multiply and divide without end.[4, 5] These out of control growths can be visualized *in vivo* with the formation of neoplasms.[6-8] The cell becomes stuck in the on state for the cell cycle and continues to replicate, making more and more genetic and proteomic material and information. This cycle is depicted in Hanahan's diagram of the "Hallmarks of Cancer" (refer to Figure 1.2).

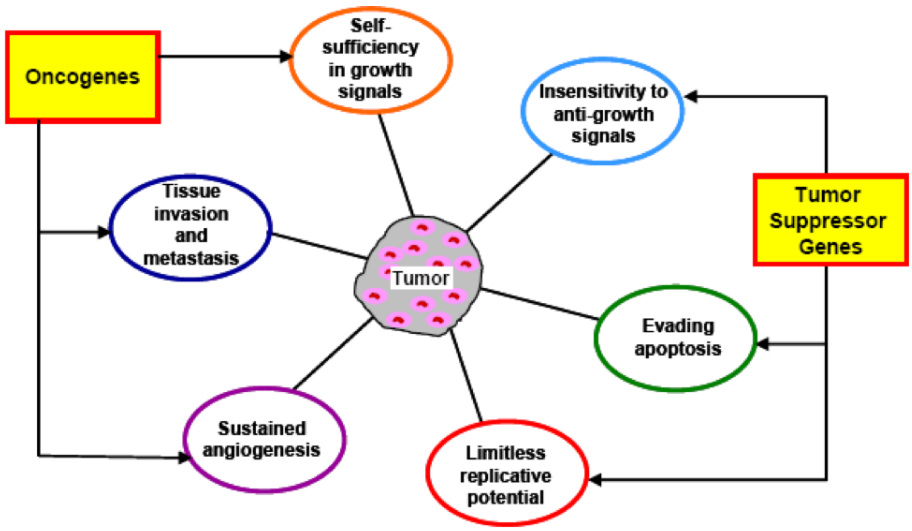

Figure 1.2: Schematic of Hallmarks of Cancer. As previously explained by Hanahan et al[9], there is both the breakdown in regulatory pathways and the amplification of uncontrollable growth. Figure modified from its original version.

These attributes are an indicator of where healthy human cells are along the lines of malignant cell progression or necessary steps that must be scientifically met to be considered an aggressive cell. Six genetic modifications[9] occur that result in the following phenotypes: (a) self-sufficiency in growth signals, (b) insensitivity to growth-inhibitory (anti-growth) signals, (c) evasion of programmed cell death (apoptosis), (d) limitless replicative potential, (e) sustained angiogenesis, and (f) tissue invasion and metastasis (Figure 1.2). Cells can enter these genetic mutation pathways through a multitude of pathways, but none will escape the cycle.

1.2.2 Receptor and Biomarker Targeting

Cancer metastasis is really where the lethality comes in as it is the metastatic cells that can break off and mutate to another organ, continuing to grow and develop or even differentiate.[10, 11] Thus, to avoid metastasis of tumors, early detection and treatment is necessary. With these theranostic MGN platforms, there is a two-prong approach to increase

cancer detection accuracy and sensitivity. For this plan we will manufacture (i) Biodiagnostic SERS assay for ultrasensitive early detection of PSA biomarker and (ii) Actively targeted Theranostic MGN platforms for SERS imaging and PTT. Both technologies rely on protein detection. Thus, protein localization, expression, and concentrations are the most important biological indicator when trying to improve cancer SERS detection.

Protein levels in the blood or serum (biomarkers) or proteins attached on the surface of the cancer cells (receptors) can both provide vital information in determining the presence of tumor tendencies. Since it is really this technology of detecting macromolecules, specifically proteins, through a SERS-beacon, that makes the multiplex capacities of the SERS MGNs impressive and useful, these biomarkers and receptors have to be the focus. Cancer is known to have uncontrollable cell cycle rates and uncontrollable rates of protein synthesis, which can also lead to excessive or overexpression of a particular receptor on the cell surface[12-14] or an overly high concentration of a mature biomarker in the blood[15, 16], both of which can be utilized for early detection.[17, 18]

1.3 Plasmonic Nanoparticles

1.3.1 Fundamentals of Plasmonics

To study the optical properties of nanoparticles, one has to also understand the behavior of electromagnetic (EM) waves on the nano level and do so by dissecting waves into their constituent parts. The study of light and other EM waves on the nanoscale level is known as nanophotonics. Within this field of nanophotonics, there is a subdivision called plasmonics that studies the interaction of EM waves with the electron cloud of metal materials. Within plasmonics, there are surface plasmon polaritons (SPP) which occur when EM waves couple to

the collective electron oscillation of a dielectric film creating a propagating wave that can be used as a waveguide.[19, 20] The other phenomenon, called a localized surface plasmon (LSP), happens when electrons within a single nanoparticle begin to oscillate, not propagate, upon incident EM wave excitation.[21] As seen in Figure 1.3, upon irradiation, electron cloud will begin to oscillate from side to side creating a dipole moment and forming a plasmon resonance. Further, this excitation creates a localization of concentrated electron 'hot spots' which create very strong EM fields that decay within tens of nms away from the surface. If the incident light source is at the resonant wavelength of the metal nanoparticle, coupling proceeds leading to enhancements in a variety of applications.

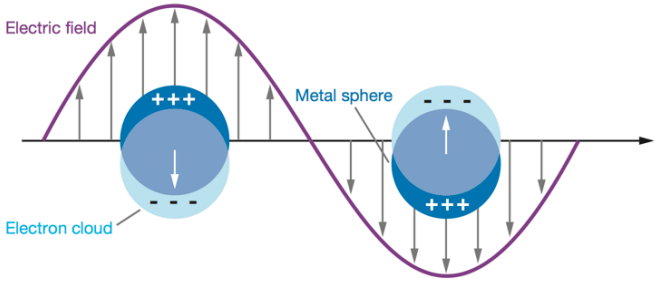

Figure 1.3: Diagram of charge oscillations resulting in plasmons for metal nanoparticle. Oscillations occur upon irradiation with electromagnetic wave. Figure modified from its original version.[22]

1.3.2 Variations in Synthesis, Size, and Shape

Plasmonic wave coupling for nanostructures usually occurs with EM waves in the visible and NIR region, where gold and silver absorb and scatter light the strongest. Gold and silver are usually chosen for nanoparticle synthesis because of their high electron density, which leads to a higher probability of hot spot formation upon excitation.[21] The capabilities of several shape- and size-controlled gold nanostructures have been studied in the past decade, [23, 24] [25, 26] and some are already in clinical trials[27, 28]. A representative demographic of the shapes and

size of particles is presented in Figure 1.4a to Figure 1.4i. The geometry and size of the nanoplatform required is dependent on the application. By modulating the dimensions of GNS the relative contribution of absorption and scattering to the total extinction cross-section can be controlled.[29] While smaller nanostructures predominantly absorb light, larger nanostructures are largely scattering. However, it has been demonstrated that for complex anisotropic nanostructures the absorption and scattering properties is not a linear relationship of the size rather dependent on their unique geometry.[30]

Scattering and absorption properties of the nanoparticles also help determine their applications. Highly scattering gold nanostructures are extensively utilized as contrast agents for optical imaging using a simple dark-field microscope,[31] and for computed tomographic (CT) imaging.[32] Nanostructures with large scattering cross-sections and high polarizability also enhance the Raman signal of molecules in their vicinity enabling surface-enhanced Raman scattering (SERS) based imaging. Lastly, it has to be considered, when moving into *in vivo* applications, that the resonance of the synthesized nanostructures overlap with the first NIR window as previously reported by Weisslader. As to not lose at on any additional signal from tissue or protein absorption, the platform should have a resonance of ~660 nm to 900 nm (Figure 1.4k), in the range of low absorption by hemoglobin and water (Figure 1.4j).

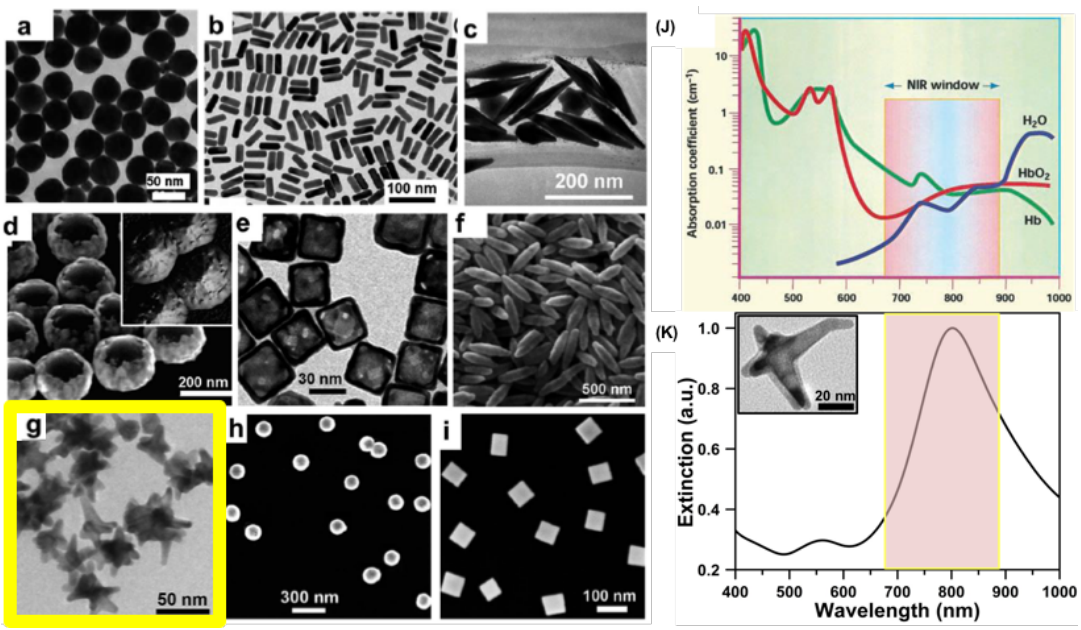

Figure 1.4: Synthesis of plasmonic nanostructures and tuning resonance to first NIR window for biological applications. (a-i) Electron microscopy conveys the wide distribution of shapes and sizes possible through various synthesis methods.[33] (j) For optimal tissue penetration with laser source, the wavelength needs to be in the range where proteins, water, and other macromolecules absorb the irradiation the least, as previously reported by Weissleder.[34] (k) This range highlighted in pink for visualization, ~660 nm to 900 nm, has strong overlap with the maximum plasmon resonance of MGNs, making them well suited for theranostic purposes.

1.3.3 Biological Applications

Engineered gold nanostructures (GNS) have emerged as a promising new platform in nanomedicine due to their unprecedented ability to manipulate incident photons and subsequently scatter or absorb light, properties which have been extensively harnessed in biomedical diagnostics and targeted therapeutics.[35, 36] Unlike conventional chemotherapy drugs or small-molecule imaging agents, GNS offer several advantages for nanomedicine. These include (i) high biocompatibility and reduced toxicity governed by surface ligands,[37] (ii) passive accumulation at tumor sites due to the enhanced permeability and retention (EPR) effect,[38] (iii) ease of bioconjugation enabling functionalization with multiple targeting groups for active tumor targeting,[39] (iv) increased stability and stealth characteristics aided by

hydrophilic polymer conjugation,[40] (v) straightforward systemic delivery which enhances circulatory half-life,[41] (vi) ability to deliver hydrophobic drugs and nucleic acids to cells by selective binding to the metal surface,[42, 43] and (vii) and integration with contrast agents for visualization of intracellular localization and tracking nanoparticles *in vivo*.[44-46]

The fact that these nanoparticles can be synthesized is significant, but it is all of the applications that they can be used that is the true breakthrough. Some of the many industries that plasmonic nanoparticles can enhance include: biosensing for bacterial or viral detection, drug delivery and discovery, solar cells, photothermal ablation, and waveguides.[47]

1.4 Surface Enhanced Raman Spectroscopy (SERS)

1.4.1 Raman Spectroscopy

The biosensing technique that works the best with the optical properties of the nanoparticles is Surface Enhanced Raman Spectroscopy (SERS). Raman spectroscopy was discovered in 1928 by the Indian scientist C. V. Raman. Raman observed that when one shined monochromatic light on a material, a majority of that light was scattered off at the same color, refer to diagram, Figure 1.5c green beam). However, he noticed that there was a very small fraction of light that scattered with a different color representing a different energy of scattered light (red beam in Figure 1.5c). He surmised that this subset of scattered light was in fact interacting with the vibrational states of the material itself, which in turn manipulated the energy of the exiting light, refer to Figure 1.5a (before) and 1.5b (after).[48] The small fraction of light that possessed this unique phenomenon was later coined as Raman scattering after its inventor. Raman scattering has both Stokes and Anti-stokes vibrations (Figure 1.5d), but the Stokes are primarily focused on for the sensing spectroscopy. The difference between Anti-stokes and

Stokes Raman is the difference in the initial and final energy levels being reversed (Figure 1.5d). Through the Raman vibrational phenomenon, one can detail the chemical environment of a molecule. Very similarly to infrared spectroscopy, different vibrational, bending, and stretching modes are obtained due to the inherent nature of a molecule behaving in response to the surrounding atoms. By observing these various bands, a Raman footprint can be created that can be used to identify a compound, and this footprint is the basis for Raman spectroscopy.[49]

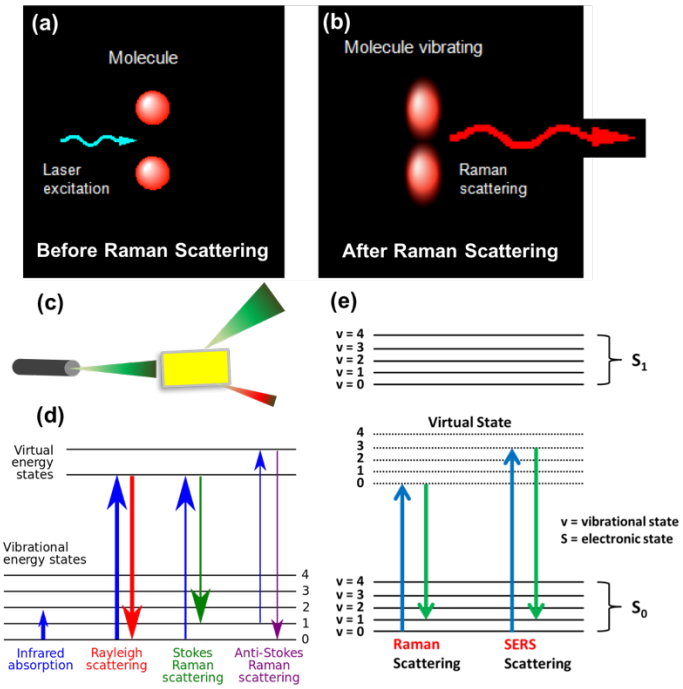

Figure 1.5: Fundamentals of Raman spectroscopy and SERS enhancement. (a-b) Observing the connection between molecule vibration to the resulting Raman scattered electromagnetic wave. Seeing the molecule before (a) and after (b) Raman scattering. (c) Cartoon demonstrating the typically small percentage (red) of Raman scattered light that results upon illumination, with the majority of exiting light existing as Rayleigh scattering (green). (d-e) Jablonski energy diagrams showing difference in energies for Rayleigh, Raman, and Surface Enhanced Raman Scattering.

1.4.2 Surface Enhanced Raman Scattering

Even though Raman spectroscopy was created in the 1920's, the field did not really gain traction until much later in the 20th century due to its weak signal in comparison to fluorescence

and Raleigh Scattering. Fluorescence has a scattering cross-section of $1E^{-15}$ cm^2/molecule while Raman has a value of $1E^{-31}$ cm^2/molecule.[50] There were multiple seminal events that lead to the adoption of Raman spectroscopy as a viable detection tool. To begin with, there was the development of the laser in the early 1960s which provided a monochromatic light source powerful enough to supplement Raman scattering. However, even with the laser source, Raman scattering was not strong enough to be preferred over the other probing technologies. This impedance was changed with the accidental observation of SERS by Fleishmann et al. in 1974 with his roughened silver electrode chemistry with pyridine.[51] Fleishmann was actually trying to monitor the chemical reaction between silver and pyridine and thought to roughen the silver electrodes as to optimize the surface area to increase reaction sites. What he did not realize was that by etching the silver, he was creating very sharp edges of which the localization of electrons would occur creating very strong EM fields. He witnessed very intense Raman scattering which was not quantitative with the chemical reaction that he was performing. Then in 1977, both Jeanmaire & Van Duyne and Albrecht & Creighton again saw the same "giant Raman effect" which could not be explained simply by the increase in scatterers.[52-55] Both groups proposed the mechanism of electromagnetic enhancement with slight deviations in their explanations of the concept. A diagram is provided in Figure 1.5e showing the idea of SERS excitation going to a higher energy level, and thus, the resulting, Raman relaxation energy would be increased. Therefore with the knowledge of utilizing plasmonic nanoparticles to provide enhanced Raman signal and with improvements in both laser technology and chemistry in the 1980s, the field of SERS exploded over the next 40 years up to present times.

1.4.3 Plasmonic Enhancement Mechanisms

The enhancement of the Raman signal occurs via two different pathways both of which take advantage of the plasmonic properties of the nanoparticle. The more robust enhancement mechanism occurs via electromagnetic enhancement which is defined by the localization of electrons creating very powerful EM fields (Figure 1.6a) that interact strongly with the incident light source.[56-58] These powerful near fields cause the Raman photons to localize within the small volumes providing more ample opportunities for the Raman photons to interact with the vibrational states of the detectable molecule.[59, 60] This near-field enhancement is usually along the lines of 4-6 orders of magnitude. The second enhancement mechanism, known as chemical enhancement, only occurs when a chemical bond is formed between the plasmonic particle and the molecule to be detected. In chemical enhancement, the Fermi levels of the nanoparticle and the detected molecule align (Figure 1.6), and hot electron transfer occurs (from particle to vicinal molecule) to facilitate the electron transferring to the excited state.[61, 62] The hot electron transfer lowers the energy required to achieve the excited state by providing an alternate route. This allows more electrons to go to the excited state which means upon relaxation more photons will be localized around the detectable molecule leading to enhancement. The chemical enhancement increases the signal by two orders of magnitude.

Lastly, if the nanostructure has the proper anisotropic geometry, the enhancement properties of the nanoantenna effect can also be utilized. Nanostructures consist of "antenna-like" spherical core that absorbs incident light and routes the light through the protrusions concentrating it at the tips. This unique geometry of MGNs gives rise to the amplification in the core and further confinement of electrons in small volumes leading to even further enhanced fields, and this process has the coined term "*nanoantenna effect*". These near-field configurations

of branched nanostructures enable a range of technological applications from highly sensitive localized surface plasmon resonance (LSPR) sensing,[63] to surface enhanced spectroscopies, to biomedicine,[64] and thermoplasmonics[65].

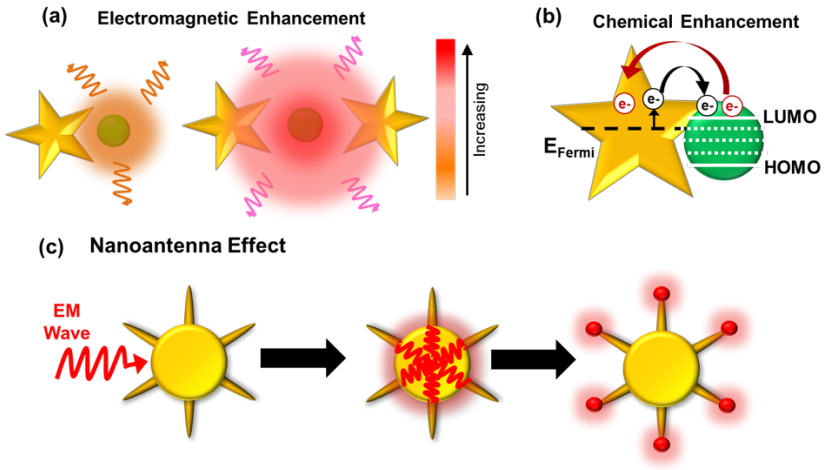

Figure 1.6: Plasmonic enhancement mechanisms of gold nanostructures. (a) Electromagnetic enhancement with strongest fields localized on the pointed tips, due to the smallest volume of electron confinement. (b) Chemical enhancement occurring when the Fermi energy of the bond or vicinal molecule aligns with the gold nanoparticles. (c) Structures representative to Multibranched Gold Nanoantennas (MGNs)[66] demonstrating the nanoantenna effect upon irradiation with electromagnetic wave. Amplification occurs in the core with further confinement of the fields on the tips.

1.4.4 SERS Biological Applications

With these enhancement mechanisms, SERS becomes a better biosensing tool than both localized surface plasmon resonance (LSPR) and fluorescence as it possesses multiple characteristics that the other techniques do not. SERS ($1E^{-21}$ M detection limit)[67] is more sensitive than LSPR ($1E^{-12}$ M detection limit)[54] while, at the same time, being more specific. In addition, unlike fluorescence, SERS is capable of multiplex detection because of its narrow peaks.[17]

Once the enhancement mechanisms were elucidated, groups began optimizing the nanoparticle shape to achieve the greatest SERS enhancement factors and sensitivities. For

ensemble SERS, enhancement factors usually range from $1E^{8}$ to $1E^{10}$, while single particle SERS has shown the capability to obtain values as great as $1E^{14}$ enhancement.[48, 61] As far as sensitivities, it has been demonstrated that as the nanoparticle forms more sharp tipped structures, the analyte detection limit decreases. Spheres have a detection limit of 1 nM while nanorods have been shown to detect concentrations down to 100 pM.[68, 69] The limit plummets once there is the introduction of a structure with multiple pointed tips such as a nanostar (limit = $1E^{-21}$ M).[70] The reason for this very low detection limit is due to the fact that these multiple pointed tips provide an abundance of electron hot spots that create an ultra-strong near field effect by creating junctions with neighboring MGNs. These junctions prove to be significant in the planar sandwich based biomarker detection systems later. In addition to detection studies, there are cellular mapping experiments performed, where nanoplatform SERS tags are providing information about the surface receptor coverage for both cell and tissue studies.[13, 71]

1.5 Plasmonic SERS Substrates for Biomolecular Detection

1.5.1 Paper-Based

Now that the SERS mechanisms, instruments, and nanoparticles have been optimized, a variety of applications are being explored. Engineers and scientists are both beginning to understand the importance and potential of this sensing technology. Groups have begun to utilize various substrates including cellulose paper to make the plasmonic nanostructure diagnostic probes more practical for use with handheld Raman instruments.[72] A paper substrate allows for a flexible, cheap and robust probe that can be readily used in the field (refer to Figure 1.7).

The flexibility and malleability of the MGN-paper substrate lend to its ability to continue through exhaustive testing without losing its sensing properties (Figure 1.7b-1.7c) .

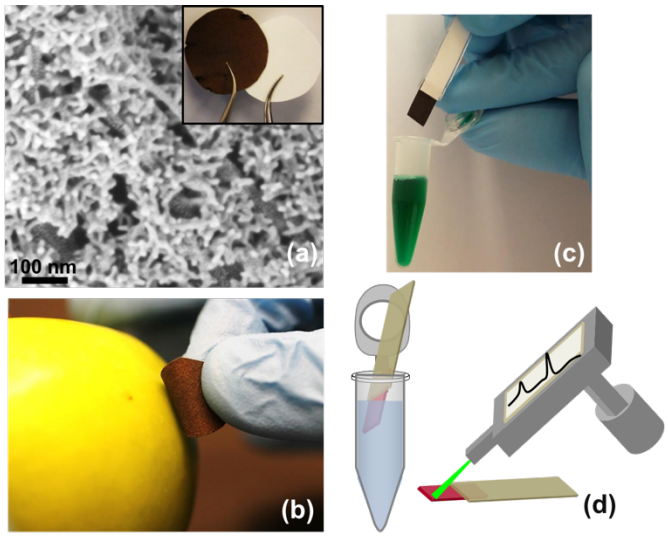

Figure 1.7: Applications of plasmonic SERS substrates for biomolecular detection. (a) Visualized under Transmission Electron Microscopy (TEM), the nanoparticles are seen adhered to the porous paper substrate. (b) The flexibility of the substrate allows for detection on contoured surfaces (apple) for real world applications. (c) Further, the SERS enhanced flexible substrate allows for a laboratory ready diagnostic tool with the potential use of being incorporated for portable (d) SERS measurements in the field.

Another application for these SERS substrates is in point of care macromolecular detection for bacterial or viral species.[73] Lastly, this tool is providing real time molecular biological tracking of various biochemical molecules during a cell cycle. This is being used to observe and trace cell replication in real time.[74] With all of these applications on the horizon, it is an exciting time for the SERS community. Since its inception, SERS has become more and more useful as a sensing tool, and with these new avenues opening up, the applications seem endless. In addition, there has been a recent push to make portable substrates that are capable of sample collection on site. Researchers have worked to create these SERS systems that are capable of detection limits that are as low as possible to detect any early onset of a disease. To attain these low detection limits, scientists have looked to various forms of spectroscopy in the

hopes of developing reliable point of care diagnostic (POCD) systems as depicted in Figure 1.7d that would allow for real time, sensitive, and accurate information.

The porosity of the MGN-paper as visualized under transmission electron microscopy provides the necessary flexibility to perform contoured swab tests as on the apple (Figure 1.7b). This malleability and versatility are ideal when trying to detect analytes through binding events or interactions specifically with the MGNs. However, when determining the platform to coat with MGNs to prepare the sandwich assay, the consideration of the complexities of MGN-sandwich architecture (refer to Figure 3.9a in Chapter 3) and the amount of binding events and specific or non-specific interactions that are occurring must be accounted. Thus, when building a complex system for ultrasensitive detection, the porosity creates an issue of structural stability, and thus why it was decided to move the sandwich assay for ultrasensitive PSA on MGN-glass to ensure the MGN dimer occurred, and the junction formed.

1.5.2 Planar Substrates

It is the belief among medical professionals that the earlier a disease or illness can be detected, the higher the likelihood that it can be treated or averted. Thus physicians and medical scientists alike have been looking for better methods of detecting macromolecules such as transcription factors, hormones, proteins, or nucleic acids that are biomarkers for certain diseases. These medical professionals are looking for systems that are not only robust and effective, but that are also portable and easy to use. To be an effective system, the instrument/probe must be able to detect the targeted molecule at very low concentrations in order to discover these diseases at their earliest onset point, thus allowing a higher chance for treatment. SERS provides a very low detection limit, as well as the capability to have multiplex

detection because of the narrow peak widths in the resulting spectra. This multiplex capability allows one to trace and track multiple components all at the same time.

To create these low create these low detection systems, researchers have developed nanoparticle substrates that when combined with a Raman beacon can be utilized to detect low concentrations of protein or other macromolecules. Li et al. has performed a sandwich assay on a glass substrate covered in gold nanotriangles with top nanoparticle probes where they detected human immunoglobulin G (IgG) in concentrations all the way down to 0.5 pg/mL.[16] Wu et al. performed a half-sandwich assay with gold/silver nanorods on glass substrates in which they utilized multiplex detection of p53 and p21 transcription factors in an early cancer detection assay.[17] Finally, Penn et al. performed a full sandwich assay with spherical nanoparticles sandwiching IgG on gold coated membranes for a detection limit of 1 ng/mL.[75] Current work utilizing MGN-glass sandwich system for SERS enhanced detection of the Prostate Specific Antigen (PSA) is ongoing using a Raman reporter (pMBA) acting as beacon and an antibody (antiPSA) acting to give specificity in the PSA detection. In addition, the PSA will be sandwiched between two layers of MGNs via a MGN-glass substrate system that will provide extremely high near-field enhancements. We believe our MGN sandwich system, we will be able create an ultra-sensitive biodiagnostic tool in the detection of PSA and that this system will be specific for only PSA because of the presence of the multiple targeting ligand, antiPSA.

1.6 Theranostic Nanoparticles for Cancer Medicine

1.6.1 Multi-Modal Imaging

There have been many advances in the field of plasmonics for cellular and tissue imaging. Researchers have used gold nanoparticles as enhanced contrast agents in magnetic

resonance imaging[76], photoacoustic tomography[77] and photothermal optical coherence tomography (PT-OCT)[78] to increase spatial resolution. Plasmonic nanostructures are ideal contrast agents for PT-OCT due to their radiative properties of which provides light scattering in tissue enhancing the contrast as well as non-radiative properties which converts absorbed light to heat thus creating temperature gradients in tissues that lead to changes in refractive index, which the instruments are more sensitive in detecting. In addition, nanoparticles have been utilized in fluorescence imaging[79] and surface enhanced Raman scattering (SERS) imaging[80] to increase sensitivity of the tracking molecule or beacon via electromagnetic and chemical enhancement, which allows for better cellular tracking. PT-OCT uses the localized heating events provided by the plasmonic nanostructures to create better contrast in imaging. The nanoparticles are acting to enhance the image with PT-OCT, but whereas in SERS they enhance the Raman signal intensity.

While PT-OCT provides high volume spatial resolution, SERS imaging provides high sensitivity. A collaborative study using dual-modal PT-OCT/SERS imaging on Athymic nude mice growing human xenograft tumors demonstrated that signal could be observed for both spectroscopies after providing circulation time post retro-orbital injection (Figure 1.8). SERS-tag labelled MGNs accumulated at the tumor, as seen by the appearance of the 1580 cm^{-1} peak of pMBA (Figure 1.8a). Further, the temperature gradient provided by the light to heat conversion efficiencies of the MGNs provided a global picture of were the MGNs accumulated throughout the volume of tumor. Thus, there is temporal, sensitive and multiplex capabilities of SERS that is complimented with the 3-D volume imaging of deep tissue by PT-OCT (Figure 1.8c).

Lastly, SERS or the theranostic nanoparticles could be combined with other spectroscopies as well that require multiplex technology. Spectroscopies such PET, MRI, or CT could also be combined with the SERS imaging for a dual-modality approach to detection.

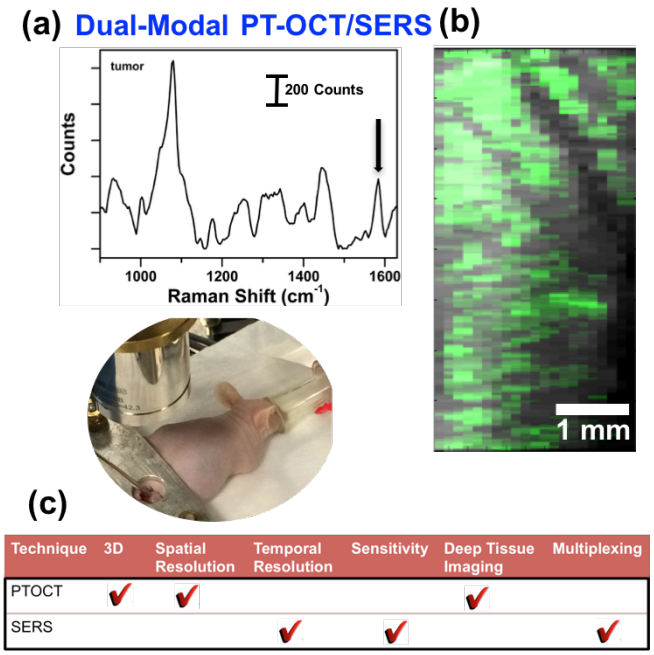

Figure 1.8: Dual-Modal PT-OCT/SERS imaging *in vivo* with single MGN platform. (a) Raman footprint recorded at the tumor site post systemic injection with SERS-labelled MGNs, showing peak at 1580 cm^{-1} for paramercaptobenzoic acid (pMBA). (b) Simultaneous Photothermal Optical Coherence Tomography (PT-OCT) was also measured showing the global distribution of the MGNs. (c) Table provided stressing how the two spectroscopies are complimentary to another.

1.6.2 Multi-Modal Therapeutics

When metal nanostructures are excited with resonant photons, the photoexcitation of the electron gas results in rapid non-equilibrium heating. The initial electronic excitation is followed by relaxation at subpicosecond timescales by means of electron-electron scattering which results in rapid increase in the surface temperature of the metal.[81, 82] The rapid heating is followed by cooling to equilibrium by energy exchange between the electrons and the lattice phonons. In the first several hundred picoseconds following excitation, the lattice cools via phonon-phonon

coupling resulting in heat dissipation into the medium surrounding the nanostructure (depicted in cartoon for Figure 1.9a). Thus, when GNS bound to cancer cells are illuminated a large temperature difference between the hot nanostructure surface and the cooler surrounding biological medium occurs resulting in abrupt local temperature increase and corresponding cell death.

Once researchers understood the fundamentals of PTT, they began to think of creative ways to use the heating effect in drug delivery. Yavuz et al. created gold nanocages and loaded them with doxorubicin, a cancer therapeutic, and then a thermal linker polyer, pNIPAAm, to control the release of the drug through temperature. This temperature was controlled by nanocage photothermal heating.[83] This concept is represented in Figure 1.9b. It is the phothermal conversion, itself, required to break the linker and release the drug.

Besides their heating properties, researchers began to see gold nanoparticles as nanocarriers that acted as vessels for drug delivery and were inert spectators of the drug therapy (Figure 1.9c) Han et al. used gold nanospheres as carriers of DNA, which were cleaved off via Ultra-Violet light, in which the gold nanoparticle was completely inert in the mechanism.[84] Both heat and light are exogenous stimuli, but there are also plenty of endogenous stimuli for which gold nanoparticles have been used for in drug delivery such as pH, ionic strength, and ligand concentration that are beyond the optics focus of this work.

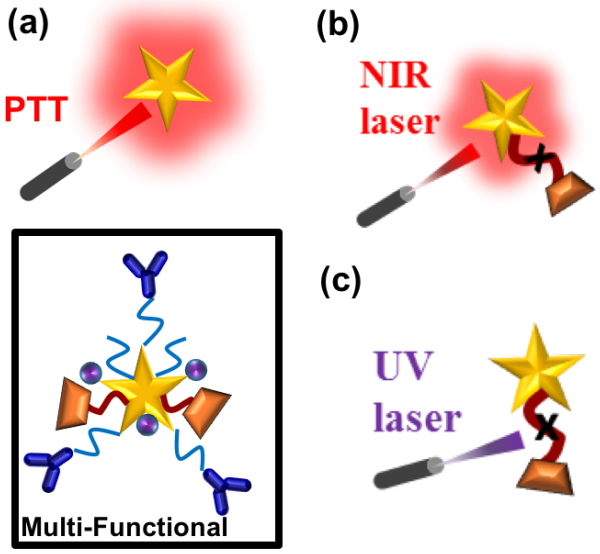

Figure 1.9: Multifunctional and combinational therapeutic approach offered by gold nanoplatforms. Diagramed are three different therapeutic approaches offered by gold nanostructures including: (a) photothermal therapy, (b) drug delivery using NIR light to convert light to heat to break linker, and (c) drug delivery via UV light to break linker where nanoparticle is simply acting as shipping vessel.

1.6.3 Cancer Theranostics

The past two decades have witnessed a tremendous increase in GNS based diagnostic agents, and therapeutic actuators. Theranostic agents can simultaneously target, diagnose, and deliver a therapeutic function enabling highly specific disease detection and treatment in a single clinical procedure. GNS based theranostic nanoprobes have been developed by either combining a single imaging and therapeutic technique, or integrating dual-modality diagnostics with multiple therapeutic functionalities. Nearly a decade ago, before the term theranostic was coined, the theranostic potential of nanoshells was demonstrated with simultaneous dark field imaging and photothermal therapy.[85-87] This was soon followed by the use of nanorods[88] and other core-shell GNS[89, 90] for imaging and therapy of malignant cells *in vitro*. In present times, there is a representative list that takes advantage of all the unique optical properties of the gold nanoparticles to combine them into unique theranostic treatments (refer Table 1.1)

To be successful against these deadly cancers, there must be the incorporation of both therapy and imaging. Thus, theranostic nanoparticles such as liposomes or other polymer encapsulations started to develop that offered both diagnostic information and therapy at the same time. However, what these particles lacked was the photothermal therapy (PTT) of the plasmonic nanoparticles. Thus, the ability to create heat from light is what separates the PNS from the other therapeutics and is what makes their therapy the most effective. The ability to perform PTT for heating and drug release in combination with the diagnostic capability put these gold nanoparticles at the forefront of the theranostic age. Such multifunctional nanostructures simultaneously enable highly specific detection of a disease followed by targeted, image-guided treatment all within a single clinical procedure.

Table 1.1: Examples of theranostic plasmonic nanostructures and their corresponding diagnostic and therapeutic modalities. List is representative of current progress in the nanomedicine field.

Plasmonic Nanostructure	Diagnostic Modality	Therapeutic Function	Targeted Cell Line	Ref.
SiO_2/Au/Fe_3O_4 Nanoshells	MRI, NIR fluorescence	Photothermal	SKBR3 breast cancer	[91, 92]
SiO_2/Au Nanoshells	PET	Photothermal	OVCAR3 ovarian cancer	[93]
			U87 human glioblastoma	[94]
Fe_3O_4/SiO_2/Au Nanoshells	MRI	Photothermal	A431 human epithelial cancer	[95]
Polymer/Au Nanoshell	Ultrasound	Photothermal	HeLa cervical cancer	[96]
Micelle/Au Nanoshell	MRI	Light induced drug release	HeLa cervical cancer	[97]
Hollow Au Nanospheres	PAT	Photothermal	U87 human glioblastoma transfected with luciferase gene	[98]
Nanostars	Two-photon fluorescence	Photothermal	SKBR3 breast cancer	[99]
	SERS	ROS generation	BT549 breast cancer	[100]
Nanoroses	MRI, Dark-field scattering	Photothermal	Primary peritoneal macrophages	[101]
Au nanoparticle-nanobubbles	Dark-field scattering	Photothermal	C4-2B prostate cancer	[102]
Au nanoparticles	CT imaging	Drug Delivery	PC3 prostate cancer	[103]
	PAT	Photothermal	SCK breast carcinoma	[104]
Au nanorods	SERS	Photothermal	HeLa cervical cancer	[105]
	NIR fluorescence	Photodynamic, Photothermal	SCC7 Squamous cell carcinoma	[106]
	Two-photon fluorescence	Drug Delivery	A549 human lung cancer	[107]
	NIR fluorescence	Photodynamic, Photothermal	A549 human lung cancer	[108]
	SERS, NIR Fluorescence	Photodynamic	HeLa cervical cancer	[109]
	X-ray, CT	Radiation, Photothermal	MGC803 gastric cancer	[110]
	MRI	Photothermal	KB human epidermoid oral carcinoma	[111]
	Dark field, Fluorescence	Drug Delivery, Photothermal	LoVo human colorectal cancer	[112]
	Dark field	Photothermal	A375 human umbilical vein cancer	[113]
	Fluorescence	Photothermal	HeLa cervical cancer	[114]
	PET	Drug Delivery	U87MG human malignant glioma	[115]

MRI = magnetic resonance imaging NIR = near-infrared PET = positron emission tomography
PAT = photoacoustic tomography ROS = reactive oxygen species
CT = computed tomography SERS = Surface enhanced Raman scattering

1.6.4 Immunoimaging and Immunotherapy

The upregulation of immune checkpoint receptor programmed death protein 1, PD-1, expressed on activated $CD8^+$ T-cells, impedes effector T-cell function by binding to its ligand, PD-L1.[116-118] Upon binding, interferons (IFN-γ) produced by activated T-cells upregulate PD-L1 expression which contributes to immunosuppression in the tumor microenvironment. Cancer immunotherapy, particularly blockade of inhibitory pathways such as PD-L1, has recently driven a perspective shift in the treatment of multiple cancers.[119-121] This underscores the significance of PD-L1 as a target receptor for immunoimaging.

The new medicinal field of immunotherapy, utilizing one's own immune system in treating disease, has allowed theranostic gold nanoplatforms another opportunity to provide unique and beneficial cancer treatment. By identifying, tracking, and understanding the immune system pathways to the point where it can be determined which receptor to manipulate for a safe, endogenous, and recruited therapy can be administered. To this point, PD-L1 receptor coverage has been linked to candidacy for immunotherapy with antiPDL1 antibodies on an individualized case basis.[2, 122] Theranostic nanoplatforms could be used for SERS imaging in detecting the PD-L1 expression on the surface of tumor and then, subsequently perform photothermal therapy, PTT-triggered drug release, or T-cell recruitment to administer therapy. Current multiplex SERS studies are being performed to demonstrate the potential of immuno-imaging by targeting the PD-L1 receptor which is a vital interaction in the T-cell immune checkpoint.[116, 122, 123] Further studies are investigating these EGFR and PD-L1 receptors in human xenograft models through *in vivo* SERS imaging. Additionally, current ongoing studies in utilizing antiPD-L1 as a therapeutic agent[3, 117, 124] open the avenue for combinational theranostic probes with multiple therapeutic or diagnostic modalities. The theranostic MGNs could induce the

recruitment of a heat shock protein or another immune response that could be used as to trigger immunotherapy.[125, 126] The high biocompatibility, photothermal capability, and straightforward surface chemistry make the MGNs a prime candidate for further theranostic individualized medicinal studies.

1.7 Bibliography

1. Abramson, V.G., et al., *Subtyping of Triple-Negative Breast Cancer: Implications for Therapy.* Cancer, 2015. **121**: p. 8-16.
2. Blau, R., et al., *Are Nanotheranostics and Nanodiagnostics-Guided Drug Delivery Stepping Stones Towards Precision Medicine?* Drug Resist. Update., 2016. **27**: p. 39-58.
3. Gelerstein, E., et al., *Regression of Intracranial Meningioma Following Treatment with Nivolumab: Case Report and Review of the Literature.* J. Clin. Neurosci., 2017. **37**(51-53).
4. Taube, J.M., et al., *Association of PD-1, PD-1 Ligands, and Other Features of the Tumor Immune Microenvironment with Response to Anti-PD-1 Therapy.* Clin. Cancer Res., 2014. **20**: p. 5064-5074.
5. Balko, J.M., T.P. Stricker, and C.L. Arteaga, *The Genomic Map of Breast Cancer: Which Roads Lead to Better Targeted Therapies?* Breast Cancer Res., 2013. **15**: p. 1-9.
6. Weintraub, K., *Biomedicine: The new gold standard.* Nature, 2013. **495**: p. S14-S16.
7. Peddi, P.F., M.J. Ellis, and C. Ma, *Molecular Basis of Triple Negative Breast Cancer and Implications for Therapy.* Int. J. Breast Cancer, 2011. **2012**: p. 1-7.
8. Balko, J.M., et al., *Molecular Profiling of the Residual Disease of Triple-Negative Breast Cancers after Neoadjuvant Chemotherapy Identifies Actionable Therapeutic Targets.* Cancer Discov., 2014. **4**(2): p. 232-245.
9. Hanahan, D. and R.A. Weinberg, *The Hallmarks of Cancer.* Cell, 2000. **100**: p. 57-70.
10. Chaffer, C.L. and R.A. Weinberg, *A perspective on cancer cell metastasis.* Science, 2011. **331**: p. 1559−1564.
11. Wirtz, D., K. Konstantopoulos, and P.C. Searson, *The physics of cancer: the role of physical interactions and mechanical forces in metastasis.* Nature Rev. Cancer, 2011. **11**: p. 512-522.
12. Wang, K., et al., *Characterizing Breast Cancer Xenograft Epidermal Growth Factor Receptor Expression by Using Near-Infrared Optical Imaging.* Acta Radiol., 2009. **50**: p. 1095-1103.
13. Lee, S., et al., *Surface-Enhanced Raman Scattering Imaging of HER2 Cancer Markers Overexpressed in Single MCF7 Cells Using Antibody Conjugated Hollow Gold Nanospheres.* Biosens. Bioelectron., 2009. **24**: p. 2260-2263.
14. Aioub, M. and M.A. El-Sayed, *A Real-Time Surface Enhanced Raman Spectroscopy Study of Plasmonic Photothermal Cell Death Using Targeted Gold Nanoparticles.* J. Am. Chem. Soc., 2016. **138**: p. 1258-1264.
15. Yang, A.-q., et al., *Rational Design of Au Nanorods Assemblies for Highly Sensitive and Selective SERS Detection of Prostate Specific Antigen.* RSC Adv., 2015. **5**: p. 38354-38360.
16. Li, M., et al., *Three-Dimensional Hierarchical Plasmonic Nano-Architecture Enhanced Surface-Enhanced Raman Scattering Immunosensor for Cancer Biomarker Detection in Blood Plasma.* ACS Nano, 2013. **7**: p. 4967-4976.
17. Wu, L., et al., *Simultaneous evaluation of p53 and p21 expression level for early cancer diagnosis using SERS technique.* Analyst, 2013. **138**: p. 3450-3456.
18. Chon, H., et al., *Simultaneous Immunoassay for the Detection of Two Lung Cancer Markers using Functionalized SERS Nanoprobes.* Chem. Commun., 2011. **47**: p. 12515-12517.

19. Fujimoto, R., et al., *Interference of the surface plasmon polaritons with an Ag waveguide probed by dual-probe scanning near-field optical microscopy.* Applied Surface Science, 2012. **258**: p. 7372-7376.
20. Maier, S.A., *Plasmonics: Fundamentals and Applications*. 2007, New York, NY: Springer Science + Business Media LLC.
21. Mayer, K.M. and J.H. Hafner, *Localized Surface Plasmon Resonance Sensors.* Chem. Rev., 2011. **111**: p. 3828–3857.
22. Willets, K.A. and R.P.V. Duyne, *Localized Surface Plasmon Resonance Spectroscopy and Sensing.* Annu. Rev. Phys. Chem., 2007. **58**: p. 267-297.
23. Fang, S., et al., *Gold Nanorods-Based Theranostics for Simultaneous Fluorescence/Two-Photon Luminescence Imaging and Synergistic Phototherapies.* J. Nanomater., 2016. **1082746**: p. 1-10.
24. Zhang, Z., et al., *Silver Nanoparticle Gated, Mesoporous Silica Coated Gold Nanorods (AuNR@MS@AgNPs): Low Premature Release and Multifunctional Cancer Theranostic Platform.* ACS Appli. Mater. Interfaces, 2015. **7**(11): p. 6211-6219.
25. Butterworth, K.T., et al., *Preclinical Evaluation of Gold-DTDTPA Nanoparticles as Theranostic Agents in Prostate Cancer Radiotherapy.* Nanomedicine, 2016. **11**(16): p. 2035-2047.
26. Yilmaz, G., et al., *Poly(methacrylic acid)-Coated Gold Nanoparticles: Functional Platforms for Theranostic Applications.* Biomacromolecules, 2016. **Epub**.
27. Shao, J., et al., *Photothermal Nanodrugs: Potential of TNF-Gold Nanospheres for Cancer Theranostics.* Sci. Rep., 2013. **3**: p. 1-9.
28. Thakor, A.S. and S.S. Gambhir, *Nanooncology: The Future of Cancer Diagnosis and Therapy.* CA-Cancer J. Clin., 2013. **63**: p. 395-418.
29. Myroshnychenko, V., et al., *Modelling the optical response of gold nanoparticles.* Chem. Soc. Rev., 2008. **37**: p. 1792-1805.
30. Trigari, S., et al., *Synthesis and modelling of gold nanostars with tunable morphology and extinction spectrum.* J. Mater. Chem., 2011. **21**: p. 6531-6540.
31. Melancon, M.P., et al., *In vitro and in vivo targeting of hollow gold nanoshells directed at epidermal growth factor receptor for photothermal ablation therapy.* Mol. Cancer Ther., 2008. **7**: p. 1730-1739.
32. Popovtzer, R., et al., *Targeted Gold Nanoparticles Enable Molecular CT Imaging of Cancer.* Nano Lett., 2008. **8**: p. 4593-4596.
33. Webb, J.A. and R. Bardhan, *Emerging Advances in Nanomedicine with Engineered Gold Nanostructures.* Nanoscale, 2014. **6**: p. 2502-2530.
34. Weissleder, R., *A Clearer Vision for In Vivo Imaging.* Nat. Biotechnol., 2001. **19**: p. 316-317.
35. Schuller, J.A., et al., *Plasmonics for extreme light concentration and manipulation.* Nat. Mater., 2010. **9**: p. 193–204.
36. Dykman, L. and N. Khlebtsov, *Gold nanoparticles in biomedical applications: recent advances and perspectives.* Chem. Soc. Rev., 2012. **41**: p. 2256-2282.
37. Alkilany, A.M., et al., *Cellular Uptake and Cytotoxicity of Gold Nanorods: Molecular Origin of Cytotoxicity and Surface Effects.* Small, 2009. **5**: p. 701-708.
38. Arvizo, R.R., et al., *Modulating Pharmacokinetics, Tumor Uptake and Biodistribution by Engineered Nanoparticles.* Plos ONE, 2011. **6**: p. e24374.

39. Chen, W.-H., et al., *Therapeutic Nanomedicine Based on Dual-Intelligent Functionalized Gold Nanoparticles for Cancer Imaging and Therapy In Vivo.* Biomaterials, 2013. **34**: p. 8798-8807.
40. Schneider, G.F., et al., *Multifunctional Cytotoxic Stealth Nanoparticles. A Model Approach with Potential for Cancer Therapy.* Nano Lett., 2009. **9**: p. 636-642.
41. Au, J.T., et al., *Gold Nanoparticles Provide Bright Long-Lasting Vascular Contrast for CT Imaging.* AJR Am. J. Roentgenol., 2013. **200**(200): p. 1347-13451.
42. Park, C., et al., *Cyclodextrin-covered gold nanoparticles for targeted delivery of an anti-cancer drug.* J. Mater. Chem., 2009. **19**: p. 2310-2315.
43. Lee, J.-S., et al., *Gold, Poly(b-amino ester) Nanoparticles for Small Interfering RNA Delivery.* Nano Lett., 2009. **9**: p. 2402-2406.
44. Peer, D., et al., *Nanocarriers as an emerging platform for cancer therapy.* Nat. Nanotech., 2007. **2** p. 751-760.
45. Dreaden, E.C., et al., *Beating cancer in multiple ways using nanogold.* Chem. Soc. Rev., 2011. **40**: p. 3391-3404.
46. Bardhan, R., et al., *Theranostic nanoshells: from probe design to imaging and treatment of cancer.* Acc. Chem. Res., 2011. **44**: p. 936-946.
47. Huang, X., et al., *Plasmonic photothermal therapy (PPTT) using gold nanoparticles.* Lasers Med. Sci., 2008. **23**: p. 217-228.
48. Bantz, K.C., et al., *Recent progress in SERS biosensing.* Phys. Chem. Chem. Phys., 2011. **13**: p. 11551–11567.
49. Shuker, R. and R.W. Gammon, *Raman-Scattering Selection-Rule Breaking and the Density of States in Amorphous Materials.* Phys. Rev. Lett., 1970. **25**: p. 222-225.
50. Campion, A. and P. Kambhampati, *Surface-Enhanced Raman Scattering.* Chem. Soc. Rev., 1998. **27**: p. 241-250.
51. Fleischmann, M., P.J. Hendra, and A.J. McQuillan, *Raman Spectra of Pyridine Adsorbed at a Silver Electrode.* Chem. Phys. Lett., 1974. **26**: p. 163-166.
52. Jeanmaire, D.L. and R.P.V. Duyne, *Surface Raman Spectroelectrochemistry Part I. Heterocyclic, Aromatic, and Aliphatic Amines Adsorbed on the Anodized Silver Electrode.* J. Electronanal. Chem., 1977. **84**: p. 1-20.
53. Creighton, J.A., C.G. Blatchford, and M.G. Albrecht, *Plasma Resonance Enhancement of Raman Scattering by Pyridine Adsorbed on Silver or Gold Sol Particles of Size Comparable to the Excitation Wavelength.* J. Chem. Soc., Faraday Trans. 2, 1979. **75**: p. 790-798.
54. Creighton, J.A., et al., *The Dependence of the Intensity of Raman Bands of Pyridine at a Silver Electrode on the Wavelength of Excitation.* Chem. Phys. Lett., 1978. **55**: p. 55-58.
55. Albrecht, M.G. and J.A. Creighton, *Anomalously Intense Raman Spectra of Pyridine at a Silver Electrode.* J. Am. Chem. Soc., 1977. **99**: p. 5215-5217.
56. Kneipp, K., et al., *Surface-enhanced Raman scattering and biophysics.* J. Phys.: Condens. Matter, 2002. **14**: p. R597–R624.
57. Markel, V.A., et al., *Near-field optical spectroscopy of individual surface-plasmon modes in colloid clusters.* Physical Reveiw B, 1999. **59**: p. 10903-10909.
58. Zeisel, D., et al., *Near-field surface-enhanced Raman spectroscopy of dye molecules adsorbed on silver island films.* Chem. Phys. Lett., 1998. **283**: p. 381-385.
59. Furtak, T.E. and J. Reyes, *A Critical Analysis of Theoretical Models for the Giant Raman Effect from Adsorbed Molecules.* Surface Science, 1980. **93**: p. 351-382.

60. García-Vidal, F.J. and J.B. Pendry, *Collective Theory for Surface Enhanced Raman Scattering.* Phys. Rev. Lett., 1996. **77**: p. 1163-1166.
61. Stiles, P.L., et al., *Surface-Enhanced Raman Spectroscopy.* Annu. Rev. Anal. Chem., 2008. **1**: p. 601-626.
62. Doering, W.E. and S. Nie, *Single-Molecule and Single-Nanoparticle SERS: Examining the Roles of Surface Active Sites and Chemical Enhancement.* J. Phys. Chem. B, 2002. **106**: p. 311-317.
63. Kumar, P.S., et al., *High-yield Synthesis and Optical Response of Gold Nanostars.* Nanotechnology, 2008. **19**: p. 015606.
64. Yuan, H., et al., *Gold Nanostars: Surfactant-free Synthesis, 3D Modelling, and Two-photon Photoluminescence Imaging.* Nanotechnology, 2012. **23**: p. 075102.
65. Rodrıguez-Oliveros, R. and J.A. Sanchez-Gil, *Gold Nanostars as Thermoplasmonic Nanoparticles for Optical Heating.* Opt. Express, 2012. **20**: p. 621 − 626.
66. Webb, J.A., et al., *Geometry-Dependent Plasmonic Tunability and Photothermal Characteristics of Multibranched Gold Nanoantennas.* J. Phys. Chem. C, 2014. **118**: p. 3696-3707.
67. Jiang, C., et al., *A chemically reactive Raman probe for ultrasensitively monitoring and imaging the in vivo generation of femtomolar oxidative species as induced by anti-tumor drugs in living cells.* Chem. Commun., 2013. **49**: p. 6647-6649.
68. Ngo, Y.H., et al., *Gold Nanoparticle−Paper as a Three-Dimensional Surface Enhanced Raman Scattering Substrate.* Langmuir, 2012. **28**: p. 8782-8790.
69. Lee, C.H., L. Tian, and S. Singamaneni, *Paper-Based SERS Swab for Rapid Trace Detection on Real-World Surfaces.* ACS Appl. Mater. Interfaces, 2010. **2**: p. 3429-3435.
70. Rodríguez-Lorenzo, L., et al., *Zeptomol Detection Through Controlled Ultrasensitive Surface-Enhanced Raman Scattering.* J. Am. Chem. Soc., 2009. **131**: p. 4616-4618.
71. Maiti, K.K., et al., *Multiplex Targeted In Vivo Cancer Detection Using Sensitive Near-Infrared SERS Nanotags.* Nano Today, 2012. **7**: p. 85-93.
72. Raza, A. and B. Saha, *In situ silver nanoparticles synthesis in agarose film supported on filter paper and its application as highly efficient SERS test stripes.* Forensic Science International, 2014: p. In press.
73. Chen, K., H. Han, and Z. Luo, *Streptococcus Suis II Immunoassay Based on Thorny Gold Nanoparticles and Surface Enhanced Raman Scattering.* Analyst, 2012. **137**: p. 1259-1264.
74. Panikkanvalappil, S.R., M.A. Mackey, and M.A. El-Sayed, *Probing the Unique Dehydration-Induced Structural Modifications in Cancer Cell DNA Using Surface Enhanced Raman Spectroscopy.* J. Am. Chem. Soc., 2013. **135**: p. 4815-4821.
75. Penn, M.A., D.M. Drake, and J.D. Driskell, *Accelerated Surface-Enhanced Raman Spectroscopy (SERS)-Based Immunoassay on a Gold-Plated Membrane.* Anal. Chem., 2013. **85**: p. 8609−8617.
76. Amendola, V., et al., *Magneto-Plasmonic Au-Fe Alloy Nanoparticles Designed for Multimodal SERS-MRI-CT Imaging.* Small, 2014. **10**: p. 2476-2478.
77. Kim, C., et al., *In Vivo Molecular Photoacoustic Tomography of Melanomas Targeted by Bioconjugated Gold Nanocages.* ACS Nano, 2010. **4**: p. 4559-4564.
78. Skala, M.C., et al., *Photothermal Optical Coherence Tomography of Epidermal Growth Factor Receptor in Live Cells Using Immunotargeted Gold Nanospheres.* Nano Lett., 2008. **8**: p. 3461-3467.

79. Bardhan, R., et al., *Nanoshells with Targeted Simultaneous Enhancement of Magnetic and Optical Imaging and Photothermal Therapeutic Response.* Adv. Func. Mater., 2009. **19**: p. 3901-3909.
80. Huang, Y., V.P. Swarup, and S.W. Bishnoi, *Rapid Raman Imaging of Stable, Functionalized Nanoshells in Mammalian Cell Cultures.* Nano Lett., 2009. **9**: p. 2914-2920.
81. Link, S. and M.A. El-Sayed, *Size and Temperature Dependence of the Plasmon Absorption of Colloidal Gold Nanoparticles.* J. Phys. Chem. B, 1999. **103**: p. 4212-4217.
82. Link, S. and M.A. El-Sayed, *Shape and size dependence of radiative, non-radiative and photothermal properties of gold nanocrystals.* Int. Rev. Phys. Chem., 2000. **19**: p. 409 - 453.
83. Yavuz, M.S., et al., *Gold nanocages covered by smart polymers for controlled release with near-infrared light.* Nat. Mater., 2009. **8**: p. 935-939.
84. Han, G., et al., *Light-Regulated Release of DNAand Its Delivery to Nuclei by Means of Photolabile Gold Nanoparticles.* Angew. Chem. Int. Ed., 2006. **45**: p. 3165-3169.
85. Loo, C., et al., *Nanoshell-Enabled Photonics-Based Imaging and Therapy of Cancer.* Tech. Cancer Res. Treat., 2004. **3**: p. 33-40.
86. Loo, C., et al., *Immunotargeted Nanoshells for Integrated Cancer Imaging and Therapy.* Nano Lett., 2005. **5**: p. 709-711.
87. Gobin, A.M., et al., *Near-Infrared Resonant Nanoshells for Combined Optical Imaging and Photothermal Cancer Therapy.* Nano Lett., 2007. **7**: p. 1929-1934.
88. Huang, X., et al., *Cancer Cell Imaging and Photothermal Therapy in the Near-Infrared Region by Using Gold Nanorods.* J. Am. Chem. Soc., 2006. **128**: p. 2115-2120.
89. Kim, J., et al., *Designed Fabrication of Multifunctional Magnetic Gold Nanoshells and Their Application to Magnetic Resonance Imaging and Photothermal Therapy.* Angew. Chem. Int. Ed., 2006. **118**: p. 7918-7922.
90. Ji, X., et al., *Bifunctional Gold Nanoshells with a Superparamagnetic Iron Oxide−Silica Core Suitable for Both MR Imaging and Photothermal Therapy.* J. Phys. Chem. C, 2007. **111**: p. 6245-6251.
91. Bardhan, R., et al., *Nanoshells Engineered for Targeted, Simultaneous Enhancement of Magnetic and Optical Imaging and Photothermal Therapeutic Response.* Adv. Func. Mater., 2009. **19**: p. 3901-3909.
92. Bardhan, R., et al., *Tracking of multimodal therapeutic nanocomplexes targeting breast cancer in vivo.* Nano Lett., 2010. **10**: p. 4920-4928.
93. Chen, W., et al., *A molecularly targeted theranostic probe for ovarian cancer.* Mol. Cancer Therap., 2010. **9**: p. 1028-1038.
94. Xie, H., et al., *Integrin αvβ3-targeted gold nanoshells augment tumor vasculature-specific imaging and therapy.* Int. J. Nanomedicine, 2011. **6**: p. 259-269.
95. Melancon, M.P., et al., *Theranostics with Multifunctional Magnetic Gold Nanoshells: Photothermal Therapy and T2* Magnetic Resonance Imaging.* Invest. Radiol., 2011. **46**: p. 132-140.
96. Ke, H., et al., *Gold-Nanoshelled Microcapsules: ATheranostic Agent for Ultrasound Contrast Imaging and Photothermal Therapy.* Angew. Chem. Int. Ed., 2011. **50**: p. 3017 -3021.

97. Ma, Y., et al., *Gold Nanoshell Nanomicelles for Potential Magnetic Resonance Imaging, Light-Triggered Drug Release, and Photothermal Therapy.* Adv. Funct. Mater., 2013. **23**: p. 815-822.
98. Lu, W., et al., *Effects of Photoacoustic Imaging and Photothermal Ablation Therapy Mediated by Targeted Hollow Gold Nanospheres in an Orthotopic Mouse Xenograft Model of Glioma.* Cancer Res., 2011. **71**: p. 6116-6121.
99. Yuan, H., et al., *In vivo particle tracking and photothermal ablation using plasmon-resonant gold nanostars.* Nanomedicine: Nanotech. Biol. Medicine, 2012. **8**: p. 1355-1363.
100. Fales, A.M., H. Yuan, and T. Vo-Dinh, *Silica-Coated Gold Nanostars for Combined Surface-Enhanced Raman Scattering (SERS) Detection and Singlet-Oxygen Generation: A Potential Nanoplatform for Theranostics.* Langmuir, 2011. **27**: p. 12186-12190.
101. Elbakry, A., et al., *Layer-by-Layer Assembled Gold Nanoparticles for siRNA Delivery.* Nano Lett., 2009. **9**: p. 2059-2064.
102. Wagner, D.S., et al., *The in vivo performance of plasmonic nanobubbles as cell theranostic agents in zebrafish hosting prostate cancer xenografts.* Biomaterials, 2010. **31**: p. 7567-7574.
103. Kim, D., Y.Y. Jeong, and S. Jon, *A Drug-Loaded Aptamer Gold Nanoparticle Bioconjugate for Combined CT Imaging and Therapy of Prostate Cancer.* ACS Nano, 2010. **4**: p. 3689-3696.
104. Shao, J., et al., *Photothermal nanodrugs: potential of TNF-gold nanospheres for cancer theranostics.* Scientific Reports, 2013. **3**: p. 1293.
105. Maltzahn, G.v., et al., *SERS-Coded Gold Nanorods as a Multifunctional Platform for Densely Multiplexed Near-Infrared Imaging and Photothermal Heating.* Adv. Mater., 2009. **21**: p. 3175-3180.
106. Jang, B., et al., *Gold Nanorod-Photosensitizer Complex for Near-Infrared Fluorescence Imaging and Photodynamic/Photothermal Therapy In Vivo.* ACS Nano, 2011. **5**: p. 1086-1094.
107. Zhang, Z., et al., *Mesoporous Silica-Coated Gold Nanorods as a Light-Mediated Multifunctional Theranostic Platform for Cancer Treatment.* Adv. Mater., 2012. **24**: p. 1418-1423.
108. Kuo, W.-S., et al., *Gold Nanorods in Photodynamic Therapy, as Hyperthermia Agents, and in Near-Infrared Optical Imaging.* Angew. Chem., 2010. **122**: p. 2771 -2775.
109. Zhang, Y., et al., *Multifunctional Gold Nanorods with Ultrahigh Stability and Tunability for In Vivo Fluorescence Imaging, SERS Detection, and Photodynamic Therapy.* Angew. Chem. Int. Ed., 2013. **52**: p. 1148 -1151.
110. Huang, P., et al., *Folic acid-conjugated Silica-modified gold nanorods for X-ray/CT imaging-guided dual-mode radiation and photo-thermal therapy.* Biomaterials, 2011. **32**: p. 9796-9809.
111. Wang, D.-W., et al., *Folate-conjugated Fe3O4@SiO2@gold nanorods@mesoporous SiO2 hybrid nanomaterial: a theranostic agent for magnetic resonance imaging and photothermal therapy.* J. Mater. Chem. B, 2013. **1**: p. 2934-2942.
112. Guo, R., et al., *Multifunctional Nanocarriers for Cell Imaging, Drug Delivery, and Near-IR Photothermal Therapy.* Langmuir, 2010. **26**: p. 5428-5434.
113. Li, Z., et al., *RGD-Conjugated Dendrimer-Modified Gold Nanorods for in Vivo Tumor Targeting and Photothermal Therapy.* Mol. Pharmaceutics, 2009. **7**: p. 94-104.

114. Maestro, L.M., et al., *Fluorescent nanothermometers provide controlled plasmonic-mediated intracellular hyperthermia.* Nanomedicine, 2013. **8**: p. 379-388.
115. Xiao, Y., et al., *Gold Nanorods Conjugated with Doxorubicin and cRGD for Combined Anti-cancer Drug Delivery and PET Imaging.* Theranostics, 2012. **2**: p. 757-768.
116. Pardoll, D.M., *The Blockade of Immune Checkpoints in Cancer Immunotherapy.* Nat. Rev. Cancer, 2012. **12**: p. 252-264.
117. Philips, G.K. and M. Atkins, *Therapeutic Uses of anti-PD-1 and anti-PD-L1 Antibodies.* Int. Immunol., 2014. **27**: p. 39-46.
118. Tumeh, P.C., et al., *PD-1 Blockade Induces Responses by Inhibiting Adaptive Immune Resistance.* Science, 2014. **515**: p. 568-571.
119. Azuma, K., et al., *Association of PD-L1 Overexpression with Activating EGFR Mutations in Surgically Resected Nonsmall-Cell Lung Cancer.* Ann. Oncol., 2014. **25**: p. 1935-1940.
120. Baptista, M.Z., et al., *Prognostic Significance of PD-L1 and PD-L2 in Breast Cancer.* Hum. Pathol., 2016. **47**: p. 78-84.
121. Callea, M., et al., *Differential Expression of PD-L1 between Primary and Metastatic Sites in Clear Cell Renal Cell Carcinoma.* Cancer Immunol. Res., 2015. **3**: p. 1158-1164.
122. Nguyen, L.T. and P.S. Ohashi, *Clinical Blockade of PD1 and LAG3 - Potential Mechanisms of Action.* Nat. Rev. Immunology, 2015. **15**: p. 45-56.
123. Greil, R., et al., *Reactivation of Dormant Anti-Tumor Immunity - A Clinical Perspective of Therapeutic Immune Checkpoint Modulation.* Cell Commun. Signal., 2017. **15**: p. 1-16.
124. Moreno, B.H. and A. Ribas, *Anti-Programmed Cell Death Protein-1/Ligand-1 Therapy in Different Cancers.* Brit. J. Cancer, 2015. **112**: p. 1421-1427.
125. Shevtsov, M. and G. Multhoff, *Heat Shock Protein–Peptide and HSP-Based Immunotherapies for the Treatment of Cancer.* Frontiers in Immunology, 2016. **7**: p. 171. PMC. Web. 9 May 2017.
126. Bear, A.S., et al., *Elimination of Metastatic Melanoma Using Gold Nanoshell-Enabled Photothermal Therapy and Adoptive T Cell Transfer.* PLoS ONE, 2013. **8.7**: p. e69073. PMC. Web. 9 May 2017.

CHAPTER 2

INVESTIGATING THE SYNTHESIS, GEOMETRY-DEPENDENT PLASMONIC TUNABILITY, AND PHOTOTHERMAL PROPERTIES OF MULTIBRANCHED GOLD NANOANTENNAS

2.1 Summary

In this chapter, we synthesized multibranched gold nanoantennas (MGNs) of variable geometry by a one-step seedless approach using 4-(2-hydroxyethyl)-1-piperazineethanesulfonic acid (HEPES) as a capping and reducing agent. This approach enables us to modulate the MGNs geometry by controlling three different parameters: [HEPES], [Au^{+3}], and pH of HEPES buffer. By altering the MGNs morphology with minimal increase in the overall dimensions, the plasmon resonances were tuned from visible to NIR range. The MGNs plasmon resonances demonstrated a non-intuitive blue-shift when pH > pKa of HEPES which we attributed to emergence of charge transfer oscillations formed when MGNs cluster to dimers and trimers. Further, due to the presence of multiple sharp protrusions, the MGNs demonstrated a refractive index sensitivity of 373 nm/RIU, which is relatively high for this class of branched nanostructures of similar size. Finally, the sharp protrusions of MGNs also give rise to intense photothermal efficiencies; ~54 °C was achieved within 5 minutes of laser illumination demonstrating the efficacy of MGNs in therapeutic applications. By modulating the mass density of MGNs, the laser flux, and time of illumination, we provide a detailed analysis of the photothermal characteristics of MGNs. Due to intense photothermal characteristics and NIR plasmon resonance, the MGNs were shown to be viable candidates for usage in future theranostic studies.

2.2 Introduction

Metal nanostructures interact with light generating surface plasmons that are governed by the nanostructure shape, size, and composition.[1, 2] While optical resonances of simple isotropic nanostructures are controlled by manipulating their size, the resonances of hierarchical anisotropic nanostructures are complex function of their geometry.[3-8] By controlling the morphology of such complex anisotropic nanostructures, the optical characteristics can be selectively tuned to achieve desirable properties.[9] Branched gold nanostructures are complex architectures with plasmon resonances that can be tuned by modulating the protrusion length and density with minimum alteration of the overall dimensions.[10-15] Typically, branched nanostructures have a core that serves as an efficient nanoscale antenna which couples to the protrusions routing incident light in unique and distinct ways.[16] Unlike other antenna-like geometries such as nanorods and nanobipyramids where the antenna strength can only be enhanced by increasing their size, in branched nanostructures the antenna efficiency can be increased by manipulating the protrusion length and number density without significantly altering the overall dimensions.[1, 17] This intense nanoantenna effect generates unprecedented electromagnetic near-fields at the sharp tips of the branched nanostructures which decay exponentially within tens of nanometers from the particle surface, thus confining regions of enhanced fields to spatially distinct regions relative to the particle.[18] These near-field configurations of branched nanostructures enable a range of technological applications from highly sensitive localized surface plasmon resonance (LSPR) sensing,[12, 13] to surface enhanced spectroscopies,[19] to biomedicine,[20-23] and thermoplasmonics.[24]

The growth of anisotropic gold nanostructures requires a selective capping agent since gold has a symmetric face-centered cubic lattice. A range of star-shaped branched nanostructures

have been synthesized by seed mediated growth processes in aqueous media with cetyltrimethylammonium bromide (CTAB),[16] polyvinylpyrrolidone,[12, 14] and sodium citrate[22] as shape-directing capping agents. While the seeded-growth method is effective, this two-step approach often gives rise to polydispersity, low yield of MGNs, or generates other shapes due to minor heterogeneities in the gold seed. Such heterogeneous star-shaped mixtures with shape impurity impact the plasmonic properties resulting in plasmon damping, linewidth broadening, and mediocre ensemble LSPR sensing capabilities (although single particle LSPR sensing yields excellent results).[16, 25, 26] In this work we have synthesized multibranched gold nanoantennas (MGNs) by a one-step seedless approach using HEPES (4-(2-hydroxyethyl)-1-piperazineethanesulfonic acid) as a capping and reducing agent. HEPES is a biological buffer extensively utilized in biochemical reactions, cellular applications, and in some cell culture media.[27-29] Here we demonstrate that HEPES mediated MGN fabrication has several advantages.

First, unlike other techniques where the concentration of Au^{3+} ions is the only parameter that controls plasmonic tunability, in this work we show plasmon resonances can be tuned from the visible to the near-infrared by modifying three different parameters: concentration of HEPES, concentration of Au^{3+}, and pH of the buffer. Therefore by modulating these distinct chemical parameters, the geometry (*i.e.* protrusion length and protrusion density of MGNs) can be altered to achieve desired optical properties. Second, since the MGNs are synthesized in a biological buffer, this allows unambiguous manipulation for biochemical and biomedical applications without the need for tedious ligand or solvent exchange for biocompatibility. Third, eliminating the seed-step in this HEPES method enables straightforward scale-up of MGNs with high reproducibility in both the plasmon peak positions and widths. Heterogeneities during scale-up

resulting in linewidth broadening is a known obstacle in the seeded growth approach.[30] The HEPES mediated MGNs generate relatively narrow peak widths giving rise to extraordinary LSPR sensing capabilities. The MGNs synthesized in this work have an ensemble refractive index sensitivity of 373 nm/RIU, which is relatively high for similarly sized branched nanostructures of this class. Finally, the multiple sharp protrusions and corresponding nanoantenna effect of MGNs gives rise to intense light to heat conversion efficiency. We investigated the photothermal characteristics and subsequent rise in temperature of MGNs resonant with a near-infrared laser at 808 nm. A temperature increase to 54 °C was measured with a thermal camera within 5 minutes of illumination. By modulating the mass density of MGNs, the laser flux, and time of illumination, an investigation of MGNs photothermal capabilities was performed.

2.3 Results and Discussion

MGNs were synthesized by reducing Au^{3+} precursor with HEPES as a reducing and capping agent.[31] The geometry of MGNs were varied by modulating the concentration of HEPES buffer from 30 – 360 mM while keeping the concentration of Au^{3+} precursor constant at 20 mM and pH constant at 7.4 ± 0.1. As the HEPES concentration was increased, larger MGNs with longer protrusion lengths were formed. The morphological evolution of MGNs with increasing HEPES concentration was characterized with scanning electron microscopy (SEM) and transmission electron microscopy (TEM) shown in Figure 2.1. SEM micrographs demonstrate the three dimensional morphology of MGNs. At 30 mM HEPES concentration, spherical gold nanoparticles of 36 ± 3 nm diameters are formed with very small protrusions (Figure 2.1c). At 100 mM, well-defined MGNs with short protrusions and overall dimensions of

41 ± 4 nm are formed (Figure 2.1d) which increases to 50 ± 3 nm at 160 mM (Figure 2.1e). The MGNs size increases to 58 ± 4 nm at 300 mM HEPES (Figure 2.1f).

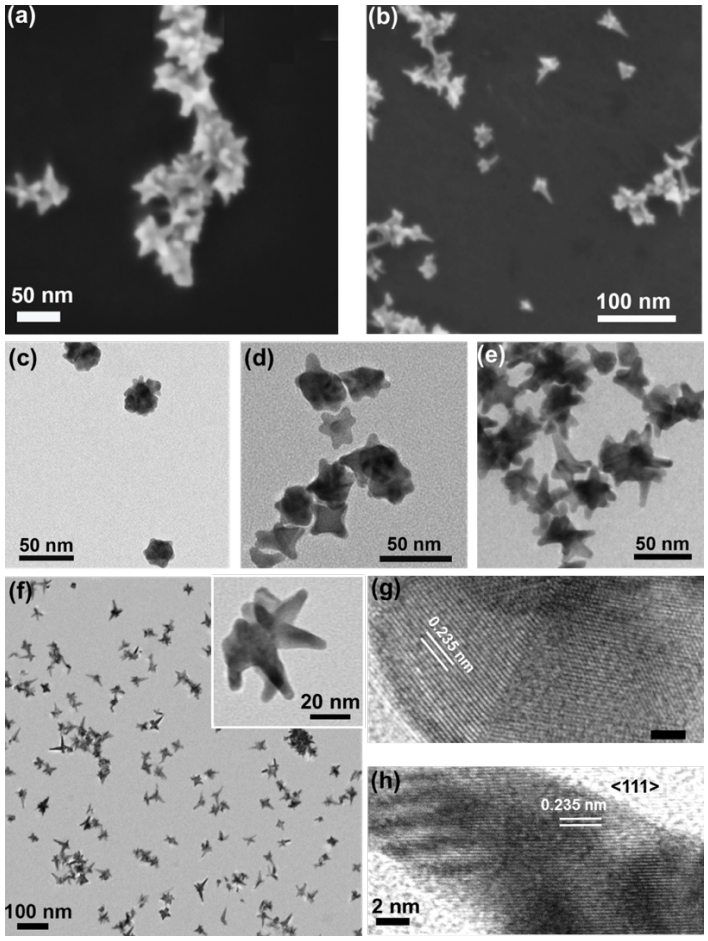

Figure 2.1: Scanning electron microscopy images of MGNs synthesized by (a) 160 mM HEPES buffer and (b) 300 mM HEPES buffer showing the three-dimensional morphology of the MGNs. Transmission electron microscopy (TEM) images of MGNs synthesized with varying HEPES concentration (c) 30 mM, (d) 100 mM, (e) 160 mM, and (f) 300 mM. High resolution TEM images of MGNs with d-spacing indicating (g) 《111》 facet in the MGN core and crystal plane twinning, and (h) growth along <111> direction for the MGN protrusion.

MGN dimensions were measured from tip-to-tip of the longest branches. We have also included the core size relative to the branch length of MGNs (Table 2.1). The electron microscopy images and size analysis demonstrate that as the concentration of HEPES is increased, the ratio of branch length to the core size increases with minimal change in overall size. The increasing HEPES also increases the density of branches on MGNs. Additional TEM

images and histograms of yield analysis of branch densities of MGNs formed with 100 mM and 300 mM HEPES are shown in Figure 2.2 and Figure 2.3.

Table 2.1: Core size and branch length as a function of HEPES concentration and corresponding plasmon resonance.

[HEPES]	Peak Position	Largest Tip-to-Tip Distance	Branch length	Ratio of Branch/Core Diameter
30 mM	577 nm	36 ± 3	4 ± 0.5	0.143
60 mM	620 nm	39 ± 3	11 ± 1	0.647
100 mM	657 nm	41 ± 4	13.5 ± 2	0.964
160 mM	704 nm	50 ± 3	Long: 23 ± 3 Short: 10 ± 1	Long: 1.353 Short: 0.588
300 mM	781 nm	58 ± 4	Long: 32 ± 4 Short: 12 ± 2	Long: 2.286 Short: 0.857

Note: With increasing concentration of HEPES, MGNs become increasingly more anisotropic and two different branch lengths are observed described as "long" and "short" here. Typically the length of 1 – 2 branches (out of 4 – 6 total branches) grew longer than the remaining branches.

The morphological evolution of MGNs with increasing [HEPES] is attributable to the amount of HEPES molecules available during the nucleation event prior to MGN formation and the weak adsorption of HEPES to Au along the <111> direction.[31] We performed high resolution TEM to investigate the role of crystal planes (Figure 2.1g, 2.1h). The measured d-spacing from the TEM images of the MGN core (Figure 2.1g). and protrusion (Figure 2.1h) clearly indicate protrusion growth and MGN formation occurs along the <111> direction. Initially, spherical gold nanoparticles nucleate in solution and HEPES binds to the nanoparticle surface. At low [HEPES]/[Au^{3+}] ratio, fewer HEPES molecules are available to bind exposing the different crystalline facets of gold nanoparticles for further Au^{3+} reduction. As the reaction

proceeds, more Au^{3+} ions are reduced on the nanoparticle surface giving rise to spherical morphology with very short protrusions (Figure 2.1c). As the [HEPES]/[Au^{3+}] ratio is increased, more HEPES molecules bind to preferred crystallographic planes with weak or no adsorption on the 《111》 family of planes (Figure 2.1d, 2.1e). Therefore as further Au^{3+} reduction occurs, preferential growth along the <111> direction transpires resulting in MGN formation. As HEPES is also a reducing agent in this synthesis, more Au^{3+} are reduced at higher HEPES concentrations on the 《111》 crystal planes yielding longer protrusions (Figure 2.1f).

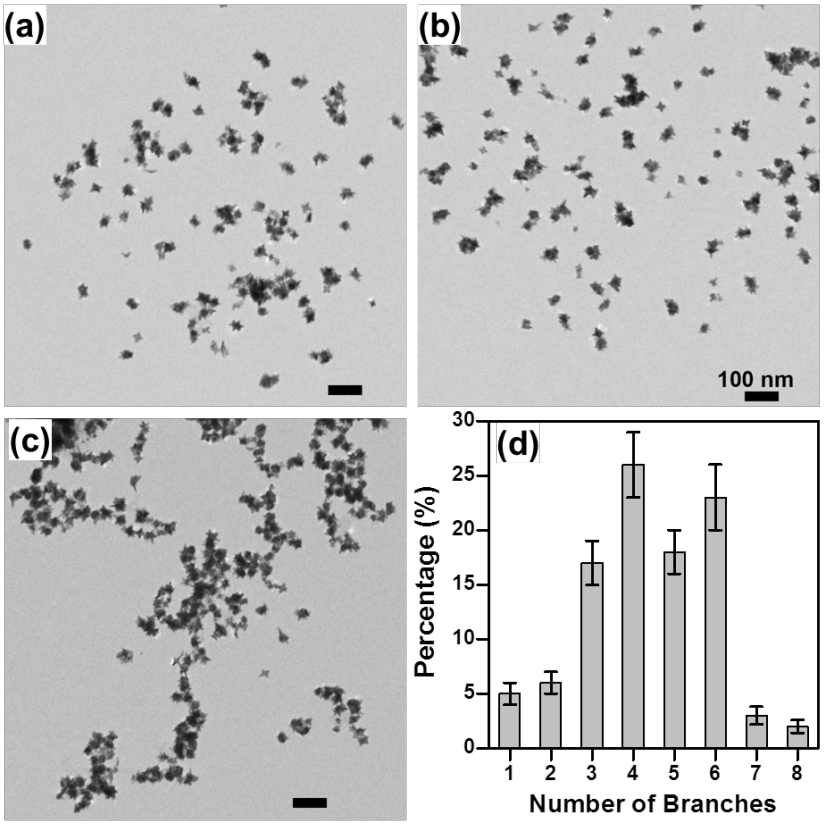

Figure 2.2: (a-c) Representative low magnification TEM images of MGNs prepared with 100 mM HEPES buffer. (d) Yield of MGNs derived from these TEM images as a function of number of branches. > 200 MGNs were analyzed. The error bars were calculated by counting the number of branches in MGNs in each representative TEM image taken at the same magnification.

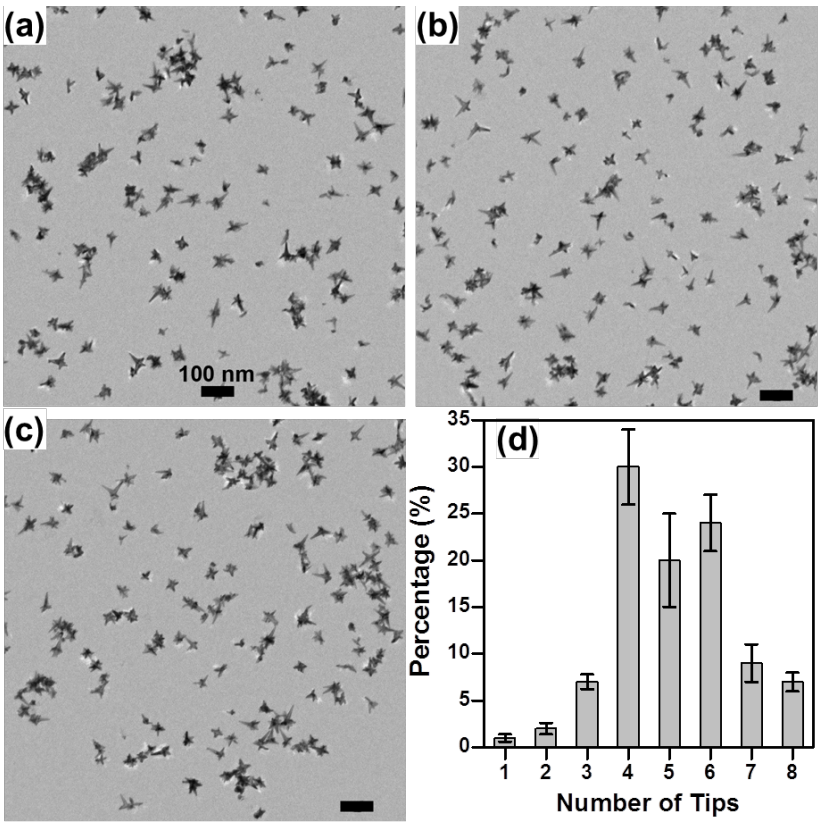

Figure 2.3: (a-c) Representative low magnification TEM images of MGNs prepared with 300 mM HEPES buffer. (d) Yield of MGNs derived from these TEM images as a function of number of branches. > 200 MGNs were analyzed. The error bars were calculated by counting the number of branches in MGNs in each representative TEM image taken at the same magnification.

By controlling the concentration of HEPES in the reaction mixture, MGN geometry is selectively modulated giving rise to tunable plasmon resonances from the visible to the near-infrared. The geometry-dependent plasmonic tunability of MGNs results in a range of vibrant colors from purple to blue to green to gray (Figure 2.4a).with increasing [HEPES]. This color-tunability is indicative of a shift in the plasmon resonance of MGNs to longer wavelengths with increase in protrusion length (Figure 2.4b). The optical resonances of a MGN arise from the hybridization of plasmons associated with the core and individual protrusions (Figure 2.4c).[26] The MGNs with short protrusions (60 mM HEPES) show a bonding plasmon mode at 620 nm, and an antibonding plasmon mode at 530 nm (Figure 2.4b). The antibonding mode is primarily

contributed by the core plasmons while the bonding plasmon resonance is predominantly composed of MGN protrusions but with a finite contribution of the core plasmons. A shoulder peak is also observed at 830 nm, which may arise from the hybridization of the plasmons of multiple protrusions of a MGN. The hybridization of the core and protrusion plasmons has dual implications: (1) it increases the extinction cross-section of the bonding MGN plasmons due to the admixture of the core plasmons in the bonding plasmon mode, and (2) enhances the dipole moment of the protrusion plasmons. The MGN core behaves as an antenna effectively increasing the near-field enhancements of the bonding plasmons. As the MGN protrusion length, width, and density increases, stronger hybridization occurs between the plasmons of the core and protrusions resulting in a larger energy-level splitting between bonding and antibonding plasmons (Figure 2.4c-ii). This enhanced hybridization gives rise to a red-shift in the MGN bonding plasmon mode and shoulder peak to longer wavelengths (Figure 2.4b). We anticipate the plasmon hybridization of symmetric MGNs where all protrusions are of equal length and symmetrically distributed around a core would be different than non-symmetric MGNs. Symmetry-breaking in nanostructures is known to give rise to higher order modes as well as enhance the intensity of the dark modes as asymmetry allows the dark modes to couple with the bright modes.[32] Non-symmetric MGNs, as observed in this work, likely gives rise to the shoulder peak observed in the long wavelength. As the HEPES concentration is increased, the asymmetry in MGNs increases (see Figure 2.1) which likely enhances the shoulder peak as well. A more thorough investigation of the plasmon hybridization of MGNs is currently underway to elucidate these mechanisms in details.

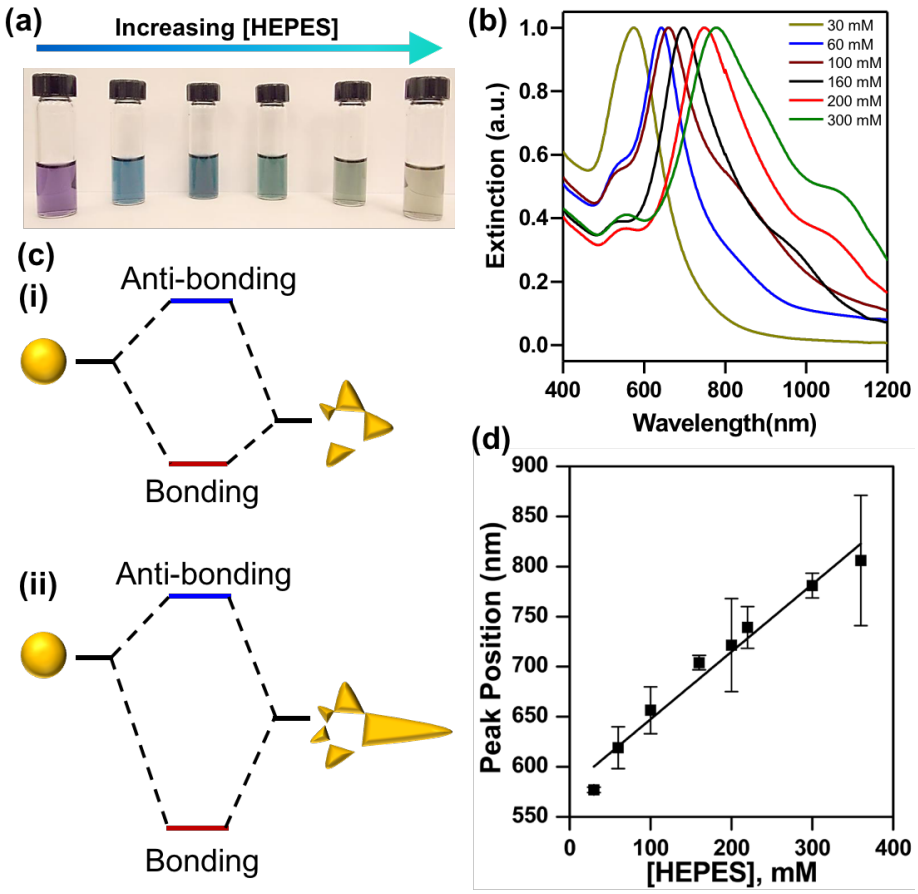

Figure 2.4: (a) Photograph of vials showing color tunability with increasing size of gold MGNs. (b) Extinction spectra of MGNs showing red shifts with increasing size achieved by controlling the concentration of HEPES. (c) Schematic representation of the concept of plasmon hybridization in the MGN. The core plasmons interact with the protrusion plasmons and form bonding and antibonding MGN plasmons (i). The energy-level splitting increases with increase in MGN protrusion length and density (ii). (d) A linear behavior of the plasmon peak positions as a function of increasing HEPES concentration is shown. Error bars were obtained from multiple (>3) experiments at each data point.

The red-shift in the optical resonance is also attributed to phase-retardation effects which arise from the oscillations of the electron cloud around the MGN.[33-35] The amplitude of the electron oscillation is augmented with increasing MGN dimensions which consequently increases the period of each oscillation, also known as plasmon lifetime. The increase in plasmon lifetime results in a decrease of the frequency of the waves, which inversely increases or red-shifts the plasmon wavelength.[33, 34] In addition, the increase in plasmon lifetime with

increasing dimensions gives rise to broadening and damping of optical resonances (Figure 2.4b). The broadening is also influenced by inhomogeneity in MGN geometry at high HEPES concentration. However, despite the heterogeneity in MGN shapes, the MGN plasmon resonances are relatively narrow compared to other branched nanostructures reported in the literature which makes them excellent LSPR sensors (see Figure 2.8 and Table 2.2).

The red-shift in the plasmon resonances of MGNs exhibit a linear relationship with increasing HEPES concentration (Figure 2.4d), demonstrating HEPES controls the MGN growth. The plasmons shift from 577 nm at 30 mM HEPES to 806 nm at 360 mM HEPES with a minimal increase of ~22 nm in the overall dimensions of the MGNs. Unlike spherical gold nanoparticles where a 20 nm increase in size only results in a few nm shift in the plasmon resonance, the significant red-shift observed for MGNs is attributed to their antenna-like behavior. In simple nanostructures such as nanospheres, the polarizability is governed by the nanosphere radius; however, in anisotropic nanostructures such as MGNs, polarizability is a function of their complex geometry.[25, 36] MGNs with multiple protrusions, therefore, have higher polarizability which gives rise to significant red-shifts in the plasmon resonances with only a small increase in overall dimensions.

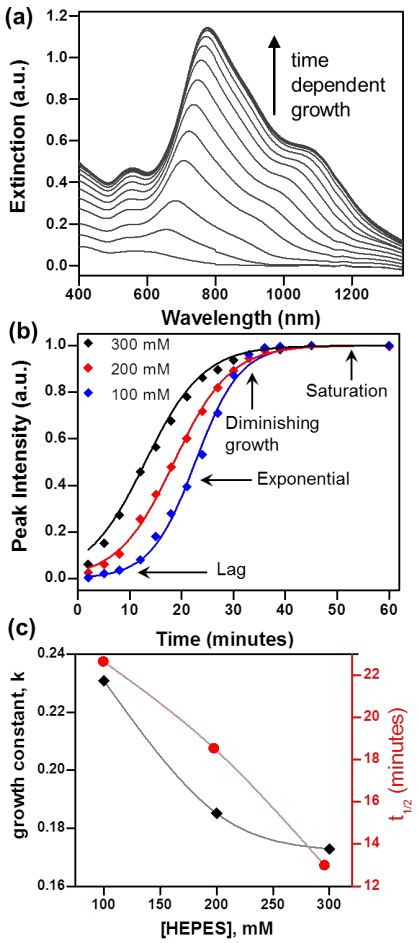

Figure 2.5: (a) Plasmon peak evolution of MGNs synthesized with 300 mM HEPES over 90 minutes. (b) Growth dynamics of MGNs of three different geometries synthesized with 300 mM HEPES, 200 mM HEPES and 100 mM HEPES. The experimental data were fit to a sigmoidal logistic function (Equation 2.1) to derive the time constant for growth. The different phases in a sigmoidal growth: lag phase, exponential phase, diminishing growth phase, and final saturation phase, are also indicated. (c) The growth time constant (k) and time at half the amplitude ($t_{1/2}$) are plotted as a function of HEPES concentration demonstrating that MGN growth dynamics is driven by [HEPES] in solution.

Besides plasmonic tunability, HEPES also controls the growth rate of MGN formation. The growth dynamics of MGNs prepared with three different HEPES concentration were examined to determine the relationship between the growth rate and [HEPES] in the aqueous media. The time-dependent growth of MGNs synthesized with 300 mM, 200 mM, 100 mM, was monitored for 90 mins (Figure 2.5a), and the spectral peak intensity was evaluated at different time points (Figure 2.5b). Reducing agents play a critical role in determining the growth

dynamics of metal nanoparticle formation. While fast reducing agents including citrate and $NaBH_4$ initiate burst nucleation followed by exponential growth,[37] weaker reducing agents such as HEPES,[38] NaOH,[14] ascorbic acid,[39] and certain phage peptides[38, 40-43] give rise to slower growth kinetics which follow a sigmoidal behavior. MGN formation dynamics followed a sigmoidal growth curve and were fit to a logistic function given by:

$$y = \frac{a}{1+e^{-k(t-t_c)}} \tag{2.1}$$

where a is the amplitude, k is the exponential growth constant, and t_c is the growth time at half the amplitude. Logistic functions are employed extensively to predict population growth,[44] cellular growth,[45] and enzymatic reaction growth.[46] The logistic function fitted to the experimental MGN growth dynamics is defined by four distinct parameters[47]: the lag phase characterizes the slow rate of Au^+ ion reduction which is accompanied by a slow nucleation of Au atoms; this is followed by exponential growth phase which is dominated by a diffusion mechanism where Au atoms rapidly diffuse in solution and locate deposition sites on the [111] crystal planes on the Au core and subsequently grow protrusion along the <111> direction; as the diffusion process slows down and most of the available Au^+ ions have reduced and Au atoms have already deposited, the formation rate diminishes which is characterized by the diminishing growth phase; and finally growth is completed and no change in the peak amplitude is observed which defines the saturation phase. Regardless of the HEPES concentration, the MGN growth is completed within 45 minutes. However, the growth-determining parameters k and t_c monotonically decrease with increasing HEPES concentration (Figure 2.5c) indicating that HEPES plays a key role in MGN growth. The trends observed in Figure 2.5c suggest that with increasing [HEPES] faster Au^{3+} reduction occurs to accelerate nucleation of MGNs resulting in a diminished lag phase. Due to rapid nucleation, the reaction proceeds faster with higher [HEPES]

and less time is required to reach half the saturation amplitude (t_c) which consequently results in smaller exponential growth constant (k). The trends in Figure 2.5c further support the original intuition that HEPES simultaneously acts as a capping and reducing agent for MGN growth.

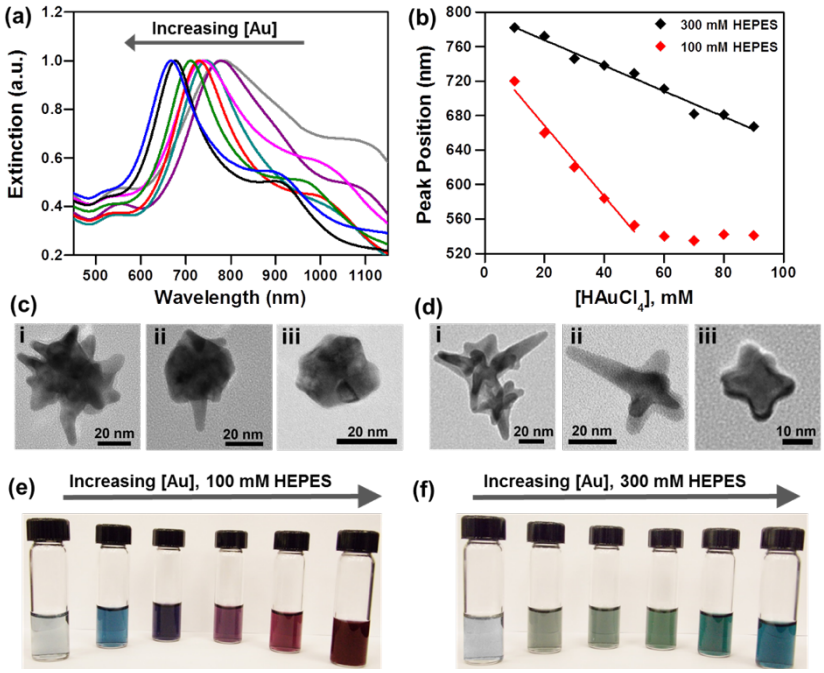

Figure 2.6: (a) Size dependent tunability of MGNs surface plasmons by modulating the [Au^{3+}] showing a blue-shift with increasing Au^{3+}. The MGNs were synthesized with 100 mM HEPES. (b) Plasmon peak positions of MGNs showing a linear blue-shift with increasing Au precursor concentration prepared with 300 mM, and 100 mM HEPES. TEM images of MGNs synthesized with (c) 100 mM HEPES and different [Au^{3+}] (i) 10 mM, (ii) 40 mM, and (iii) 90 mM, and (d) 300 mM HEPES and different [Au^{3+}]] (i) 10 mM, (ii) 40 mM, and (iii) 90 mM. (e-f) Photograph of vials showing an entire spectrum of colors as the MGN morphology changed with increasing [Au^{3+}]. MGNs were prepared with (e) 100 mM HEPES and (f) 300 mM HEPES.

In addition to the HEPES concentration, the geometry-dependent plasmon resonances of MGNs are also manipulated by altering the concentration of the Au precursor, $HAuCl_4$, in the growth solution (Figure 2.6a). While keeping the [HEPES] constant (300 mM, 100 mM) and pH constant at 7.4 ± 0.1, [Au^{3+}] was increased from 10–90 mM and the plasmon resonance was observed to blue-shift from 782 nm to 667 nm for the MGNs synthesized with 300 mM HEPES and from 720 nm to 535 nm for those prepared with 100 mM HEPES (Figure 2.6a, 2.6b). The

blue-shifts in the plasmon peak position follows a linear trend for both 300 mM and 100 mM, however, it saturates at ~530 nm when $[Au^{3+}] \geq 60$ mM for the MGNs synthesized with 100 mM HEPES indicating formation of sphere-like structures. TEM analysis of the MGNs revealed that at low $[Au^{3+}]$, MGNs with a higher density of longer protrusions are formed (Figure 2.6c-i and Figure 2.6d-i); the protrusion length and density decreases with increasing $[Au^{3+}]$ (Figure 2.6c-ii and Figure 2.6d-ii) and finally at 90 mM $[Au^{3+}]$ spherical nanostructures (Figure 2.6c-iii) or MGNs with very short protrusions are formed (Figure 2.6d-iii). The decrease in protrusion length and density with increasing Au^{3+} concentration can be attributed to the ratio of $[HEPES]/[Au^{3+}]$. High $[HEPES]/[Au^{3+}]$ ratio results in the formation of fewer Au nuclei and a high concentration of HEPES binding to the nuclei. Nucleation is followed by oriented growth along the《111》 family of planes resulting in MGNs with multiple protrusions. As the $[HEPES]/[Au^{3+}]$ ratio decreases, a larger density of Au nuclei are formed which likely cluster together leaving fewer binding sites for HEPES, and the clusters may also block the <111> crystallographic direction. This gives rise to MGNs with shorter and fewer protrusions and eventually at very high $[Au^{3+}]$ more sphere-like MGNs are formed. This geometry-dependent plasmon resonance shift is accompanied with color tunability of the MGN suspension. An entire spectrum of colors is generated for MGNs prepared with 100 and 300 mM HEPES and varying $[Au^{3+}]$ (Figure 2.6e, 2.6f).

Plasmonic tunability was also achieved by modulating the pH of the reaction from 6.61 – 8.6 while keeping [HEPES] constant and $[Au^{3+}]$ constant at 20 mM. HEPES buffer at 100 mM and 300 mM was prepared and the pH of the buffer was varied with 1 M NaOH. We monitored the pH of the reaction medium at the beginning and end of MGNs synthesis and the pH remained constant throughout the synthesis. The plasmon resonances of MGNs synthesized with 100 mM

HEPES (Figure 2.7a) demonstrated a peak at 574 nm at pH 6.61 indicating sphere-like nanostructure formation. TEM micrographs of the pH 6.61 reaction (Figure 2.7b-i) showed ~85 nm Au nanospheres with very short protrusions. As the pH is increased to 7.44 the protrusion length increases and the MGN spherical core diameter decreases giving rise to ~ 41 nm MGNs (Figure 2.7b-ii). While the overall dimensions of MGNs decreases with increasing pH, the increase in protrusion length results in stronger coupling to light giving rise to red-shift in the plasmon resonance. As the pH is increased further, a non-intuitive behavior is observed, where the plasmon peak resonance blue shifts (pH 7.69, 8.03) and then red shifts again at high pH (pH 8.27, 8.6). This trend was observed for MGNs synthesized with 100 mM and 300 mM HEPES (Figure 2.7c). This non-intuitive trend of plasmon peak position as a function of pH is explained both in terms of chemical transformations occurring at different pH, as well as optical transformations occurring in the MGN reaction mixture.

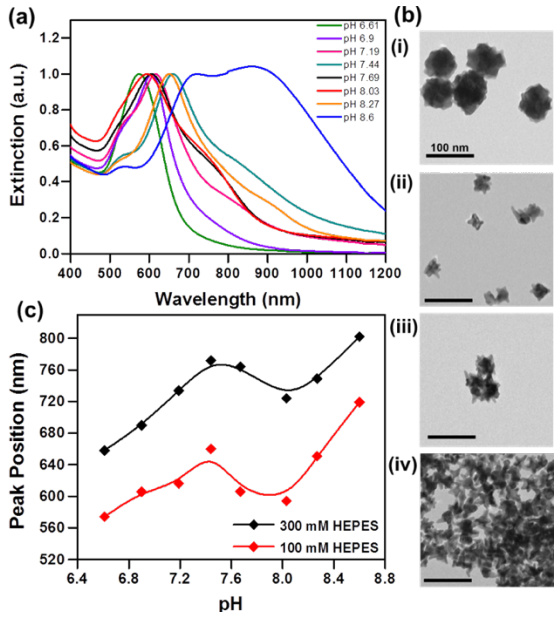

Figure 2.7: Tunability of plasmon resonance of MGNs by modulating the pH of the HEPES buffer while keeping [HEPES] constant at 100 mM and [$HAuCl_4$] constant at 20 mM. (b) TEM micrographs of MGNs synthesized at various pH with 100 mM HEPES (i) pH 6.61, (ii) pH 7.44, (iii) pH 8.03, and (iv) pH 8.60. The scale bar is 100 nm in b (i-iv). (c) Plasmon peak position as a function of HEPES buffer for 100 mM and 300 mM HEPES showing a unique trend with increasing pH.

The chemical transformation referred above is the change in charge of the HEPES molecule (pKa = 7.5) at different pH. The tertiary amine in the piperazine ring in a HEPES molecule play key roles as capping and reducing reagent for metal nanoparticle synthesis.[31, 48, 49] Further, the HEPES/Au binding dynamics is also mediated via radical chemistry, in which the nitrogen atom in the tertiary amine must be a deprotonated cationic free radical to bind to Au ions and reduce to form Au nanoparticles.[48-50] When the pH of the reaction mixture < pKa of HEPES, the solution is acidic and the nitrogen in the tertiary amine is protonated. The protonation of the amine group in turn decreases the binding affinity of HEPES for the Au surface including the <111> and <110> directions. Au reduction, therefore, occurs along all the crystal planes resulting in the formation of spherical particles with larger radii and small protrusions (Figure 2.7b-i). When pH ~ pKa i.e. pH 7.44, the piperazine ring is in its neutral state and is not protonated. It forms cationic free radicals and preferentially binds to the different crystalline facets of Au except the <111> direction giving rise to MGNs (Figure 2.7b-ii). When pH> pKa, the ethanesulfonic acid group (pKa ~1.5) of HEPES is deprotonated and becomes negatively charged and increase the ionic strength of the basic solution. It has been shown that metal nanoparticles cluster together in solutions with high ionic strength to balance the charges and reach equilibrium.[49, 51] At pH (8.03) slightly greater than 7.5, the MGNs form higher-order clusters including dimers and trimers (Figure 2.7b-iii), and at extremely high pH (8.6) MGNs aggregate to large clusters to counteract the excessive charges (Figure 2.7b-iv).

The optical transformation which contributes to the unusual trend observed in Figure 2.7c is attributed to MGN clustering at pH > pKa of HEPES. The red-shift in the plasmon resonance at very high pH (pH 8.27, 8.6) can be simply explained by phase retardation effects due to the formation of large aggregates yielding a plasmon shift to longer wavelengths, resonance

broadening, and increase in aggregate peak (~ 900 nm). The blue-shift in the plasmon resonance at pH slightly higher than pKa (pH 7.69 and 8.03) may be attributable to the formation of charge transfer plasmons in closely interacting MGN dimers and trimers. Charge-transfer plasmons have been shown previously both experimentally and theoretically in gold nanoshell dimers,[52, 53] solid metal nanoparticle dimers and Yagi-Uda antennas,[54, 55] and other strongly interacting nanoparticle assemblies.[56] A blue-shift is expected when metal nanoparticles are either in contact or separated by distances short enough to permit a conductive overlap; such an overlap would give rise to a collective charge oscillation over the two/three particles comprising the dimer/trimer. When the MGN dimers/trimers are coupled within the near-field limit, the surfaces in the contact zone are instantaneously polarized with opposite signs for the charge. This enhances the stability of the charge-transfer plasmon and results in blue-shift.[52] However, future in-depth studies examining single MGN dimers/trimers will be needed to elucidate the possibility of charge transfer plasmons in overlapping MGN clusters.

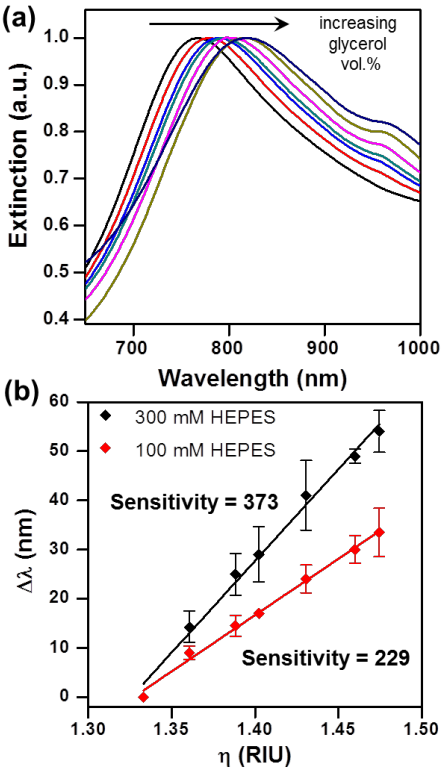

Figure 2.8: (a) Refractive index sensing with gold MGNs synthesized with 300 mM HEPES showing red-shift in plasmon resonance with increasing glycerol vol.% in the aqueous suspension. (b) LSPR shifts of MGNs of two different sizes synthesized with 300 mM (black), and 100 mM HEPES (red) plotted as a function of refractive index of media. The refractive index was controlled by altering the glycerol vol. %. The LSPR sensitivities are indicated. The error bars were calculated from multiple experiments performed at each glycerol vol.%.

The surface plasmon resonances of the MGNs are highly sensitive to the alterations in refractive index (RI) of the surrounding medium.[57] The RI sensitivities of MGNs of two different sizes were measured by modifying the RI of the surrounding aqueous medium with additions of various volume% of glycerol.[58] MGNs were centrifuged once and re-dispersed in H_2O (1.33), 20 vol.% glycerol (1.36), 40 vol.% (1.38), 50 vol.% (1.40), 70 vol.% (1.43), 90 vol.% (1.46), and 100 vol.% (1.475). The numbers within the brackets are RI of the medium with the different volumes of glycerol additions. The plasmon resonance of MGNs red shift to longer wavelengths with increasing volume % of glycerol in the surrounding aqueous medium (Figure 2.8a). As the RI of the medium increases, it screens the electron oscillation in the metal

decreasing the plasmon energy and resulting in a red-shift of the plasmon wavelength.[57] This electron screening also results in plasmon broadening and damping, which is observable specifically at glycerol vol.% ≥ 90%. Sensitivity, *S*, is defined as $S = \frac{\Delta\lambda}{\eta}$ where $\Delta\lambda$ is change in plasmon wavelength relative to H_2O and η is RI of the medium. *S* of MGNs synthesized with 100 mM (41 nm size) and 300 mM (58 nm size) HEPES were determined from the slope of the linear fit in Figure 2.8b. The 58 nm MGNs had a LSPR sensitivity of 373 nm/RIU and the 41 nm MGNs had a sensitivity of 229 nm/RIU. The LSPR sensitivities are reproducible as indicated by the error bars in Figure 2.8b. The error bars were calculated from multiple experiments performed at each glycerol vol.%. The MGNs were stable in glycerol solutions and no visible or spectral aggregation was observed at low glycerol concentrations (≤ 70%). While slow aggregation did occur at higher glycerol concentrations, not within the time frame of LSPR measurements.

The LSPR sensitivity of MGNs is compared to other nanostructure shapes of similar size, and also to star-shaped and other branched nanostructures (Table 2.2). We note that Table 2.2 only represents LSPR sensitivity of ensemble measurements, single particle measurements are not compared here. We also note that Table 2.2 is not an exhaustive list; we have provided the most comparable nanostructures. A more detailed list of refractive index sensitivity of a range of nanostructures can be found in ref [57]. It is known that LSPR sensitivity enhances with increasing nanostructure size due to higher polarizability of larger nanostructures.[3, 25] It is therefore noteworthy that the HEPES-mediated 58 nm MGNs have higher sensitivity compared to the larger size nanostars from ref. [13] and [59]. The high sensitivity of HEPES-mediated MGNs is attributed to the intense nanoantenna effect where the multiple sharp protrusions interact strongly with incident light giving rise to extraordinary near-field intensities and

consequently enhanced sensing capabilities.[18] Despite the variations in protrusion length and density (Figure 2.2, 2.3), MGNs demonstrate relatively high LSPR sensitivity for this class of branched nanostructures.

Table 2.2: Comparison of refractive index sensitivity of gold nanostructures of various shapes (Note: This table only represents ensemble measurements).

Nanoparticle Shape	**Nanoparticle Size**	**LSPR Sensitivity (nm/RIU)**	**Ref.**
nanospheres	50 nm diameter	60	[57]
nanocubes	44 nm edge length	83	[57]
nanorods	26 nm length (small)	156	[60]
nanoboxes	30 nm edge length (wall thickness = 15 nm)	210	[61]
nanobipyramids	50 nm length	212	[58]
peanut-like nanorods	43 nm length	220	[60]
dog-bone like nanorods	56 nm length	238	[60]
nanorattles	~40 nm length	285	[62]
nanoframes	42 nm wall length	516	[63]
nanoprisms	42 nm edge length	578	[64]
nanobranches	80 nm length	703	[58]
nanostars	~80 nm tip-to-tip	326	[13]
nanostars	~105 nm tip-to-tip	218	[59]
This work: MGNs 300 mM HEPES	**~58 nm tip-to-tip**	**373**	
This work: MGNs 100 mM HEPES	**~41 nm tip-to-tip**	**229**	

The light to heat conversion efficiency of plasmonic nanostructures has been explored extensively in nanomedicine from light induced gene therapy,[65-67] and drug delivery,[68-70] to photothermal ablation.[71-76] Photothermal conversion has been studied by ultrafast

dynamics[77] and is attributed to a combination of electron-electron scattering, electron-phonon coupling, and phonon-phonon coupling which results in heat dissipation to the surrounding media. Plasmonic nanostructures with sharp tips and protrusions are known to strongly interact with light generating intense near-fields and a high density of hot energetic electrons at the tips. These energetic electrons eventually thermalize to the surrounding medium producing heat.[78] The multiple sharp protrusions of MGNs, specifically those synthesized in the near-infrared, are ideal candidates for light-to-heat conversion both due to their unique geometry as well as spectral overlap with commercially available laser diodes.

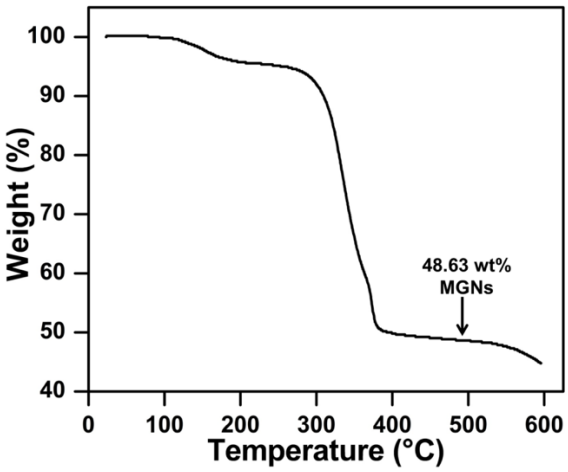

Figure 2.9: Thermogravimetric analysis of solid state MGNs prepared with 300 mM HEPES corresponding to extinction = 1.64 at 60-fold dilution factor.

Here we have probed the photothermal capabilities of MGNs resonant at ~790 nm by measuring the maximum temperature of the suspensions by varying the mass of MGNs in 50 μL droplets, as well as time of illumination and laser power. The mass of MGNs was determined by thermogravimetric analysis (Figure 2.9). Using an IR thermal camera, images of the MGN suspension (Figure 2.10ai-aii) and a deionized water control (Figure 2.10aiii-aiv) were captured during laser irradiation with a 808 nm NIR laser at 11.28 W/cm^2. The thermal images demonstrate that MGNs increase the temperature by ~30 °C relative to room temperature within

10 minutes of illumination; however, in the absence of MGNs (control) only a 4.2 °C temperature increase is achieved. Since the amount of MGNs directly controls the heat generated by laser irradiation, MGNs at different particle masses were illuminated for 10 minutes (Figure 2.10b). A maximum temperature of 54.9 °C was achieved within 10 minutes of laser treatment for a nominal amount of 184 µg. This rapid light to heat conversion with increasing mass of MGNs is attributed to the intense nanoantenna effect which results from the sharp protrusions and the corresponding electron hot spots generated in the junction of MGNs in close vicinity. Strong electromagnetic fields generated in these junctions gives rise to enhanced light absorption and thus higher light to heat conversion.

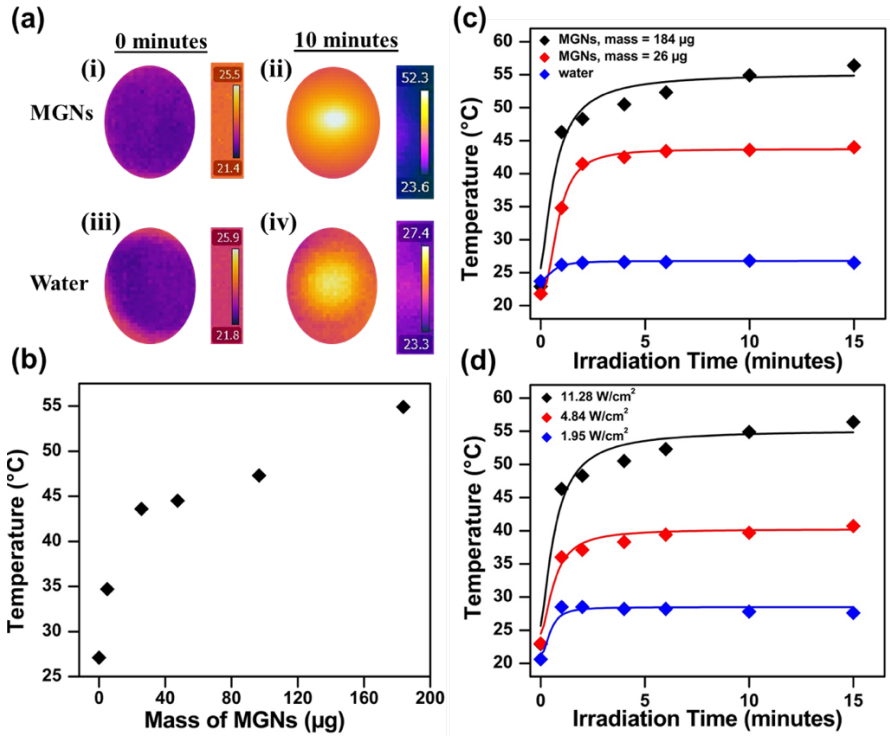

Figure 2.10: (a) Infrared thermal images of an aqueous MGN suspension, mass of MGNs = 184 µg, illuminated with 808 nm laser at (i) 0 and (ii) 10 minutes with deionized water as a control at (iii) 0 and (iv) 10 minutes. The MGN suspension and water were illuminated at a flux of 11.28 W/cm^2. (b) Maximum temperature achieved of varying MGN particle masses (in 50 µL volumes) irradiated with 808 nm laser for 10 minutes. (c) Temperature profile as a function of time for two different mass of MGNs as well as (d) different power densities is shown. For (d) mass of MGNs = 184 µg.

Temperature as a function of time was also recorded and an exponential increase in temperature (Figure 2.10c) was observed for increasing mass of MGNs. It is notable that 184 µg of MGNs demonstrated a 23.4 °C temperature increase within one minute and only incrementally increased after 2 minutes. This study demonstrates the promise of MGNs for delivering photothermal based therapeutics in cancer cells *in vitro* and *in vivo*. Since hyperthermia and subsequent tumor destruction occurs within the 41–47 °C temperature range, this indicates that for a nominal 26 µg of MGNs in the tumor tissue, tumor ablation can be achieved.[79] Li and co-workers have also demonstrated that ~7% of injected dose (ID) of gold nanostructures can reach tumors *in vivo* when actively targeted to cancer cell receptors via antibodies and peptides.[80] This indicates that if MGNs are actively targeted to cancer cells and assuming that 7% ID accumulates in tumors for mice with an average body weight of 20 g, only 18.57 µg/g of MGNs dose would be needed to achieve ~43 °C, and 131µg/g of dose would be required to achieve ~55 °C which may be necessary for aggressive cancer cells (detailed calculations below). These numbers are on par with injected dose of nanorods *in vivo*[81] and ~53X (18.57 µg/g) and ~7X (131µg/g) less relative to nanoparticles.[82]

Calculations of amount of MGNs that will be necessary for photothermal experiments

According to Figure 7c in the main text, 26 µg of MGNs is sufficient to induce hyperthermia in tumors *in vivo*. This indicates that if MGNs are actively targeted to cancer cells and assuming that 7% of the injected dose of MGNs accumulates in tumors, then 371.428 µg of MGNs need to be injected.

$$\frac{7}{100} \times 371.428\ \mu g = 26\ \mu g$$

If experiments were performed in nude mice (nu/nu) with an average body weight of 20 g, then only 18.57 µg/g of MGNs dose would be needed to achieve ~43 °C.

$$\frac{371.428\ \mu g\ MGNs}{20\ g\ mice} = 18.57\ \mu g/g$$

For the higher dosage where 184 µg is needed to induce a temperature of ~55 °C , then 131µg/g of dose would be required which may be necessary for aggressive cancer cells.

$$\frac{7}{100} \times 2628.57\ \mu g = 184\ \mu g$$

$$\frac{2628.57\ \mu g\ MGNs}{20\ g\ mice} = 131.42\ \mu g/g$$

In addition to the length of time of laser irradiation, we also investigated the effect of different laser flux on the photothermal conversion efficiency of MGNs. An exponential increase in temperature was observed analogous to the trend seen for increasing MGN mass (Figure 2.10d). While a maximum temperature of 56.4 °C was observed for the highest power density (11.28 W/cm^2), a relatively high light to heat conversion was also achieved at 4.84 W/cm^2 resulting in a final temperature of 40.7 °C which is sufficient for tumor ablation. This mass-, time- and flux-dependent temperature increase indicates that for applications requiring benign temperatures (gene delivery), a short treatment time at low MGNs dosage and low flux is sufficient, while for photothermal therapy of aggressive cancer cells a higher MGNs dosage, higher laser illumination, and longer treatment time would be more suitable to generate higher temperatures.

2.4 Conclusions

In summary, we have demonstrated the synthesis, characterization, and geometry dependent tunability of plasmon resonances of MGNs formed by a straightforward, seedless, one-step approach using HEPES buffer. The MGN geometry is modulated by manipulating three different chemical parameters: [HEPES], [Au^{3+}], and pH of reaction medium. By changing these parameters, the plasmon resonances were tuned from the visible to the near-infrared without

significant alterations of the overall dimensions. The evolution of plasmon resonances as a function of pH of the reaction medium demonstrated a non-intuitive blue-shift in the plasmon resonance when pH was slightly > pKa of HEPES which was attributed to charge transfer plasmons in MGN dimers and trimers; this was followed by a red-shift at pH > pKa which was attributed MGN clustering to larger aggregates. Finally due to the sharp protrusions of the MGNs, enhanced refractive index sensing capabilities were observed and sensitivity of 373 nm/RIU was achieved. The MGNs sensitivity is relatively high for similarly sized branched nanostructures of this class and is attributed to the high polarizability of the MGNs mediated by their anisotropic geometry. The sharp protrusions and corresponding nanoantenna effect also gives rise to intense photothermal conversion efficiencies for a nominal MGNs mass of only 26 μg. MGNs demonstrated an increase in temperature to 56.4 °C within 10 minutes of laser treatment which is analogous to other branched nanostructures shown previously.[76] The simple fabrication process, broad tunability of plasmon resonances, high LSPR sensitivity, and strong photothermal conversion efficiencies make these nanoscale antennas excellent for surface enhanced spectroscopies, sensing of chemical and biological analytes, thermoplasmonics, bioimaging and therapeutics (theranostics), and for probing fundamental optical processes.

2.5 Methods

A. MGN Synthesis. Gold MGNs were synthesized with HEPES buffer.[31] All reagents were purchased from Sigma-Aldrich.

Changing Morphology through [HEPES]: The concentration of HEPES buffer in aqueous media was varied between 30 to 360 mM. Briefly, 3 mL of milli-Q water (18 Mohms) was added to 2 mL of an appropriate concentration of aqueous HEPES at pH 7.4 ± 0.1 in a 15 mL centrifuge

tube (Corning Co.). The pH was adjusted with 1 M NaOH. The solution was mixed immediately by gently inverting the centrifuge tube. Next, 50 μL of 20 mM aqueous $HAuCl_4$ was added to the 5 mL HEPES solution followed by gentle inversion of the tube. We note that the solution should not be vortexed or stirred as this will disrupt particle formation. The solution was left to react at room temperature for 70 minutes. Upon completion, a color change in the MGN solution occurred ranging from purple to bluish-green to grey depending on [HEPES]. The MGNs can be stored at 4° C for up to a month.

Changing HEPES/$HAuCl_4$ ratio: MGNs were synthesized following the above procedure keeping [HEPES] constant at 100 mM and 300 mM pH 7.4 ± 0.1, and varying [$HAuCl_4$] between 10 - 90 mM. Reaction volumes and times were the same as above.

Changing pH of Reaction: MGNs were synthesized following the above procedure with HEPES concentration at 100 and 300 mM and 20 mM $HAuCl_4$ while altering the pH of the HEPES buffer between 6.61-8.60 with 1 M NaOH. Reaction volumes and times were the same as above.

Growth Dynamics Studies**:** MGNs were synthesized with [HEPES] (100, 200 and 300 mM) pH 7.4 ± 0.1 with 50 μL of 20 mM $HAuCl_4$ as described previously, and these syntheses were monitored with UV-vis at different time points between 2 - 90 minutes and the maximum intensity in the extinction spectrum for each time point was determined.

B. MGN Characterization. A Varian Cary 5000 UV-vis NIR spectrophotometer (Agilent Technologies) with dual beam capabilities was used to measure the extinction of the MGN solutions using a 1 cm path length cuvette. The MGN size and geometry were characterized using Philips CM20T TEM at 200 keV, Osiris TEM at 200 keV, and a Zeiss Merlin SEM (Oak Ridge National Lab). MGN samples were centrifuged at 4000 rpm for 5 minutes (x2) and washed with deionized water prior to SEM/TEM sample preparation. MGN sizes were evaluated

from TEM images averaging over a distribution of ~100 individual stars for each HEPES concentration. MGNs mass was determined by Thermogravimetric Analyzer with an Instrument Specialist's TGA-1000.

C. Refractive Index Sensing. For LSPR sensing, MGN syntheses for 100 mM and 300 mM HEPES were scaled up: 16 mL aqueous HEPES (100 and 300 mM) pH 7.4 ± 0.1, 24 mL deionized water and 400 uL of 20 mM $HAuCl_4$ were reacted for 75 minutes. The solutions were centrifuged once at 6000 rpm for 20 min, supernatant was removed, and 3 mL of aqueous HEPES at pH 7.4 ± 0.1 was added to stabilize the MGNs. The refractive index of aqueous solutions was changed by varying the volume % of glycerol (0-100%) in the aqueous media. Stabilized MGNs were added to the different glycerol-water mixtures at 10-fold dilution and the plasmon peak positions were examined with a UV-vis NIR spectrophotometer.

D. Photothermal Heating of Aqueous MGN Solutions. For photothermal experiments, the MGN synthesis for 300 mM HEPES was scaled up to a total volume of 200 mL. The MGNs were washed and reconstituted to 5X- 200X the original concentration using aqueous HEPES at pH 7.4 ± 0.1 for dilutions.

A 1 W near-infrared laser diode at 808 nm (L808P1WJ) was set up with current (Thorlabs, LDC240C) and thermoelectric controllers (TEDC200C), and the laser beam was collimated to a spot size of 1.2 mm diameter with a lens (C230TME-B) and a silver polished mirror (PF10-03-P01). All parts were purchased from Thorlabs. MGN suspensions were illuminated at 11.28 W/cm^2 for the time- and mass-dependent measurements and at 11.28, 4.84, and 1.95 W/cm^2 for the flux-dependent study. Power densities were measured using a power meter (Thorlabs, PM130D). Aqueous 50 μL droplets of MGN suspensions on glass slides were heated by light illumination, and the maximum temperatures of the MGN solutions were

monitored using an IR camera and software from FLIR Systems (T440). The water droplet size was ~ 3 mm and MGN droplet size ~ 1.8 mm. Temperatures were monitored for 15 minutes for all experiments taking readings at 0, 1, 2, 4, 6, 10, and 15 minute time points. The solution with MGN mass = 184 μg was used in the power density comparison. MGN particle masses were determined gravimetrically using TGA of solid state samples to determine the mass of MGNs relative to mass of HEPES ligands. The temperature rise in photothermal experiments has been provided as a function of the mass of MGNs present in a 50 μl droplet of suspension.

2.6 Bibliography

1. Giannini, V., et al., *Plasmonic Nanoantennas: Fundamentals and Their Use in Controlling the Radiative Properties of Nanoemitters.* Chem. Rev., 2011. **111**: p. 3888 − 3912.
2. Cortie, M.B. and A.M. McDonagh, *Synthesis and Optical Properties of Hybrid and Alloy Plasmonic Nanoparticles.* Chem. Rev., 2011. **111**: p. 3713 − 3735.
3. Myroshnychenko, V., et al., *Modelling the Optical Response of Gold Nanoparticles.* Chem. Soc. Rev., 2008. **37**: p. 1792 − 1805.
4. Murphy, C.J., et al., *Anisotropic Metal Nanoparticles: Synthesis, Assembly, and Optical Applications.* J. Phys. Chem. B, 2005. **109**: p. 13857 − 13870.
5. Huang, L., et al., *Synthesis of Gold Nanotadpoles by a Temperature-Reducing Seed Approach and the Dielectrophoretic Manipulation.* J. Phys. Chem. C, 2007. **111**: p. 16154 − 16160.
6. Sajanlal, P.R., et al., *Anisotropic nanomaterials: structure, growth, assembly, and functions.* Nano Reviews, 2011. **2**: p. 5883.
7. Bardhan, R., et al., *Au Nanorice Assemble Electrolytically into Mesostars.* Acs Nano, 2009. **3**: p. 266 − 272.
8. Song, H.-M., et al., *Plasmon-Resonant Nanoparticles and Nanostars with Magnetic Cores: Synthesis and Magnetomotive Imaging.* ACS Nano, 2010. **4**: p. 5163-5173.
9. Lim, B. and Y. Xia, *Metal Nanocrystals with Highly Branched Morphologies.* Angew. Chem. Int. Ed., 2011. **50**: p. 76 − 85.
10. Kooij, E.S., et al., *From Nanorods to Nanostars: Tuning the Optical Properties of Gold Nanoparticles.* Coll. and Surf. A: Physicochem. Eng. Aspects, 2012. **413**: p. 231 − 238.
11. Rodrıguez-Lorenzo, L., et al., *Reshaping and LSPR tuning of Au nanostars in the presence of CTAB.* J. Mater. Chem., 2011. **21**: p. 11544 − 11549.
12. Kumar, P.S., et al., *High-yield Synthesis and Optical Response of Gold Nanostars.* Nanotechnology, 2008. **19**: p. 015606.
13. Barbosa, S., et al., *Tuning Size and Sensing Properties in Colloidal Gold Nanostars.* Langmuir, 2010. **26**: p. 14943 − 14950.
14. Kedia, A. and P.S. Kumar, *Controlled reshaping and plasmon tuning mechanism of gold nanostars.* J. Mater. Chem. C, 2013. **1**: p. 4540-4549.
15. Maiorano, G., et al., *Monodispersed and size-controlled multibranched gold nanoparticles with nanoscale tuning of surface morphology.* Nanoscale, 2011. **3**: p. 2227-2232.
16. Nehl, C.L., H. Liao, and J.H. Hafner, *Optical Properties of Star-Shaped Gold Nanoparticles.* Nano Lett., 2006. **6**: p. 683 − 688.
17. Novotny, L. and N.v. Hulst, *Antennas for Light.* Nat. Photonics, 2011. **5**: p. 83 − 90.
18. Bosman, M., et al., *Surface Plasmon Damping Quantified with an Electron Nanoprobe.* Nat. Sci. Reports, 2013. **3**: p. 1 − 7.
19. Khoury, C.G. and T. Vo-Dinh, *Gold Nanostars For Surface-Enhanced Raman Scattering: Synthesis, Characterization and Optimization.* J. Phys. Chem. C, 2008. **112**: p. 18849 − 18859.
20. Yuan, H., et al., *In vivo Particle Tracking and Photothermal Ablation Using Plasmon-Resonant Gold Nanostars.* Nanomedicine: Nanotech. Biol. and Med., 2012. **8**: p. 1355 − 1363.

21. Rodríguez-Lorenzo, L., et al., *Plasmonic Nanosensors with Inverse Sensitivity by Means of Enzyme-guided Crystal Growth.* Nat. Mater., 2012. **11**: p. 604 − 607.
22. Yuan, H., et al., *Gold Nanostars: Surfactant-free Synthesis, 3D Modelling, and Two-photon Photoluminescence Imaging.* Nanotechnology, 2012. **23**: p. 075102.
23. Plascencia-Villa, G., et al., *Advanced microscopy of star-shaped gold nanoparticles and their adsorption-uptake by macrophages.* Metallomics, 2013. **5**: p. 242-250.
24. Rodrıguez-Oliveros, R. and J.A. Sanchez-Gil, *Gold Nanostars as Thermoplasmonic Nanoparticles for Optical Heating.* Opt. Express, 2012. **20**: p. 621 − 626.
25. Kelly, K.L., et al., *The Optical Properties of Metal Nanoparticles: The Influence of Size, Shape, and Dielectric Environment.* J. Phys. Chem. B, 2003. **107**: p. 668 − 677.
26. Hao, F., et al., *Plasmon Resonances of a Gold Nanostar.* Nano Lett., 2007. **7**: p. 729−732.
27. Grabb, M.C. and D.W. Choi, *Ischemic Tolerance in Murine Cortical Cell Culture: Critical Role for NMDA Receptors.* J. Neuroscience, 1999. **19**: p. 1657 − 1662.
28. Shipman, C., *Evaluation of 4-(2-Hydroxyethyl)-1-piperazineëthanesulfonic Acid (HEPES) as a Tissue Culture Buffer* Exp. Biol. Med., 1969. **130**: p. 305 − 310.
29. Bowman, C.M., et al., *Hepes may Stimulate Cultured Endothelial Cells to Make Growth-retarding Oxygen Metabolites* In Vitro Cell. Develop. Biol., 1985. **21**: p. 140 − 142.
30. Wilcoxon, J.P. and P.P. Provencio, *Heterogeneous Growth of Metal Clusters from Solutions of Seed Nanoparticles.* J. Am. Chem. Soc., 2004. **126**: p. 6402 − 6408.
31. Xie, J., J.Y. Lee, and D.I.C. Wang, *Seedless, Surfactantless, High-Yield Synthesis of Branched Gold Nanocrystals in HEPES Buffer Solution.* Chem. Mater., 2007. **19**: p. 2823 − 2830.
32. Hao, F., et al., *Symmetry Breaking in Plasmonic Nanocavities: Subradiant LSPR Sensing and a Tunable Fano Resonance.* Nano Lett., 2008. **8**: p. 3983–3988.
33. Ringe, E., et al., *Plasmon Length: A Universal Parameter to Describe Size Effects in Gold Nanoparticles.* J. Phys. Chem. Lett., 2012. **3**: p. 1479−1483.
34. Ringe, E., et al., *Correlating the Structure and Localized Surface Plasmon Resonance of Single Silver Right Bipyramids.* Nanotechnology, 2012. **23**: p. 444005.
35. Bardhan, R., et al., *Metallic Nanoshells with Semiconductor Cores: Optical Characteristics Modified by Core Medium Properties.* ACS Nano, 2010. **4**: p. 6169 − 6179.
36. Hao, E., G.C. Schatz, and J.T. Hupp, *Synthesis and Optical Properties of Anisotropic Metal Nanoparticles.* J. Fluorescence, 2004. **14**: p. 331 − 341.
37. Burda, C., et al., *Chemistry and Properties of Nanocrystals of Different Shapes.* Chem. Rev., 2005. **105**: p. 1025 − 1102.
38. Stanley, S.K., et al., *Inhibitory Effects of a Phage-Derived Peptide on Au Nanocrystal Nucleation and Growth.* Langmuir, 2009. **25**: p. 10886-10892.
39. Busbee, B.D., S.O. Obare, and C.J. Murphy, *An Improved Synthesis of High-Aspect-Ratio Gold Nanorods* Adv. Mater., 2003. **15**: p. 414-416.
40. Coppage, R., et al., *Determining Peptide Sequence Effects That Control the Size, Structure, and Function of Nanoparticles.* ACS Nano, 2012. **6**: p. 1625-1636.
41. Yu, J., M.L. Becker, and G.A. Carri, *The Influence of Amino Acid Sequence and Functionality on the Binding Process of Peptides onto Gold Surfaces.* Langmuir, 2012. **28**: p. 1408-1417.

42. Slocik, J.M., M.O. Stone, and R.R. Naik, *Synthesis of Gold Nanoparticles Using Multifunctional Peptides.* Small, 2005. **1**: p. 1048-1052.
43. Yu, J., M.L. Becker, and G.A. Carri, *A Molecular Dynamics Simulation of the Stability-Limited Growth Mechanism of Peptide-Mediated Gold-Nanoparticle Synthesis.* Small, 2010. **6**: p. 2242-2245.
44. Miranda, L.C.M. and C.A.S. Lima, *On the Logistic Modeling and Forecasting of Evolutionary Processes: Application to Human Population Dynamics.* Technological Forecasting and Social Change, 2010. **77**: p. 699 − 711.
45. Abadi, A.H., et al., *Discovery of Colon Tumor Cell Growth Inhibitory Agents Through a Combinatorial Approach* Eur. J. Med. Chem., 2010. **45**: p. 90 − 97.
46. Hatzivassiliou, G., et al., *RAF Inhibitors Prime Wild-type RAF to Activate the MAPK Pathway and Enhance Growth.* Nature, 2010. **464**: p. 431 − 435.
47. Kahm, M., et al., *Grofit: Fitting Biological Growth Curves with R.* J. Statistical Software, 2010. **33**: p. 1 − 21.
48. Rong, C., et al., *Fabrication of Gold Nanoparticles with Different Morphologies in HEPES Buffer.* Rare Metals, 2010. **29**: p. 180 − 186.
49. Habib, A., M. Tabata, and Y.G. Wu, *Formation of Gold Nanoparticles by Good's Buffers.* Bull. Chem. Soc. Jpn., 2005. **78**: p. 262 − 269
50. Hegetschweiler, K. and P. Saltman, *Interaction of Copper (I1) with N-(2-Hydroxyethyl)piperazine-N'-ethanesulfonic Acid (HEPES).* Inorg. Chem. , 1986. **25**: p. 107 − 109.
51. Elghanian, R., et al., *Selective Colorimetric Detection of Polynucleotides Based on the Distance-Dependent Optical Properties of Gold Nanoparticles* Science, 1997. **277**: p. 1078 − 1081.
52. Chandra, M., A.-M. Dowgiallo, and K.L. Knappenberger, *Controlled Plasmon Resonance Properties of Hollow Gold Nanosphere Aggregates.* J. Am. Chem. Soc., 2010. **132**: p. 15782 − 15789.
53. Lassiter, J.B., et al., *Close Encounters between Two Nanoshells.* Nano Lett., 2008. **8**: p. 1212 − 1218.
54. David, C. and F.J.G.d. Abajo, *Spatial Nonlocality in the Optical Response of Metal Nanoparticles.* J. Phys. Chem. C, 2011. **115,** : p. 19470 − 19475.
55. Abajo, F.J.G.d., *Nonlocal Effects in the Plasmons of Strongly Interacting Nanoparticles, Dimers, and Waveguides.* J. Phys. Chem. C, 2008. **112**: p. 17983 − 17987.
56. Wu, L., et al., *Fowler–Nordheim Tunneling Induced Charge Transfer Plasmons between Nearly Touching Nanoparticles.* ACS Nano, 2013. **7**: p. 707 − 716.
57. Mayer, K.M. and J.H. Hafner, *Localized Surface Plasmon Resonance Sensors.* Chem. Rev., 2011. **111**: p. 3828 − 3857.
58. Chen, H., et al., *Shape- and Size-Dependent Refractive Index Sensitivity of Gold Nanoparticles.* Langmuir, 2008. **24**: p. 5233−5237.
59. Dondapati, S.K., et al., *Label-free Biosensing Based on Single Gold Nanostars as Plasmonic Transducers.* ACS Nano, 2010. **4**: p. 6318-6322.
60. Chen, H., et al., *Shape-Dependent Refractive Index Sensitivities of Gold Nanocrystals with the Same Plasmon Resonance Wavelength.* J. Phy. Chem. C, 2009. **113**: p. 17691-17697.
61. Cao, M., M. Wang, and N. Gu, *Optimized Surface Plasmon Resonance Sensitivity of Gold Nanoboxes for Sensing Applications.* J. Phy. Chem. C, 2009. **113**: p. 1217-1221.

62. Khalavka, Y., J. Becker, and C. Sönnichsen, *Synthesis of Rod-Shaped Gold Nanorattles with Improved Plasmon Sensitivity and Catalytic Activity.* J. Am. Chem. Soc., 2009. **131**: p. 1871-1875.
63. Xiao, J. and L. Qi, *Surfactant-assisted, shape-controlled synthesis of gold nanocrystals.* Nanoscale, 2011. **3**: p. 1383-1396.
64. Joshi, G.K., et al., *Designing Efficient Localized Surface Plasmon Resonance-Based Sensing Platforms: Optimization of Sensor Response by Controlling the Edge Length of Gold Nanoprisms.* J. Phy. Chem. C, 2012. **116**: p. 20990-21000.
65. Barhoumi, A., et al., *Light-induced release of DNA from plasmon-resonant nanoparticles: Towards light-controlled gene therapy.* Chemical Physics Letters, 2009. **482**: p. 171-179.
66. Huschka, R., et al., *Gene Silencing by Gold Nanoshell-Mediated Delivery and Laser-Triggered Release of Antisense Oligonucleotide and siRNA.* ACS Nano, 2012. **6**: p. 7681-7691.
67. Wijaya, A., et al., *Selective Release of Multiple DNA Oligonucleotides from Gold Nanorods.* ACS Nano, 2009. **3**: p. 80-86.
68. Agarwal, A., et al., *Remote Triggered Release of Doxorubicin in Tumors by Synergistic Application of Thermosensitive Liposomes and Gold Nanorods.* ACS Nano, 2011. **5**: p. 4919-4926.
69. Shen, S., et al., *Targeting mesoporous silica-encapsulated gold nanorods for chemo-photothermal therapy with near-infrared radiation.* Biomaterials, 2013. **34**: p. 3150-3158.
70. Yavuz, M.S., et al., *Gold nanocages covered by smart polymers for controlled release with near-infrared light.* Nat. Mater., 2009. **8**: p. 935-939.
71. Bardhan, R., et al., *Nanoshells with Targeted Simultaneous Enhancement of Magnetic and Optical Imaging and Photothermal Therapeutic Response.* Adv. Func. Mater., 2009. **19**: p. 3901-3909.
72. Choi, M.-R., et al., *Delivery of nanoparticles to brain metastases of breast cancer using a cellular Trojan horse.* Cancer Nano, 2012(3): p. 47-54.
73. Choi, W.I., et al., *Tumor Regression In Vivo by Photothermal Therapy Based on Gold-Nanorod-Loaded, Functional Nanocarriers.* ACS Nano, 2011. **5**: p. 1995-2003.
74. Goodrich, G.P., et al., *Photothermal therapy in a murine colon cancer model using near-infrared absorbing gold nanorods.* J. Biomed. Optics, 2010. **15**: p. 0180011-0180018.
75. Wang, J., et al., *Selective photothermal therapy for breast cancer with targeting peptide modified gold nanorods.* Dalton Trans., 2012. **41**: p. 11134-11144.
76. Wang, Y., et al., *Comparison Study of Gold Nanohexapods, Nanorods, and Nanocages for Photothermal Cancer Treatment.* ACS Nano, 2013. **7**: p. 2068-2077.
77. Link, S., et al., *Laser-Induced Shape Changes of Colloidal Gold Nanorods Using Femtosecond and Nanosecond Laser Pulses.* J. Phys. Chem. B, 2000. **104**: p. 6152-6163.
78. Rodríguez-Oliveros, R. and J.A. Sánchez-Gil, *Gold Nanostars as Thermoplasmonic Nanoparticles for Optical Heating.* Opt. Express, 2012. **20**: p. 621-626.
79. Huang, X., et al., *Plasmonic Photothermal Therapy (PPTT) Using Gold Nanoparticles.* Lasers Med Sci., 2008. **23**: p. 217-228.
80. Melancon, M.P., et al., *In Vitro and In Vivo Targeting of Hollow Gold Nanoshells Directed at Epidermal Growth Factor Receptor for Photothermal Ablation Therapy.* Mol. Cancer Ther., 2008. **7**: p. 1730-1739.

81. Maltzahn, G.v., et al., *Computationally Guided Photothermal Tumor Therapy Using Long-Circulating Gold Nanorod Antennas.* Cancer Res., 2009. **69**: p. 3892-3900.
82. Sonavane, G., K. Tomoda, and K. Makino, *Biodistribution of Colloidal Gold Nanoparticles After Intravenous Administration: Effect of Particle Size.* Colloids Surf. B Biointerfaces, 2008. **66**: p. 274-280.

CHAPTER 3

BRANCHED NANOANTENNA-INTEGRATED SUBSTRATES FOR ULTRASENSITIVE BIOMOLECULAR SERS DETECTION

3.1 Summary

Platforms integrated with plasmonic nanostructures and combined with surface enhanced Raman spectroscopy (SERS) offer a versatile and multiplex-capable tool for ultrasensitive optical detection of analytes on any surface. Here, we incorporated multibranched gold nanoantennas (MGNs) on inexpensive filter paper to design MGN-paper dipsticks and swabs for SERS mediated sensing of chemicals, proteins, and pesticides adsorbed on fruit. MGNs are anisotropic nanostructures consisting of a core which serves as the antenna and protrusions that serve as emitters redistributing incident light. The nanoantenna effect gives rise to intense electromagnetic fields on the tips of the protrusions that enabled a detection of 100 pM of 1,4-benzenedithiol and 100 fM of human serum albumin labeled with indocyanine green with the MGN-paper dipsticks. Further, MGN-paper solid swabs enabled the detection of 62.5 pg of solid-state 4-aminothiophenol on a planar surface, and 26.3 μg of methyl parathion adsorbed on an apple. Finite difference time domain simulations demonstrated that the nanoantenna effect can be systematically modulated by altering the core-to-protrusion ratio to generate a ~65x enhancement in the electromagnetic fields localized on the protrusions which may ultimately result in sub-femtomolar to zeptomolar detection sensitivities. Lastly, incorporating protein detection via SERS tag technology with the concept of junction field strength, we designed an

MGNs sandwich architecture using MGN-glass and obtained a detection signal for prostate specific antigen (PSA) at concentrations as low as 5 fg/mL.

3.2 Introduction

Paper-based diagnostic platforms and analyte sensors have gained tremendous attention in the past decade due to their scalability and low cost.[1, 2] Paper-based assays can be processed to be flexible, portable, disposable, and easy to operate. The commercially available lateral flow assays (LFAs) for the detection of pregnancy hormones are excellent examples. While inexpensive, LFAs are limited to providing a qualitative "yes or no" type of detection and have poor sensitivity.[1] Alternatively, paper substrates incorporated with metal nanostructures and combined with a highly specific and sensitive optical diagnostic tool such as surface-enhanced Raman spectroscopy (SERS) enable an extraordinary limit of detection and accurate identification of analytes.[3, 4] Metal nanostructures when photoexcited couple incident light to conduction band electrons, generating surface plasmon resonances. These plasmon resonances give rise to both light scattering into the far-field and electromagnetic fields near the nanostructure surface.[5-7] The near-field and far-field properties are governed by the geometry, dimensions, and composition of the metal nanostructures. In this work, low-cost filter paper integrated with multibranched gold nanoantennas (MGNs) has been designed for the detection of chemical and biomolecular species mediated by SERS. MGNs are anisotropic plasmonic nanostructure which consist of a core that serves as the receiver antenna and the protrusions serve as emitters confining the re-radiated light into a localized area resulting in enhanced local fields.[8] By modulating the core-to-protrusion ratio, the nanoantenna effect can be manipulated to generate intense local fields on the protrusion tips that can couple with vicinal molecules and

significantly augment their optical readout.[8-12] Plasmonic nanostructure mediated optical enhancements have been extensively harnessed in a range of applications from surface-enhanced spectroscopies[13-17] and nanomedicine[18-21] to solar devices and photodetectors.[22, 23]

Recently SERS detection of analytes on paper substrates incorporated with metal nanospheres and nanorods has been investigated and sub-nanomolar sensitivities have been achieved.[24-28] This work reports the use of anisotropic branched nanostructures for paper based dipsticks and swabs for SERS-mediated chemical and biosensing. MGN integrated paper platforms combined with SERS offer a novel and transformational approach to ultrasensitive sensing of trace analytes because *(i)* MGNs facilitate a higher concentration of charges localized at the sharp tips of the protrusions due to the quasi-static lightning-rod effect,[8, 29] which give rise to orders of magnitude higher fields relative to spherical and prolate-shaped nanoparticles, *(ii)* the synthesis of MGNs and their incorporation on paper is straightforward enabling scalable manufacturing of plasmonic paper substrates, *(iii)* relative to fluorescence assays, Raman probes are not prone to photodestruction, and SERS provides excellent multiplexing capability due to narrow spectral widths,[30] and *(iv)* SERS allows rapid diagnosis and, relative to colorimetric sensors, provides simultaneous qualitative and quantitative detection of analytes. MGN integrated paper sensors when combined with inexpensive and lightweight handheld Raman systems will ultimately facilitate their use in remote locations providing instant results and unparalleled detection of trace chemicals without the need for time-consuming lab analysis.

In this work we demonstrate the multimodal capability of MGN-paper dipsticks and swabs for SERS mediated detection of chemicals and biomolecules, as well as pesticides adsorbed on fruits. MGN-paper dipsticks were used to detect 1,4-benzenedithiol and the lowest concentration detected was 100 pM and an enhancement factor (EF) of $4.7E^9$ which is one of the

highest reported EF values on porous paper substrates. The dipsticks were also utilized for detection of human serum albumin, a large multi-domain protein abundant in the plasma, with a detection of 100 fM. Further, the versatility of MGN-paper platforms was established by using them as swabs to detect solid state 4-aminothiophenol on a flat surface, achieving a detection of 62.5 pg. Finally, MGN-paper solid swabs were also used to detect methyl parathion, a toxic but widely used organophosphate pesticide, adsorbed on an apple demonstrating that MGN-paper swabs would be applicable for analyte detection on any surface with varied morphology and curvature. The high sensitivities achieved with MGN-paper were attributed to a combination of chemical enhancement and electromagnetic enhancement propagated by the nanoantenna effect of MGNs.

Finite difference time domain (FDTD) simulations were performed to emphasize that the nanoantenna effect can be augmented by modulating the MGN morphology. These simulations show that significant field enhancements are achieved by controlling the morphology of MGNs and that the junction fields created in the small volumes of two neighboring MGNs in a dimer are even further augmented to surpass the field strength of the monomer MGN. Therefore, by incorporating protein detection via SERS tag technology, with the concept of junction field strength, we designed a SERS sandwich biodiagnostic assay using MGN-glass substrates and obtained a detection limit for prostate specific antigen (PSA) of 5 fg/mL. Sandwich architectures involving both top-down synthesis[31, 32] or bottom-up deposition[33] have been investigated for point of care (POC) diagnostic systems that offer specificity and ultra-sensitivity.[34] These are used for early detection[35] and even multiplex[36, 37] bar code recognition. By combining electromagnetic and chemical enhancements within the MGN junctions[38, 39], we are able to detect proteins at unmatched detection limits, allowing for these SERS systems to serve as

diagnostic tools in the recognition of the early onset of disease by measuring physiological biomarkers. As these were aqueous, proof of concept studies, future SERS sandwich assays will include serum analysis of PSA levels, as an indicator for early prostate cancer detection.[33, 36]

3.3 Results and Discussion

Multibranched gold nanoantennas (MGNs) were synthesized via the HEPES-mediated growth method as described in our previous work.[8] MGNs consist of spherical cores with ~4-6 protrusions, and the protrusions often varied in length (Figure 3.1a inset). Using 300 mM HEPES, MGNs of ~58 nm were obtained (Figure 3.1a). By modulating the concentration of HEPES, the plasmon resonance of MGNs can be tuned from the visible to the near-infrared.[8] The MGNs peak position was tuned to 800 nm to overlap with the Raman laser wavelength (Figure 3.1b). The experimental extinction spectrum is an ensemble measurement, and, due to variations in the number of protrusions and length of protrusion, a broad resonance is expected. FDTD simulations were performed on a single MGN with overall dimensions 50 nm from tip-to-tip and a core diameter of 10 nm. Simulated results demonstrated good overlap with experimental peak position but with narrow bandwidth consistent with those observed for single particle measurements.[10, 11] Prior to acquiring Raman spectra, cellulose filter paper was soaked in MGN solution; the filter paper demonstrated a color change upon saturation with MGNs (Figure 3.1c inset). Paper soaked in MGNs (MGN-paper) had an estimated coverage of ~90-95 % (Figure 3.1c). High magnification scanning electron microscopy (SEM) micrograph (Figure 3.1d) shows the three dimensional topography of the MGN-paper which suggests MGNs have multiple binding conformations. The orientation of MGNs on the paper substrate directly controls analyte binding and the corresponding enhancements observed in the SERS spectra.

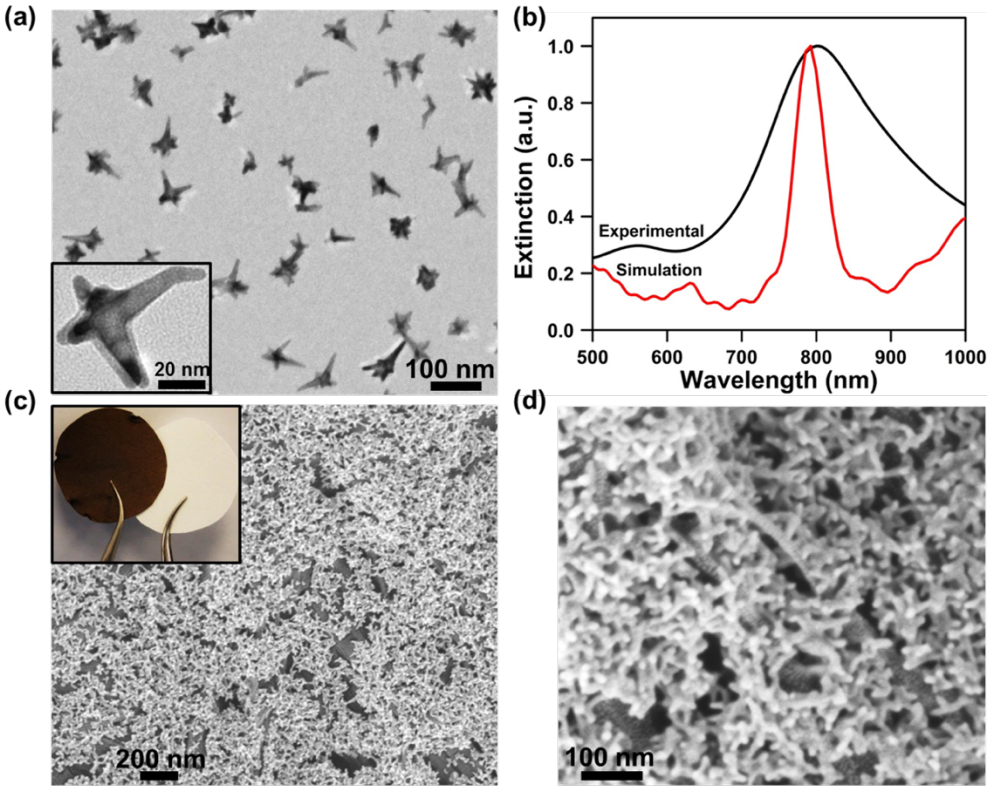

Figure 3.1: (a) TEM micrographs of MGNs demonstrating their anisotropic geometries (inset shows high magnification image of a single MGN). (b) Ensemble extinction spectrum of the synthesized MGNs overlaid with simulated extinction spectrum of a single MGN. (c) SEM micrograph of MGN-paper showing % coverage. Inset displays the associated color change of the filter paper upon MGN saturation. (d) High resolution SEM of the MGN-paper showing the topography of the paper with different MGN orientations.

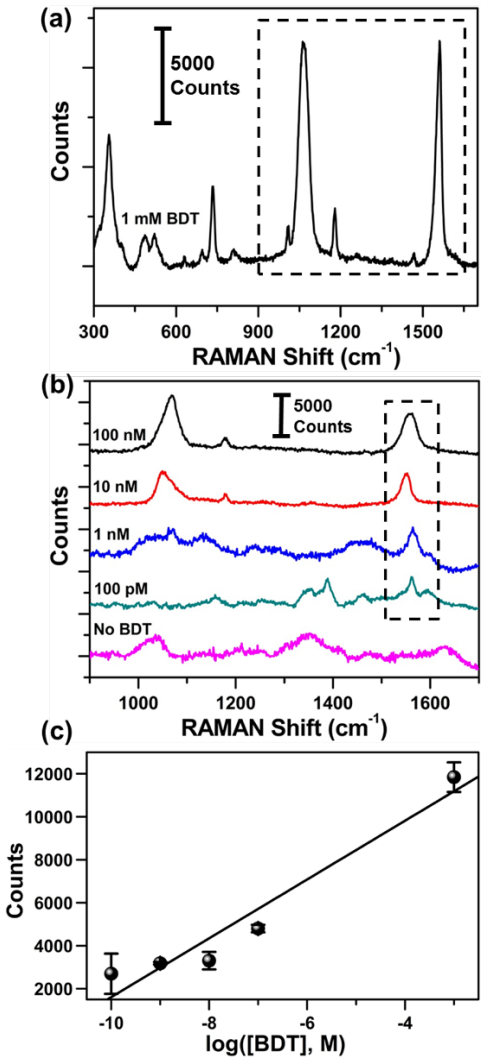

Figure 3.2: (a) SERS detection of 1 mM 1,4-Benzenedithiol (BDT) using MGN-paper. (b) SERS spectra of varying [BDT] taken with MGN-paper showing the detection of the 1560 cm^{-1} peak down to 100 pM. (c) Spectral intensity of the 1560 cm^{-1} peak as a function of log([BDT]) displaying a linear increase in intensity with increasing log([BDT]). The error bars represent >3 measurements per concentration. Linear Fit: $y = 1367.72x + 15286.51$ with an $R^2 = 91.8$ %.

The sensitivity of MGN-paper dipsticks was analyzed with a model molecule, 1,4-Benzenedithiol (BDT), which is known to form a strong covalent bond with gold surface via the thiol groups. The MGN-paper dipsticks were soaked in varying concentrations of BDT ranging from 1 mM to 100 pM; the dipsticks were allowed to dry followed by acquiring Raman spectra at multiple areas of the MGN-paper. SERS spectra of 1 mM BDT was used to identify the

Raman footprint (Figure 3.2a) which shows five pronounced peaks consistent with those found in the literature.[24, 25] The peak at 1560 cm^{-1} is due to phenyl ring stretching; 1179 cm^{-1} due to C-H bending; 1065 cm^{-1} due to the contribution of multiple modes including C-S stretching, C-H in-plane bending, and phenyl ring breathing. The peaks at 734 cm^{-1} and 355 cm^{-1} are due to the 7a and 6a vibrational modes of the benzene ring respectively in accordance to Wilson notation.[40, 41] To probe the detection limit of MGN-paper dipsticks, we focused on the 1560 cm^{-1} peak of BDT due to the strong interaction of MGNs with phenyl rings. We note that while nanorods have been shown to bind strongly to moieties corresponding to the 1065 cm^{-1} peak of BDT,[25] the MGNs interact with ring structures thus amplifying the 1560 cm^{-1} peak. We observed this process during the synthesis of MGNs where the [110] planes interacted strongly with the piperazine ring structure of the 4-(2-hydroxyethyl)-1-piperazineethanesulfonic acid (HEPES) molecule during the capping step.[8]

The lowest concentration that yielded an observable SERS signal with MGN-paper dipsticks was 100 pM of BDT as shown in Figure 3.2b which is on par with that reported in the literature.[25] The high SERS detection limit of BDT on MGN-paper is attributed to a combination of the electromagnetic and chemical enhancements. Electromagnetic enhancement is contributed by the nanoantenna effect arising from the light that is redistributed through the MGN core to the protrusions. This results in intense electromagnetic field hot spots localized on the tips of the protrusions which further amplify the SERS signal. The CE is contributed by the dynamical charge transfer of hot electrons created upon photoexcitation of MGNs. Hot electrons are typically long-lived and can transfer into the lowest unoccupied molecular orbital (LUMO) of BDT. The electron subsequently transfers back to the metal with modified internal molecular vibrations which is followed by Stokes scattering giving rise to chemical enhancement. The

chemical enhancement is mediated by the covalent bond formed between the thiol group of BDT and Au, resulting in the direct interaction of the electronic states of BDT with those of MGNs.

We observed slight deviations in the 1560 cm^{-1} peak position between concentrations of BDT which we attributed to variations in binding conformations of BDT, i.e. the angle of the BDT molecule depending on the orientation of the MGN protruding from the paper substrate.[42] Also note that the Raman peaks arising from the cellulose of the filter paper do not overlap with the BDT Raman footprint. The intensity of the 1560 cm^{-1} SERS peak on MGN-paper was plotted as a function of the log([BDT]) and the lowest concentration detected was 100 pM. A linear increase in spectral intensity was observed (Figure 3.2c) demonstrating MGN-paper can quantifiably probe picomolar concentrations of analyte molecules.

We quantified the enhancement factor (EF) of MGN-paper in detecting BDT molecules by using pristine filter paper soaked in BDT as a control. The enhancement factor control assay was performed on a plain filter paper instead of MGN-paper (see experimental section). For the control paper, 250 μL of 28.82 mM BDT solution was used while 250 μL of 100 pM BDT was utilized for the MGN-paper. EF was calculated using the following equation:

$$EF = \frac{I_{SERS}}{I_{RAMAN}} \times \frac{N_{RAMAN}}{N_{SERS}} \tag{3.1}$$

where I_{SERS} and I_{Raman} are the intensities of BDT on MGN-paper and plain filter paper respectively, and N_{SERS} and N_{Raman} are the number of molecules of BDT on MGN-paper and plain filter paper respectively. Since both assays (plain filter paper vs. MGN-paper) utilized 250 uL of volume for the dip test, the number of molecules of BDT for each system is calculated by multiplying the concentration by the volume and by Avogadro's number. It is assumed that in both cases the BDT molecules will adsorb on the paper similarly which implies the number of BDT molecules within the laser spot for either the plain filter or MGN-paper depends only on the

concentration of the BDT solution used. EF can then be calculated by accounting for the relative number of molecules illuminated with the same laser intensity for the plain filter paper vs. the MGN-paper. *The MGN-paper gives an enhancement factor of $4.7E^9$ for BDT which, to our best knowledge, is one of the highest reported values for paper-based SERS substrates.*

In addition to probing BDT molecules, the sensitivity of plasmonic paper dipsticks was also analyzed for detection of human serum albumin (HSA), a large multidomain protein synthesized in the liver and the most abundant protein in the blood plasma.[43] The Raman footprints of proteins are typically weak and difficult to distinguish. Therefore, proteins are often conjugated with Raman tags that allow for more precise analysis. In this study, HSA was labeled with indocyanine green (ICG) and the Raman peaks of ICG were analyzed to determine the concentration of HSA. ICG, a US Food and Drug Administration (FDA) approved dye, is known to completely bind to plasma proteins with 95% bound to albumin after intravenous injection.[44] Due to this strong association of ICG to HSA and ICG's well-known Raman spectral characteristics, it was utilized as a Raman reporter to detect HSA. Figure 3.3a shows a photograph of a MGN-paper dipstick with HSA-ICG in phosphate buffer. The dipsticks were prepared by soaking MGN-paper in HSA for two hours followed by soaking in ICG solution for two hours in a HSA:ICG ratio of 2:1. The Raman footprint of HSA-ICG conjugate on MGN-paper was determined by probing a ratio of 42 μM HSA:21 μM ICG (Figure 3.3b). The peaks observed were consistent with that observed previously by Kneipp et al.[45] To assess HSA detection sensitivity on plasmonic paper we focused on the 1258:1294 cm^{-1} double peak which is attributed to the methyl groups that protrude off of the ring structure of ICG.[46-48] By varying the HSA:ICG ratio the lowest concentration that yielded an observable SERS signal was 100 fM of HSA on MGN-paper (Figure 3.3c).

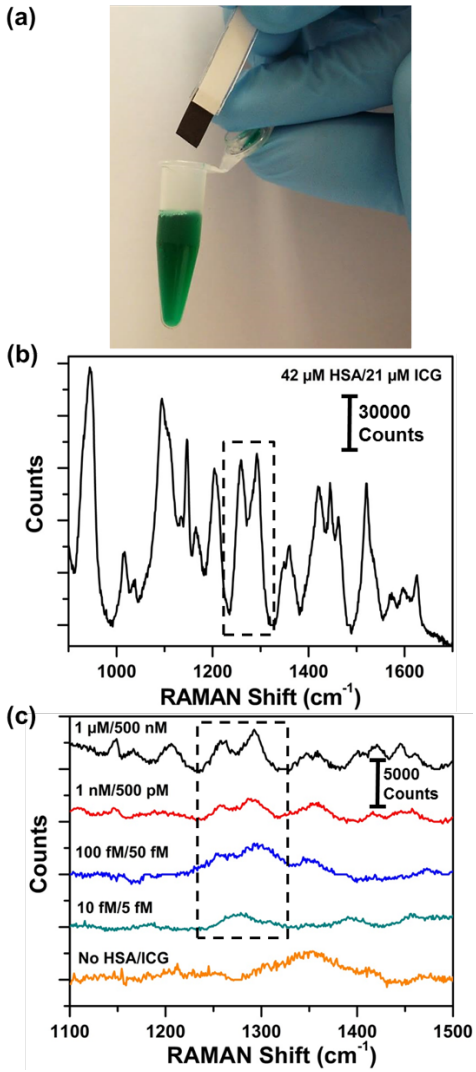

Figure 3.3: (a) A photo of the MGN-paper dipstick used for protein detection. (b) SERS detection of 42 µM:21 µM human serum albumin:indocynanine green (HSA:ICG). The ratio of [HSA]:[ICG] was kept constant at 2:1. (c) SERS spectra of varying [HSA]:[ICG] taken with MGN-paper showing the detection of the 1258:1294 cm^{-1} double peak down to 100 fM.

At concentrations below 100 fM there is insufficient HSA bound to the MGN-paper which results in ICG directly adsorbing on the MGN-paper. This lack of HSA can be observed by the double peak overlapping to form one broad singlet at 10 fM (Figure 3.3c). Further, we performed control experiments of ICG alone to assess HSA/ICG binding conformations. MGN paper was dipped in 20 µM ICG for 2 hours (no HSA), followed by air drying for 2 hours prior to SERS measurements. Raman measurements were also recorded on solid ICG. The spectra

were normalized to their 1294 cm^{-1} peaks and the relative intensities of the 1258 and 1294 cm^{-1} peaks were examined (Figure 3.4). In the presence of HSA, the ratio of the 1258:1294 cm^{-1} peaks is nearly 1:1, while for both the ICG alone bound to MGN-paper and ICG solid, the ratio of 1258:1294 cm^{-1} peaks is ~0.6. This dip in the 1258 cm^{-1} peak has been observed previously when ICG binds to a gold surface alone.[45] This difference in the ratio of the 1258:1294 cm^{-1} peaks is attributed to the conformational stability of ICG in the presence of HSA. The polymethine groups of ICG are stabilized when bound to HSA relative to solid ICG or when ICG binds to the MGN-paper by itself.[19, 49] To observe how this conformational stability changes as the HSA/ICG concentrations are lowered, we compared the peak ratios for the whole range of HSA/ICG tested (Table 3.1). As the [HSA] decreases, there is a conformational shift by the ICG molecule within the confines of its HSA complex. This can be observed by the 1258:1294 cm^{-1} ratio decreasing from 1:1 at higher HSA/ICG to ~0.7 at low HSA/ICG concentrations. However, this conformational shift is distinct from the ICG bound to the MGN-paper itself (ratio = ~0.6). This definitive difference between the two cases is observed in the lack of signal demonstrated by the ICG controls at low concentrations as described in the next section.

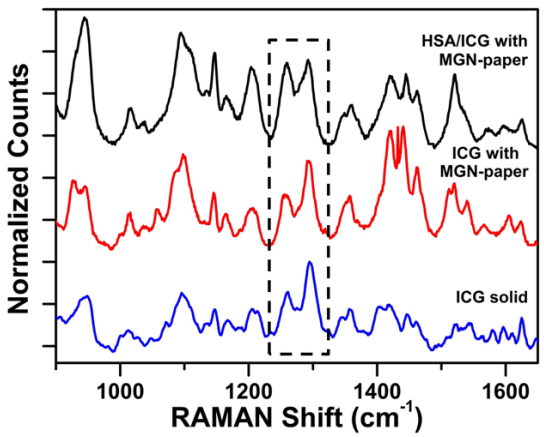

Figure 3.4: SERS detection of 42 µM:21 µM HSA:ICG with MGN-paper dipstick (black). SERS detection of 20 µM ICG with MGN-paper dipstick (red). Raman of solid ICG (blue). Spectra were normalized to their respective 1294 cm^{-1} peaks and then stacked for comparison. Boxed region focuses on the intensity ratios of the 1258:1294 cm^{-1} peaks for each sample.

Table 3.1: Comparison of the ratio of 1258 to 1294 cm^{-1} peak intensities within the double peak of various human serum albumin (HSA)/indocyanine green (ICG) probes to determine their respective binding conformations.

Probe with Substrate	**Ratio of 1258:1294 cm^{-1} peaks**
HSA/ICG with MGN-paper (42 μM/21 μM)	0.962
HSA/ICG with MGN-paper (1 μM/500 nM)	0.717
HSA/ICG with MGN-paper (1 nM/500 pM)	0.712
HSA/ICG with MGN-paper (100 fM/50 fM)	0.676
HSA/ICG with MGN-paper (10 fM/5 fM)	*N/A
ICG with MGN-paper (20 μM)	0.600
ICG solid	0.644

*The ratio for 10 fM/5 fM HSA/ICG could not be calculated because of the overlapping of the double peak to form a broad singlet.

To test whether there was any non-specific interactions occurring between the ICG and MGN-paper as the concentration of HSA/ICG was lowered, further control experiments were performed with 500 nM and 500 pM ICG. As the HSA decreases to a very low concentration, there is a possibility that the ICG molecules could find their way to the MGN-paper surface and be enhanced. However, no ICG SERS signal was obtained in the absence of HSA at the low concentrations of 500 nM and 500 pM (Figure 3.5). Without the added stability from the HSA, the ICG does not provide any signal. These control tests with ICG alone at low concentrations validate that, for low detection, the SERS signal only arises when the MGN-paper-HSA-ICG system obtains the proper conformation, and this is only possible in the presence of HSA. Thus, our MGN-paper dipstick, when used in conjugation with the ICG-labeled HSA, is a viable protein detection tool.

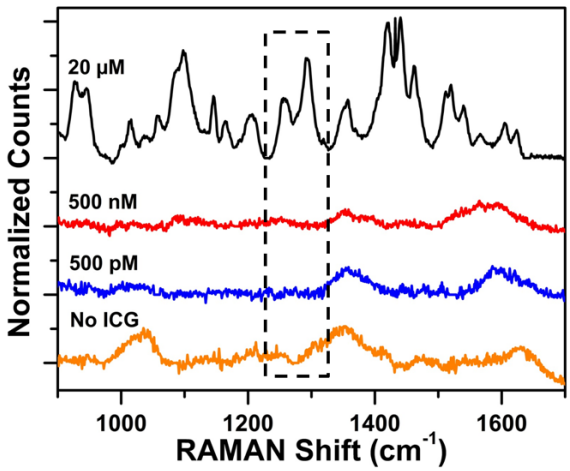

Figure 3.5: SERS detection of 20 µM ICG with MGN-paper dipstick (black). Attempted SERS detection of 500 nM (red) and 500 pM (blue) ICG with MGN-paper dipstick displaying the absence of ICG molecules. The Raman spectra of the MGN-paper (orange) is provided to distinguish peaks originating from the MGN-paper substrate itself. Spectra were normalized to the maximum peak for each corresponding sample and then stacked for comparison. Boxed region focuses on the intensity ratios of the 1258:1294 cm^{-1} peaks for each sample.

We note that enhancement factor could not be established for HSA detection due to the intense fluorescence signal from ICG on plain filter paper without MGNs (control experiment). Since fluorescence is a stronger phenomenon than Raman scattering, the Raman peaks were not observable for the control experiment which consisted of 1.022 mM:511 μM HSA:ICG on plain paper. This observation is consistent with that noted previously by Kneipp et al.[45] In the presence of MGNs, the metal quenches the fluorescence signal from the ICG molecule allowing the Raman footprint to be displayed.[18, 19] This study demonstrates that the MGN-paper dipsticks will ultimately enable the development of point of care diagnostics for the detection of a range of biomolecules from antibody-antigen to DNA/RNA, with the use of appropriate Raman tags. This work can be further extended to label-free detection of proteins on plasmonic paper albeit at the expense of high sensitivity.

While MGN-paper dipsticks are suitable for detecting probe molecules in solution, for solid analytes present in trace quantities dipsticks would be less practical. Plasmonic paper-based

swabs are ideal for ultrasensitive detection of solids present on either planar or non-planar surfaces. We demonstrate the efficacy of MGN-paper swabs for detection of two different solid state analytes: 4-Aminothiophenol (4-ATP) on a flat surface, and methyl parathion on an apple. Since solid state samples were analyzed, all detection values were reported in grams instead of concentration. 4-ATP is a model molecule that has been extensively investigated for SERS on rigid substrates, such as Si and glass, due to the strong Raman cross-section of the phenol moiety and 4-ATP's affinity to bind to Au surfaces via the thiol group. We therefore chose 4-ATP for our initial assessment of the detection sensitivity of MGN-paper swabs. The analysis was performed by dissolving the 4-ATP in ethanol and dropping a 100 µL volume over a 4 cm^2 area of a clean bench top. The solution was allowed to completely dry followed by swabbing the area with a wetted MGN-paper to detect the 4-ATP (inset of Figure 3.6a). The Raman footprint of 4-ATP (Figure 3.6a) is described by the Wilson notation for benzene ring modes: 1577 cm^{-1} is due to the C-C stretching and 8b ring modes; 1172 cm^{-1} due to C-H bending and 9a ring modes; 1075 cm^{-1} due to C-S stretching and 7a ring modes; 1003 cm^{-1} due to the C-C bending as well as 18a ring modes; and 387 cm^{-1} due to the C-C torsion modes.[50-54] As discussed previously, since MGNs interact strongly with ring structures, the 1577 cm^{-1} peak was chosen to probe the sensitivity of the MGN-paper swabs. The lowest concentration of 4-ATP that yielded an observable SERS signal with MGN-paper swabs was 62.5 pg (Figure 3.6b), which is relatively low compared to that observed previously.[28] We note that the Raman peaks from the filter paper without 4-ATP (at ~1040 cm^{-1} and 1340 cm^{-1}) do not interfere with the vibrational footprint of 4-ATP. We attribute this high sensitivity of MGN-paper swabs to the electromagnetic enhancement and chemical enhancement as discussed earlier. Overall the MGN-paper dipsticks have a higher sensitivity relative to the swabs (100 pM BDT vs. 5 nM 4-ATP),

which has been observed previously for paper-based SERS substrates.[25] This is likely because chemical interactions between molecules and the MGN surface occur more readily in solution vs. in the solid state enabling a higher SERS signal with the dipsticks as compared to the swabs. This initial analysis demonstrates that MGN-paper swabs are ideal for ultrasensitive detection of trace analytes and will be suitable for field use. *We therefore chose a real-world analyte, methyl parathion, adsorbed on an apple and examined the detection on MGN-paper swabs.*

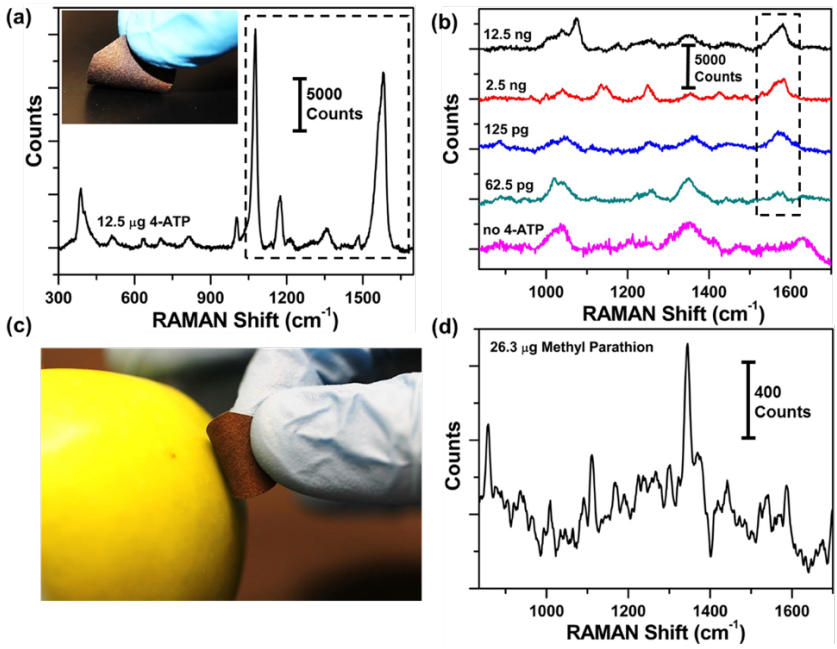

Figure 3.6: (a) SERS detection of 12.5 µg of 4-Aminothiophenol (4-ATP) using MGN-paper. Inset shows the use of MGN-paper swab on the bench top for 4-ATP detection. (b) SERS spectra of varying masses of 4-ATP detected with MGN-paper demonstrating the sensitivity of the 1577 cm^{-1} peak down to 62.5 pg. (c) Photo showing the use of MGN-paper swab for detecting methyl parathion adsorbed on an apple. (d) SERS spectra of 26.3 µg of methyl parathion on MGN-paper displaying the Raman footprint.

Methyl parathion is a toxic, organophosphorus chemical agent commonly utilized as a pesticide on fruits and vegetables.[55, 56] Methyl parathion was dissolved in ethanol, and a 100 µL volume was dropped over a 4 cm^2 area of a thoroughly cleaned apple. A wetted MGN-paper was swabbed across the apple surface (Figure 3.6c), and, subsequently, Raman spectra were recorded. The SERS footprint of the 26.3 µg methyl parathion detected by the MGN-paper swab

(Figure 3.6d) shows the 1586 cm^{-1} peak due to phenyl ring stretching mode, 1345 cm^{-1} peak due to the symmetric stretching mode of the NO_2 group, 1110 cm^{-1} peak due to C-N vibrational mode, and the 861 cm^{-1} peak due to the P-O stretching mode.[57] We note that the Raman footprint of methyl parathion did not overlap with any of the broad peaks from the filter paper itself. The low sensitivity of MGN-paper swab in the detection of methyl parathion is attributed to two effects: (1) unlike 4-ATP, methyl parathion does not have a thiol or amine group to form a covalent bond with the MGN surface which precludes any chemical enhancement; (2) unlike 4-ATP which was detected on a planar, non-porous surface, the porosity and curvature of the apple surface result in some of the methyl parathion seeping through the skin resulting in lower available concentrations of methyl parathion for detection. However, this study demonstrates the versatility of MGN-paper and its ability to detect a multitude of chemicals due to the intense electromagnetic fields generated on the MGN protrusions.

We have thus far demonstrated that MGN-paper dipsticks and swabs enabled detection of 100 fM of labeled proteins, 100 pM of label-free analytes, and 62.5 pg of solid-state chemicals. These detection ranges result from the intense nanoantenna effect where light is redistributed from the spherical MGN core (antenna) to the protrusions (emitters).[5] The nanoantenna effect creates localized hotspots on the tips of the protrusions resulting in enhanced SERS signal of analytes in proximity to MGNs. We use FDTD simulations to demonstrate that this antenna behavior can be substantially improved by modulating the geometry of MGNs. The results of this simulation may ultimately enable us to achieve sub-femtomolar to zeptomolar.[34] sensitivities by modulating junction plasmonic effects.

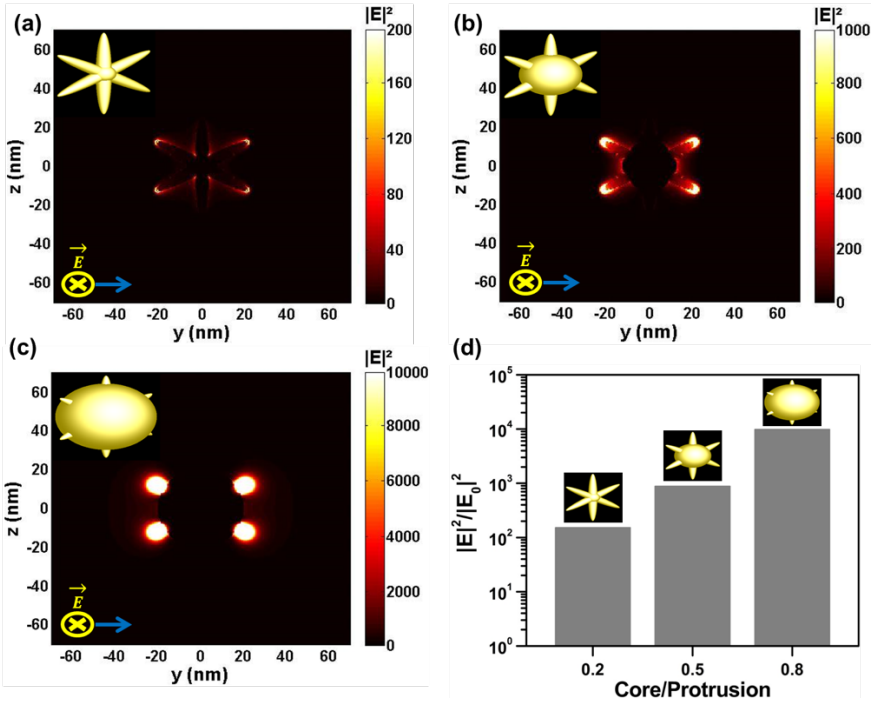

Figure 3.7: Finite difference time domain (FDTD) simulations of MGNs with spherical cores of diameter (a) 10 (a), (b) 25, and (c) 40 nm. Profiles were collected at a wavelength of 790 nm. A plane wave of intensity one was injected along the x-axis with propagation occurring along the y-axis. Color bars represent the intensities of the resulting electric fields. The insets display the actual geometries of the respective MGNs being simulated. (d) Bar graph of electric field enhancement as a function of core/protrusion ratio is shown with images of the respective MGNs above each bar. Actual $|E|^2/|E_0|^2$ values for increasing core/protrusion ratio are as follows: 152 (0.2), 878 (0.5), and 9830 (0.8).

Symmetric MGNs with six protrusions were simulated (Figure 3.7a-3.7c) by keeping the overall dimensions constant at 50 nm (i.e. tip-to-tip distance across the MGN) and varying the diameter of the core to 10 nm, 25 nm, and 40 nm. A plane wave was injected along the x-axis, and propagation along the y-axis was observed to calculate electric field enhancements. The color profiles represent the field intensity with the corresponding numerical values displayed to the right on the color bar. The electric-field intensity profiles at 790 nm (Figure 3.7a-3.7c) clearly demonstrate (1) the nanoantenna effect where the near-fields are localized on the tips of the protrusions and (2) the enhancement in nanoantenna effect with increasing core diameter of MGNs. Increasing dimensions of the antenna results in enhanced light scattering by the MGN

core; the scattered light is subsequently redirected to the protrusions. The MGN protrusions then emit the amplified light to the tips which is observable in the simulated near-field intensity profiles.

The nanoantenna effect can be further understood by the plasmon hybridization model of MGNs discussed in our previous work.[8] The plasmon resonances and corresponding electromagnetic fields of an MGN arise from the hybridization of the core and individual protrusion plasmons.[58] Plasmon hybridization results in an antibonding mode which is primarily contributed by the core plasmons while the bonding mode is predominantly composed of MGN protrusions but with a finite contribution of the core plasmons. An increase in the core diameter results in an increase in the admixture of the core plasmons in the bonding plasmon mode of the protrusions. This subsequently amplifies the dipole moment of the protrusion plasmons. The enhanced nanoantenna effect is reflected in Figure 3.7d where the intensity of the electric-field enhancements are shown as a function of increasing core-to-protrusion ratios from 0.2 (10 nm core) to 0.5 (25 nm core), and 0.8 (40 nm core). The electric field enhancements were calculated by dividing the near-field intensity by the incident field intensity. A 5.8x and 64.7x enhancement is observed in near field intensities as the core-to-protrusion ratio is increased from 0.2 to 0.5, and 0.8 respectively.

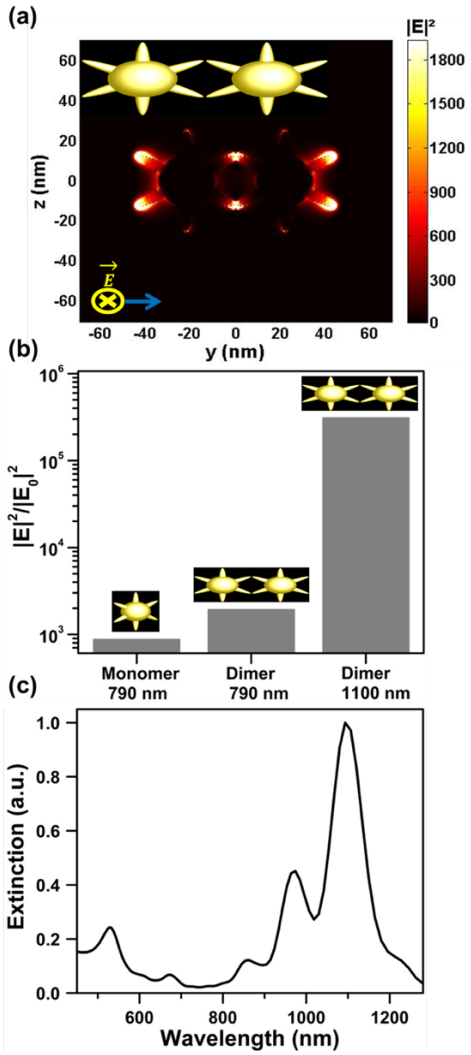

Figure 3.8: a) Finite difference time domain (FDTD) simulation of a 25 nm core MGN dimer. Profile was collected at a wavelength of 790 nm. A plane wave of intensity one was injected along the x-axis with propagation occurring along the y-axis. Color bar represents the intensity of the resulting electric field. The inset displays the actual geometry of the dimer. (b) Bar graph of electric field enhancement as a function of MGN dimerization is shown with images of the respective MGNs above each bar. Actual $|E|^2/|E_0|^2$ values for monomer vs. dimer of 25 nm core MGNs are as follows: 878 (Monomer, 790 nm), 1930 (Dimer, 790 nm), and 311000 (Dimer, 1100 nm). The dimers were calculated with a gap distance of 1 nm between adjacent MGNs and showed a 2.2x enhancement at 790 nm with a 354.2x enhancement at 1100 nm over a single MGN. (c) Simulated extinction spectrum of a dimer of 25 nm core MGNs displaying diminished monomer peak with enhanced dimer peak.

In addition to the nanoantenna effect, electric field can also be enhanced by MGN clusters. As evident from Figure 3.1c-3.1d the MGNs are closely packed on the filter paper which will result in strong interaction between adjacent MGNs giving rise to intense hot-spots.

These hot-spots will directly contribute to the observed SERS signal on MGN paper dipsticks and swabs. Nanoparticle clusters, specifically dimers of nanostructures, have been extensively studied to engineer hot-spots for SERS applications.[59-66] To understand the effect of interparticle interaction between adjacent MGNs, we have performed FDTD simulations of dimers of MGNs where each MGN has a core diameter of 25 nm and 50 nm overall dimension (Figure 3.8a). The interparticle distance between MGNs is 1 nm which results in a 2.2x enhancement at 790 nm and a 354.2x electric field enhancement at 1100 nm (Figure 3.8b). This dramatic increase in the electric field enhancement upon dimerization is further displayed by the increased dimer mode at 1100 nm at the expense of a diminishing monomer peak in the simulated extinction spectra (Figure 3.8c). These calculations demonstrate by manipulating the gap distance and number of MGNs in a cluster, hot-spots can be engineered to yield intense electromagnetic fields which can directly contribute to improved SERS signal on any substrate. This also implies MGN trimers, quadrumers, and higher-order clusters will give rise to even higher enhancement in SERS signal of molecules within the MGN junctions.

The results of these simulations have several implications: (1) it enables design rules to build MGNs and other plasmonic nanoantennas with enhanced near-field intensities which will amplify signal transduction in a range of surface-enhanced spectroscopies; (2) it demonstrates a route to develop plasmonic paper dipsticks and swabs with unparalleled SERS detection capabilities to ultimately reach near-zeptomolar sensitivity; and (3) it also provides an approach for SERS detection in both *in-vitro* and *in-vivo* applications where the size of the nanoantenna must be <100 nm to improve cellular delivery and permeation. We also note that in our previous work we have demonstrated that by altering the concentration of the gold precursor and the pH of the HEPES buffer, the geometry of the MGNs can be modified to increase the core-to-

protrusion ratio.[8] While these simulations provide emphasis on the core to protrusion length ratio only, we anticipate that the protrusion width and density will also likely effect the plasmon hybridization and the resulting energy-level splitting between bonding and antibonding plasmons which consequently impacts the nanoantenna effect.

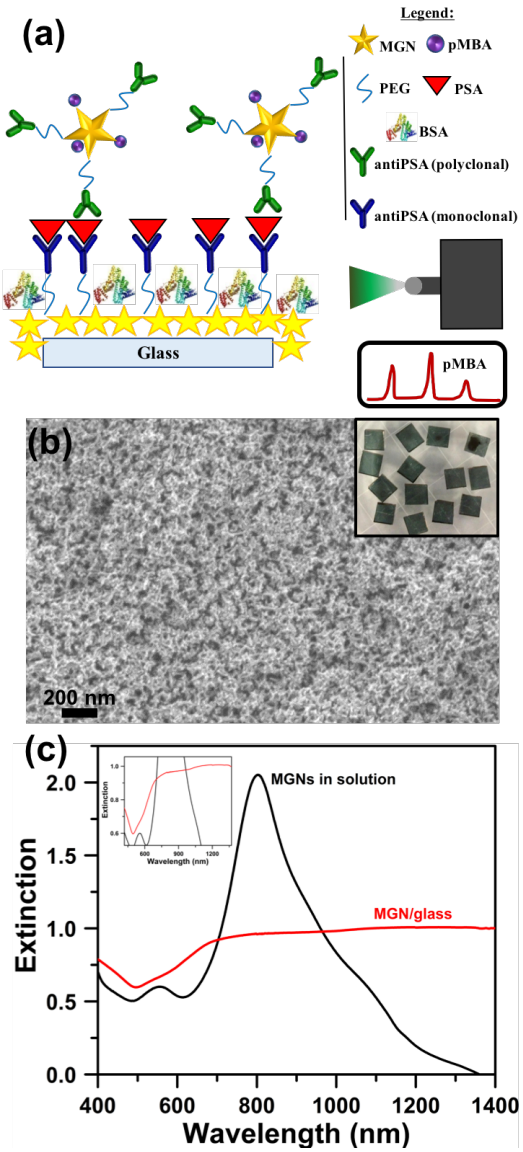

Figure 3.9: MGN-glass sandwich architecture for Prostate Specific Antigen (PSA) detection. (a) Schematic of Biodiagnostic SERS assay demonstrating the PSA molecule to be detected (red) through a SERS tag (purple, pMBA) beacon bound to the top probe MGNs. (b) Scanning electron microscopy of MGN-glass after 3-5 nm gold sputtering to enhance conductivity of glass substrate. Inset, a representative brightfield image of a MGN-glass batch preparation. (c) UV-vis spectroscopy of both the liquid phase and solid state MGN-glass, showing a blue shift due to refractive index change of the medium.

Various nanostructures[33, 38, 39] and morphologies[67-69] can be utilized for these SERS sensing assays depending on the plasmonic material incorporated. The multiplex and ultrasensitive[34, 37] properties of these platforms are attracting interest. The tool, however, of making proteins detectable, which normally have weak Raman cross-sections[70], via SERS-beacon plasmonic nanoparticle enhancement is of great significance in the design and development of theranostic nanoprobes.[69, 71]

Dimer simulations revealing that junctions between two neighboring MGNs could create tremendous field strengths provided data to support the concept of the complex sandwich architecture SERS assay for biomarker detection. To construct the assay, planar glass was utilized, and MGNs were incorporated into MGN-glass substrates. Again, integrating protein detection via SERS beacon technology with the concept of junction field strength, we synthesized antiPSA-pMBA-MGNs top probes for the Sandwich assay. Methods for the Biodiagnostic assay are provided in Appendix B. Briefly, two layers of MGNs in near proximity to one another create hot spot, junction fields leading to strong detection of signal even if a low concentration of analyte is present. Schematic of the Biodiagnostic SERS assay is provided in Figure 3.9a. The assay is meant to capture and detect the antigen (Prostate Specific Antigen) even in low concentration because of the plasmonic enhancement of the pMBA (paramercaptobenzoic acid) beacon via the MGNs SERS enhancement. Electron microscopy(Figure 3.9b) reveals the surface coverage of the MGN-glass substrates utilized in the study with particle layer visualized with a color change after MGN coating (Figure 3.9b inset). MGNs for MGN-glass preparation were synthesized with peak resonance at ~800 nm, expecting a blue shift when moving to the solid MGN-glass substrate due to the refractive index change of the surrounding medium (water to air) (Figured 3.9c). Also, ideal resonance for both the MGN-

glass bottom layer and the top functionalized antiPSA-pMBA-MGNs is in this range as to align with the 785 nm laser utilized in the SERS studies and potential NIR lasers for therapies.

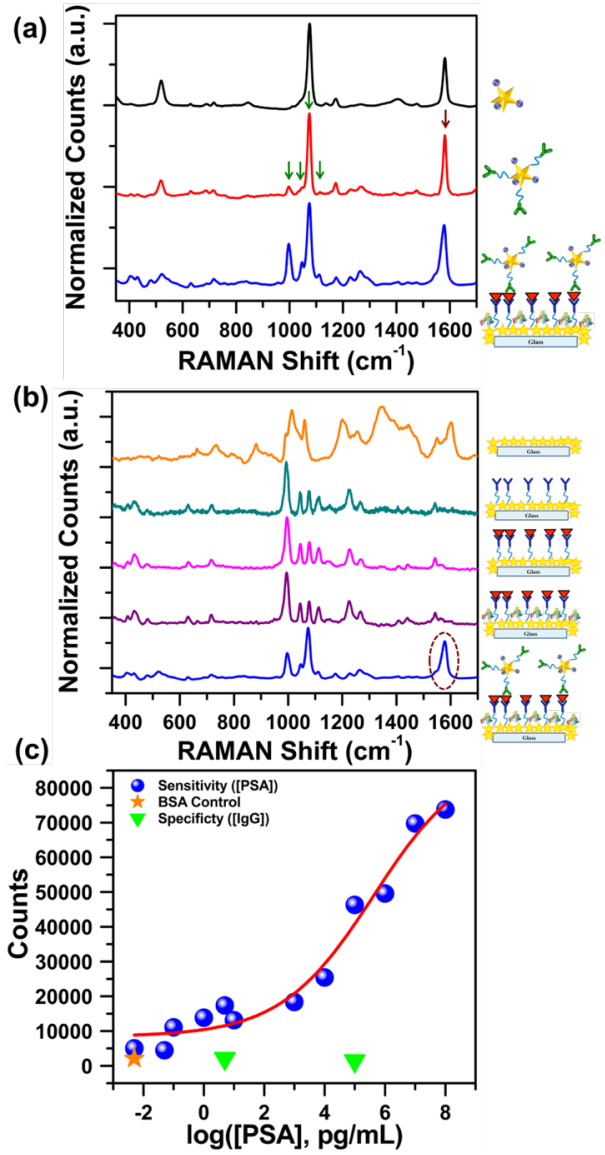

Figure 3.10: SERS Biodiagnostic assay for ultrasensitive PSA detection via MGN junction geometry. (a) SERS sandwich control verifying that the 1580 cm^{-1} peak arises from the pMBA bound in the antiPSA-pMBA-MGNs beacon (maroon arrow). Also, displayed is the 4 peak pattern from 1000 – 1200 cm^{-1} corresponding to the antibody and PEG branching (green arrows). (b) Sandwich control demonstrating that the 1580 cm^{-1} peak only displays with the antiPSA-pMBA-MGNs top probe bound (maroon circle). (c) Sensitivity study measuring $I_{SERS1580}$ for [PSA] concentrations ranging from = 5 fg/mL to 100 µg/mL (blue spheres). BSA control refers to sandwich assay with no target (PSA) present (orange star), and the specificity control (green triangles) refers to the IgG protein taking the place of the target (PSA) protein in the sandwich assay. BSA = (Bovine Serum Albumin), PSA = Prostate Specific Antigen, IgG = Immunoglobulin G.

After designing and constructing the MGN-glass SERS biodiagnostic assay, experiments were performed to determine the detection limit and fidelity of the system for false positives and specificity. To begin, the SERS peak selected for detection/quantification had to be distinguishable from all the rest of the peaks and footprints that were present in the complex system. Thus, the 1580 cm^{-1} peak[72, 73] for the antiPSA-pMBA-MGNs SERS beacon was selected to be the indicator of a positive result (Figure 3.10a, maroon arrow). Further, four peak pattern, in the 1000-1200 cm^{-1} region, occurred upon the addition of OPSS-PEG-antiPSA to the pMBA-MGNs and is thus attributed to the antibody and PEG branching (Figure 3.10a, green arrows). The density of peaks located in the region of the 1074 cm^{-1} peak of pMBA were deterrents in selecting this peak for detection. Therefore, it was determined that the 1580 cm^{-1} for pMBA beacon was the correct peak to monitor for successful PSA detection.

Within the SERS sandwich assay, the signal was only obtained with the presence of the MGN top probe of the junction (Figure 3.10b). Refer to maroon circle around 1580 cm^{-1} peak, corresponding to antiPSA-pMBA-MGNs top probes (Figure 3.10b). To test the sensitivity limit of the junction system for detection of [PSA], concentrations were tested from 5 fg/mL to 100 μg/mL (Figure 3.10c, blue spheres). After data processing, $I_{SERS1580}$ as a function of the log ([PSA], pg/mL) was plotted, and the points were fit to a sigmoidal growth curve with similar equation as used in Chapter 2 (refer to Equation 2.1). Signal was still detectable even with concentrations as low as 5 fg/mL [PSA]. In this linear regime, a bottom monolayer of substrate MGNs is assumed.

In addition, the Bovine Serum Albumin (BSA) alone control, with no target (PSA) present, was performed. For this test, the sandwich assay was completed with same steps except for buffer addition instead of antigen incubation (Figure 3.10c, orange star). No signal above

baseline was observed for this control. Lastly, Specificity control was performed, repeating the biodiagnostic assay except incubating with non-specific protein, Immunoglobulin G (IgG), instead of the target antigen (PSA). The control was attempted with multiple [IgG] concentrations, and no signal was observed (Figure 3.10c, green triangles). Thus, the lack of signal from either the BSA control assay or the IgG specificity control, demonstrates that the SERS sandwich assay has low probability for false positives with non-specific binding. The absence of signal from the IgG control demonstrates that the PSA detection will outcompete non-specific proteins when it comes time to move the assay into serum studies. The specificity of the two antibody layers for the binding event of the correct antigen (PSA), provide the assay with high fidelity while the two MGNs in a junction event, as part of the MGN-glass sandwich assay, provide unmatched detection limits. These characteristics of the Biodiagnostic SERS system make it ideal for real-world applications.

3.4 Conclusions

In summary, this work demonstrates the integration of MGNs on inexpensive filter paper to design dipsticks for SERS mediated label-free chemical detection of a concentration as low as 100 pM and labeled-protein detection of a concentration of 100 fM. Further MGN-paper swabs were also constructed for analyte sensing, and 62.5 pg was the lowest concentration detected, as well as detection of real-world samples, such as pesticides on a fruit. The experimental results and analysis provided by FDTD simulations demonstrate that the intense nanoantenna effect of MGNs gives rise to both electromagnetic and chemical enhancements which enable such high sensitivities on both porous, flexible and planar, rigid substrate. We anticipate the results of this work will help establish the SERS mediated MGN-substrates as a rapid response platform for a

range of applications including food quality control, quantification of water contaminants, biothreats such as anthrax detection for national security, explosive and chemical warfare detection, environmental sensing, as well as human health monitoring such as detection of cancer biomarkers and blood-type testing. The low cost of paper and straightforward synthesis of MGNs will ultimately enable commercialization of a MGN-paper point-of-care assay with extraordinary sensitivity, specificity, with rapid and reliable readout, and high scalability. Further the incorporation of the MGNs SERS-beacon technology for protein recognition, permitted the ultrasensitive detection of prostate specific antigen (5 fg/mL, PSA), and we envision that this technology will prove to be a vital theranostic tool *in vivo*, as well. The plasmonic MGNs are quite unique due to their versatility across substrates and their usage for a variety of biosensing tests, both properties making them ideal for real-world applications.[36]

3.5 Methods

A. MGN-paper Synthesis. All reagents were purchased from Sigma-Aldrich except 1,4-Benzenedithiol (Alfa Aesar). As described previously, MGNs were synthesized via the HEPES-mediated growth process.[8] Briefly, the reaction was scaled up to 250 mL: 100 mL of 300 mM HEPES pH 7.4 ± 0.1, 150 mL of milli-Q water (18 MΩ), and 2.5 mL of 20 mM aqueous $HAuCl_4$; mixed by inversion and left to react at room temperature for 75 minutes. Reaction volume was then concentrated down to ~ 3 mL by centrifugation (6000 rpm for 20 min) with an additional spin of the supernatant to capture all of the MGNs. Next, Whatman cellulose filter paper (Grade #2, 42.5 mm, 8 μm pores) was soaked in the concentrated MGN solution for ~ 40 hours with constant shaking. Upon saturation, MGN-paper was rinsed with milli-Q water, dried with N_2 stream, and allowed to air dry for 3.5 hours.

B. MGN-paper Characterization. A Varian Cary 5000 UV-vis NIR spectrophotometer (Agilent Technologies) was used to measure the extinction of the MGN solutions using a 1 cm path length cuvette. The MGNs were characterized using a Philips CM20T TEM at 200 keV and an Osiris TEM at 200 keV. MGN-paper was visualized using a Zeiss Merlin SEM; samples were sputtered with ~3-5 nm layer of Au prior to SEM.

C. Raman Measurements and Analysis. Using an Invia Raman microscope (Renishaw) with a 785 nm wavelength laser source, Raman measurements were obtained. All spectra were recorded using a 50x objective with a ~1 μm spot size at a power of 2.2 mW with a 10 second acquisition time. To attain control spectra (not enhancement factor control), the footprint of the MGN-paper with no analyte was collected. For each dip/swab test, an individual piece of MGN-paper was utilized. Upon completion of the respective test, a mapping of the MGN substrate was performed, in which multiple spectra were collected per substrate. These multiple spectra were acquired at different locations within the MGN substrate to the test the whole sample. For further analysis, each individual spectrum was baseline corrected to remove any contributions from the fluorescence background of the MGNs. This correction was performed using OriginPro 8 software. Raman intensities were then determined from the baseline corrected spectra and plotted against the respected concentrations.

D. 1,4-Benzenedithiol Dip Test with MGN-paper. 1,4-Benzenedithiol (BDT) dilutions were made in 100% ethanol. Pieces of MGN-paper were soaked in [BDT] for ~16 hours; followed by gentle rinsing with ethanol, drying with N_2 stream, and air drying for 1.5 hours. Raman measurements were recorded on dried MGN-paper with BDT.

E. Human Serum Albumin Dip Test with MGN-paper using Indocyanine Green Probe. Human serum albumin (HSA) (MW = 66478 g/mol) dilutions were prepared with 8.65 mM

Na_2HPO_4 pH 7.4 ± 0.1, being sure to only pipette for mixing. Indocyanine green (ICG) (photosensitive) solutions were prepared with milli-Q water (18 MΩ) as the solvent. For all assays, the HSA:ICG ratio was kept constant at 2:1. MGN-paper was soaked in [HSA] for 2 hours, followed by immediate immersion into [ICG] for another 2 hours. The paper substrates were then dried at room temperature for 2 hours prior to Raman measurements. The power of the excitation laser was adjusted depending on the fluorescence background from ICG. For lower concentrations, 3.77 mW was used, while for 42 μM HSA, 388 μW power was used. For intensity comparisons over the various [HSA], the count outputs were normalized according to the powers used.

A control experiment was performed with ICG alone on MGN-paper. 20 μM, 500 nM, and 500 pM aqueous ICG solutions were prepared, and MGN-paper was soaked in the ICG solutions for 2 hours (no HSA soaking), followed by air drying at room temperature for 2 hours. Raman measurements were performed at a very low power of 4.69 μW due to the extremely strong fluorescence of the ICG molecule. The spectra were normalized to their 1294 cm^{-1} peak for comparison to the SERS of the HSA/ICG dip test and the Raman of the ICG solid alone. A Raman spectrum of solid powdered ICG was collected at a low power of 4.69 μW due to the strong fluorescence of the ICG. The spectra were normalized to their 1294 cm^{-1} peak as described previously. As for the 500 nM and 500 pM ICG controls, 2.2 mW power was used as an attempt to obtain signal. Since there was no ICG signal for the 500 nM and 500 pM control samples, these spectra, in addition to the 20 μM ICG control, were normalized to their maximum peak to compare for the presence of SERS signal of ICG.

F. 4-Aminothiophenol Swab Test on Bench Top with MGN-paper. 4-Aminothiophenol (4-ATP) dilutions were made with 100% ethanol as the solvent. Prior to the swab test a 4 cm^2 area

of bench top was cleaned with acetone, isopropyl alcohol, and 100% ethanol to eliminate any contamination. 100 μL volumes of [4-ATP] were dropped on a 4 cm^2 area of bench top, allowed to dry, and then wiped with a piece of wetted MGN-paper (wetted with ethanol). The samples were allowed to dry and Raman spectra were recorded.

G. Methyl Parathion Swab Test on Apple with MGN-paper. Methyl parathion dilutions were made with 100% ethanol. Prior to the swab test, the 4 cm^2 area of the apple piece was cleaned with acetone, isopropyl alcohol, and 100% ethanol. In this test, multiple apples were studied with 2-3 experiments performed per apple i.e. a 100 μL droplet of methyl parathion was applied on the apple and swabbed with MGN-paper. Each droplet was placed as to not cross-contaminate with a previous study. SERS spectra were collected from multiple locations on the MGN-paper, and experiments were repeated for reproducibility. The bare apples were cleaned with acetone, isopropyl alcohol, and 100% ethanol prior to applying methyl parathion. A baseline correction was performed for each spectrum to remove any contributions from the fluorescence background of MGNs prior to plotting using OriginPro 8.

H. Finite Difference Time Domain (FDTD) Simulations of MGNs. Lumerical Inc. FDTD solutions software was used to perform single particle FDTD simulations on MGNs of varying core/protrusion ratios with water as surrounding media. Overall dimension of MGN (tip-to-tip distance) was kept constant at 50 nm, while the spherical core diameter was modified to 10, 25, and 40 nm. A total-field scattered-field (TFSF) plane wave source was injected along the x-axis, and propagation was observed along the y-axis. By collecting the scattering and absorption data from the simulation, the single particle extinction was calculated. Finally, the near-field profile data at 790 nm was collected and plotted using MATLAB software.

I. Protocols for MGN-glass SERS sandwich assay for PSA detection: All methods for the development and execution of the PSA detection platform are provided in Appendix A. Procedures include: MGN-glass preparation (A.1), synthesis of top probe antiPSA-pMBA-MGNs (A.2), and experimental design of SERS Biodiagnostic MGN sandwich assay (A.3).

3.6 Bibliography

1. Liana, D.D., et al., *Recent Advances in Paper-Based Sensors.* Sensors, 2012. **12**: p. 11505-11526.
2. Shah, P., X. Zhu, and C.-z. Li, *Development of paper-based analytical kit for point-of-care testing.* Expert Rev. Mol. Diagn., 2013. **13**: p. 83-91.
3. Polavarapua, L. and L.M. Liz-Marzan, *Towards low-cost flexible substrates for nanoplasmonic sensing.* Phys. Chem. Chem. Phys., 2013. **15**: p. 5288-5300.
4. Penn, M.A., D.M. Drake, and J.D. Driskell, *Accelerated Surface-Enhanced Raman Spectroscopy (SERS)-Based Immunoassay on a Gold-Plated Membrane.* Anal. Chem., 2013. **85**: p. 8609−8617.
5. Giannini, V., et al., *Plasmonic Nanoantennas: Fundamentals and Their Use in Controlling the Radiative Properties of Nanoemitters.* Chem. Rev., 2011. **111**: p. 3888–3912.
6. Schuller, J.A., et al., *Plasmonics for Extreme Light Concentration and Manipulation.* Nat. Mater., 2010. **9**: p. 193-204.
7. Jain, P.K. and M.A. El-Sayed, *Plasmonic Coupling in Noble Metal Nanostructures.* Chem. Phys. Lett., 2010. **487**: p. 153-164.
8. Webb, J.A., et al., *Geometry-Dependent Plasmonic Tunability and Photothermal Characteristics of Multibranched Gold Nanoantennas.* J. Phys. Chem. C, 2014. **118**: p. 3696-3707.
9. Bardhan, R., et al., *Au nanorice assemble electrolytically into mesostars.* ACS Nano, 2009. **3**: p. 266-272.
10. Hao, F., et al., *Plasmon Resonances of a Gold Nanostar.* Nano Lett., 2007. **7**: p. 729-732.
11. Nehl, C.L., H. Liao, and J.H. Hafner, *Optical Properties of Star-Shaped Gold Nanoparticles.* Nano Lett., 2006. **6**: p. 683 − 688.
12. Jiang, L., et al., *Synthesis of Fivefold Stellate Polyhedral Gold Nanoparticles with {110}-Facets via a Seed-Mediated Growth Method.* Small, 2013. **9**: p. 705-710.
13. Zayak, A.T., et al., *Harnessing Chemical Raman Enhancement for Understanding Organic Adsorbate Binding on Metal Surfaces.* J. Phys. Chem. Lett., 2012. **3**: p. 1357-1362.
14. Lee, S.J. and M. Moskovits, *Remote Sensing by Plasmonic Transport.* J. Am. Chem. Soc., 2012. **134**: p. 11384-11387.
15. Singh, A.K., et al., *Development of a Long-Range Surface-Enhanced Raman Spectroscopy Ruler.* J. Am. Chem. Soc., 2012. **134**: p. 8662-8669.
16. Wang, Z., et al., *SERS-Fluorescence Joint Spectral Encoding Using Organic-Metal-QD Hybrid Nanoparticles with a Huge Encoding Capacity for High-Throughput Biodetection: Putting Theory into Practice.* J. Am. Chem. Soc., 2012. **134**: p. 2993-3000.
17. Lal, S., et al., *Tailoring Plasmonic Substrates for Surface Enhanced Spectroscopies.* Chem. Soc. Rev., 2008. **37**: p. 898-911.
18. Bardhan, R., et al., *Fluorescence Enhancement by Au Nanostructures: Nanoshells and Nanorods.* ACS Nano, 2009. **3**: p. 744-752.
19. Bardhan, R., N.K. Grady, and N.J. Halas, *Nanoscale Control of Near-Infrared Fluorescence Enhancement Using Au Nanoshells.* Small, 2008. **4**: p. 1716-1722.
20. Choi, M.-R., et al., *Delivery of nanoparticles to brain metastases of breast cancer using a cellular Trojan horse.* Cancer Nanotechnol., 2012. **3**: p. 47-54.

21. Webb, J.A. and R. Bardhan, *Emerging advances in nanomedicine with engineered gold nanostructures.* Nanoscale, 2014. **6**: p. 2502-2530.
22. Qi, J., et al., *Highly Efficient Plasmon-Enhanced Dye-Sensitized Solar Cells through Metal@Oxide Core-Shell Nanostructure.* ACS Nano, 2011. **5**: p. 7108-7116.
23. Brown, M.D., et al., *Plasmonic Dye-Sensitized Solar Cells Using Core-Shell Metal-Insulator Nanoparticles.* Nano Lett., 2011. **11**: p. 438-445.
24. Lee, C.H., et al., *Highly Sensitive Surface Enhanced Raman Scattering Substrates Based on Filter Paper Loaded with Plasmonic Nanostructures.* Anal. Chem., 2011. **83**: p. 8953-8958.
25. Lee, C.H., L. Tian, and S. Singamaneni, *Paper-Based SERS Swab for Rapid Trace Detection on Real-World Surfaces.* ACS Appl. Mater. Interfaces, 2010. **2**: p. 3429-3435.
26. Yu, W.W. and I.M. White, *A simple filter-based approach to surface enhanced Raman spectroscopy for trace chemical detection.* Analyst, 2012. **137**: p. 1168-1173.
27. Nergiz, S.Z., et al., *Biomimetic SERS substrate: peptide recognition elements for highly selective chemical detection in chemically complex media.* J. Mater. Chem. A, 2013. **1**: p. 6543-6549.
28. Yu, W.W. and I.M. White, *Inkjet-printed paper-based SERS dipsticks and swabs for trace chemical detection.* Analyst, 2013. **138**: p. 1020-1025.
29. Calander, N. and M. Willander, *Theory of surface-plasmon resonance optical-field enhancement at prolate spheroids.* J. Appl. Phys., 2002. **92**: p. 4878-4884.
30. Wu, L., et al., *Simultaneous evaluation of p53 and p21 expression level for early cancer diagnosis using SERS technique.* Analyst, 2013. **138**: p. 3450-3456.
31. Bishnoi, S.W., et al., *SERS Biodetection Using Gold-Silica Nanoshells and Nitrocellulose Membranes.* Anal. Chem., 2011. **83**: p. 4053-4060.
32. Zhang, Q., et al., *Porous Au Nanoparticles with Tunable Plasmon Resonances and Intense Field Enhancements for Single-Particle SERS.* J. Phys. Chem. Lett., 2014. **5**: p. 370-374.
33. Li, M., et al., *Three-Dimensional Hierarchical Plasmonic Nano-Architecture Enhanced Surface-Enhanced Raman Scattering Immunosensor for Cancer Biomarker Detection in Blood Plasma.* ACS Nano, 2013. **7**: p. 4967-4976.
34. Rodríguez-Lorenzo, L., et al., *Zeptomol Detection Through Controlled Ultrasensitive Surface-Enhanced Raman Scattering.* J. Am. Chem. Soc., 2009. **131**: p. 4616-4618.
35. Yang, A.-q., et al., *Rational Design of Au Nanorods Assemblies for Highly Sensitive and Selective SERS Detection of Prostate Specific Antigen.* RSC Adv., 2015. **5**: p. 38354-38360.
36. Wu, L., et al., *Simultaneous Evaluation of p53 and p21 Expression Level for Early Cancer Diagnosis Using SERS Technique.* Analyst, 2013. **138**(3450-3456).
37. Chon, H., et al., *Simultaneous Immunoassay for the Detection of Two Lung Cancer Markers using Functionalized SERS Nanoprobes.* Chem. Commun., 2011. **47**: p. 12515-12517.
38. Campion, A. and P. Kambhampati, *Surface-Enhanced Raman scattering.* Chem. Soc. Rev., 1998. **27**: p. 241-250.
39. Kneipp, K., et al., *Surface-Enhanced Raman Scattering and Biophysics.* J. Phys.: Condens. Matter, 2002. **14**: p. R597–R624.
40. Cho, S.H., et al., *Raman Spectroscopic Study of 1,4-Benzenedithiol Adsorbed on Silver.* J. Phys. Chem., 1995. **99**: p. 10594-10599.

41. Joo, S.W., S.W. Han, and K. Kim, *Adsorption of 1,4-Benzenedithiol on Gold and Silver Surfaces: Surface-Enhanced Raman Scattering Study.* J. Colloid Interf. Sci., 2001. **240**: p. 391-399.
42. Camargo, P.H.C., et al., *Measuring the surface-enhanced Raman scattering enhancement factors of hot spots formed between an individual Ag nanowire and a single Ag nanocube.* Nanotechnology, 2009. **20**: p. 1-8.
43. Crispell, K.R., B. Porter, and R.T. Nieset, *Studies of Plasma Volume Using Human Serum Albumin Tagged with Radioactive Iodine.* J. Clin. Invest., 1950. **29**: p. 513-516.
44. Schaafsma, B.E., et al., *The clinical use of indocyanine green as a near-infrared fluorescent contrast agent for image-guided oncologic surgery.* J. Surg. Oncol., 2011. **104**: p. 323-332.
45. Kneipp, J., et al., *Optical Probes for Biological Applications Based on Surface-Enhanced Raman Scattering from Indocyanine Green on Gold Nanoparticles.* Anal. Chem., 2005. **77**: p. 2381-2385.
46. Yang, J.-P. and R.H. Callender, *The Resonance Raman Spectra of Some Cyanine Dyes.* J. Raman. Spectrosc., 1985. **16**: p. 319-321.
47. Akins, D.L., *Resonance-Enhanced Raman Scattering by Aggregated 2,2'-Cyanine on Colloidal Silver.* J. Colloid Interf. Sci., 1982. **90**: p. 373-379.
48. Kneipp, K., G. Hinzmann, and D. Fassler, *Surface-Enhanced Raman Scattering of Polymethine Dyes on Silver Colloidal Particles.* Chem. Phys. Lett., 1983. **99**: p. 503-506.
49. Soper, S.A. and Q.L. Mattingly, *Steady-State and Picosecond Laser Fluorescence Studies of Nonradiative Pathways in Tricarbocyanine Dyes: Implications to the Design of Near-IR Fluorochromes with High Fluorescence Efficiencies.* J. Am. Chem. Soc., 1994. **116**: p. 3744-3752.
50. Zhao, H., et al., *Fabrication of small-sized silver NPs/graphene sheets for high-quality surface-enhanced Raman scattering.* J. Colloid Interf. Sci., 2012. **375**: p. 30-34.
51. Hu, X., et al., *Surface-Enhanced Raman Scattering of 4-Aminothiophenol Self-Assembled Monolayers in Sandwich Structure with Nanoparticle Shape Dependence: Off-Surface Plasmon Resonance Condition.* J. Phys. Chem. C, 2007. **111**: p. 6962-6969.
52. Kim, K. and H.S. Lee, *Effect of Ag and Au Nanoparticles on the SERS of 4-Aminobenzenethiol Assembled on Powdered Copper.* J. Phys. Chem. B, 2005. **109**: p. 18929-18934.
53. Kim, K. and J.K. Yoon, *Raman Scattering of 4-Aminobenzenethiol Sandwiched between Ag/Au Nanoparticle and Macroscopically Smooth Au Substrate.* J. Phys. Chem. B, 2005. **109**: p. 20731-20736.
54. Zheng, J., et al., *Surface-Enhanced Raman Scattering of 4-Aminothiophenol in Assemblies of Nanosized Particles and the Macroscopic Surface of Silver.* Langmuir, 2003. **19**: p. 632-636.
55. Tanner, P.A. and K.-H. Leung, *Spectral Interpretation and Qualitative Analysis of Organophosphorus Pesticides Using FT-Raman and FT-Infrared Spectroscopy.* Appl. Spectrosc., 1996. **50**: p. 565-571.
56. Skoulika, S.G., C.A. Georgiou, and M.G. Polissiou, *FT-Raman spectroscopy — analytical tool for routine analysis of diazinon pesticide formulations.* Talanta, 2000. **51**: p. 599-604.
57. Li, J.F., et al., *Shell-isolated nanoparticle-enhanced Raman spectroscopy.* Nature, 2010. **464**: p. 392-395.

58. Bao, K., H. Sobhani, and P. Nordlander, *Plasmon hybridization for real metals.* Chinese Sci. Bull., 2010. **55**: p. 2629-2634.
59. Ou, F.S., et al., *Hot-Spot Engineering in Polygonal Nanofinger Assemblies for Surface Enhanced Raman Spectroscopy.* Nano Lett., 2011. **11**: p. 2538-2542.
60. Chirumamilla, M., et al., *3D Nanostar Dimers with a Sub-10-nm Gap for Single-/Few-Molecule Surface-Enhanced Raman Scattering.* Adv. Mater., 2014. **26**: p. 2353-2358.
61. Li, A. and S. Li, *Large-Volume Hot Spots in Gold Spiky Nanoparticle Dimers for High-Performance Surface-Enhanced Spectroscopies.* Nanoscale, 2014. **6**: p. 12921-12928.
62. Lassiter, J.B., et al., *Close Encounters between Two Nanoshells.* Nano Lett., 2008. **8**: p. 1212-1218.
63. Li, W., et al., *Dimers of Silver Nanospheres: Facile Synthesis and Their Use as Hot Spots for Surface-Enhanced Raman Scattering.* Nano Lett., 2009. **9**: p. 485-490.
64. McMahon, J.M., et al., *Gold nanoparticle dimer plasmonics: finite element method calculations of the electromagnetic enhancement to surface-enhanced Raman spectroscopy.* Anal. Bioanal. Chem., 2009. **394**: p. 1819-1825.
65. Kühler, P., et al., *Plasmonic DNA-Origami Nanoantennas for Surface-Enhanced Raman Spectroscopy.* Nano Lett., 2014. **14**: p. 2914−2919.
66. Chen, G., et al., *Measuring Ensemble-Averaged Surface-Enhanced Raman Scattering in the Hotspots of Colloidal Nanoparticle Dimers and Trimers.* J. Am. Chem. Soc., 2010. **132**: p. 3644-3645.
67. Chen, K., H. Han, and Z. Luo, *Streptococcus Suis II Immunoassay Based on Thorny Gold Nanoparticles and Surface Enhanced Raman Scattering.* Analyst, 2012. **137**: p. 1259-1264.
68. Zhao, S., et al., *Ultrasensitive SERS Detection of VEGF Based on a Self-Assembled Ag Ornamented–Au Pyramid Superstructure.* Biosensors and Bioelectronics, 2015. **68**: p. 593-597.
69. Xia, X., et al., *Silica-Coated Dimers of Silver Nanospheres as Surface-Enhanced Raman Scattering Tags for Imaging Cancer Cells.* Interface Focus, 2013. **3**: p. 20120092.
70. Movasaghi, Z., S. Rehman, and I.U. Rehman, *Raman Spectroscopy of Biological Tissues.* Appl. Spectrosc. Rev. **42**: p. 493-541.
71. Willets, K.A., *Super-resolution imaging of SERS hot spots.* Chem. Soc. Rev., 2014. **43**: p. 3854-3864.
72. Ye, W., et al., *Fluoride-Assisted Galvanic Replacement Synthesis of Ag and Au Dendrites on Aluminum Foil with Enhanced SERS and Catalytic Activities.* J. Mater. Chem., 2012. **22**: p. 18327-18334.
73. Xu, P., et al., *Field-Assisted Synthesis of SERS-Active Silver Nanoparticles Using Conducting Polymers.* Nanoscale, 2010. **2**: p. 1436-1440.

CHAPTER 4

THERANOSTIC GOLD NANOANTENNAS FOR SIMULTANEOUS MULTIPLEXED RAMAN IMAGING AND PHOTOTHERMAL THERAPY *IN VITRO* AND *IN VIVO* VIA HUMAN XENOGRAFT STUDIES

4.1 Summary

In this study, we demonstrate the theranostic capability of actively-targeted, site-specific multibranched gold nanoantennas (MGNs) in triple negative breast cancer (TNBC) cells *in vitro* and *in vivo* via xuman xenografts. By utilizing multiplexed surface enhanced Raman spectroscopic (SERS) imaging, enabled by the narrow peak widths of Raman signatures, we simultaneously targeted the epidermal growth factor receptor (EGFR) and immune checkpoint receptor programmed death ligand 1 (PD-L1) overexpressed on MDA-MB-231 TNBC cells. A mixture of MGNs functionalized with antiEGFR antibodies and Raman tag para-mercaptobenzoic acid (pMBA), and MGNs functionalized with antiPDL1 antibodies and Raman tag 5,5-dithio-bis-(2-nitrobenzoic acid) (DTNB) were incubated with cells. SERS imaging revealed a cellular traffic map of MGNs localization by surface binding and receptor-mediated endocytosis, enabling targeted diagnosis of both biomarkers. Further, cells incubated with antiEGFR-pMBA-MGNs and illuminated with an 808 nm laser for 15 min at 4.7 W/cm^2 exhibited photothermal cell death only within the laser spot. Control experiments with antibody conjugated MGNs in EGFR low-expressing MCF7 breast cancer cells, as well as, cells incubated with MGNs without antibodies, showed no cell death after laser illumination (indicated by live/dead cell fluorescence assay). Lastly, the cocktail of functionalized MGNs was administered

in vivo to immunodeficient mice growing 231 breast cancer tumors, and the SERS signal was monitored over time. By pre-blocking the EGFR and PD-L1 receptors, a ~30 % decrease in SERS signal was observed, demonstrating the active targeting capabilities of the theranostic MGNs. The overall investigation reveals an image-guided light-triggered therapeutic approach combining multiplexed optical imaging with spatiotemporal control and receptor-specific treatment with biocompatible theranostic nanoprobes.

4.2 Introduction

Theranostic nanostructures that combine both diagnostic and therapeutic components within a single nanoscale platform have attracted significant interest in the past decade,[1-4] as they enable both highly specific detection of disease markers and subsequent targeted, image-guided treatment all within a single clinical procedure. Gold nanostructures are particularly suited for multifunctional theranostics due to their high biocompatibility, and straightforward surface chemistry enabling functionalization of multiple molecules including targeting moieties, contrast agents, and charge-neutralizing polymers. The theranostic capabilities of several shape- and size-controlled gold nanostructures have been studied in the past decade,[5, 6] [7-9] [10-13] and some are already in clinical trials.[14] However, the combination of multiplexed imaging enabling targeted detection of multiple receptors with a therapeutic modality has not been demonstrated successfully. In this work, we show the theranostic functionality of near-infrared resonant multibranched gold nanoantennas (MGNs) in triple negative breast cancer (TNBC) cells *in vitro* by combining surface-enhanced Raman scattering (SERS) imaging with photothermal therapy (PTT). MGNs consist of an “antenna-like” spherical core that absorbs incident light, and the light is then routed through the protrusions and concentrated at the tips.[15] This unique

geometry of MGNs gives rise to the "*nanoantenna effect*" generating intense electromagnetic near fields in their vicinity which is not only advantageous for SERS but also useful for efficiently converting resonant light to heat for PTT.[16] Further, the one-step synthesis of MGNs in the presence of a biological buffer, 2-[4-(2-hydroxyethyl) piperazin-1-yl]ethanesulfonic acid, HEPES (pH 7.4) promotes its biocompatibility. HEPES binds weakly to gold surfaces, which facilitates straightforward surface modification with Raman-active molecules and antibodies for targeted detection. In addition, their sub-100 nm size is ideal for cellular uptake, enabling rapid surface binding and endocytosis in cells.

SERS Imaging has rapidly progressed from a bench-scale spectroscopic tool to a pre-clinical diagnosis technique.[17-20] Relative to other clinical imaging techniques, SERS offers high cellular-level spatial resolution[21, 22] and the capability to perform multiplexing facilitated by the narrow spectral characteristics of the vibrational signature of Raman molecules.[23, 24] This enables the detection of multiple receptors with high specificity but unlike fluorescence, SERS imaging is not limited by tissue autofluorescence and photobleaching.[25-27] The combination of this pre-clinical imaging technique with a therapeutic modality mediated by MGNs is highly desirable to allow the detection of multiple biomarkers of breast cancer and simultaneously induce externally controlled light-mediated therapy.

In this work we targeted two key receptors, epidermal growth factor receptor (EGFR) and the immunomarker programmed death ligand 1 (PD-L1) in TNBC cells. TNBC is highly aggressive and one of the most lethal types of breast cancer due to the lack of response to endocrine treatment and other targeted therapies.[28, 29] EGFR, a transmembrane glycoprotein that is a member of the erbB family of tyrosine kinase, have been implicated in the pathogenesis

and progression of up to 80% of TNBCs.[30, 31] EGFR gene amplification and gene mutation both contribute to the overexpression of this receptor, and recently monoclonal antibodies and small-molecule inhibitors targeting EGFR has shown improved outcomes in TNBC.[28] This indicates the significance of EGFR as a potential therapeutic target for TNBC. In addition to EGFR,[32, 33] the immune checkpoint ligand, PD-L1, has also been shown to be overexpressed in breast cancer cells.[34-36] The upregulation of immune checkpoint receptor programmed death protein 1, PD-1, expressed on activated $CD8^+$ T-cells impedes effector T-cell function by binding to its ligand, PD-L1.[37-39] Upon binding, interferons (IFN-γ) produced by activated T-cells upregulates PD-L1 expression which contributes to immunosuppression in the tumor microenvironment. Cancer immunotherapy, particularly blockade of inhibitory pathways such as PD-L1, has recently driven a paradigm shift in the treatment of multiple cancers.[40] This underscores the significance of PD-L1 as a target receptor for immunoimaging. We successfully demonstrated simultaneous detection of both EGFR and PD-L1 *in vitro* and *in vivo* with a mixture of MGNs functionalized with Raman tag, para-mercaptobenzoic acid (pMBA) and antiEGFR antibodies, and Raman tag 5,5-dithio-bis-(2-nitrobenzoic acid (DTNB) and antiPD-L1 antibodies. Further, antibody-conjugated MGNs demonstrated a higher uptake in cancer cells relative to passive uptake, and a significantly higher cell death via photothermal therapy. We also verified the active targeting capability of the antibody-conjugated MGNs by observing a ~30 % drop in SERS signal *in vivo* when pre-blocking with antiEGFR and antiPDL1 antibodies. We anticipate the findings of this work will translate to further theranostic studies *in vivo*, contributing insights into the emerging field of immunoimaging and immunotherapy.

4.3 Results and Discussion

MGNs were synthesized via a one-step HEPES-mediated synthesis as described in our previously reported work.[15] The average size of the MGNs, including the core and protrusions, was ~65 ± 7 nm (branch-to-branch length) as visualized under transmission electron microscopy, TEM, (Figure 4.1a). The heterogeneity in dimension is correlated to the variable protrusion length and protrusion density occurring during the synthesis process.[15] The plasmon resonance of MGNs was tuned to ~800 nm prior to functionalization (Figure 4.1b) to enable absorption of tissue-penetrating near-infrared light (690–900 nm). The near-infrared light absorption is advantageous for both SERS imaging and PTT, as an ~800 nm laser can be utilized to activate both processes. MGNs were further functionalized with antibodies to enable site-specific, targeted delivery of both diagnostic and therapeutic function in a model triple negative breast (TNBC) cancer cell line, MDA-MB-231. MGNs were therefore functionalized with antiEGFR antibodies via a heterobifunctional PEG linker, OPSS-PEG-NHS ester. In this bioconjugation chemistry, the thiols on the orthopyridyl disulphide (OPSS) group form a covalent link with the gold surface whereas the N-hydroxysuccinimide (NHS) ester reacts with the amines of the antibodies to form an amide bond. Further, the MGNs were tagged with a Raman molecule, para-mercaptobenzoic acid (pMBA) to enable SERS imaging, and coated with an additional layer of polyethylene glycol (PEG) to neutralize any surface charge and minimize off-target interactions. Zeta potential of MGNs was -4.3 ± 1 mV after PEG coating, indicating their desirable near-neutral surface. Detailed methods are provided in the supporting information. The successful functionalization of antibodies, pMBA, and PEG was monitored with a spectrophotometer, and a ~32 nm red shift in the plasmon resonance was observed due to an increase in the local refractive index of the MGNs (Figure 4.1b).[41-43] The functionalization was further confirmed with TEM

(Figure 4.1c) which showed a uniform ~5 nm conformal layer of the three components around MGNs. The Raman footprint of the final functionalized MGNs, antiEGFR-pMBA-MGNs, was confirmed by examining the SERS spectra (Figure 4.1d-i) which showed dominant peaks at 1074 cm^{-1} and 1580 cm^{-1} peaks corresponding to C-C stretching modes and ring stretching modes of pMBA.[44] The weaker peaks between 1000 – 1200 cm^{-1} correspond to the antibody and PEG branching, as determined through control experiments.

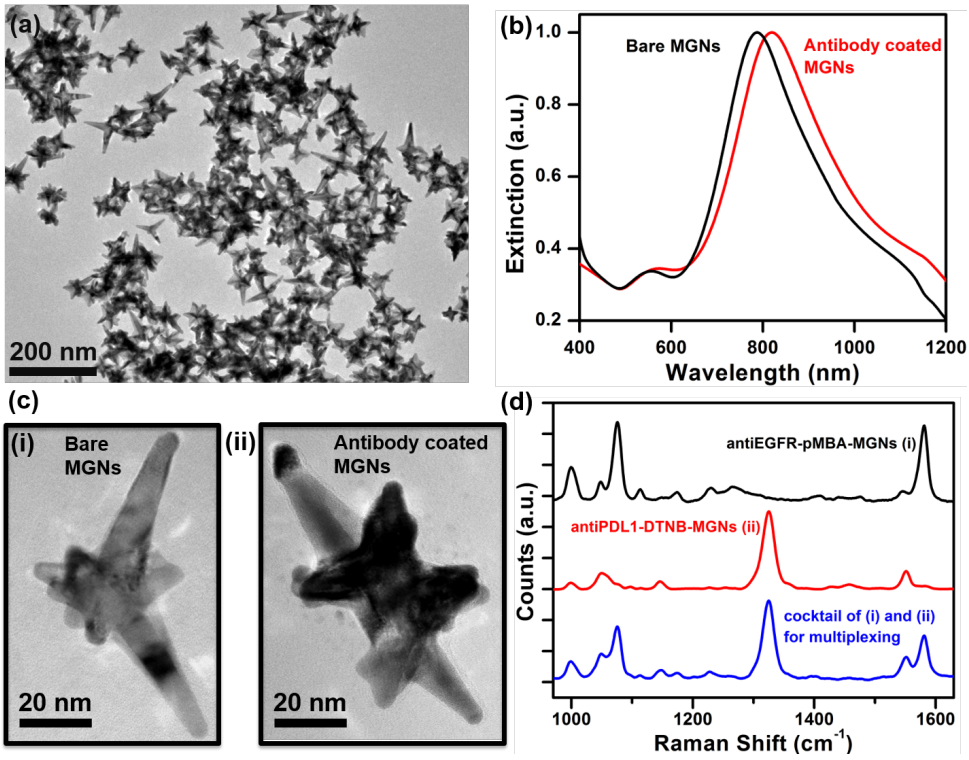

Figure 4.1: Characterization of antibody labeled MGNs. (a) Low magnification TEM micrograph of MGNs. (b) Extinction spectra of MGNs showing a red-shift after functionalization with antibodies, Raman molecule, and PEG. (c) High resolution TEM images of MGNs both (i) before and (ii) after functionalization showing ~5 nm conformal layer. (d) SERS footprint of MGNs functionalized with (i) antiEGFR/pMBA/PEG, (ii) antiPDL1/DTNB/PEG, and (iii) MGNs mixture (1:1) combining (i) and (ii) that was utilized for multiplexed Raman imaging showing distinguishable peaks at 1074 cm^{-1} and 1580 cm^{-1} corresponding to pMBA, and at 1325 cm^{-1} and 1551 cm^{-1} corresponding to DTNB.

To further investigate the ability of MGNs for multiplexed SERS imaging, the PD-L1 biomarker was targeted, as it has been found in numerous tumor types including breast cancer

and is overexpressed in MDA-MB-231 cells.[45, 46] MGNs were functionalized with antiPDL1 antibodies via the same heterobifunctional linker, and Raman molecule 5,5-dithio-bis-(2-nitrobenzoic acid (DTNB) via gold-thiol bond. The MGNs were further coated with an additional layer of PEG for stability. The Raman footprint of the functionalized MGNs, antiPD-L1-DTNB-MGNs, was assessed with SERS (Figure 4.1d-ii), and dominant peaks at 1325 cm^{-1} and 1551 cm^{-1} corresponding to symmetric stretching mode of the nitro group of DTNB, and ring stretching mode, respectively, was observable.[47] The SERS spectra of the mixture of MGNs utilized for multiplexing (antiEGFR-pMBA-MGNs + antiPDL1-DTNB-MGNs) at 1:1 ratio demonstrated distinguishable peaks from both pMBA and DTNB with minimal overlap (Figure 4.1d-iii) which enabled us to successfully detect both EGFR and PD-L1 receptors *in vitro* and *in vivo* with high sensitivity and specificity.

By attaching an active targeting moiety, the distribution of surface receptors can be visualized via the MGN enhanced SERS signal with single cell resolution. To demonstrate these targeting capabilities, the Epidermal Growth Factor Receptor (EGFR), part of the ErB3 family of proteins, was chosen as a target in the TNBC cancer cell line MDA MB 231 cells.[48] While lacking the progesterone, estrogen, and Her2/neu receptors, multiple studies have demonstrated the overexpression of EGFR in the 231 cells.[32, 33] Further, to validate the overexpression of EGFR and demonstrate the validity of utilizing it as a target, a fluorescent secondary antibody assay was performed. MDA MB 231 cells were cultured to ~90 % confluency. The cells were then fixed, followed by washing, and incubated with blocking solution to any prevent non-specific binding. The cells were washed again and then incubated with the primary monoclonal antiEGFR protein. Wells were washed, and only specifically bound antiEGFR remained on the surface of the 231 cells. Next, a secondary antibody specific for the Fc region of the primary

antiEGFR was added to the cells. This secondary antibody was labeled with phycoerythrin (PE), a fluorescent protein with excitation at 488 nm and emission 565-605 nm. Again, the cells were washed and then imaged using a Zeiss Confocal microscope (Figure 4.2). Acquiring the fluorescent image demonstrated the high signal arising from the secondary antibody bound to the primary antiEGFR (Figure 4.2a). Further by overlapping the fluorescent signal with the brightfield of the cells (Figure 4.2b), it was visualized that the secondary antibody and hence the primary anti-EGFR localized on the surface of the 231 cells (Figure 4.2c). The fluorescent signal was localized on the edges of the cells, suggesting surface binding, which would only occur via specific EGFR:antiEGFR binding events as the assay included a blocking step. These binding events and the success of the secondary antibody test confirmed the overexpression of EGFR on the surface of the 231 cells and verified the potential of using EGFR in active targeting mechanisms.

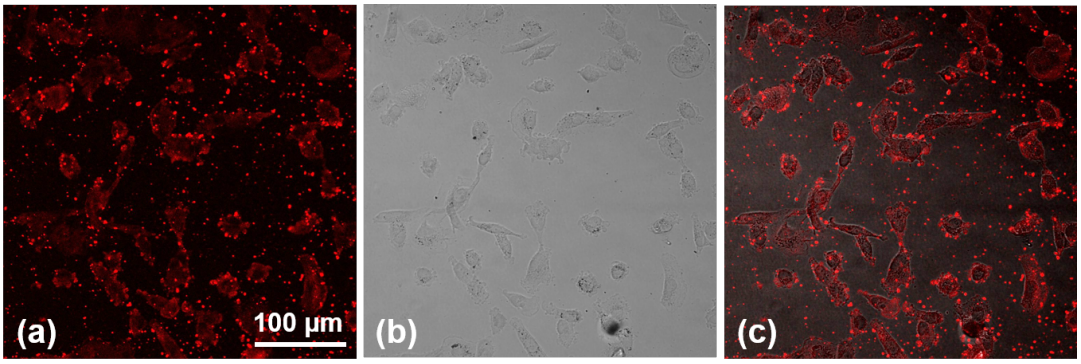

Figure 4.2: Fluorescent secondary antibody assay confirming Epidermal Growth Factor Receptor (EGFR) overexpression in MDA MB 231 cells. (a) Confocal fluorescent imaging of MDA-MB-231 cells after incubation with primary monoclonal antiEGFR, followed by a phycoerythin-labeled secondary antibody specific for the primary antiEGFR (excitation at 488 nm and emission 565-605 nm). (b) Brightfield images of the cells were also captured, and the (c) overlap was performed demonstrating surface binding.

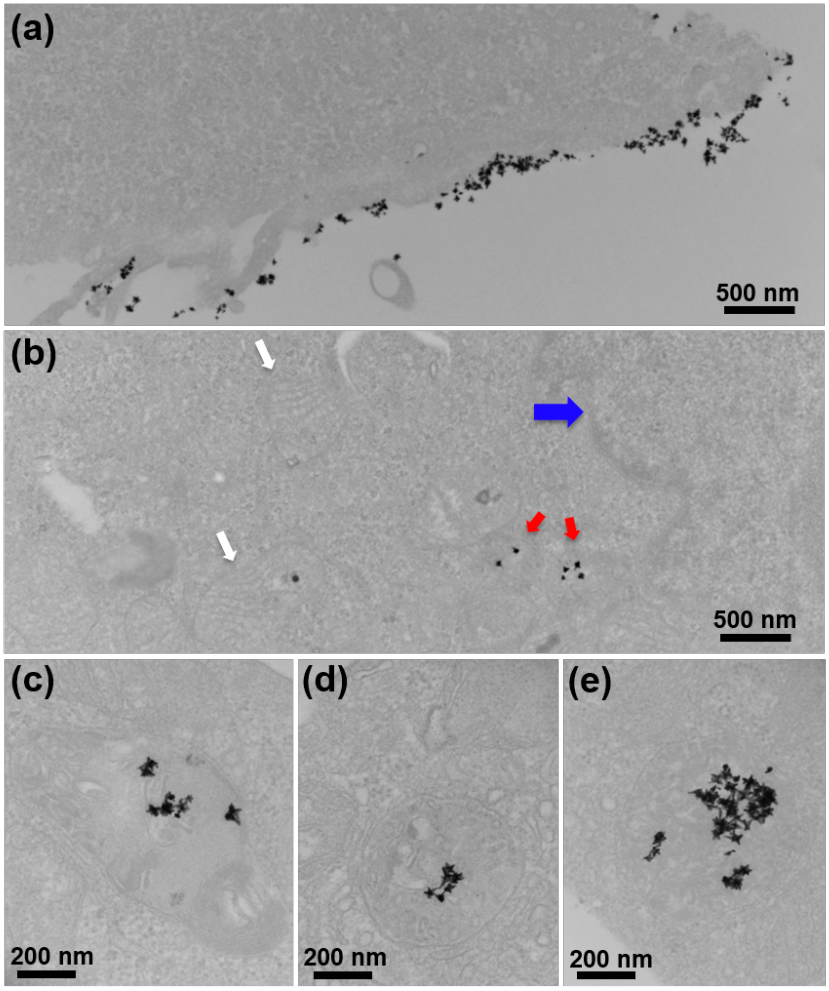

Figure 4.3: Cellular binding and uptake of antibody-coated MGNs by MDA-MB-231 cells. (a) Transmission electron micrographs of cells incubated with antiEGFR-pMBA-MGNs for 16 h show both (a) surface binding and (b) internalization by cells. Arrows denote organelles (blue = nucleus, white = mitochondria) with MGNs present in cytoplasm (red). (c-e) High magnification images show internalization occurs via intracellular vesicles ranging ~400-500 nm in size. Both on the surface and within these vesicles, the MGNs maintain their morphology.

Once EGFR was demonstrated to be a valid target, we performed SERS imaging targeting the EGFR biomarker on MDA-MB-231 cells. Cells were cultured on 6-well plate dishes to ~90 % confluency, followed by incubation with antiEGFR-pMBA-MGNs (170 µg/mL) for 16 h at 37 °C and repeated washing. After fixation, cells were visualized in TEM to confirm surface binding and internalization of MGNs. The functionalized MGNs were both localized on the surface (Figure 4.3a) and internalized within (Figure 4.3b) the cells. MGNs were also found

in cytoplasmic vesicles, demonstrating endocytosis (Figure 4.3c-4.3e). We also note that MGNs maintained their structural integrity in cells and that they were not found within the nucleus or mitochondria, which is in agreement with what has previously been reported.[49, 50]

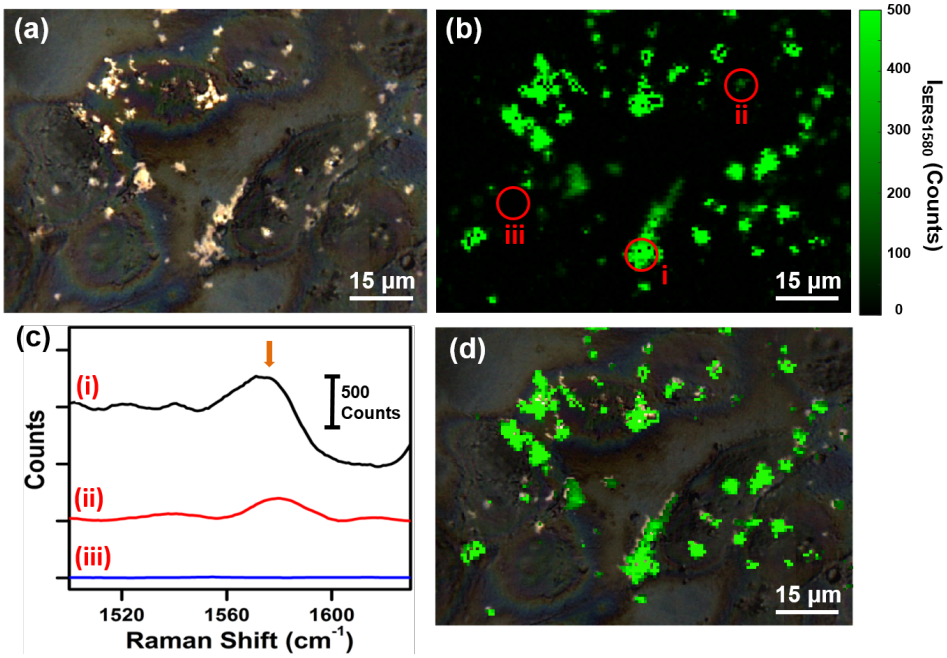

Figure 4.4: SERS singleplex mapping of MDA-MB-231 cells with antiEGFR-pMBA-MGNs. (a) Brightfield image of cells after 16 h incubation with antiEGFR-pMBA-MGNs provides coordinates for Raman map. (b) Spatial Raman intensity map of the 1580 cm^{-1} peak corresponding to pMBA, with spectra recorded at 0.75 µm steps for the rectangular area in (a). (c) Selected SERS spectra corresponding to indicated points on SERS map in (b) representing (i) high or (ii) low pMBA signal as well as (iii) no signal or cell response. Arrow denotes 1580 cm^{-1} peak of interest for pMBA. (d) Overlap of (a) and (b) showing direct correlation between SERS map and the localization of the MGNs.

The targeted SERS mapping of MDA-MB-231 cells was performed by growing the cells on calcium fluoride (CaF_2) disks to minimize autofluorescence, thus enabling higher resolution SERS mapping. Cells were incubated with antiEGFR-pMBA-MGNs (170 µg/mL) for 16 h at 37 °C followed by repeated washing, fixation, and imaging with a Raman microscope. The bright spots in the brightfield confocal image (Figure 4.4a) show scattering from MGNs localization on the cell surface. The rectangular area of the brightfield image provides the x and y coordinates for the SERS mapping. The Raman spectra of the cells were collected at 0.75 µm steps,

providing a biochemical "traffic map" of the cells in the area. Static spectra were recorded with a 1200 cm^{-1} center with 10 s acquisition times at 2 mW power. Raman intensity of the 1580 cm^{-1} peak, which corresponds to the C-C stretching modes and ring stretching modes of pMBA, was plotted as a function of position after analysis and background subtraction creating a ~100 μm x 100 μm SERS map (Figure 4.4b). The 1580 cm^{-1} peak of pMBA does not overlap with Raman peaks of intracellular lipid and provides an accurate means to demonstrate localization of antiEGFR-pMBA-MGNs by examining the intensity. SERS point spectra were collected from the SERS map at selected locations indicating high (Figure 4.4c-i), low (4.4c-ii), and no pMBA signals (4.4c-iii) which directly correspond to the amount of antiEGFR-pMBA-MGNs localized in and on the surface of the cells. The intense SERS signal in areas with high concentration of MGNs arises from the formation of SERS hot spots where strong electromagnetic and chemical enhancements occur.[51-53] Further, the brightfield image overlapped with the SERS map (Figure 4.4d) shows excellent correlation with the MGNs distribution demonstrating the efficacy of SERS in targeted imaging of the EGFR biomarker in TNBC cells. We also performed control studies where MGNs conjugated to pMBA without antibodies (pMBA-MGNs) at the same condition and concentration were incubated in MDA-MB-231 cells on CaF2 disks, and SERS maps were obtained (Figure 4.5). The relatively weak Raman signal observable in these control experiments suggests that highly specific detection of EGFR is achieved only by MGNs labeled with the targeting antibodies.

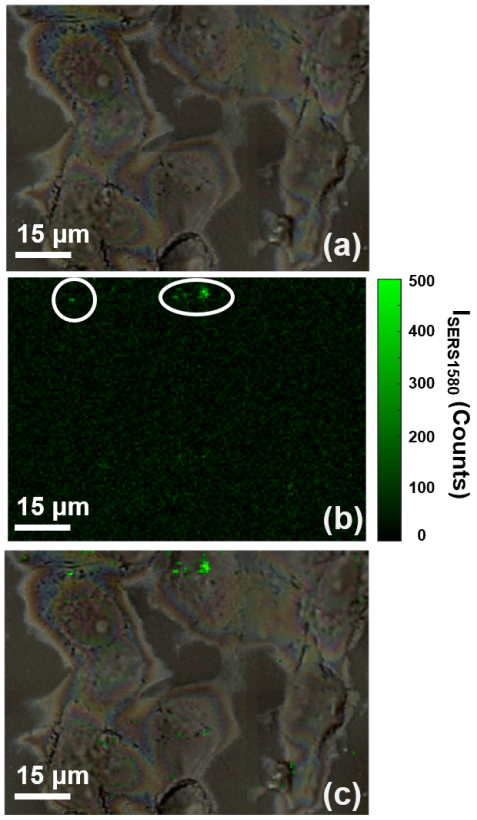

Figure 4.5: SERS singleplex mapping of MDA MB 231 cells with pMBA-MGNs. (a) Brightfield image of cells after 16 h incubation with pMBA-MGNs provides coordinates for Raman map. (b) Spatial Raman intensity map of the 1580 cm^{-1} peak corresponding to pMBA, with spectra recorded at 0.75 µm steps for the rectangular area in (a). (c) Overlap of (a) brightfield and (b) SERS map demonstrating low signal and minor surface binding of MGNs lacking targeting antibody.

The immune checkpoint receptor PD-1 and its ligand PD-L1 have been shown to be overexpressed in many sub-types of breast cancer including in MDA-MB-231 TNBC cells.[34-36] Immunotherapies with checkpoint blockade have already demonstrated tremendous success in multiple cancers and are now in clinical trials.[46, 54, 55] Therefore, multiplexed targeted detection of PD-L1 combined with EGFR offers a transformational approach to ultimately impact personalized immunotherapies. We performed multiplexed SERS imaging by simultaneously incubating cells with a mixture of antiPDL1-DTNB-MGNs and antiEGFR-pMBA-MGNs in a 1:1 ratio (refer to Methods). Because the vibrational signature of DTNB and

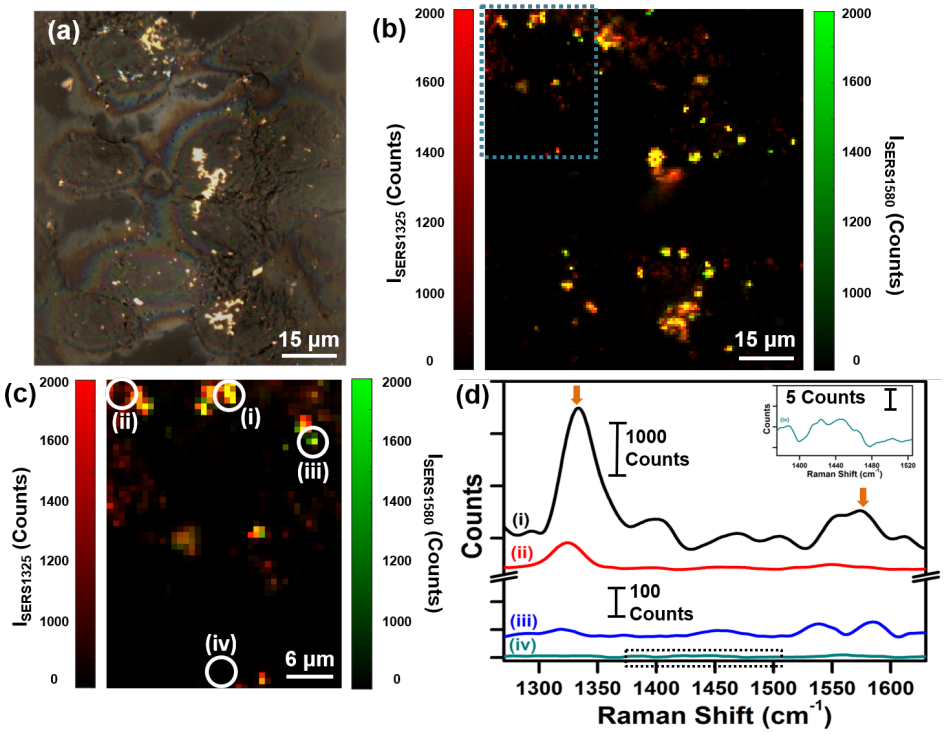

Figure 4.6: SERS multiplex mapping of MDA-MB-231cells with (1:1) mixture of antiEGFR-pMBA-MGNs to antiPDL1-DTNB-MGNs. (a) Brightfield image of cells after 16 h incubation provides coordinates for multiplex Raman map. (b) Overlap of spatial Raman intensity maps of both 1325 cm^{-1} peak for DTNB and 1580 cm^{-1} peak for pMBA, recorded at 0.75 µm steps. (c) Magnified view of the blue rectangular area from "b" shows Raman intensity plot of both $I_{SERS1325}$ and $I_{SERS1580}$ indicating a cellular "traffic map" with various points selected (d) demonstrating (i) signal from both probes, (ii) DTNB alone, (iii) pMBA alone, and (iv) no signal from probes or intracellular lipids (dashed box). Arrows denote peaks of interest, 1325 cm^{-1} peak for DTNB and 1580 cm^{-1} peak for pMBA.

pMBA do not overlap, this approach allows us to detect both PD-L1 and EGFR by mapping the signal of DTNB (1325 cm^{-1}) and pMBA (1580 cm^{-1}) respectively. Brightfield image (Figure 4.6a) shows an image of cells with light scattering from MGNS localized on cell surface. A Raman spectral map of ~100 µm x 100 µm was measured with 0.75 µm steps, and the intensity of 1325^{-1} peak ($I_{SERS1325}$) and 1580 cm^{-1} peak ($I_{SERS1580}$) was plotted together as a function of position (Figure 4.6b). Strong signal is observable from both DTNB and pMBA, and the high spatiotemporal resolution of Raman allows us to qualitatively evaluate the localization of individual receptor bound MGNs. The intensities of the 1325 cm^{-1} peak and of the 1580 cm^{-1}

peak are plotted individually (Figure 4.7a, 4.7c) and overlapped (4.7b) as a function of position. A magnified view of local traffic map of multiplexed SERS footprint is shown in Figure 4.6c correlating the distribution of PD-L1 and EGFR in the cells. Note that strong signal is observed where multiple MGNs cluster giving rise to SERS enhancements via hot spots. Specific locations on the magnified SERS map (Figure 4.6c) and corresponding SERS spectra (Figure 4.6d) indicate spatial localization from both probes (Figure 4.6d-i), DTNB alone (4.6d-ii), pMBA alone (4.6d-iii), or signal only from cellular lipids at 1440 cm^{-1} (4.6d-iv).[56] We note that the intrinsic Raman peaks of biological lipids are typically very weak, necessitating the use of labeled MGNs for characterizing receptor expression.

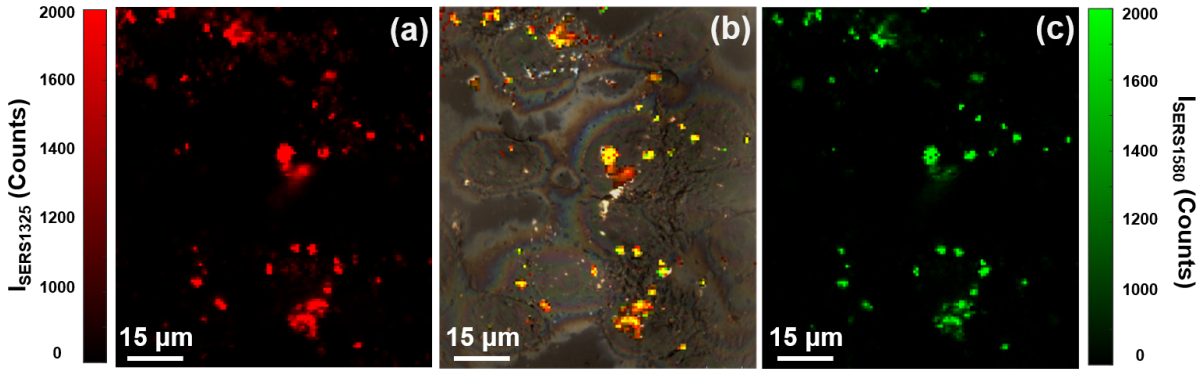

Figure 4.7: SERS multiplex mapping of MDA MB 231 cells with (1:1) mixture (antiEGFR-pMBA-MGNs to antiPDL1-DTNB-MGNs) additional plots. After 16 h incubation with (1:1) cocktail, spatial Raman intensity maps of (a) 1325 cm^{-1} peak for DTNB and (c) 1580 cm^{-1} peak for pMBA were recorded at 0.75 µm steps. Coordinates for map were provided by brightfield image from Fig. 4a and the (b) overlap of "a" and "c" with the brightfield shows localization of the mixture of antibody labeled MGNs on the surface.

Further, to demonstrate that the observed Raman signal results from specific binding of antibody-conjugated MGNs rather than due to clustering via non-specific binding, we performed a control study where 4 µg/mL monoclonal antiPDL1 (1 h, 37 °C) was introduced in cells to block the PD-L1 receptors prior to incubating with a 1:1 mixture of antiPDL1-DTNB-MGNs and antiEGFR-pMBA-MGNs (170 µg/mL). The brightfield image of the cells (Figure 4.8a) as well

as a SERS map (Figure 4.8b) at every 0.75 μm step indicated that the blocking of receptors results in significantly fewer MGNs binding to cells (Figure 4.8c). The multiplexed SERS "traffic map" presented for the experimental group (Figure 4.6b) and control group (Figure 4.8b) demonstrate that MGNs are both sensitive and specific in detecting biomarkers of cancer when conjugated with targeting moieties. In addition, SERS imaging provides a qualitative assessment of the distribution of both biomarkers in the cellular environment. We note that due to the possible co-localization of EGFR and PD-L1 on the cell surfaces, a quantitative evaluation of the distribution of these receptors with SERS maps would be more challenging and would require sub-10 nm resolution. This technology has the potential to move into in vivo tissue models and determine the volume detection of receptors on a tumor sample, which could be utilized in the determination of candidacy for certain individualized medicine movement.[54, 55, 57]

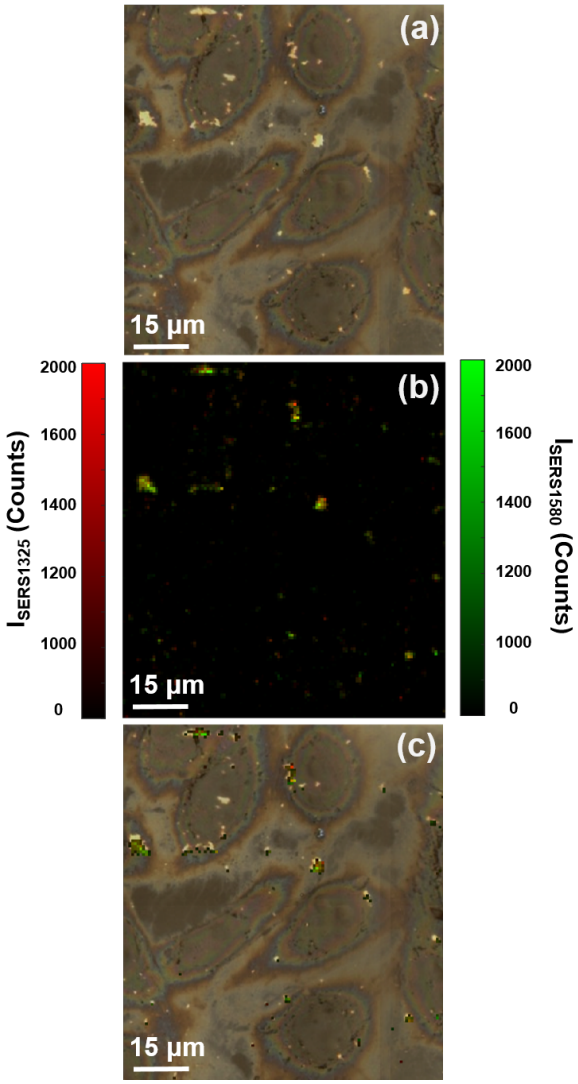

Figure 4.8: Blocking PD-L1 SERS multiplex mapping of MDA MB 231 cells with (1:1) mixture (antiEGFR-pMBA-MGNs to antiPDL1-DTNB-MGNs). Cells were pre-blocked with monoclonal antiPDL1 for 1 h. (a) Brightfield image of cells after 16h incubation with (1:1) mixture provides coordinates for multiplex Raman map. (b) Overlap of spatial Raman intensity maps of both $I_{SERS1325}$ for DTNB and $I_{SERS1580}$ for pMBA recorded at 0.75 µm steps. (c) Overlap of brightfield and SERS map (both $I_{SERS1325}$ and $I_{SERS1580}$) to compare the effects of blocking on surface binding.

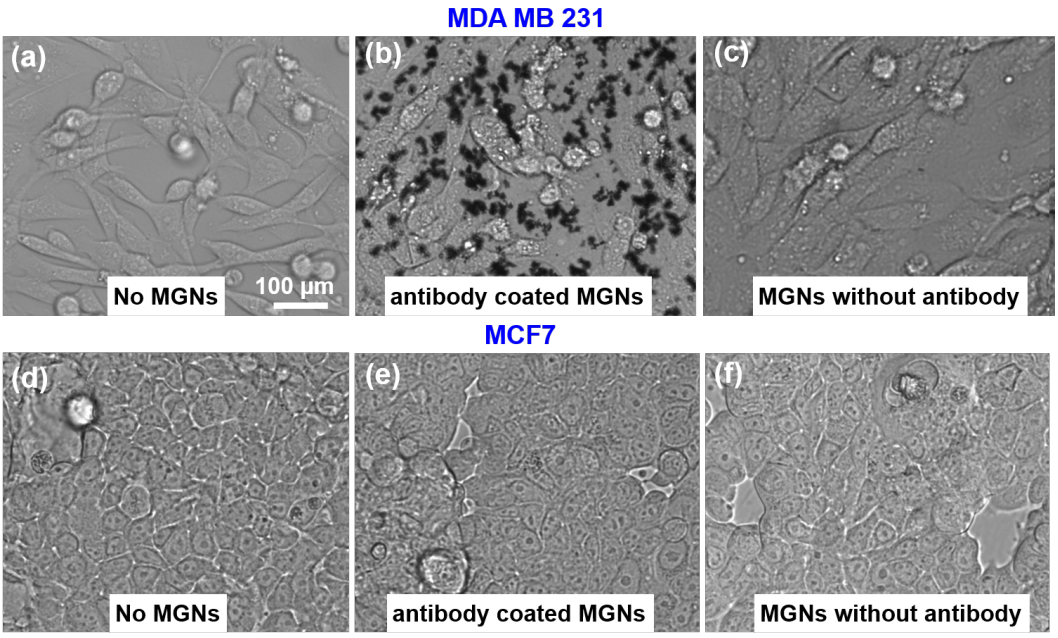

Figure 4.9: Live phase contrast images of (a) MDA-MB-231 breast cancer cells without any MGNs, (b) after 16 h of incubation with antiEGFR-pMBA-MGNs, and (c) after 16 h of incubation with pMBA-MGNs without antibodies. (d) Phase contrast images of control breast cancer cell line MCF7 (d) without any MGNs, (e) after incubation with antiEGFR-pMBA-MGNs, and (f) after incubation with pMBA-MGNs without antibodies, with incubation times also 16 h durations.

Antibody-conjugated theranostic MGNs not only enable high resolution cellular mapping of cancer cells, they are ideal for inducing targeted cell death via photothermal therapy (PTT). We incubated MDA-MB-231 cells with antiEGFR-pMBA-MGNs and also performed control experiments where MGNs without antibodies (pMBA-MGNs) were utilized. Phase contrast images before (Figure 4.9a) and after incubating with MGNs demonstrated that cells incubated with antiEGFR-pMBA-MGNs (Figure 4.9b) at 170 µg/mL for 16 h at 37 °C had a higher receptor-specific uptake relative to cells that were incubated with pMBA-MGNs without any antibodies (Figure 4.9c). We note that both antibody conjugated MGNs and MGNs without antibodies were functionalized with a final layer of PEG to minimize cellular toxicity and non-specific binding. This concentration of 170 µg/mL MGNs was measured by thermogravimetric analysis[15, 58] (TGA) and was determined to be appropriate for enabling MGNs to be localized

on the cell surface and achieve the necessary temperature increase to allow photothermal therapy.[59] As a result, this MGN concentration was utilized throughout this study.

The increased uptake of antiEGFR-pMBA-MGNs in cells clearly shows that (i) EGFR receptors are overexpressed in MDA-MB-231 cells as supported by our florescence assay in Figure 4.2, (ii) active targeting of MGNs is enabled likely by both surface-bound receptors and receptor-mediated endocytosis,[60-63] and (iii) MGNs without antibodies have a low passive uptake in cells within 16 h of incubation.[60, 64] To further demonstrate the efficacy of MGNs in specifically targeting EGFR-overexpressing breast cancer cells, MCF7 was chosen as a control cell line, due to its very low EGFR expression.[65, 66] Unlike the spindle morphology of the MDA-MB-231 cells, these MCF7 cells have more of a brick-shaped morphology and tend to grow in closer proximity to one another (Figure 4.9d). Phase contrast images clearly demonstrated that MGNs are not bound to cells either via active targeting (Figure 4.9e) or via passive uptake (Figure 4.9f) demonstrating that antiEGFR conjugated MGNs are ideal for achieving highly specific and sensitive PTT with minimal off-target cell death. We note that the morphology of both cell lines is unchanged in the presence of the MGNs and that no cytotoxic effects were observable.

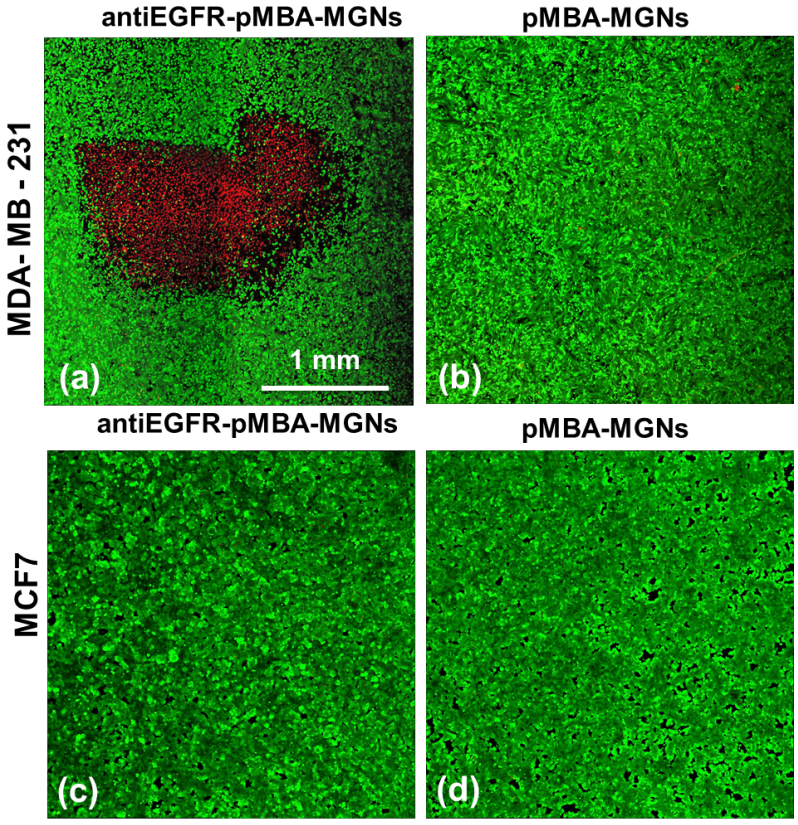

Figure 4.10: Confocal fluorescence images of live cells stained with Calcein-AM (Green) and dead cells stained by propidium iodide (Red) showing cell death via photothermal therapy 4 h post illumination with an 808 nm laser, 2 x 2 mm spot size, and 4.7 W/cm^2 pump fluence. Localized cell death was only observed with (a) antiEGFR-pMBA-MGNs, and no cell death was observed with (b) pMBA-MGNs. No cell death was observed for the control MCF7 cells with (c) antiEGFR-pMBA-MGNs, and (d) pMBA-MGNs. Note: The necrotic cells are only found within the laser spot.

Photothermal therapy was performed in both MDA-MB-231 cells and control, MCF7, cells with antiEGFR-pMBA-MGNs and pMBA-MGNs (Figure 4.10). The plasmon resonance of the antiEGFR-pMBA-MGNs was tuned to overlap with an 808 nm diode laser utilized for PTT, and the concentration of nanoparticles utilized was analogous to that used in SERS measurements (170 μg/mL). All culture dishes were illuminated for 15 min with the 808 nm laser at 4.7 W/cm^2 with a spot size of ~2 mm x 2 mm. A live/dead cell assay with calcein/propidium iodide stains clearly demonstrated that site-specific necrotic cell death was only observable when EGFR overexpressing MDA-MB-231 cells were incubated with antiEGFR

conjugated MGNs and illuminated with laser (Figure 4.10a). Cells incubated with pMBA-MGNs (no antibodies) showed no observable cell death due to the low passive uptake of MGNs in cells (Figure 4.10b). Control experiments with EGFR low-expressing MCF7 cells also demonstrated no cell death with both antiEGFR-pMBA-MGNs (Figure 4.10c) and pMBA-MGNs (Figure 4.10d). PTT with antibody conjugated MGNs demonstrates that active targeting enables higher cellular accumulation, minimal non-specific binding and off-site toxicities, and a highly specific and sensitive spatiotemporal control of cell death externally triggered with low near-infrared laser powers. Our control experiments also show that the 808 nm laser alone did not induce any cell death (Figure 4.11a), and in the absence of laser, the antiEGFR-pMBA-MGNs were not cytotoxic to the cells (Figure 4.11b).

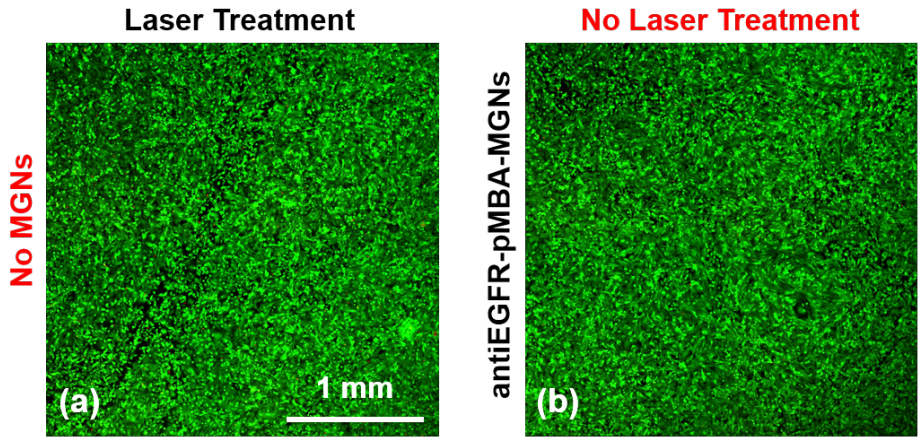

Figure 4.11: Photothermal therapy control assays, laser alone and antiEGFR-pMBA-MGNs alone. Confocal fluorescence images with live/dead cell stain (calcein AM/propidium iodide) showing no cell death in the MDA MB 231 cultures due to unwanted effects. (a) No observable cell death was detected when the 231 cells were illuminated in the absence of antiEGFR-pMBA-MGNs. (b) Further the antiEGFR-pMBA-MGNs were not toxic to the cells following 16 h of incubation and repeated washing.

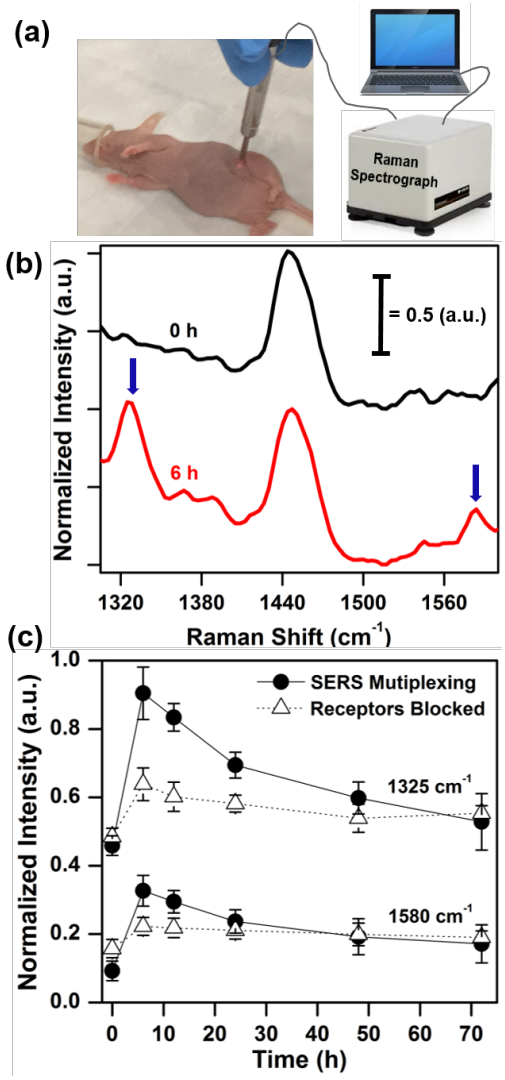

Figure 4.12: Longitudinal multiplex SERS imaging *in vivo* with actively targeted MGNs, and the effect of receptor blockage. (a) Portable SERS imaging system with maneuverable hand-held probe allowed for fast, non-invasive SERS measurements on the surface of the Human xenografts (MDA MB 231) growing in athymic mouse. Readings were monitored before and at time intervals after retro-obrital injection of the mixture of (antiEGFR-pMBA-MGNs to antiPDL1-DTNB-MGNs). (b) The appearance of the 1325 cm^{-1} peak for DTNB and 1580 cm^{-1} peak for pMBA can be observed after 6 h. (c) Longitudinal studies were performed monitoring the signal of the two SERS probes for an experimental group and a control receptor blocked group of mice. The control group was pre-blocked with both antiEGFR and antiPDL1 through intraperitoneal injection 2 h prior to injection of MGNs. Raman intensity for both the 1325 cm^{-1} peak for DTNB and 1580 cm^{-1} peak for pMBA were normalized to the 1440 cm^{-1} lipid peak after smoothing and background subtraction. A ~30% drop in signal is observed due to the receptor blockage on the surface of the tumor. n=4 for each group subset.

After demonstrating that the mixture of antibody coated MGNs were capable of distinguishing two separate targets on the cellular level, we next investigated the performance of the cocktail of antiEGFR-pMBA-MGNs to antiPDL1-DTNB-MGNs *in vivo* utilizing human xenograft models in athymic nude mice. Theranostic gold nanoparticles are attracting interest for *in vivo* applications because of their adaptability to offer combinational theranostics[12, 67, 68] or multi-modal imaging.[47, 69, 70] We moved our functionalized MGNs studies *in vivo* by growing MDA MB 231 breast cancer tumors in the mammary fat pad of the mouse, injecting cells in the subcutaneous layer for tumor growth. The mixture was injected at 2:1 antiEGFR-pMBA-MGNs to antiPDL1-DTNB-MGNs for the *in vivo* and *ex vivo* studies due to the intense SERS signal of DTNB at the [MGNs] concentrations used for these studies.[47, 71] Using a portable SERS imaging system and a handheld probe, a longitudinal study was performed on the mouse subjects over 72 h time course, measuring the intensity of the two SERS tags of the functionalized MGNs (Figure 4.12a). At the site of the tumor, non-invasive, topical measurements were acquired before and at time intervals after retro-obrital injection. The appearance of the 1325 cm^{-1} peak for DTNB and 1580 cm^{-1} peak for pMBA are observed after 6 h as indicated by the arrows in Figure 4.12b. After background subtraction and normalizing to an endogenous peak of the tumor tissue (lipid, 1440 cm^{-1}), the SERS intensity was plotted for both the DTNB and pMBA peaks with maximum SERS intensity occurring at 6 h post retro-orbital injection (Figure 4.12c). Further, the active targeting capabilities of the antibody coated MGNs were investigated by having a control group study that was pre-blocked with antiEGFR and antiPDL1 monoclonal antibodies through intraperitoneal injection, 2 h prior to MGN injection. A drop in SERS signal of ~30% was observed due to the receptor blockage on the surface of the tumor (Figure 4.12c). Thus, the antibody coated MGNs not only have the multiplex ability to

detect two receptors simultaneously *in vivo*, the targeting capabilities ensure site specificity and avoidance of off-target accumulation as well.

For further analysis and to demonstrate the spatial resolution of the SERS imaging technology, *ex vivo* experiments were performed on the xenograft tumors post removal at 6 h after actively targeted MGNs injection (2:1 mixture). The tumor was removed from the mouse, frozen, and sectioned for imaging. Bright-widefield imaging of silver stained tissue section from mammary fat pad tumor showed antibody coated MGNs accumulation as indicated by the white arrows in Figure 4.13a. A control tumor section silver stained, which had no MGNs injected into the mouse was also captured (Figure 4.13b). Side by side visualization confirmed presence of actively targeted MGNs at 6 h post injection. Additionally, vasculature and tissue morphology were not modified by MGN injection and accumulation as seen by side by side comparison of tumors both with and without actively targeted MGNs added respectfully (Figure 4.13c-4.13d).

Lastly, a spatial SERS map of the tumor cross-section was collected, 6 h post injection with actively targeted MGNs. Brightfield micrograph of tumor slice provided x and y coordinates for SERS mapping of tissue cross-section (Figure 4.13e). Acquiring Raman chemical footprints at 50 μm steps, the rectangular area in Figure 4.13e was measured, followed by Direct Classical Least Squares (DCLS) component mapping of the 1325 cm-1 peak corresponding to DTNB of the antiPDL1-DTNB-MGNs (Figure 4.13f). DCLS utilizes characteristics of the peak geometry as parameters to determine similarity for spectra in a large dataset. As seen by Figure 4.13f, signal was localized on the periphery of the tumor cross section where more vasculature is concentrated when comparing to necrotic core. This ability to monitor and trace surface receptor coverages through MGNs enhanced tags is a prime advantage of SERS spectroscopy because of its combination of multiplex technology with high spatiotemporal resolution.

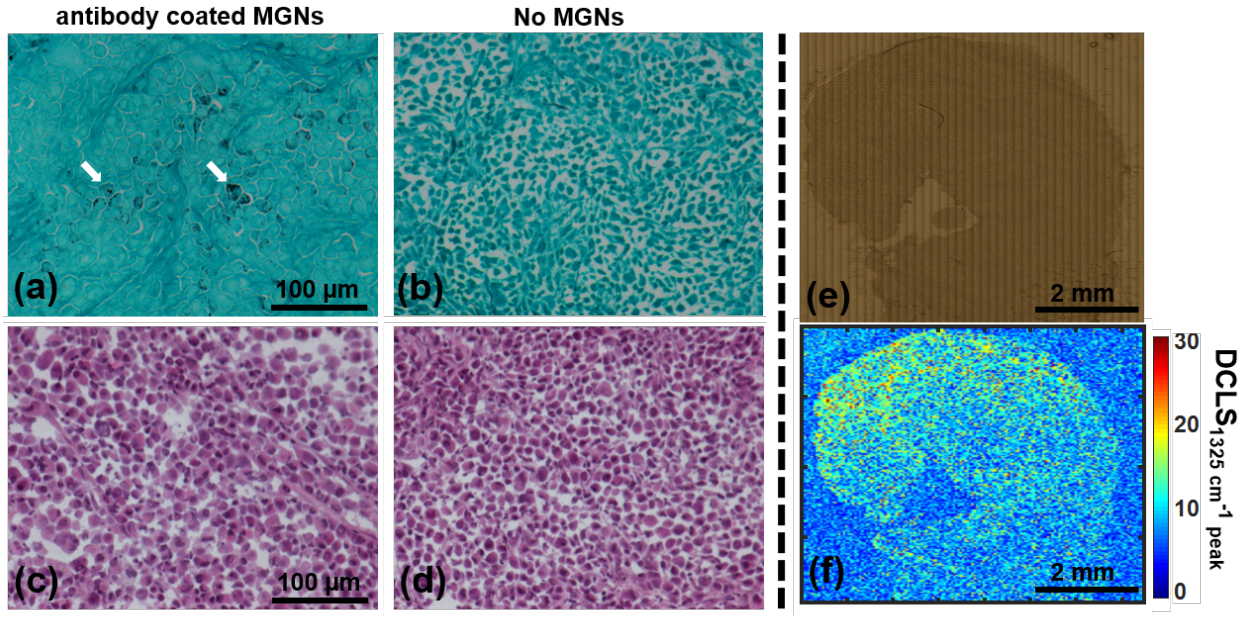

Figure 4.13: *Ex vivo* analysis and SERS spatial mapping of MDA MB 231 tumors after excision from mice injected with actively targeted MGNs. Tumor removed from mouse at maximum SERS signal (max accumulation), 6 h post retro-orbital injection with actively targeted MGNs. (a) Bright-widefield imaging of silver stained tissue section from mammary fat pad tumor (human xenograft). White arrows indicate MGNs accumulation. (b) For comparison, also provided is a control tumor slice silver stained, which had no MGNs injected to the mouse. (c-d) Images of tumor sections for Histology (H and E) staining for side by side comparison of +/- actively targeted MGN addition, also visualized with bright-widefield microscopy. (e-f) *Ex vivo* SERS spatial mapping of tumor section from tumor removed 6 h post injection with actively targeted MGNs. (e) Brightfield image of tumor tissue slice provides coordinates for Raman map. (f) Spatial Raman map demonstrating the Direct Classical Least Squares (DCLS) component analysis of the 1325 cm^{-1} peak corresponding to DTNB of the antiPDL1-DTNB-MGNs incorporated in the cocktail MGN injection. Spectra recorded at 50 µm steps for the rectangular area in (e).

4.4 Conclusions

Overall in this work, we demonstrate the theranostic capabilities of MGNs conjugated with antibodies and Raman tags *in vitro* and *in vivo* by combining multiplexed diagnosis of biomarkers EGFR and PD-L1 in triple negative breast cancer cells via SERS followed by photothermal therapy in the cellular studies. The strong SERS signal enabled by both electromagnetic and chemical enhancement by MGNs, as well as the narrow vibrational

signatures of Raman allowed us to create cellular "traffic maps" facilitating highly sensitive and specific detection of both biomarkers. In addition, the SERS enhancement allowed for the detection of the MGN probes amidst all of the signal from biological tissue *in vivo*, and the blocking study revealed the active targeting advantage of the antibody coated MGNs. Further, the nanoantenna effect with MGNs gives rise to enhanced light-to-heat conversion when illuminated with a near-infrared light and subsequent photothermal cell death only within the laser spot, avoiding off-target toxicities. We envision this work will not only impact the design of new theranostic nanoprobes capable of imaging multiple biomarkers of cancer and light-controlled therapeutic response but also provide an avenue to diagnose TNBC tumors that typically do not respond to endocrine and targeted treatments. Further, the successful detection of immune checkpoint ligand PD-L1 will ultimately enable theranostic MGNs to provide a quantitative measure of immunomarkers and allow predictive, personalized image-guided immunotherapies with minimal toxicity.[54, 55, 57]

4.5 Methods

A. MGN Synthesis. Reagents purchased from Sigma-Aldrich include both (4-(2-hydroxyethyl)-1-piperazineethanesulfonic acid) (HEPES) and gold(III) chloride trihydrate (HAuCl4) for MGN synthesis. For functionalization, Raman tags 4-mercaptobenzoic acid (pMBA) and 5,5'-Dithiobis(2-nitrobenzoic acid) (DTNB) were purchased from TCI America with methoxy-polyethlyene glycol-thiol (mPEG-SH, M_w 5000 g/mol, Jenkem Technology) obtained for particle surface passivation. Lastly, for sterile aqueous buffers, sodium bicarbonate ($NaHCO_3$, Acros Organics) and sodium phosphate dibasic (Na_2HPO_4, Fisher Scientific) were utilized for linker chemistry and particle resuspension, respectively.

The following chemistry was scaled for 60 mL batches of the three types of particles used in the study: antiEGFR-pMBA-MGNs, antiPDL1-DTNB-MGNs, and pMBA-MGNs. The process could be scaled up or down depending on yield requirements by modifying volumes, but the number of centrifuge spins and centrifuge speeds should be maintained. Also, maintaining a cold temperature for the functionalized MGNs prevents aggregation over the course of the synthesis process and keeps the particles stable. Lastly, mixing by vortexing should be avoided during the chemistry and be replaced by mixing through inversion, pipetting, and stir plate as noted over the course of the procedure.

MGNs were synthesized through the seedless, one-step HEPES growth protocol, as previously described.[15, 59, 72] A scaled up 60 mL batch of MGNs was prepared by synthesizing two 30 mL batches simultaneously and combining after the reaction reached completion. Briefly, 18 mL of Milli-Q water (18 MΩ) was added to 12 ml 200 mM HEPES (pH 7.40 ± 0.1), mixing by gentle inversion. Quickly, 300 µl of 20 mM tetrachloroauric(III) acid ($HAuCl_4$) was added, again mixing my inversion and leaving to react at room temperature for 75 minutes. Plasmon resonance of the MGNs, through the functionalization process, was monitored using UV-vis spectroscopy with optimal initial resonance of the solution phase MGNs at 780 ± 10 nm. This resonance is best because of its spectral overlap with the 785 nm laser utilized for Surface Enhanced Raman Spectroscopy (SERS) and the 808 nm laser used for photothermal therapy (PTT).

B. OPSS-PEG-NHS Ester Chemistry with Antibody.

OPSS-PEG-antiEGFR: Orthopyridyl-disulfide poly(ethylene glycol)-N-hydroxysuccinimide ester (OPSS-PEG-NHS ester, M_w 2000 g/mol, JenKem Technology) and Human EGF R/ErbB1 antibody (antiEGFR, R & D Systems) were purchased in lyophilized forms. Chemistry to form

the amide linkage from the ester group of OPSS-PEG-NHS with amine groups on the antibody structure was modified and troubleshooted from previously reported methods.[71, 73, 74] OPSS-PEG-NHS was resuspended in 100 mM pH 8.6 ± 0.1 Sodium Bicarbonate ($NaHCO_3$) buffer to a concentration of 160 mg/mL, only immediately prior to reaction with antiEGFR as the ester is sensitive to water hydrolysis. Also reconstituted in 100 mM $NaHCO_3$ (pH 8.6 ± 0.1) buffer, the antiEGFR protein was prepared at a concentration of 1 mg/mL. The higher pH bicarbonate buffer is used for the OPSS-antibody reaction as the amide reaction is favored at higher pH.[75-77] Preparing on ice as to prevent protein aggregation, the 160 mg/mL OPSS-PEGS-NHS solution was added at a (1:9) volumetric ratio[74] to the 1 mg/mL antiEGFR. For scaling, specifically the 60 mL antiEGFR-pMBA-MGNs batch required an 80 µL OPSS-PEG-antiEGFR reaction. After ensuring OPSS-PEG-NHS was completely resuspended through pipetting, 8 µL of 160 mg/mL OPSS-PEG-NHS was added to 72 µL of 1 mg/mL antiEGFR, mixed, and left to react for 24 h on an inverter at 4 °C.

OPSS-PEG-antiPDL1: Human CD274 (B7-H1, PD-L1) antibody (antiPDL1, BioLegend) was acquired from BioLegend already resuspended at 1 mg/mL stock in phosphate-buffered solution, pH 7.2. The OPSS-PEG-antiPDL1 reaction was prepared in the same manner as the OPSS-PEG-antiEGFR reaction and then further diluted 5-fold with 100 mM $NaHCO_3$ (pH 8.6 ± 0.1) buffer to ensure that the linker-antibody reaction occurred at the favorable pH 8.6. Thus, the 80 uL reaction, 8 µL of 160 mg/mL OPSS-PEG-NHS to 72 µL of 1 mg/mL antiPDL1, was prepared and then diluted to 400 µL. Reaction was also mixed by pipetting and left to react for 24 h on an inverter at 4 °C.

C. Synthesis of Actively Targeted (Antibody) MGNs (antiEGFR-pMBA-MGNs and antiPDL1- DTNB-MGNs).

Quantification of MGNs and Calculations for Determining Concentration and Scalability: At points during the functionalization process, a known quantity of MGNs was required to allow for proper labelling efficiencies. To determine MGN concentration, an equation was developed from previous Thermogravimetic Analyzer[15, 58] and UV-vis spectroscopy side by side, correlative studies (Equation 4.1). Extinction spectra of MGNs was recorded with a 1 cm pathlength cuvette at 60-fold dilution. A simultaneous thermogravimetric analyzer (TGA) study was performed on the same sample to quantify mass of MGNs per volume. Refer to previously shown Thermogravimetric data in Chapter 2, Figure 2.9. The following equation was utilized for synthesis and scaling:

$$[MGN]\left(\frac{mg}{mL}\right) = \left(\frac{9.38\ mg}{ml}\right) \times \left(\frac{Extinction}{1.64}\right) \times \left(\frac{Dilution\ Factor}{60}\right) \quad (4.1)$$

Equation 4.1 assumes Beers law applies and that the extinction is linearly related to concentration (mg/ml).[78, 79] From a large multitude of synthesis replicates, the tendency of linearity between the concentration of MGNs and extinction has been verified by repeated agreement with mathematical calculations. Equation was utilized in calculations for all functionalized MGN chemistries.

antiEGFR-pMBA-MGNs: Again, functionalization chemistry was monitored for shifts in plasmon resonance due to phase retardation effects from the change in immediate local refractive index due to the layering around the MGNs.[41-43] To begin, 60 mL MGNs at 170 µg/mL (Ext. = 1.79) at max plasmon resonance ~780 nm in the NIR region were synthesized. Ideal for nanomedicine work because of the weak absorption by biological tissue and proteins, MGN resonance in this regime allows for better penetration depth during therapy for future *in vivo*

studies.[80] MGNs were kept on ice through functionalization process. 4-mercaptobenzoic acid (pMBA), dissolved in 100 % ethanol, was added to the MGNs in a small volume with high concentration, adapting from previous methods for SERS-tag labelling to gold nanoparticles.[71, 81-83] With slow stirring, 6 µL of 10 mM pMBA was injected to 60 mL of MGNs, mixing for 10 min at 4 ^{0}C and monitoring the shift in resonance due to the binding event via thiol linkage. Next, the 60 mL was split into 20 mL aliquots (x3), and centrifuged at 6000 rpm for 20 min. Supernatant was completely decanted to remove any unbound pMBA, and pellets were combined in 3 mL total volume with Milli-Q (MQ) water. The resonance and concentration were again recorded, and the functionalized MGNs were further diluted to 1.14 mg/mL (Ext. = 12.0) with Milli-Q water for a total volume of 6.5 mL of particles.

Chemistry ratio for OPSS-PEG-antibody to SERS-tag-MGNs was modified and troubleshooted from other literature methods.[73, 74, 77, 84] Briefly, 80 µL of OPSS-PEG-antiEGFR reaction ($[antiEGFR]_{Final}$ = 0.9 mg/mL) was added to 5.95 mL pMBA-labeled-MGNs at 1.14 mg/mL (Ext. = 12.0), pipetting to mix. Antibody with MGNs reaction was then left to react for 24 h on an inverter at 4 C. Post 24 h incubation, PEGylation chemistry[59, 85, 86] was performed to passivate any free surface area to negate charge effects by the antiEGFR-pMBA-MGNs. To the aqueous MGNs mixture, 700 µL of 5 µM polyethlyene glycol-thiol (mPEG-SH, M_w 5000 g/mol) was added in a cold reaction vessel and slowly stirred for 10 min at room temperature. The ~6.75 mL volume was split into 2.25 mL aliquots (x3) and filled to 4.5 mL volumes with Milli-Q water, mixing by inversion to wash any unbound OPSS-PEG-NHS or mPEG-SH. Particles were then centrifuged at 4000 rpm for 10 min, and supernatant was completely removed under sterile conditions. Pellets were resuspended in 200 µL of sterile 8.6 mM pH 7.40 ± 0.1 (Na_2HPO_4) monophosphate buffer, with resonance and concentration again

measured. If necessary, dilute final [antiEGFR-pMBA-MGNs] with the sterile monophosphate buffer to 5 mg/mL, rechecking concentration. For cellular assays, functionalized MGNs were further diluted to 170 μg/mL with normal media (no FBS) as this concentration was previously shown to have strong SERS and photothermal activity.[15, 59]

antiPDL1-DTNB-MGNs: To synthesize the complementary MGNs particles, the functionalization method was repeated with similar steps but substituting antiPDL1 as the targeting moiety and 5,5'-Dithiobis(2-nitrobenzoic acid) (DTNB) as the SERS tag. Slight modification in method was due to the 5-fold dilution of the OPSS-PEG-antiPDL1 reaction to obtain a higher pH. An initial 60 mL MGNs at 170 μg/mL (Ext. = 1.79), plasmon resonance ~780 nm, was again synthesized. With slow stirring, 6 μL of 10 mM DTNB was added to 60 mL of MGNs reacting for 10 min at 4 °C. After centrifugation and resuspension with MQ water to 1.14 mg/mL (Ext. = 12.0) for a total volume of 6.5 mL of particles, the antiPDL1 targeting moiety was added to the MGN solution. Pipetting to mix, 400 μL of OPSS-PEG-antiPDL1 reaction ($[antiPDL1]_{Final}$ = 0.18 mg/mL) was added to 5.95 mL DTNB-labeled-MGNs at 1.14 mg/mL (Ext. = 12.0). The reaction was again left to react for 24 h at 4 °C on inverter. The final PEGylation, wash, centrifugation, and sterile resuspensions steps were the same for antiPDL1-DTNB-MGNs as for the antiEGFR-pMBA-MGNs. After resuspending in 200 μL of sterile 8.6 mM Na_2HPO_4 pH 7.40 ± 0.1, resonance and concentration were recorded, and dilution to 5 mg/mL was performed if necessary. antiPDL1-DTNB-MGNs were also incorporated in normal media (no FBS) for cellular assays.

(1:1) cocktail prep of antiEGFR-pMBA-MGNs to antiPDL1-DTNB-MGNs: In preparing a (1:1) mixture of the two types of antibody-labeled MGNs, a 60 mL batch of each of the respective particle was prepared. After final resuspension steps in sterile 8.6 mM Na2HPO4 pH 7.40 ± 0.1,

the resonance and concentration of the two antibody-labeled MGNs were determined respectively. Each solution was diluted to 5 mg/mL. Then the antiEGFR-pMBA-MGNs were mixed at an equivalent (1:1) volumetric ratio with the antiPDL1-DTNB-MGNs, assuming there was no change in the overall MGNs concentration. Plasmon resonance and concentration of the (1:1) cocktail were measured, and the particles were diluted in normal media (no FBS) to 170 μg/mL with equal volumetric ratio.

D. Synthesis of MGNs lacking Targeting Moiety (pMBA-MGNs). MGNs without targeting moiety, but SERS tag and PEG bound, pMBA-MGNs, were synthesized via modified version of previous procedures.[59, 85, 86] With slow stirring, 6 μL of 10 mM 4-mercaptobenzoic acid (pMBA) was added to 60 mL of MGNs (170 μg/mL (Ext. = 1.79), resonance ~780 nm) reacting for 10 min at 4 °C. Next, 6 mL of 50 μM polyethlyene glycol-thiol (mPEG-SH, M_w 5000 g/mol) was added on ice, incubating for 5 min, before splitting to 20 mL aliquots (x3), and centrifuging at 6000 rpm for 20 min. Excess pMBA and PEG were removed by full decanting, and pellets were combined in 3 mL total volume with Milli-Q (MQ) water. Plasmon resonance and concentration were again recorded, and the functionalized MGNs were diluted to 1.14 mg/mL (Ext. = 12.0) with MQ water for a total volume of 6.5 mL of particles. To be certain of surface neutrality of the pMBA-MGNs, a second addition of mPEG-SH was performed. To the aqueous 5.95 mL pMBA-labeled-MGNs at 1.14 mg/mL (Ext. = 12.0), 200 μl of 5 μM mPEG-SH was added in a cold vessel for 10 minutes with constant stirring at room temperature. Next, the ~6 mL volume was split into 2 mL aliquots (x3) and filled to 4 mL volumes with Milli-Q water. The particles were mixed by inversion for washing, followed by centrifuging at 4000 rpm for 10 min to remove excess pMBA or PEG. Sterile decanting was again performed with complete removal of the supernatant followed by resuspension in 200 μL of sterile 8.6 mM pH 7.40 ± 0.1

(Na_2HPO_4) monophosphate buffer. Concentration and final resonance of the pMBA-MGNs were quantified, diluting to 5 mg/mL if necessary. pMBA-MGNs were also maintained at 170 μg/mL with normal media (no FBS) for cellular assays.

E. Characterization of Antibody-Labelled MGNs. To monitor the functionalization process of the MGNs and to characterize their optical properties, several spectroscopy techniques were measured both before after functionalization with antibodies, Raman tag, and PEG (denoted antibody-tag-MGNs). Both MGNs and antibody-tag-MGNs were imaged with an Osiris transmission electron microscope (TEM) at 200 keV to ensure the proper morphology and functionalization of the particles. Further, a Varian Cary 5000 UV-vis NIR spectrophotometer (Agilent Technologies) was used to measure the extinction and plasmon resonance of the MGNs using a 1 cm path length cuvette. Lastly, Raman spectroscopy of the particles was recorded to observe relative labeling efficiency of the Raman tag and to ensure that the antibody was bound to the MGNs via the OPSS-PEG-NHS linker chemistry. After the completion of synthesis and functionalization chemistry, 20 μL droplets of 5 mg/mL of the antibody-tag-MGNs (3 different samples) were placed on plain glass slides and dried at room temperature for 1 h in the hood. Raman spectra of the solid state samples of antiEGFR-pMBA-MGNs, antiPDL1-DTNB-MGNs, and (1:1) mixture were recorded using an Invia Raman microscope (Renishaw) with a 785 nm wavelength laser source with 1200 lines/mm grating in high confocal mode. Static spectra (1200 cm^{-1} center) were recorded using a 100x objective with a ~1 μm spot size at a power of 2 mW with a 10 s acquisition time. SERS footprint plotted after fluorescence and background subtraction, normalizing to tallest peak to show peak proximity and location for pMBA, DTNB, and their combination.

F. Fluorescent Secondary Antibody Assay Testing Epidermal Growth Factor Receptor Overexpression in MDA MB 231 cells. MDA-MB-231 cells, purchased from ATCC (HTB-26), were cultured in Dulbecco's Modified Eagle's medium (DMEM, Gibco) supplemented with 10% fetal bovine serum (FBS, ATCC) and 1% penicillin/streptomycin (Gibco) and maintained at 37 ^{0}C and 5% CO_2. For optimal experimental design, cellular assays were performed only after allowing for 14 days of culture to ensure that the cells were in their native state, maintaining media changes every 2 days. MDA MB 231 cells were seeded on a 96-well plate, 12,500 cells per well, and allowed to grow to ~90 % confluency (48 h). Cells were then fixed with cytofix/cytoperm (BD Biosciences), incubating for 20 min at room temperature. Fixative was removed, and the cells were washed with MilliQ (MQ) water (x2). Next, the cells were blocked to prevent any non-specific binding by incubating with 1x animal free blocking solution (Cell Signaling Technology) for one h at 4 °C. Blocking solution was removed, following by washing with MQ water (x2). Cells were next incubated with Human EGF R/ErbB1 antibody (monoclonal mouse antiEGFR, R & D Systems, 100 μg/mL) diluted in 8.6 mM pH 7.40 ± 0.1 (Na_2HPO_4) monophosphate buffer for 24 h at 4 °C. After 24 h, the cells were washed with monophosphate buffer (x2), and next incubated with secondary antibody (Mouse IgG_{2B} PE-conjugated, R & D Systems, 2 μg/mL) diluted in 8.6 mM pH 7.40 ± 0.1 (Na_2HPO_4) monophosphate buffer for 2 h at 4 °C. This secondary antibody is specific for the Fc region of the primary antiEGFR and is complexed with phycoerythrin (PE), a fluorescent protein with excitation at 488 nm and emission 565-605 nm. Again, the cells were washed with monophosphate buffer (x2) and then visualized under fluorescent microscopy using a Zeiss LSM 710 confocal microscope, leaving in monophosphate buffer during imaging and storage at 4 °C.

G. Transmission Electron Microscope Imaging of Surface Binding and Uptake of Antibody-Labeled MGNs for MDA MB 231 Cells. Cells were again cultured for 14 days prior to experiment maintaining media changes every 2 days. While finishing antiEGFR-pMBA-MGN synthesis, 350,000 cells were seeded on 35 mm cell culture dishes, 48 h prior to day of experiment. After 48 h of growth, checking that the cells had a ~90 % confluent layer, new media (no FBS) supplemented with 170 μg/mL antiEGFR-pMBA-MGNs was added, and the cells were further incubated for another 16 h at 37 ^{0}C. Next, the cells were washed with cacodylate buffer before fixing in 2.5% gluteraldehyde in 0.1M cacodylate buffer at room temperature for 1 hour, followed by 4°C overnight. Sample processing and imaging was handled by the Vanderbilt Cell Imaging Shared Resource-Research Electron Microscope facility.

Additional processing was performed to maintain cellular organelle structure. The samples were post-fixed in 1% osmium tetraoxide at room temperature then washed with 0.1M cacodylate buffer (x3). Post fixation, the samples were dehydrated through a graded ethanol series followed by incubation in 100% ethanol and propylene oxide (PO) with two exchanges of pure PO. Finally, cell samples were embedded in epoxy resin and polymerized at 60°C for 48 hours. For thin section preparation, ultra-thin slices (70-80 nm) were cut from block and added to copper grids for imaging. The grids were further stained with 2% uranyl acetate and lead citrate. Imaging was performed using a Philips/FEI Tecnai T12 electron microscope operating at 200 keV.

H. SERS Singleplex Mapping of MDA MB 231 cells (Active vs. Passive): For SERS mapping experiments, 231 cells were seeded on Calcium Fluoride disks (CaF_2, 20 x 2 mm Raman grade, Crystran Ltd.) after cells had been in culture for 14 days. CaF_2 disks were placed inside 35 mM cell culture dishes, and 350,000 cells were seeded in the dishes. After 48 h of growth, checking

that the cells had a ~90 % confluent layer, the disks were removed from the culture dishes and placed in a secondary container for the MGN incubation step. Now incubating only on the disks, the cells were incubated with new media (no FBS, nDMEM) supplemented with either 170 μg/mL antiEGFR-pMBA-MGNs or 170 μg/mL pMBA-MGNs for 16 h at 37 ^{0}C. Next, the cells were washed with nDMEM (x2) and then placed back in complete media (with FBS, cDMEM) to equilibrate for 2 h at 37 ^{0}C. Cells were then fixed with cytofix/cytoperm (BD Biosciences), incubating for 20 min at room temperature. Fixative was removed, and the cells were washed with MilliQ (MQ) water (x2). All volume was removed, and the cells were dried at 4 ^{0}C overnight.[69]

Both the MGNs coated with antibody (antiEGFR-pMBA-MGNs, 170 μg/mL) case and the non-targeted MGNs (pMBA-MGNs, 170 μg/mL) assay were treated the same for SERS mapping and data collection, as well as processing. After allowing the samples to dry overnight at 4 °C, the cells on the CaF_2 disks were visualized using an inVia Raman (Renishaw) brightfield microscope. Using an 100x objective, a video montage of the cells was captured, and the resulting brightfield image provided x,y coordinates for the Raman instrument to record SERS chemical footprints of a rectangular area of ~100 μm by 100 μm. Recording spectra with 0.75 μm steps, the invia Raman microscope took measurements of the cells with a 785 nm wavelength laser source with 1200 lines/mm grating in high confocal mode. Static spectra (1200 cm^{-1} center) were recorded using a 100x objective with a ~1 μm spot size at a power of 2 mW with a 10 s acquisition time. SERS intensity map analysis of the 1580 cm^{-1} peak corresponding to the functionalized MGN localization was performed using Wire 3.4 for cosmic ray removal, MATLAB for smoothing, background subtraction, and intensity plotting, and, lastly, Adobe

Photoshop graphic software for overlap with brightfield image. Refer to Analysis of SERS maps section for complete data processing procedure.

I. SERS Multiplex Imaging of MDA MB 231 cells (No Block and Blocking PD-L1 Receptor).

Multiplex with (1:1) Cocktail with 231 cells: Again, CaF_2 disks were seeded with 231s inside 35 mm culture dishes with 350,000 cells as previously stated. Checking for ~90 % confluent layer after 48 h growth, the disks were removed and placed into a new container. Cells were incubated with new media (no FBS, nDMEM) supplemented with 170 μg/mL (1:1) cocktail antiEGFR-pMBA-MGNs to antiPDL1-DTNB-MGNs for 16 h at 37 ^{0}C. Next, cells were washed with nDMEM (x2) followed by placement back in complete media (with FBS, cDMEM) to equilibrate for 2 h at 37 ^{0}C. After 2 h, fixing with cytofix/cytoperm (BD Biosciences), incubating for 20 min at room temperature, removing fixative, and washing with MilliQ (MQ) water (x2). Volume was completely removed, followed by drying overnight at 4 ^{0}C.

After drying overnight, the cells on the disk were visualized using an inVia Raman (Renishaw) brightfield microscope, collecting a video montage of the cells using an 100x objective. Brightfield image corresponded to x,y coordinates for rectangular area of ~100 μm by 100 μm. Spectra were recorded with 0.75 μm steps again with the invia Raman microscope. Measurement conditions for the multiplex cell studies were the same as for singleplex: 785 nm wavelength laser source, 1200 lines/mm grating in high confocal mode, static spectra (1200 cm^{-1} center), 100x objective with a ~1 μm spot size, power of 2 mW, and 10 s acquisition time. SERS intensity multiplex map analysis of the 1580 cm^{-1} peak for the antiEGFR-pMBA-MGNs and the 1325 cm^{-1} peak corresponding to the antiPDL1-DTNB-MGNs were performed using the same software and method as singleplex: Wire 3.4 for cosmic ray removal; MATLAB for smoothing,

background subtraction, and intensity plotting; and Adobe Photoshop graphic software for overlap with brightfield image. Analysis of SERS maps section has full data processing procedure included.

Multiplex with (1:1) Cocktail with 231 cells after Blocking PD-L1 Receptor: To test the fidelity of the multiplex technology, a blocking PD-L1 receptor control experiment was performed to determine the specificity and mapping capability of this (1:1) cocktail of functionalized antibody-specific MGNs. 231s were seeded on CaF_2 disks with the same method as with the multiplex study: 350,000 cells added to 35 mm culture dish with disk inside dish, allowing 48 h for cells to grow to ~90 % confluency. After removing to new container, the cells were pre-blocked by incubating with nDMEM supplemented with 4 μg/mL Human CD274 (B7-H1, PD-L1) antibody (monoclonal antiPDL1) for 1 h at 37 ^{0}C.[48, 87, 88] Cells were washed with nDMEM (x2), followed by placement in nDMEM supplemented with 170 μg/mL (1:1) cocktail antiEGFR-pMBA-MGNs to antiPDL1-DTNB-MGNs for 16 h at 37 ^{0}C. After washing again with nDMEM (x2), cells were placed back in cDMEM to equilibrate for 2 h at 37 ^{0}C. Fixation process followed same protocol as for (1:1) cocktail multiplex case, using fixative from BD Biosciences and drying at 4 °C overnight.

Brightfield video montage of 231 cells was collected with 100x objective of inVia Raman (Renishaw) microscope, corresponding to x,y coordinates for rectangular area of ~100 μm by 100 μm. Spectra were recorded with 0.75 μm steps with same measurement conditions for block studies as for the non-block multiplex assay. SERS intensity multiplex map analysis of $I_{SERS1580}$ and $I_{SERS1325}$ to determine the effect of blocking PD-L1 receptor on distribution of antiEGFR-pMBA-MGNs and antiPDL1-DTNB-MGNs for the 231 cells was also performed using same software and method as non-block multiplex, refer to Analysis of SERS maps section.

J. Analysis of SERS Imaging Maps (Singleplex, Multiplex, PD-L1 Block). Running Wire 3.4 software with an Invia (Renishaw) Raman microscope, all SERS maps were a collection of ~100 μm x 100 μm cellular areas with 0.75 um steps. Snake path acquisition was utilized, creating a dataset of ~15,000 spectra. The dataset was a matrix with (x,y) coordinates, wavenumber cm^{-1}, and Raman intensity. Using the wire 3.4 software, cosmic ray removal was performed with nearest neighbor method implemented to ensure the scaling of the spectra was not jeopardized. To make the handling of the dataset easier following cosmic ray removal, the wire 3.4 wxd file was converted into a text file and imported into MATLAB R2016a software. A custom code was built using MATLAB software to perform smoothing and background fluorescent subtraction. Following the modified polyfit method[89], an automated approach was applied to perform background subtraction of fluorescence using polynomial fitting to uncover SERS peaks even at low intensity regimes.[89] The software runs an iterative process fitting the selected polynomial to the data to remove background, coming as close to baseline to subtract out all fluorescence without losing any Raman peaks or jeopardizing data fidelity. Prior to implementing the modified polyfit method on the data set, truncation was performed, and the data underwent smoothing and data differentiation using the Savitzsky and Golay method.[90-92] The S and G filter used order of 5 and coefficient value of 61. After smoothing, a 7^{th} order polynomial was utilized for fluorescent background subtraction through an iterative process with a threshold of 0.0001. The threshold of the fit could be modified to lengthen or shorten processing time.

There are multiple methods for multivariate analysis that were beyond the scope of this study.[93, 94] Specific analysis depends on the phase/state of the sample and whether calibration curves with known concentrations of analytes corresponding to signal can be obtained. Analysis should be selected based on the parameters of the study and what data is required. For future

studies, component mapping methods such as direct classical least squares (DCLS), principal component analysis (PCA), or k-means clustering could be incorporated while having another strong identifier spectra to normalize or quantify against.[23, 93, 94] However, due to the SERS effect, the Raman tags were very distinguishable and allowed for simple intensity analysis of the various peaks in accordance to what has been done in the literature previously.[21, 95-98] Thus, after the dataset was smoothed and subtracted for fluorescence, the intensity as a function of position for either the 1580 cm^{-1} peak of pMBA ($I_{SERS1580}$) or the 1325 cm^{-1} peak of DTNB ($I_{SERS1325}$) was plotted using MATLAB, with (x,y) coordinates corresponding to the brightfield image. Next, using Adobe Photoshop graphic software, overlaps of $I_{SERS1580}$ and brightfield were performed for the singleplex case for both plus and minus antibody MGNs. For the multiplex and blocking studies, a spatial map overlap of $I_{SERS1580}$ and $I_{SERS1325}$ was completed (in MATLAB) as well as layering all 3 components ($I_{SERS1580}$, $I_{SERS1325}$, and brightfield, in Photoshop). Lastly, the MATLAB code also had a built-in spectral plotter and exporter that allowed for the visualization of the SERS footprint at any respective spatial location. Raman footprints representing $I_{SERS1580}$ and $I_{SERS1325}$ data were obtained using this built-in plotter and data exporter.

K. Spatially Controlled Photothermal Ablation of Breast Cancer Cells Utilizing Actively-Targeted MGNs. Both MDA-MB-231 (HTB-26) and MCF7 (HTB-22) breast cancer cell lines were purchased from ATCC. The 231s were cultured in Dulbecco's Modified Eagle's medium (DMEM, Gibco) supplemented with 10% fetal bovine serum (FBS, ATCC) and 1% penicillin/streptomycin (Gibco). MCF7s were cultured in Eagles's Minimum Essential medium (EMEM, ATCC) supplemented with 10% fetal bovine serum (FBS, ATCC), 1% penicillin/streptomycin (Gibco), and 0.01 mg/mL human recombinant insulin (Invitrogen). Both

cell lines were maintained at 37 ^{0}C and 5% CO_2 and were cultured for 14 days prior to seeding for photothermal therapy (PTT) experiments with media changes every 2 days. Culturing on 35 mm culture dishes for PTT experiment, 231s were seeded at 350,000 cells 48 h prior to MGN incubation step, while MCF7s were seeded at 700,000 cells 144 hr prior to MGN addition. Both cells lines were cultured to ~90 % confluent layers on day of MGN addition, and their growths and morphologies were confirmed through phase contrast imaging performed with a Zeiss Observer Z1 microscope.

The two cell lines were incubated with new media (no FBS, nDMEM or nEMEM) supplemented with either 170 μg/mL antiEGFR-pMBA-MGNs or 170 μg/mL pMBA-MGNs for 16 h at 37 ^{0}C. Next, the cells (231s and MCF7s) were washed with nDMEM or nEMEM (x2), and then place back in complete media (with FBS, cDMEM or cEMEM) prior to irradiation with laser. The localization of antiEGFR-pMBA-MGNs and pMBA-MGNs was compared for the two cell types through visualization with a Zeiss Observer Z1 microscope.

Custom photothermal therapy laser optics were purchased from Thorlabs and built to provide controlled light to heat conversion. The optics included an 808 nm laser diode (L808P1WJ), a current controller (LDC240C), a thermoelectric controller (TEDC200C), a collimating lens (C230TME-B), and a silver polished mirror (PF-10-03-P01). The photothermal set up was also completed with an aluminum block wrapped with anti-reflecting black films and a 37 ^{0}C heating mantle to simulate biological conditions. Calipers and a power meter (Thorlabs, PM130D) were used to measure the laser spot size (2 x 2 mm) and power density (4.7 W/cm^2) used in the study.

After allowing to equilibrate at 37 ^{0}C for 2 h, the cells were illuminated for 15 min at 4.7 W/cm^2 pump fluence with an 808 nm laser, spot size of 2 x 2 mm. The cells were then place

back in the 37 ^{0}C incubator. After 4 h, fresh complete media was added with Calcein AM (5 μM) and Propidium Iodide (PI, 1 μM) (Live/Dead stain) and incubated for 20 min at 37 ^{0}C. After 20 min, media was changed again, and the cells were left at 37 ^{0}C until imaging. A Zeiss LSM 710 confocal microscope was utilized for fluorescent imaging of the cells to view the stain (Live/Dead) and visualize any cell death via necrosis.

Additional controls were performed on the MDA MB 231 cells to show that the 808 nm laser alone did not induce any cell death and that the antiEGFR-pMBA-MGNs were not cytotoxic to the cells. For laser alone control, 231s were cultured to ~90 % confluency in the 35 mm culture dish and put through the whole PTT procedure but without particles present, steps include: incubating with nDMEM for 16 h at 37 ^{0}C, washing with nDMEM (x2), incubating with cDMEM through illumination, 15 min at 4.7 W/cm^2 pump fluence, and staining with calcein/PI after 4 h at 37 ^{0}C. Lastly, 231 cells at 90 % confluency were incubated with nDMEM supplemented with 170 μg/mL antiEGFR-pMBA-MGNs for 16 h at 37 ^{0}C, washing with nDMEM (x2), incubating with cDMEM but without illumination, and then staining with calcein/PI after 4 h at 37 ^{0}C. These controls were verified through fluorescent imaging with a Zeiss LSM 710 confocal microscope.

L. *In vivo* and *ex vivo* Protocols. All methods for *in vivo* and *ex vivo* experiments with human breast (MDA MB 231) tumor xenografts in athymic mice are provided in Appendix B. Procedures include: mammary fat pad tumor growth (B.1), synthesis of actively targeted MGNs (B.2), SERS longitudinal assays with portable Raman (B.3), histology and silver staining (B.4) and SERS mapping (B.5) of ex vivo tumor sections.

4.6 Bibliography

1. Chen, W., et al., *Structural-Engineering Rationales of Gold Nanoparticles for Cancer Theranostics.* Adv. Mater., 2016. **Epub**.
2. Tian, L., et al., *Stimuli-Responsive Gold Nanoparticles for Cancer Diagnosis and Therapy.* J. Funct. Biomater., 2016. **7**(19): p. 1-31.
3. Webb, J.A. and R. Bardhan, *Emerging Advances in Nanomedicine with Engineered Gold Nanostructures.* Nanoscale, 2014. **6**: p. 2502-2530.
4. Zhao, N., et al., *Gold Nanoparticles for Cancer Theranostics: A Brief Update.* J. Innov. Opt. Health Sci., 2016. **9**(4): p. 1-10.
5. Chen, W., et al., *Targeting of Pancreatic Cancer with Magneto-Fluorescent Theranostic Gold Nanoshells.* Nanomedicine, 2014. **9**: p. 1209-1222.
6. Bardhan, R., et al., *Nanoshells with Targeted Simultaneous Enhancement of Magnetic and Optical Imaging and Photothermal Therapeutic Response.* Adv. Func. Mater., 2009. **19**: p. 3901-3909.
7. Liu, Y., et al., *Human Induced Pluripotent Stem Cells for Tumor Targeted Delivery of Gold Nanorods and Enhanced Photothermal Therapy.* ACS Nano, 2016. **10**: p. 2375-2385.
8. Maltzahn, G.v., et al., *SERS-Coded Gold Nanorods as a Multifunctional Platform for Densely Multiplexed Near-Infrared Imaging and Photothermal Heating.* Adv. Mater., 2009. **21**(31): p. 3175-3180.
9. Zhang, Z., et al., *Silver Nanoparticle Gated, Mesoporous Silica Coated Gold Nanorods (AuNR@MS@AgNPs): Low Premature Release and Multifunctional Cancer Theranostic Platform.* ACS Appli. Mater. Interfaces, 2015. **7**(11): p. 6211-6219.
10. Barbosa, S., et al., *Targeted Combinatorial Therpay Using Gold Nanostars as Theranostic Platforms.* J. Phys. Chem. C, 2014. **118**: p. 26313-26323.
11. Gao, Y., et al., *Multifunctional Gold Nanostar-Based Nanocomposite: Synthesis and Application for Noninvasive MR-SERS Imaging-Guided Photothermal Ablation.* Biomaterials, 2015. **60**: p. 31-41.
12. Liu, Y., et al., *A Plasmonic Gold Nanostar Theranostic Probe for In Vivo Tumor Imaging and Photothermal Therapy.* Theranostics, 2015. **5**(9): p. 946-960.
13. Liu, Y., et al., *Quintuple-Modality (SERS-MRI-CT-TPL-PTT) Plasmonic Nanoprobe for Theranostics.* Nanoscale, 2013. **5**: p. 12126-12131.
14. Shao, J., et al., *Photothermal Nanodrugs: Potential of TNF-Gold Nanospheres for Cancer Theranostics.* Sci. Rep., 2013. **3**: p. 1-9.
15. Webb, J.A., et al., *Geometry-Dependent Plasmonic Tunability and Photothermal Characteristics of Multibranched Gold Nanoantennas.* J. Phys. Chem. C, 2014. **118**(3696-3707).
16. Webb, J.A., et al., *Ultrasensitive Analyte Detection with Plasmonic Paper Dipsticks and Swabs Integrated with Branched Nanoantennas.* J. Mater. Chem. C, 2014. **2**: p. 10446-10454.
17. Andreou, C., S.A. Kishore, and M.F. Kircher, *Surface-Enhanced Raman Spectoscopy: A New Modality for Cancer Imaging.* J. Nucl. Med., 2015. **56**: p. 1295-1299.
18. Jermyn, M., et al., *Intraoperative Brain Cancer Detection with Raman Spectroscopy in Humans.* Science Trans. Med., 2015. **7**(274): p. 1-9.

19. Karabeber, H., et al., *Guiding Brain Tumor Resection Using Surface-Enhanced Raman Scattering Nanoparticles and a Hand-Held Scanner.* ACS Nano, 2014. **8**(10): p. 9755-9766.
20. Kircher, M.F., et al., *A Brain Tumor Molecular Imaging Strategy Using a New Triple-Modality MRI-Photoacoustic-Raman Nanoparticle* Nat. Med., 2012. **18**: p. 829-835.
21. Maiti, K.K., et al., *Multiplex Targeted In Vivo Cancer Detection Using Sensitive Near-Infrared SERS Nanotags.* Nano Today, 2012. **7**: p. 85-93.
22. Kang, J.W., et al., *High Resolution Live Cell Raman Imaging Using Subcellular Organelle-Targeting SERS-Sensitive Gold Nanoparticles with Highly Narrow Intra-Nanogap.* Nano Lett., 2015. **15**: p. 1766-1772.
23. Matschulat, A., D. Drescher, and J. Kneipp, *Surface-Enhanced Raman Scattering Hybrid Nanoprobe Multiplexing and Imaging in Biological Systems.* ACS Nano, 2010. **4**: p. 3259-3269.
24. Zavaleta, C.L., et al., *Multiplexed Imaging of Surface Enhanced Raman Scattering Nanotags in Living Mice Using Noninvasive Raman Spectroscopy.* Proc. Natl. Acad. Sci. USA, 2009. **106**: p. 13511-13516.
25. Ando, J., et al., *Dynamic SERS Imaging of Cellular Transport Pathways with Endocytosed Gold Nanoparticles.* Nano Lett., 2011. **11**: p. 5344-5348.
26. Kennedy, D.C., et al., *Development of Nanoparticle Probes for Multiplex SERS Imaging of Cell Surface Proteins.* Nanoscale, 2010. **2**: p. 1413-1416.
27. Zhang, Y., et al., *Molecular Imaging with SERS-Active Nanoparticles.* Small, 2011. **7**(23): p. 3261-3269.
28. Abramson, V.G., et al., *Subtyping of Triple-Negative Breast Cancer: Implications for Therapy.* Cancer, 2015. **121**: p. 8-16.
29. Peddi, P.F., M.J. Ellis, and C. Ma, *Molecular Basis of Triple Negative Breast Cancer and Implications for Therapy.* Int. J. Breast Cancer, 2011. **2012**: p. 1-7.
30. Balko, J.M., et al., *Molecular Profiling of the Residual Disease of Triple-Negative Breast Cancers after Neoadjuvant Chemotherapy Identifies Actionable Therapeutic Targets.* Cancer Discov., 2014. **4**(2): p. 232-245.
31. Balko, J.M., T.P. Stricker, and C.L. Arteaga, *The Genomic Map of Breast Cancer: Which Roads Lead to Better Targeted Therapies?* Breast Cancer Res., 2013. **15**: p. 1-9.
32. Ferraro, D.A., et al., *Inhibition of Triple-Negative Breast Cancer Models by Combinations of Antibodies to EGFR.* PNAS, 2013. **110**(5): p. 1815-1820.
33. Park, H.S., et al., *High EGFR Gene Copy Number Predicts Poor Outcome in Triple-Negative Breast Cancer.* Modern Pathol., 2014. **27**: p. 1212-1222.
34. Baptista, M.Z., et al., *Prognostic Significance of PD-L1 and PD-L2 in Breast Cancer.* Hum. Pathol., 2016. **47**: p. 78-84.
35. Cimino-Mathews, A., et al., *PD-L1 (B7-H1) Expression and the Immune Tumor Microenvironment in Primary and Metastatic Breast Carcinomas.* Hum. Pathol., 2016. **47**: p. 52-63.
36. Moreno, B.H. and A. Ribas, *Anti-Programmed Cell Death Protein-1/Ligand-1 Therapy in Different Cancers.* Brit. J. Cancer, 2015. **112**: p. 1421-1427.
37. Pardoll, D.M., *The Blockade of Immune Checkpoints in Cancer Immunotherapy.* Nat. Rev. Cancer, 2012. **12**: p. 252-264.
38. Philips, G.K. and M. Atkins, *Therapeutic Uses of anti-PD-1 and anti-PD-L1 Antibodies.* Int. Immunol., 2014. **27**: p. 39-46.

39. Tumeh, P.C., et al., *PD-1 Blockade Induces Responses by Inhibiting Adaptive Immune Resistance.* Science, 2014. **515**: p. 568-571.
40. Callea, M., et al., *Differential Expression of PD-L1 between Primary and Metastatic Sites in Clear Cell Renal Cell Carcinoma.* Cancer Immunol. Res., 2015. **3**: p. 1158-1164.
41. Myroshnychenko, V., et al., *Modelling the Optical Response of Gold Nanoparticles.* CHem. Soc. Rev., 2008. **37**: p. 1792–1805.
42. Chen, H., et al., *Shape- and Size-Dependent Refractive Index Sensitivity of Gold Nanoparticles.* Langmuir, 2008. **24**: p. 5233−5237.
43. Hao, F., et al., *Plasmon Resonances of a Gold Nanostar.* Nano Lett., 2007. **7**: p. 729−732.
44. Xu, P., et al., *Field-assisted synthesis of SERS-active silver nanoparticles using conducting polymers.* 2010. **2**: p. 1436-1440.
45. Mittendorf, E.A., et al., *PD-L1 Expression in Triple Negative Breast Cancer.* Cancer Immunol. Res., 2014. **2**(4): p. 361-370.
46. Soliman, H., F. Khalil, and S. Antonia, *PD-L1 Expression is Increased in a Subset of Basal Type Breast Cancer Cells.* PloS One, 2014. **9**(2): p. 1-10.
47. Wang, C., et al., *Polyethylenimine-Interlayered Silver-Shell Magnetic-Core Microspheres as Multifunctional SERS Substrates.* J. Mater. Chem. C, 2015. **3**: p. 8684-8693.
48. Melancon, M.P., et al., *In Vitro and In Vivo Targeting of Hollow Gold Nanoshells Directed at Epidermal Growth Factor Receptor for Photothermal Ablation Therapy.* Mol. Cancer Ther., 2008. **7**: p. 1730-1739.
49. Chithrani, B.D., A.A. Ghazani, and W.C.W. Chan, *Determining the Size and Shape Dependence of Gold Nanopartilce Uptake into Mammalian Cells.* Nano Lett., 2006. **6**(2006): p. 662-668.
50. Levy, R., et al., *Gold Nanoparticles Delivery in Mammalian Live Cells: A Critical Review.* Nano Rev., 2010. **1**.
51. Kneipp, K., et al., *Single Molecule Detection Using Surface-Enhanced Raman Scattering (SERS).* Phys. Rev. Lett., 1997. **78**: p. 1667-1670.
52. Maier, S.A., *Plasmonics: Fundamentals and Applications*. 2007, New York, NY: Springer Science + Business Media LLC.
53. Nie, S.M. and S.R. Emery, *Probing Single Molecules and Single Nanoparticles by Surface-Enhanced Raman Scattering.* Science, 1997. **275(5303)**: p. 1102-1106.
54. Nguyen, L.T. and P.S. Ohashi, *Clinical Blockade of PD1 and LAG3 - Potential Mechanisms of Action.* Nat. Rev. Immunology, 2015. **15**: p. 45-56.
55. Taube, J.M., et al., *Association of PD-1, PD-1 Ligands, and Other Features of the Tumor Immune Microenvironment with Response to Anti-PD-1 Therapy.* Clin. Cancer Res., 2014. **20**: p. 5064-5074.
56. Movasaghi, Z., S. Rehman, and I.U. Rehman, *Raman Spectroscopy of Biological Tissues.* Appl. Spectrosc. Rev. **42**: p. 493-541.
57. Blau, R., et al., *Are Nanotheranostics and Nanodiagnostics-Guided Drug Delivery Stepping Stones Towards Precision Medicine?* Drug Resist. Update., 2016. **27**: p. 39-58.
58. Soetan, N., et al., *Morphology-Directed Catalysis with Branched Gold Nanoantennas.* J. Phys. Chem. C, 2016. **120**: p. 10320-10327.
59. Ou, Y.-C., et al., *Gold Nanoantenna-Mediated Photothermal Drug Delivery from Thermosensitive Liposomes in Breast Cancer.* ACS Omega, 2016. **1**: p. 234-243.

60. Petros, R.A. and J.M. DeSimone, *Strategies in the Design of Nanoparticles for Therapeutic Applications.* Nat. Rev. Drug Discovery, 2010. **9**(8): p. 615-627.
61. Wang, A.Z., R. Langer, and O.C. Farokhzad, *Nanoparticle Delivery of Cancer Drugs.* Annu. Rev. Med., 2012. **63**: p. 185-198.
62. Kang, B., et al., *Strategies for Using Nanoprobes to Perceive and Treat Cancer Activity: A Review.* J. Bio. Eng., 2017. **11(13)**: p. 1-12.
63. Rejman, J., et al., *Size-Dependent Internalization of Particles via the Pathways of Clathrin-and Caveolae-Mediated Endocytosis.* Biochem. J., 2004. **377**: p. 159-169.
64. Mitra, S., et al., *Tumour Targeted Delivery of Encapsulated Dextran–Doxorubicin Conjugate Using Chitosan Nanoparticles as Carrier.* J. Controlled Release, 2001. **74**(1–3): p. 317-323.
65. Kirk, J., et al., *Selective Toxicity of TGF-α-PE40 to EGFR-positive Cell Lines: Seletive Protection of Low EGFR-expressing Cell Lines by EGF.* Brit. J. Cancer, 1994. **69**: p. 988-994.
66. Xu, Y.-H., et al., *Characterization of Epidermal Growth Factor Receptor Gene Expression in Malignant and Normal Human Cell Lines.* Proc. Natl. Acad. Sci. USA, 1984. **81**: p. 7308-7312.
67. Qian, X., et al., *In Vivo Tumor Targeting and Spectroscopic Detection with Surface-Enhanced Raman Nanoparticle Tags.* Nat. Biotechnol., 2008. **26**: p. 83-90.
68. Yigit, M.V. and Z. Medarova, *In Vivo and Ex Vivo Applications of Gold Nanoparticles for Biomedical SERS Imaging.* Am. J. Nucl. Med. Imaging, 2012. **2**(2): p. 232-241.
69. Nima, Z.A., et al., *Circulating Tumor Cell Identification by Functionalized Silver-Gold Nanorods with Multicolor, Super-Enhanced SERS and Photothermal Resonances.* Sci. Rep., 2014. **4**: p. 4752-4759.
70. Zhang, Y., et al., *Multifunctional Gold Nanorods with Ultrahigh Stability and Tunability for In Vivo Fluorescence Imaging, SERS Detection, and Photodynamic Therapy.* Angew. Chem. Int. Edit, 2012. **51**: p. 1-5.
71. Wu, L., et al., *Simultaneous Evaluation of p53 and p21 Expression Level for Early Cancer Diagnosis Using SERS Technique.* Analyst, 2013. **138**(3450-3456).
72. Xie, J., J.Y. Lee, and D.I.C. Wang, *Seedless, Surfactantless, High-Yield Synthesis of Branched Gold Nanocrystals in HEPES Buffer Solution.* Chem. Mater., 2007. **19**: p. 2823 − 2830.
73. Bishnoi, S.W., et al., *SERS Biodetection Using Gold-Silica Nanoshells and Nitrocellulose Membranes.* Anal. Chem., 2011. **83**: p. 4053-4060.
74. Lowery, A.R., et al., *Immunonanoshells for Targeted Photothermal Ablation of Tumor Cells.* Int. J. Nanomed., 2006. **1**: p. 149-154.
75. Gobin, A.M., J.J. Moon, and J.L. West, *EphrinA1-Targeted Nanoshells for Photothermal Ablation of Prostate Cancer Cells.* Int. J. Nanomed., 2008. **3**: p. 351-358.
76. Hermanson, G.T., *Bioconjugate Techniques*. Second ed. 2008, Cambridge, Massachusetts: Academic Press.
77. Hirsch, L.R., et al., *A Whole Blood Immunoassay Using Gold Nanoshells.* Anal. Chem., 2003. **75**: p. 2377-2381.
78. Villringer, A. and B. Chance, *Non-Invasive Optical Spectroscopy and Imaging of Human Brain Function.* TINS, 1997. **20**: p. 435-442.
79. Gill, S.C. and P.H.v. Hippel, *Calculation of Protein Extinction Coefficients from Amino Acid Sequence Data.* Anal. Biochem., 1989. **182**: p. 319-326.

80. Weissleder, R., *A Clearer Vision for In Vivo Imaging.* Nat. Biotechnol., 2001. **19**: p. 316-317.
81. Chen, K., H. Han, and Z. Luo, *Streptococcus Suis II Immunoassay Based on Thorny Gold Nanoparticles and Surface Enhanced Raman Scattering.* Analyst, 2012. **137**: p. 1259-1264.
82. Kang, H., et al., *Near-Infrared SERS Nanoprobes with Plasmonic Au/Ag Hollow-Shell Assemblies for In Vivo Multiplex Detection.* Adv. Func. Mater., 2013. **23**: p. 3719-3727.
83. Zou, X., E. Ying, and S. Dong, *Seed-Mediated Synthesis of Branched Gold Nanoparticles with the Assistance of Citrate and Their Surface-Enhanced Raman Scattering Properties.* Nanotechnology, 2006. **17**: p. 4758-4764.
84. Singh, A.K., et al., *Gold Nanorod Based Selective Identification of Escherichia Coli Bacteria using Two-Photon Rayleigh Scattering Spectroscopy.* ACS Nano, 2009. **3**: p. 1906-1912.
85. Manson, J., et al., *Polyethylene Glycol Functionalized Gold Nanoparticles: The Influence of Capping Density on Stability in Various Media.* Gold. Bull., 2011. **44**: p. 99-105.
86. Rahme, K., et al., *PEGylated Gold Nanoparticles: Polymer Quantification as a Function of PEG Lengths and Nanoparticle Dimensions.* RSC Adv., 2013. **3**: p. 6085-6094.
87. Li, J.-L., et al., *In Vitro Cancer Cell Imaging and Therapy Using Transferrin-Conjugated Gold Nanoparticles.* Cancer Lett., 2009. **274**: p. 319-326.
88. Shukla, R., et al., *Laminin Receptor Specific Therapeutic Gold Nanoparticles (198AuNP-EGCg) Show Efficacy in Treating Prostate Cancer.* Proc. Natl. Acad. Sci. USA, 2012. **109**: p. 12426-12431.
89. Lieber, C.A. and A. Mahadevan-Jansen, *Automated Method for Subtraction of Fluorescence from Biological Raman Spectra.* Appl. Spectrosc., 2003. **57**: p. 1363-1367.
90. Gorry, P.A., *General Least-Squares Smoothing and Differentiation by the Convolution (Savitzky-Golay) Method.* Anal. Chem., 1990. **62**: p. 570-573.
91. Luo, J., K. Ying, and J. Bai, *Savitzky–Golay Smoothing and Differentiation Filter for Even Number Data.* Signal Process., 2005. **85**: p. 1429-1434.
92. Savitzky, A. and M.J.E. Golay, *Smoothing and Differentiation of Data by Simplified Least Squares Procedures.* Anal. Chem., 1964. **36**: p. 1627-1639.
93. Shinzawa, H., et al., *Multivariate Data Analysis for Raman Spectroscopic Imaging.* J. Raman. Spectrosc., 2009. **40**: p. 1720-1725.
94. Zhang, L., M.J. Henson, and S.S. Sekulic, *Multivariate Data Analysis for Raman Imaging of a Model Pharmaceutical Tablet.* Analytica Chimica Acta, 2005. **545**: p. 262-278.
95. Gregas, M.K., et al., *Tracking SERS-Active Nanoprobe Intracellular Uptake for Chemical and Biological Sensing.* Proc. of SPIE, 2007. **6755**: p. 67550H1-67550H11.
96. Kim, H.-M., et al., *Large Scale Synthesis of Surface-Enhanced Raman Scattering Nanoprobes with High Reproducibility and Long-Term Stability.* J. Ind. Eng. Chem., 2016. **33**: p. 22-27.
97. Lee, S., et al., *Surface-Enhanced Raman Scattering Imaging of HER2 Cancer Markers Overexpressed in Single MCF7 Cells Using Antibody Conjugated Hollow Gold Nanospheres.* Biosens. Bioelectron., 2009. **24**: p. 2260-2263.
98. Xia, X., et al., *Silica-Coated Dimers of Silver Nanospheres as Surface-Enhanced Raman Scattering Tags for Imaging Cancer Cells.* Interface Focus, 2013. **3**: p. 20120092.

CHAPTER 5

SUMMARY AND OUTLOOK

Overall in this work, tunable multibranched gold nanoantennas (MGNs) were synthesized with plasmon resonance in the first NIR window to allow for better tissue penetration during *in vivo* studies. We were able to modulate the MGNs geometry, which allowed for great maneuverability in the resulting resonance range. Further, due to the presence of multiple sharp protrusions, the MGNs demonstrated a refractive index sensitivity of 373 nm/RIU, as well as, intense photothermal efficiencies, rising the temperature of surrounding medium to ~54 °C within 5 minutes of laser illumination. These light to heat conversion capacities of the MGNs were also shown to deliver actively targeted photothermal therapy to EGFR overexpressing MDA MB 231 cells *in vitro*. Having both imaging and therapeutic components in one platform is beneficial for future *in vivo* theranostic studies with a single systemic injection.

Beyond liquid phase MGNs, we moved into solid MGN-substrates for ultrasensitive, flexible, and versatile detection. We incorporated MGNs on inexpensive filter paper to design MGN-paper dipsticks and swabs for SERS mediated sensing of various protein and biochemical analytes. A detection limit of 100 fM of human serum albumin complexed with indocyanine green using MGN-paper dipsticks was achieved. Incorporating protein detection via SERS beacon technology with the concept of junction field strength, we designed a sandwich architecture detection assay using MGN-glass and obtained a 5 fg/mL detection limit for prostate specific antigen (PSA). These initial tests were proof of concept studies envisioning a diagnostic tool for early detection of prostate cancer through blood or serum analysis of PSA levels. To improve MGN-substrates for future biomolecular SERS detection, the incorporation of a planar

yet flexible substrate that is not overly porous, potentially a polymer film, would be beneficial. In this approach, the benefits of the flexible, versatile, and robust material are combined with the capacity to have complex architectures as with the planar systems.

The ability to trace surface receptor coverages through MGNs enhanced SERS-tags is advantageous because of the combination of multiplex technology with high spatiotemporal resolution. We showed the theranostic capability of actively targeted MGNs in triple negative breast cancer (TNBC) cells *in vitro* and *in vivo* via human xenografts. Enabled by the narrow peak widths of Raman signatures, we simultaneously targeted the epidermal growth factor receptor (EGFR) and immune checkpoint receptor, programmed death ligand 1 (PD-L1). We acquired 2-dimensional (2-D) SERS cellular "traffic maps" facilitating highly sensitive and specific detection of EGFR and PD-L1. In addition, the SERS enhancement provided detection of the MGNs probes amidst signal from biological tissue *in vivo*, and a receptor blocking study revealed ~30 % decrease in SERS signal verifying the active targeting properties of the antibody coated MGNs. Moving forward, SERS 3-D volume maps visualize receptor distribution on a global perspective and have the potential to provide valuable information in determining candidacy for the treatment of the cancer. Furthermore, current ongoing studies in utilizing antiPDL1 as a therapeutic agent provide potential for combinational theranostic probes with multiple therapeutic or diagnostic modalities.

The work presented demonstrates the versatile and adaptable potential of the synthesized theranostic MGNs to provide a quantitative measure of biomolecules and to allow for predictive, personalized, and image-guided immunotherapies with minimal toxicity. These theranostic nanoplatforms offer a multifunctional tool that will facilitate the transition to individualized cancer medicine.

APPENDIX A

PROCEDURES FOR MGN-GLASS SERS BIODIAGNOSTIC ASSAY FOR ULTRASENSITIVE DETECTION OF PROSTATE SPECIFIC ANTIGEN (PSA)

A.1 MGN-glass Preparation

A.1.1 Synthesis

1. Reagents and Materials
   - **cellulose paper**
     cellulose filter paper (Grade #2, 42.5 mm, 8 μm pores) (Whatman)
   - **glass**
     microscope glass slides (25.4x76.2mm (1"x3") (PEARL)
   - **PVP**
     Poly(4-vinylpyridine) MW~60000 g/mol (Sigma Aldrich)
   - **HEPES:**
     (4-(2-hydroxyethyl)-1-piperazineethanesulfonic acid) (Sigma-Aldrich)
   - **Gold Salt**:
     gold(III) chloride trihydrate (HAuCl4) (Sigma-Aldrich)

2. **Timeline** Day 1: Piranha clean, PVP coat glass, also Make HEPES
   Day 2: PVP curing and MGN Prep (250 mL batches)
   Day 3: MGN centrifuging/concentration and soaking glass in MGNs
   Day 4: Rinse and Dry to receive final product.

3. **Protocol**

   Day 1:

   To synthesis the large volumes of MGNs required to prepare the MGN-glass, a large batch of HEPES buffer is required. Solution phase MGNs at 780 ± 10 nm are ideal beasuse of the first NIR biological window. Thus, 200 mM HEPES pH 7.4 ± 0.1 was utilized for synthesis, and 250 mL of HEPES was prepared using the method described in section A.2.2. For step by step buffer process, refer to this section.

   Plain microscope glass from PEARL was utilized as the substract to coat with the MGNs. First the surface of the glass had to be completely to ensure strong functionlaziation with the Poly(4-vinylpyridine) layer. Also noted, one side of the glass piece has to scratch to denote that it is the bottom aside as building a sandwich assay in only one direction nso bottom side will not be involved nor coated. Thus, the glass was pre-cut into ~4 mm x 4 mm square glass pieces and then soaked in piranha solution (3:1 Sulfuric Acid:Hydrogen Peroxide) at 55 ^{0}C on a hot plate, covering to protect from any bubbles. Next the glass pieces were soaked in MQ water for 10 min at room temperature, followed by washing

with MQ water first and Isopropyl Alcohol second. Glass was next dried with Nitrogen stream and stored at room temperature in parafilmed petri dish untl further usage.

Next, using Poly(4-vinylpyridine) (PVP) MW~60000 g/mol (Sigma Aldrich), 1 wt % PVP solution was prepared. 0.45 g of PVP was dissolved in 45 mL total volume, using 90 % ethanol as solvent. Much vortexing and even sonication was required to get the PVP to go into solution. Finally, the glass pieces were faced scratched side down in a plastic petri dish and were submerged in the 45 mL of 1 wt % PVP solution. The dish was covered and left at room temperate for 24 h for surface functionalization to occur. Yield is usually about ~15 pieces of 4x4 mm glass per 300 mL MGN batch. This could be improved in the future with possible different soaking techniques.

Day 2:

A scaled up 250 mL batch of MGNs was prepared by synthesizing nine 30 mL batches simultaneously and combining after the reaction reached completion. The synthesis could also be achieved by reacting in a 500 mL round bottom in one huge 250 mL reaction volume. However, it has been the experience that smaller batches tend to give narrower plasmon resonances due to more monodisperse MGNs. Thus, the more exact plasmon tuning, smaller batches in large numbers are preferred. If polydispersity is not an issue for the technology purpose, then the large batch chemistry could also be incorporated. Briefly, 18 mL of Milli-Q water (18 MΩ) was added to 12 ml 200 mM HEPES (pH 7.40 ± 0.1), mixing by gentle inversion. Quickly, 300 µl of 20 mM tetrachloroauric(III) acid ($HAuCl_4$, Sigma-Aldrich, #520918) was added, again mixing my inversion and leaving to react at room temperature for 75 minutes. Plasmon resonance of the MGNs, through the functionalization process, was monitored using UV-vis spectroscopy with optimal initial resonance of the solution phase MGNs at 780 ± 10 nm. The MGN batches were stored at 4 °C overnight until coated step.

Next, now that the PVP had functionalized the glass for 24 h, the glass pieces were rinsed with 90 % ethanol and dried with a nitrogen stream. The glass pieces were then left to cure at room temperature for 24 h on the benchtop with lid closed.

Day 3:

Post 24 h PVP cure time, the glass pieces were stored in the petri dish, parafilming to maintain shelf life until usage for MGN coating. The 250 mL MGNs volume was removed from 4 °C and sonicated 10 min prior to centrifugation to disturb any clusters forming in the solutiom phase MGNs. The 250 mL MGN volume was then concentrated down to ~ 3 mL by centrifugation (6000 rpm for 20 min) with an additional spin of the supernatant to capture all of the MGNs. Next, the PVP-coated glass (15 pieces) was soaked in the concentrated MGNs solution for 24 h with constant 77 RPM shaking on benchtop plate shaker. The soaking occurred in 35 mm culture dishes at room temperature.

Day 4:

After the 24 h MGN soak, the pieces were rinsed gently with MQ water and dried with Nitrogen stream. The MGN-glass pieces were stored in a petri dish, parafilming to maintain shelf life. The MGN-glass batches have maintained performed for 3-4 months with proper storage at room temperature. If imaging through transmission elecetron microscopy, the MGN-glass samples need to be sputtered with 3-5 nm to increase the conductance of the glass and create for better visualization.

A.1.2 Characterization

1. To study the optical properties of the MGN-glass, several spectroscopy techniques were utilized in its probing. A Varian Cary 5000 UV-vis NIR spectrophotometer (Agilent Technologies) was used to measure the extinction of the MGNs in solutions using a 1 cm path length cuvette. Further, extinction spectra of the MGN-glass was also recorded in solid state. The MGN-glass was visualized using a Zeiss Merlin SEM, sputtering samples were with ~3-5 nm layer of Au prior to SEM. Moreover, prior to incorporating in the sandwich assay, SERS spectra of the MGN-glass alone were acquired to determine if the MGN-substrate material itself had its own spectral characteristics. Using an inVia Raman (Renishaw) brightfield microscope, spectra were recorded with: 785 nm wavelength laser source, 1200 lines/mm grating, extended spectra, 50x objective with power of 2 mW, and 30 s acquisition time. SERS footprint plotted after fluorescence and background subtraction using Wire 3.4 software. Lastly, Finite Difference Time Domain (FDTD) studies were performed on dimer geometries of MGNs to determine what would be the best nanoantenna structure to incorporate into the MGN-glass substrates. For full details, refer to *Chapter 3 methods for MGNs dimer FDTD simulations (refer to Chapter 3.5)*.

A.2 Synthesis of antiPSA-pMBA-MGNs for Sandwich Assay Top Probe

A.2.1 Reagents and Materials

- **HEPES**
  (4-(2-hydroxyethyl)-1-piperazineethanesulfonic acid) (Sigma-Aldrich)
- **Gold Salt**
  gold(III) chloride trihydrate (HAuCl4) (Sigma-Aldrich)
- **Raman tag, pMBA**
  4-mercaptobenzoic acid (pMBA) (TCI America)
- **OPSS-PEG-NHS ester**
  Orthopyridyl-disulfide poly(ethylene glycol)-N-hydroxysuccinimide ester (OPSS-PEG-NHS ester, M_w 2000 g/mol, JenKem Technology)
- **Monophosphate**
  sodium phosphate dibasic (Na_2HPO_4, Fisher Scientific)
- **Bicarbonate**
  sodium bicarbonate ($NaHCO_3$, Acros Organics)
- **Tris**
  [Tris(hydroxymethyl)aminomethane] (Sigma-Aldrich)
- **CaCl2**
  Calcium Chloride (Sigma-Aldrich)
- **NaCl**
  Sodium Chloride (Sigma-Aldrich)
- **10x PBS**
  Phosphate Buffered Saline pH 7.4 (Gibco)
- **antiPSA, monoclonal**
  Human Kallikrein 3/PSA antibody (monoclonal mouse raised antibody, R & D Systems)
- **antiPSA, polyclonal**
  Human Kallikrein 3/PSA antibody (polyclonal goat raised antibody, R & D Systems)
- **Recombinant Human PSA**
  Recombinant Human Kallikrein 3/PSA protein (antigen, R & D Systems)
- **FL-secondary antibody for antiPSA**
  Mouse IgG_{2A} PE-conjugated (monoclonal rat raised antibody, R & D Systems, Phycoerythrin)
- **BSA**
  Bovine Serum Albumin (Sigma-Aldrich)
- **IgG from Human Serum**
  Purified Immunolglobulin G (Sigma Aldrich)

A.2.2 Buffer Preparation

1. **200 mM HEPES pH 7.40 ± 0.1 buffer for MGNs Synthesis**

   -HEPES prep must be with Aqua Regia cleaned glass as it is for MGN synthesis.

   Glassware and Materials: (x1) 600 mL Beaker
   (x1) 250 mL Graduated Cylinder
   (x1) stir bar

   - Add ~11.916 g of HEPES (Sigma Aldrich, #H4034) to 600 mL beaker.
   - Add 190 mL MQ water.
   - Let stir for ~40 min with large stir bar to dissolve.
   - Always checking pH with stir bar stirring.
   - Calibrate pH meter with pH 7 and 10 standards, check pH.
   - Prepare 1 M NaOH solution from solid pellets and MQ water.
   - Add 1 mL 1 M NaOH, check pH, continually stirring.
   - Wash electrode in between readings with MQ water and dab dry.
   - Keep adding 1 mL 1 M NaOH (20-25 mL) and monitoring to pH 7.40 ± 0.1.
   - Take out stir bar, fill to 250 mL with MQ water in graduated cylinder.
   - Vortex again and record final pH reading of buffer.
   - Put buffer in sterile 50 mL conical tubes (x5) and store at room temperature.
   - HEPES buffer not autoclaved for MGN synthesis.

2. **8.6 mM Na_2HPO_4 pH 7.40 ± 0.1 Monophosphate buffer for MGN Resuspension**

   -Buffer autoclaved post preparation for sterility:

   Glassware and Materials: (x1) 50 mL Centrifuge tube
   (x1) 125 mL Erlenmeyer flask
   (x1) stir bar
   (x1) aluminum foil
   (x1) autoclave tape

   - Add ~48 mg of Na_2HPO_4 (Fisher Scientific, S374) to 50 mL Tube.
   - Add 32 mL MQ water.
   - Let stir for ~40 min with conical stir bar to dissolve.
   - Always checking pH with conical stir bar stirring, vortex after each addition.
   - Calibrate pH meter with pH 7 and 10 standards, check pH.
   - Add 1 µL 5 M HCl, check pH, vortexing to mix in between readings.
   - Wash electrode in between readings with MQ water and dab dry.
   - Keep adding 1 µL 5 M HCl (10-15 µL) and monitoring to pH 7.40 ± 0.1.
   - Take out stir bar, fill to 40 mL with MQ water.
   - Vortex again and record final pH reading of buffer.
   - Put the buffer in a clean Erlenmeyer flask (125 mL).
   - Cover with foil, add autoclave tape, and put in secondary container.
   - Autoclave using liquid cycle.
   - Post-autoclaving, let cool, and put in sterile 50 mL conical tube in biohood.
   - Store at 4 ^{0}C.

3. **100 mM $NaHCO_3$ pH 8.6 ± 0.1 Bicarbonate buffer for antiPSA Resuspension**

-Buffer autoclaved post preparation for sterility:

Glassware and Materials: (x1) 50 mL Centrifuge tube
(x1) 125 mL Erlenmeyer flask
(x1) stir bar
(x1) aluminum foil
(x1) autoclave tape

- Add ~335 mg of $NaHCO_3$ (Acros Organics, #123360050) to 50 mL Tube.
- Add 32 mL MQ water.
- Let stir for ~40 min with conical stir bar to dissolve.
- Always checking pH with conical stir bar stirring, vortex after each addition.
- Calibrate pH meter with pH 7 and 10 standards, check pH.
- Prepare 1 M NaOH solution from solid pellets and MQ water.
- Add 2 µL 1 M NaOH, check pH, vortexing to mix in between readings.
- Wash electrode in between readings with MQ water and dab dry.
- Keep adding 2 µL 5 1 M NaOH (6-8 µL) and monitoring to pH 8.60 ± 0.1.
- Take out stir bar, fill to 40 mL with MQ water.
- Vortex again and record final pH reading of buffer.
- Put the buffer in a clean Erlenmeyer flask (125 mL).
- Cover with foil, add autoclave tape, and put in secondary container.
- Autoclave using liquid cycle.
- Post-autoclaving, let cool, and put in sterile 50 mL conical tube in biohood.
- Store at 4 ^{0}C.

4. **TCN pH 7.4 ± 0.1 for PSA Resuspension (50 mM Tris, 10 mM $CaCl_2$, 150 mM NaCl)**

-Buffer autoclaved post preparation for sterility:

Glassware and Materials: (x1) 50 mL Centrifuge tube
(x1) 125 mL Erlenmeyer flask
(x1) stir bar
(x1) aluminum foil
(x1) autoclave tape

- Add ~243 mg of Tris solid (Sigma-Aldrich, #252859) to 50 mL Tube.
- Add ~44 mg of $CaCl_2$ solid (Sigma-Aldrich, #C4901) to 50 mL Tube.
- Add ~351 mg of NaCl solid (Sigma-Aldrich, #S7653) to 50 mL Tube.
- Add 25 mL MQ water.
- Let stir for ~1 h with conical stir bar to dissolve.
- Always checking pH with conical stir bar stirring, vortex after each addition.
- Calibrate pH meter with pH 7 and 10 standards, check pH.
- Add 25-50 µL 5 M HCl, check pH, vortexing to mix in between readings.
- Wash electrode in between readings with MQ water and dab dry.
- Keep adding 25 µL 5 M HCl (300-350 µL) and monitoring to pH 7.40 ± 0.1.
- Take out stir bar, fill to 40 mL with MQ water.
- Vortex again and record final pH reading of buffer.
- Put the buffer in a clean Erlenmeyer flask (125 mL).
- Cover with foil, add autoclave tape, and put in secondary container.
- Autoclave using liquid cycle.

- Post-autoclaving, let cool, and put in sterile 50 mL conical tube in biohood.
- Store at 4 ^{0}C.

5. **1x PBS pH 7.4 ± 0.1 buffer for IgG Resuspension**

-Buffer autoclaved post preparation for sterility:

Glassware and Materials: (x1) 50 mL Centrifuge tube
(x1) 125 mL Erlenmeyer flask
(x1) stir bar
(x1) aluminum foil
(x1) autoclave tape

- Add 4 mL 10x PBS pH 7.4 stock (Gibco) to 50 mL Tube.
- Add 32 mL MQ water.
- Let stir for ~40 min with conical stir bar to dissolve.
- Always checking pH with conical stir bar stirring, vortex after each addition.
- Calibrate pH meter with pH 7 and 10 standards, check pH.
- Add 1 µL 5 M HCl, check pH, vortexing to mix in between readings.
- Wash electrode in between readings with MQ water and dab dry.
- Keep adding 1 µL 5 M HCl (3-6 µL) and monitoring to pH 7.40 ± 0.1.
- Take out stir bar, fill to 40 mL with MQ water.
- Vortex again and record final pH reading of buffer.
- Put the buffer in a clean Erlenmeyer flask (125 mL).
- Cover with foil, add autoclave tape, and put in secondary container.
- Autoclave using liquid cycle.
- Post-autoclaving, let cool, and put in sterile 50 mL conical tube in biohood.
- Store at 4 ^{0}C.

A.2.3 Protein Resuspension

1. **antiPSA, Monoclonal**

Sterile Conditions:

- ✓ antiPSA monoclonal antibody (R & D Systems), part #MAB13442. Was shipped as 500 µg amount.
- ✓ Let the antibody thaw on ice for ~20-30 min.
- ✓ Pellet the solid down in the centrifuge before moving to biohood.
- ✓ Check that appearance of white solid is observable in tube.
- ✓ In the biohood, dissolve the 500 µg of antiPSA monoclonal antibody in 500 µL 100 mM NaHCO3 (pH 8.6 ± 0.1) buffer by gently pipetting, no vortexing.
- ✓ Pipette until solid is completely resuspended, but avoid bubbles as they are indicator of protein aggregation.
- ✓ Aliquot in 15 µL aliquots (1 mg/mL), putting the aliquots on ice. Should get about ~33 aliquots. Store at -20 ^{0}C.
- ✓ Avoid repeating the freeze/thaw process of the protein more than once if possible.

2. **antiPSA, Polyclonal**

Sterile Conditions:

- ✓ antiPSA polyclonal antibody (R & D Systems), part #AF1344. Was shipped as 100 µg amount.
- ✓ Let the antibody thaw on ice for ~20-30 min.
- ✓ Pellet the solid down in the centrifuge before moving to biohood.
- ✓ Check that appearance of white solid is observable in tube.
- ✓ In the biohood, dissolve the 100 µg of antiPSA polyclonal antibody in 100 µL 100 mM NaHCO3 (pH 8.6 ± 0.1) buffer by gently pipetting, no vortexing.
- ✓ Pipette until solid is completely resuspended, but avoid bubbles as they are indicator of protein aggregation.
- ✓ Aliquot in 10 µL aliquots (1 mg/mL), putting the aliquots on ice. Should get about ~10 aliquots. Store at -20 ^{0}C.
- ✓ Avoid repeating the freeze/thaw process of the protein more than once if possible.

3. **Prostate Specific Antigen**

Sterile Conditions:

- ✓ Recombinant Human Kallikrein 3/PSA (R & D Systems), part #1344-SE. Was shipped as 10 µg amount.
- ✓ Let the antibody thaw on ice for ~20-30 min.
- ✓ Pellet the solid down in the centrifuge before moving to biohood.
- ✓ Check that appearance of white solid is observable in tube.
- ✓ In the biohood, dissolve the 10 µg of PSA protein in 100 µL TCN buffer by gently pipetting, no vortexing.
- ✓ Pipette until solid is completely resuspended, but avoid bubbles as they are indicator of protein aggregation.
- ✓ Aliquot in 10 µL aliquots (100 µg /mL), putting the aliquots on ice. Should get about ~10 aliquots. Store at -20 ^{0}C.
- ✓ Avoid repeating the freeze/thaw process of the protein more than once if possible.

4. **Immunoglobulin G**

Sterile Conditions:

- ✓ Immunoglobulin G from human serum (Sigma-Aldrich), part #I4506. Was shipped as 10 mg amount.
- ✓ Let the antibody thaw on ice for ~20-30 min.
- ✓ Pellet the solid down in the centrifuge before moving to biohood.
- ✓ Check that appearance of white solid is observable in tube.
- ✓ Need to measure out 2 mg of IgG protein.
- ✓ In the biohood, dissolve the 2 mg of IgG protein in 1 mL 1x PBS pH 7.4 buffer by gently pipetting, no vortexing.
- ✓ Pipette until solid is completely resuspended, but avoid bubbles as they are indicator of protein aggregation.
- ✓ Aliquot in 50 µL aliquots (2 mg /mL), putting the aliquots on ice. Should get about ~20 aliquots. Store at -20 ^{0}C.
- ✓ Avoid repeating the freeze/thaw process of the protein more than once if possible.

A.2.4 Functionalization Chemistry

1. **antiPSA-pMBA-MGNs Chemistry**
   Procedure for functionalization chemistry for biodiagnostic top probe is a modified version of what was explained previously *in vitro* in *Chapter 4 methods for antiEGFR-pMBA-MGNs (refer to Chapter 4.5)*.

2. **Differences Between Two Chemistry Protocols**
   i.) 30 mL batch functionalized MGNs instead of 60 mL.
   ii.) pMBA + MGNs reaction was for 2 min instead of 10 min at 4 ^{0}C as stated in section 4.5.
   iii.) For OPSS-PEG-NHS + antiPSA (pAb) reaction, this was a polyclonal antibody for top probe, not moncolonal as stated in section 4.5.
   iv.) OPSS-PEG-antiPSA + pMBA-MGNs reaction was for 30 min instead of 24 hr at 4 ^{0}C as stated in section 4.5.
   v.) No PEGylation chemistry was performed on the antiEGFR-pMBA-MGNs.
   vi.) Final product resuspension volume was 600 µL instead of 200 µL.

3. **Brief Review of Procedure**
   MGNs Synthesis: 30 mL batch of MGNs was prepared. Briefly, 18 mL of Milli-Q water (18 MΩ) was added to 12 ml 200 mM HEPES (pH 7.40 ± 0.1), mixing by gentle inversion. Quickly, 300 µl of 20 mM tetrachloroauric(III) acid (HAuCl4, Sigma-Aldrich, #520918) was added, again mixing my inversion and leaving to react at room temperature for 75 minutes. Plasmon resonance of the MGNs, through the functionalization process, was monitored using UV-vis spectroscopy with optimal initial resonance of the solution phase MGNs at 780 ± 10 nm.

   antiPSA-pMBA-MGNs: Again, functionalization chemistry was monitored for shifts in plasmon resonance due to phase retardation effects from the change in immediate local refractive index due to the layering around the MGNs. To begin, 30 mL MGNs at 170 µg/mL (Ext. = 1.79) at max plasmon resonance ~780 nm in the NIR region were synthesized. MGNs were kept on ice through functionalization process. 4-mercaptobenzoic acid (pMBA), dissolved in 100 % ethanol, was added to the MGNs in a small volume with high concentration, slow stirring, 3 µL of 10 mM pMBA was injected to 30 mL of MGNs, mixing for 2 min at 4 °C.

   30 mL was split into 5 mL aliquots (x6), centrifuged at 6000 rpm for 20 min. Supernatant was completely decanted to remove any unbound pMBA, and pellets were combined in 1.5 mL total volume with Milli-Q (MQ) water. The resonance and concentration were again recorded, and the functionalized MGNs were further diluted to 1.14 mg/mL (Ext. = 12.0) with Milli-Q water for a total volume of 3 mL of particles.

For OPSS-PEG-antiPSA procedure, refer to OPSS-PEG-antiEGFR procedure (section 4.5) as they were the same except OPSS-PEG-antiPSA is prepped in 40 µL, while the OPSS-PEG-antiEGFR was prepared at 80 µL volume. Both were prepared at (1:9) volume ratio of antibody to OPSS-PEG-NHS linker and reacted for at 4 ^{0}C for 24 h. 35 µL of OPSS-PEG-PSA reaction (polyclonal $[antiPSA]_{Final}$ = 0.9 mg/mL) was added to 2.6 mL pMBA-labeled-MGNs at 1.14 mg/mL (Ext. = 12.0), pipetting to mix. Antibody with MGNs reaction was then left to react for 30 min on an inverter at 4 ^{0}C.

Post 30 min incubation, the ~2.6 mL volume was split into 1.3 mL aliquots (x2) and filled to 2.6 mL volumes with Milli-Q water, mixing by inversion to wash any unbound OPSS-PEG-NHS. Particles were then centrifuged at 4000 rpm for 10 min, and supernatant was completely removed under sterile conditions. Pellets were resuspended in 600 µL of sterile 8.6 mM pH 7.40 ± 0.1 (Na_2HPO_4) monophosphate buffer, with resonance and concentration again measured. If necessary, dilute final [antiPSA-pMBA-MGNs] with the sterile monophosphate buffer to 1.5 mg/mL, rechecking concentration. For biodiagnostic PSA assays, functionalized MGNs were further diluted to 686 µg/mL with sterile monophosphate buffer. The particle prep for the antiPSA-pMBA-MGNs was finished on day of sandwich assay, and then stored at 4 ^{0}C on ice until usage. These antiPSA-pMBA-MGNs act as the tope probe in the biodiagnostic sandwich assay for detection.

A.3 SERS Biodiagnostic MGN Sandwich Assay: Experimental Design

A.3.1 Timeline and Overview of Biodiagnostic SERS Assay

Day 1:

Tasks - buffer prep, protein resuspension and aliquoting, HEPES prep:
- Proteins to aliquot - PSA, antiPSA (mAb), antiPSA (pAb), IgG
- Buffers - monophosphate buffer, bicarbonate buffer, TCN buffer, 1x PBS pH 7.4,
- HEPES - 200 mM HEPES pH 7.4

Day 2:

Tasks - OPSS-PEG-antiPSA (mAb) 24 h reaction:
- Start OPSS-PEG-antiPSA (mAb) 24 h reaction. Product used to attach monoclonal antiPSA to MGN-glass.

Day 3:

Tasks - OPSS-PEG-antiPSA (pAb) 24 h reaction, MGNs synthesis, bind mAb + MGN-glass:
- Day 1 of top probe synthesis: start OPSS-PEG-antiPSA (pAb) 24 h reaction.
  - Product used for chemistry with pMBA-MGN and OPSS-PEG-antiPSA (pAb)
  - Prepare 30 mL batch of MGNs for combination chemistry
- Start OPSS-PEG-antiPSA (mAb) + MGN-glass for 24 hr reaction

Day 4:

Tasks - Finish top probe synthesis, Sandwich assay, SERS measurements of Sandwich assay:
- Day 2 of top probe synthesis: after attaching pMBA to form pMBA-MGNs, start OPSS-PEG-antiPSA (pAb) + pMBA-MGNs for 30 min reaction. Finish functionalization chemistry of antiPSA-pMBA-MGNs.
- Perform the actual MGN biodiagnostic sandwich assay for PSA detection.
- Acquire Raman spectra of sandwich assay samples, after let dry for 1-2 h at 4 ^{0}C

A.3.2 Experimental Procedure of Sandwich Assay

Day 1:

For the 1st day of the Biodiagnostic assay, sterile buffers are first prepared for protein resuspension including: 200 mM HEPES pH 7.40 ± 0.1, 8.6 mM Na2HPO4 pH 7.40 ± 0.1, 100 mM NaHCO3 pH 8.6 ± 0.1, TCN pH 7.4 ± 0.1, and 1x PBS pH 7.4 ± 0.1. Refer to section A.2.2 for exact steps on buffer preparation. After buffers were prepared, the four proteins were reconstituted and resuspended. These proteins include: recombinant Human PSA, antiPSA (mAb), antiPSA (pAb), and IgG. Refer to section A2.3 for exact steps on protein resuspension.

Day 2:

On day 2 of Biodiagnostic assay, the OPSS-PEG-antiPSA (mAb) reaction for the monoclonal antiPSA to bind the bottom MGN-glass was initiated. For each sample, 13 µL of the OPSS-PEG-antiPSA is required. Thus, for 6 samples, will prep 130 µL to have extra.

Making one large rxn for all 6 bottom probes
Immediately proceed to the reaction step.
OPSS-PEG-antiPSA (mAb) binding monoclonal #1 [1 = 160 mg/mL OPSS-PEG-NHS]
Add 13 µL of 160 mg/mL OPSS-PEG-NHS (resuspend in sterile bicarb buffer)
Add 117 µL of 1 mg/mL of Anti-PSA monoclonal antibody (resuspend in bicarb buffer)
Pipette up and down gently to mix
Let react at 4 ^{0}C for 24 h

Day 3:

Day 3 of Biodiagnostic assay includes the first day of top probe synthesis.
The OPSS-PEG-antiPSA (pAb) reaction was initiated. This polyclonal antibody is used for top probe MGN synthesis. Also for top probe synthesis, 30 mL batch of MGNs was synthesized as well. Lastly, OPSS-PEG-antiPSA (mAb) was dropped on MGN-glass samples to prepare the bottom probe antiPSA (mAb) in binding to the MGN-glass surface.

MGNs synthesis -
Briefly, 18 mL of Milli-Q water (18 MΩ) was added to 12 ml 200 mM HEPES (pH 7.40 ± 0.1), mixing by gentle inversion. Quickly, 300 µL of 20 mM tetrachloroauric(III) acid (HAuCl4, Sigma-Aldrich, #520918) was added, again mixing my inversion and leaving to react at room temperature for 75 minutes. Ideal plasmon resonance at ~780 nm in solution phase to begin functionalization chemistry.

Immediately proceed to the reaction step.
OPSS-PEG-antiPSA (pAb) Binding monoclonal #1 [1 = 160 mg/mL OPSS-PEG-NHS]
Add 4 µL of 160 mg/mL OPSS-PEG-NHS (resuspend in sterile bicarb buffer).
Add 36 µL of 1 mg/mL of Anti-PSA polyclonal antibody (resuspend in sterile bicarb).
Pipette up and down gently to mix.
Let react at 4 ^{0}C for 24 h.

bind mAb + MGN-glass: OPSS-PEG-antiPSA (mAb) binding with MGN-Glass.
Just Drop 13 µL of OPSS-PEG-antiPSA (mAb) (0.9 mg/mL) per MGN-glass piece. Spread the volume as to cover the whole glass piece.
Let bind mAb + MGN-glass react at 4 ^{0}C for 24 h.
Did not do any washing to MGN/glass before OPSS-PEG-antiPSA soaking.

Day 4:

The fourth day is the busiest in the assay. The top probe chemistry has to be finished. The actual sandwich assay is performed, and the SERS measurements, determining the results of the actually assay are also recorded on this day after drying the samples.

Overview of steps for Day 4:
-Soak at 4 ^{0}C with MGN/glass and OPSS-PEG-antiPSA (mAb) (24 h)
-Did 13 µL here of 0.9 mg/mL antibody
-2 h soak at 4 ^{0}C with MGN/glass-antibody with PSA (in TCN, no Brij-35)
-Did 13 µL of [PSA]
-1 h soak at 4 ^{0}C with with blocking buffer (1 wt % BSA in monophosphate buffer)
-Did 13 µL 1 mg/mL BSA in monophosphate buffer (no Tween-20)
-Rinse with monophosphate buffer (100 µL monophosphate (x3))
-1 h soak at 4 ^{0}C with top polyclonal probe func-MGNs (antiPSA-pMBA-MGNs)
-Did 13 µL of final Combo MGNs, 0.69 mg/mL
-Rinse with monophosphate buffer (100 µL monophosphate (x3))
-Then dried for 1-2 h at 4 ^{0}C and record SERS spectra

1.) get ice and MQ water.
2.) Sonicate MGNs for 10-15 min
3.) take UV-vis of MGNs for initial plasmon resonance
4.) Put all of your buffers on ice: TCN, monophosphate, 1x PBS
5.) Make up 1 wt % BSA (in monophosphate, only pipetting), leave on ice
Add 0.1 g BSA (Sigma, A3059-10g) in 15 mL tube (ended up 0.1002 g)
Fill to 10 mL line with
monophosphate buffer
pipette to mix. (no vortex).
Leave BSA on ice for later usage.

6.) Thaw PSA, thaws on ice (aliquot found in -20 ^{0}C)
7.) Thaw IgG, thaws on ice (aliquot found in -20 ^{0}C)
8.) Make up PSA dilutions (dilute with TCN, only pipetting), leave on ice
Step 8: Make up PSA dilutions: The PSA comes in 8 µL aliquots at 100 µg/mL. The whole dilution process needs to be done on ice because this is a protein. In addition, only pipetting, no vortex b/c this is a protein. You will make serial dilutions with the TCN buffer found in 4 ^{0}C fridge.

Thaw x4, 8 µL 100 mg/mL aliquots and combine.

Make up serial dilutions in large eppies (5).

100 µg/mL (32 µL) (A)	50 µg /mL (32 µL) (B)
	16 µL of 100 µg/mL
	16 µL of TCN
	pipette to mix.
1 µg/mL (300 µL)	100 ng/mL (300 µL) (C)
6 µL of 50 µg/mL	30 µL of 1 µg/mL
294 µL of TCN	270 µL of TCN
pipette to mix.	pipette to mix.

10 ng/mL (300 µL)	1 ng/mL (300 µL) (D)
30 µL of 100 ng/mL	30 µL of 10 ng/mL
270 µL of TCN	270 µL of TCN
pipette to mix.	pipette to mix.

Leave the protein tubes on ice so that PSA doesn't aggregate

9.) Make up IgG dilutions (dilute with 1x PBS, only pipetting), leave on ice
Step 9: Make up IgG dilutions: The IgG comes in 50 µL aliquot at 2 mg/mL. The whole dilution process needs to be done on ice because this is a protein. In addition, only pipetting, no vortex b/c this is a protein. You will make serial dilutions with the 1x PBS buffer found in 4 ^{0}C fridge.

Make up serial dilutions in small eppies (7).

2 mg/mL (50 µL)

1 mg/mL (60 µL)	100 µg/mL (300 µL) (E)	50 µg/mL (300 µL)
30 µL of 2 mg/mL	30 µL of 1 mg/mL	150 µL of 100 µg/mL
30 µL of 1x PBS	270 µL of 1x PBS	150 µL of 1x PBS
pipette to mix.	pipette to mix.	pipette to mix.

1 µg/mL (300 µL)	100 ng/mL (300 µL)
6 µL of 50 uGu/mL	30 µL of 1 µg/mL
294 µL of 1x PBS	270 µL of 1x PBS
pipette to mix.	pipette to mix.

10 ng/mL (300 µL)	1 ng/mL (300 µL) (F)
30 µL of 100 ng/mL	30 µL of 10 ng/mL
270 µL of 1x PBS	270 µL of 1x PBS
pipette to mix.	pipette to mix.

Leave the protein tubes on ice so that PSA doesn't aggregate

10.) make pMBA (start in glovebox, can vortex)
11.) start antigen soak (2 h), 13 µL of [PSA] per MGN/glass (no wash prior to antigen)
start IgG soak (2 h), 13 µL of [IgG] per MGN/glass (no wash prior to IgG soak)
Step 11: PSA/IgG (antigen) soak
Drop 13 µL of the various [PSA] on its corresponding MGN/glass piece,
Drop 13 µL of the various [IgG] on its corresponding MGN/glass piece,

Drop the 13 µL in the center and spread as usual, then leave for 2 hr at 4 ^{0}C (lid closed).

One piece of MGN/glass is meant for one PSA/IgG concentration

A.) 100 µg/mL PSA
B.) 50 µg/mL PSA
C.) 100 ng/mL PSA
D.) 1 ng/mL PSA
E.) 100 µg/mL IgG (No PSA)
F.) 1 ng/mL IgG (No PSA)

No washing before or after this step

12.) Finish functionalization chemistry to finish prep of antiPSA-pMBA-MGNs
Before adding to the glass, need to dilute to make sure that they have
MGNs = 686 µg/mL

For step by step procedure for antiPSA-pMBA-MGNs chemistry for 30 mL batch, refer to section A.2.4 for exact methods for functionalization chemistry.

13.) next do blocking buffer soak (1 h) (no wash prior to BSA soak)
(13 µL per MGN-glass) 1 wt % BSA in monophosphate

Step 13: BSA soak
Drop 13 µL of the 1 wt % BSA MGN/glass piece,

Drop the 13 µL in the center and spread as usual, then leave for 1 h at 4 C (lid closed).

14.) wash with monophosphate (3 small rinses in wash, 100 µL per rinse)
15.) next do antiPSA-pMBA-MGNs (pAb) (1 h) (13 µL at 686 µg/mL = MGNs)
Step 15: antiPSA-pMBA-MGNs
Drop 13 µL of 686 ug/ml antiPSA-pMBA-MGNs

Drop the 13 µL in the center and spread as usual, then leave for 1 hr at 4 C (lid closed).
16.) wash with monophosphate (3 small rinses in wash, 100 µL per rinse)
17.) dry at 4 C (1-2 h) (with lid slightly ajar)
18.) Collect SERS point maps for the biodiag MGN-glass samples

A.3.3 Raman Measurements of Sandwich Assay

1. After allowing samples to dry for 2 h at 4 C, SERS spectra of the MGN-glass biodiagnostic sandwich assay were recorded. Using an Invia Raman microscope (Renishaw) with a 785 nm wavelength laser source, point maps of the Biodiagnostic samples were captured for the differing [PSA]. A video montage of the MGN-glass samples was captured, and the resulting brightfield image provided x,y coordinates (for point spectra) for the Raman instrument to record SERS chemical footprints. All spectra were recorded with: 785 nm wavelength laser source, 1200 lines/mm grating, extended spectra, 50x objective with power of 2 mW, and 30 s acquisition time. For further analysis, each individual spectrum was baseline corrected to remove any contributions

from the fluorescence background of the MGNs. Wire 3.4 was utilized for data processing of the sandwich assay results. Cosmic ray removal was performed with nearest neighbor method implemented to ensure the scaling of the spectra was not jeopardized. Data truncation and smoothing was also performed using Wire3.4 software. Lastly, background subtraction was performed in Wire using a polynomial fit. $I_{SERS1580}$ peak corresponding the pMBA in the antiPSA-pMBA-MGNs, was determined from the baseline corrected spectra and then plotted against the respected [PSA].

A.3.4 Biodiagnostic Control Assays: Testing Specificity and No Antigen

1. To ensure that the biodiagnostic assay is operating with the proper fidelity. Multiple controls were required. The Bovine Serum Albumin (BSA) alone control is the control where the whole biodiagnostic experiment is completed except for incorporating TCN buffer instead of PSA for the antigen incubation step (2 h). For this control, we see no signal. This observation makes sense, considering we want the biodiagnostic assay to limit the amount of non-specific binding that occurs which would result in false positive results.

2. Lastly, Specificity control was performed, repeating the biodiagnostic assay except incubating with non-specific protein, Immunoglobulin G (IgG), instead of the target antigen (PSA). The control was attempted with multiple [IgG] concentrations, and no signal was observed. Thus, the lack of signal from either the BSA control assay or the IgG specificity control, demonstrates that the SERS sandwich assay has low probability for false positives with non-specific binding. The absence of signal from the IgG control demonstrates that the PSA detection will outcompete non-specific proteins when it comes time to move the assay into serum studies. The specificity of the two antibody layers for the binding event of the correct antigen (PSA), provide the assay with high fidelity while the two MGNs in a junction event, as part of the MGN-glass sandwich assay, provide unmatched detection limits

APPENDIX B

PROCEDURES FOR *IN VIVO* SERS IMAGING AND *EX VIVO* TUMOR STUDIES

B.1 Mammary Fat Pad Tumor Growth

1. Human MDA-MB-231 cells, purchased from ATCC (HTB-26), were cultured in Dulbecco's Modified Eagle's medium (DMEM, Gibco) supplemented with 10% fetal bovine serum (FBS, ATCC) and 1% penicillin/streptomycin (Gibco) and maintained at 37 0C and 5% CO2. For optimal experimental design, cellular and *in vivo* assays were performed only after allowing for 14 days of culture to ensure that the cells were in their native state, maintaining media changes every 2 days.
2. MDA-MB-231 cells were kept in culture at ~50-70 % confluency, not letting them become too confluent and entering their exponential growth phase.
3. On day of 231 injection for the immune-compromised nude mice, the cells should be ~75 % confluent.
4. Also, the athymic nude mice should only be ~3.5 weeks upon 231 injection to obtain optimal results as far as human xenograft adhering and continuing to grow.
5. Day of injection, the cells were dislodged from the culture flask using trypsin, followed by quenching with complete media (cDMEM).
6. The cell number was determined using a scepter cell counter using optical density.
7. Next, the cells were centrifuged at 100 g for 8 min, washing twice with nDMEM to remove any FBS from interfering during xenograft growth in the mice.
8. The cells were resuspended in nDMEM at 2E7 cells/mL and left on ice until injection.
9. Ensuring that the mice are ready for injection, the Matrigel (Corning) was thawed ~2 h prior to injection so was in liquid form, but still cold when it comes times for usage.
10. Matrigel was added (1:1) volume ratio to the cell stock to give overall 1E7 cells/mL.
11. Next, performing a subcutaneous injection in the mammary fat pad around the 5^{th} nipple (left side), 100 µL of the cell solution were injected, observing a bulb forming upon successful injection (total cells injected = 1E6 cells).
12. Tumors should form in ~14 days, monitoring the mice for any forms of discomfort and checking the tumor size 3-4 times per week with calipers.
13. The tumors are ready for imaging when diameter is ~6-7 mm.
14. If the tumors become larger than 15 mm in diameter in any direction, then the mice must be sacrificed.
15. Having consistent tumor size on day of imaging is vital to having consistent results.

B.2 Synthesis of Actively Targeted MGNs Cocktail for *in vivo* Experiments

B.2.1 Reagents and Materials

- **HEPES:**
  (4-(2-hydroxyethyl)-1-piperazineethanesulfonic acid) (Sigma-Aldrich)
- **Gold Salt**:
  gold(III) chloride trihydrate (HAuCl4) (Sigma-Aldrich)
- **Raman tag, pMBA**
  4-mercaptobenzoic acid (pMBA) (TCI America)
- **Raman tag, DTNB**
  5,5'-Dithiobis(2-nitrobenzoic acid) (DTNB) (TCI America)
- **OPSS-PEG-NHS ester:**
  Orthopyridyl-disulfide poly(ethylene glycol)-N-hydroxysuccinimide ester (OPSS-PEG-NHS ester, M_w 2000 g/mol, JenKem Technology)
- **mPEG-SH (5000 g/mol)**
  methoxy- polyethlyene glycol-thiol (mPEG-SH, M_w 5000 g/mol, Jenkem Technology)
- **Bicarbonate:**
  sodium bicarbonate ($NaHCO_3$, Acros Organics)
- **10x PBS:**
  Phosphate Buffered Saline pH 7.4 (Gibco)
- **antiEGFR**
  Human EGF R/ErbB1 antibody (monoclonal mouse raised antibody, R & D Systems)
- **antiPDL1**
  Human CD274 (B7-H1, PD-L1) antibody (monoclonal mouse raised antibody, BioLegend)
- **FL-secondary antibody for antiEGFR**
  Mouse IgG_{2B} PE-conjugated (monoclonal rat raised antibody, R & D Systems, Phycoerythrin)
- **Fixative solution**
  cytofix/cytoperm (BD Biosciences)
- **Blocking solution**
  1x animal free blocking solution (Cell Signaling Technology)

B.2.2 Buffer Preparation

1. **200 mM HEPES pH 7.40 ± 0.1 buffer for MGNs Synthesis**
   -HEPES prep must be with Aqua Regia cleaned glass as it is for MGN synthesis.
   Glassware and Materials: (x1) 600 mL Beaker
   (x1) 250 mL Graduated Cylinder
   (x1) stir bar
   - Add ~11.916 g of HEPES (Sigma Aldrich, #H4034) to 600 mL beaker.

- Add 190 mL MQ water.
- Let stir for ~40 min with large stir bar to dissolve.
- Always checking pH with stir bar stirring.
- Calibrate pH meter with pH 7 and 10 standards, check pH.
- Prepare 1 M NaOH solution from solid pellets and MQ water.
- Add 1 mL 1 M NaOH, check pH, continually stirring.
- Wash electrode in between readings with MQ water and dab dry.
- Keep adding 1 mL 1 M NaOH (20-25 mL) and monitoring to pH 7.40 ± 0.1.
- Take out stir bar, fill to 250 mL with MQ water in graduated cylinder.
- Vortex again and record final pH reading of buffer.
- Put buffer in sterile 50 mL conical tubes (x5) and store at room temperature.
- HEPES buffer not autoclaved for MGN synthesis.

2. **100 mM $NaHCO_3$ pH 8.6 ± 0.1 Bicarbonate buffer for antiEGFR Resuspension**

-Buffer autoclaved post preparation for sterility:

Glassware and Materials: (x1) 50 mL Centrifuge tube
(x1) 125 mL Erlenmeyer flask
(x1) stir bar
(x1) aluminum foil
(x1) autoclave tape

- Add ~335 mg of $NaHCO_3$ (Acros Organics, #123360050) to 50 mL Tube.
- Add 32 mL MQ water.
- Let stir for ~40 min with conical stir bar to dissolve.
- Always checking pH with conical stir bar stirring, vortex after each addition.
- Calibrate pH meter with pH 7 and 10 standards, check pH.
- Prepare 1 M NaOH solution from solid pellets and MQ water.
- Add 2 µL 1 M NaOH, check pH, vortexing to mix in between readings.
- Wash electrode in between readings with MQ water and dab dry.
- Keep adding 2 µL 5 1 M NaOH (6-8 uL) and monitoring to pH 8.60 ± 0.1.
- Take out stir bar, fill to 40 mL with MQ water.
- Vortex again and record final pH reading of buffer.
- Put the buffer in a clean Erlenmeyer flask (125 mL).
- Cover with foil, add autoclave tape, and put in secondary container.
- Autoclave using liquid cycle.
- Post-autoclaving, let cool, and put in sterile 50 mL conical tube in biohood.
- Store at 4 ^{0}C.

3. **1x PBS pH 7.4 ± 0.1 buffer for MGN Resuspension**

-Buffer autoclaved post preparation for sterility:

Glassware and Materials: (x1) 50 mL Centrifuge tube
(x1) 125 mL Erlenmeyer flask
(x1) stir bar
(x1) aluminum foil
(x1) autoclave tape

- Add 4 mL 10x PBS pH 7.4 stock (Gibco) to 50 mL Tube.
- Add 32 mL MQ water.

- Let stir for ~40 min with conical stir bar to dissolve.
- Always checking pH with conical stir bar stirring, vortex after each addition.
- Calibrate pH meter with pH 7 and 10 standards, check pH.
- Add 1 µL 5 M HCl, check pH, vortexing to mix in between readings.
- Wash electrode in between readings with MQ water and dab dry.
- Keep adding 1 µL 5 M HCl (3-6 µL) and monitoring to pH 7.40 ± 0.1.
- Take out stir bar, fill to 40 mL with MQ water.
- Vortex again and record final pH reading of buffer.
- Put the buffer in a clean Erlenmeyer flask (125 mL).
- Cover with foil, add autoclave tape, and put in secondary container.
- Autoclave using liquid cycle.
- Post-autoclaving, let cool, and put in sterile 50 mL conical tube in biohood.
- Store at 4 ^{0}C.

B.2.3 Protein Resuspension

1. **antiEGFR, Monoclonal**

   Sterile Conditions:

   ✓ antiEGFR monoclonal antibody (R & D Systems), part #MAB1095.
   Was shipped as 500 µg amount.
   ✓ Let the antibody thaw on ice for ~20-30 min.
   ✓ Pellet the solid down in the centrifuge before moving to biohood.
   ✓ Check that appearance of white solid is observable in tube.
   ✓ In the biohood, dissolve the 500 µg of antiEGFR monoclonal antibody in 500 µL 100 mM NaHCO3 (pH 8.6 ± 0.1) buffer by gently pipetting, no vortexing.
   ✓ Pipette until solid is completely resuspended, but avoid bubbles as they are indicator of protein aggregation.
   ✓ Aliquot in 15 µL aliquots (1 mg/mL), putting the aliquots on ice.
   Should get about ~33 aliquots. Store at -20 ^{0}C.
   ✓ Avoid repeating the freeze/thaw process of the protein more than once if possible.

2. **antiPDL1, Monoclonal**

   Sterile Conditions:

   ✓ antiPDL1 monoclonal antibody (BioLegend), part #329728.
   Was shipped already reconstituted in phosphate-buffered solution pH 7.2
   5 mg, in 5.21 mL buffer for ~1 mg/mL antiPDL1 stock
   ✓ Aliquoted in 100 µL aliquots (1 mg/mL), putting the aliquots on ice.
   Should get about ~50 aliquots. Store at 4 ^{0}C as recommended by vendor.
   ✓ Avoid repeating the freeze/thaw process of the protein more than once if possible.

B.2.4 Functionalization Chemistry

1. **(2:1) cocktail prep of antiEGFR-pMBA-MGNs to antiPDL1-DTNB-MGNs** Procedure for functionalization chemistry for in vivo is a modified version of what was explained previously *in vitro* for *Chapter 4 methods for (1:1) cocktail prep of antiEGFR-pMBA-MGNs to antiPDL1-DTNB-MGNs (refer to Chapter 4.5).*

2. **Differences Between Two Chemistry Protocols**
   - i.) 300 mL batch functionalized MGNs per SERS tag/antibody combination instead of 60 mL per combination.
   - ii.) Resuspension for final MGN product was in 1x PBS pH 7.4 ± 0.1 for *in vivo* studies, changed from 8.6 mM (Na_2HPO_4) pH 7.40 ± 0.1.
   - iii.) Final product resuspension volume was 850 µL instead of 200 µL.

3. **Brief Review of Procedure**

   MGNs Synthesis:

   300 mL batch per SERS tag/antibody combination is enough for ~7 mice at (2:1) 6 mg/mL, 200 µL injections. For each nanoprobe, A scaled up 300 mL batch of MGNs was prepared by synthesizing ten 30 mL batches simultaneously and combining after the reaction reached completion. Briefly, 18 mL of Milli-Q water (18 MΩ) was added to 12 ml 200 mM HEPES (pH 7.40 ± 0.1), mixing by gentle inversion. Quickly, 300 µl of 20 mM tetrachloroauric(III) acid (HAuCl4, Sigma-Aldrich, #520918) was added, again mixing my inversion and leaving to react at room temperature for 75 minutes. Plasmon resonance of the MGNs, through the functionalization process, was monitored using UV-vis spectroscopy with initial resonance of the solution phase MGNs at 780 ± 10 nm.

   antiEGFR-pMBA-MGNs: Again, functionalization chemistry was monitored for shifts in plasmon resonance due to phase retardation effects from the change in immediate local refractive index due to the layering around the MGNs. To begin, 300 mL MGNs at 170 µg/mL (Ext. = 1.79) at max plasmon resonance ~780 nm in the NIR region were synthesized. MGNs were kept on ice through functionalization process. 4-mercaptobenzoic acid (pMBA), dissolved in 100 % ethanol, was added to the MGNs in a small volume with high concentration, slow stirring, 30 µL of 10 mM pMBA was injected to 300 mL of MGNs, mixing for 10 min at 4 °C.

   300 mL was split into 50 mL aliquots (x6), centrifuged at 6000 rpm for 20 min. Supernatant was completely decanted to remove any unbound pMBA, and pellets were combined in 15 mL total volume with Milli-Q (MQ) water. The resonance and concentration were again recorded, and the functionalized MGNs were further diluted to 1.14 mg/mL (Ext. = 12.0) with Milli-Q water for a total volume of 31 mL of particles.

   For OPSS-PEG-antiEGFR *in vivo* procedure, refer to OPSS-PEG-antiEGFR *in vitro* procedure (section 4.5) as they were the same except OPSS-PEG-antiEGFR for *in vivo* is prepped in 480 µL, while the OPSS-PEG-antiEGFR *in vitro* was prepared at 80 µL volume. Both were prepared at (1:9) volume ratio of antibody to OPSS-PEG-NHS linker and reacted for at 4 ^{0}C for 24 h. 480 µL of OPSS-PEG-PSA reaction (monoclonal

[antiEGFR]$_{Final}$ = 0.9 mg/mL) was added to 29.75 mL pMBA-labeled-MGNs at 1.14 mg/mL (Ext. = 12.0), pipetting to mix. Antibody with MGNs reaction was then left to react for 24 h on an inverter at 4 ^{0}C.

Post 24 h incubation, PEGylation chemistry was performed. To the aqueous MGNs mixture, 2.1 mL of 5 μM polyethlyene glycol-thiol (mPEG-SH, Mw 5000 g/mol) was added in a cold reaction vessel and slowly stirred for 10 min at room temperature. The ~31.85 mL volume was split into 5.30 mL aliquots (x6) and filled to 10 mL volumes with Milli-Q water, mixing by inversion to wash any unbound OPSS-PEG-NHS or mPEG-SH. Particles were then centrifuged at 4000 rpm for 10 min, and supernatant was completely removed under sterile conditions. Pellets were resuspended in 850 μL of sterile 1x PBS pH 7.4 ± 0.1 with resonance and concentration again measured. If necessary, dilute final [antiEGFR-pMBA-MGNs] with the sterile 1x PBS buffer to 6 mg/mL, rechecking concentration. For *in vivo* longitudinal study, functionalized MGNs were utilized at 6 mg/mL concentration. The particle prep for the antiEGFR-pMBA-MGNs was finished night before zero time point day and then stored at 4 ^{0}C on ice until usage.

antiPDL1-DTNB-MGNs: To synthesize the complementary MGNs particles, the functionalization method was repeated with similar steps but substituting antiPDL1 as the targeting moiety and 5,5'-Dithiobis(2-nitrobenzoic acid) (DTNB) as the SERS tag. Slight change in method was due to the 5-fold dilution of the OPSS-PEG-antiPDL1 reaction for a higher pH. A big batch of 300 mL MGNs at 170 μg/mL (Ext. = 1.79), resonance ~780 nm, was again synthesized. With slow stirring, 30 μL of 10 mM DTNB was added to 300 mL of MGNs reacting for 10 min at 4 °C. After centrifugation and resuspension with MQ water to 1.14 mg/mL (Ext. = 12.0) for a total volume of 31 mL of particles, the antiPDL1 targeting moiety was added to the MGN solution. 2.4 mL of OPSS-PEG-antiPDL1 reaction ([antiPDL1]Final = 0.18 mg/mL) was added to 29.75 mL DTNB-labeled-MGNs at 1.14 mg/mL (Ext. = 12.0). The reaction was left to react for 24 h at 4 °C on inverter. The final PEGylation, wash, centrifugation, and sterile resuspensions steps were same for antiPDL1-DTNB-MGNs as for the antiEGFR-pMBA-MGNs for *in vivo* studies. After resuspending in 850 μL of sterile 1x PBS pH 7.4 ± 0.1, resonance and concentration were checked, and dilution to 6 mg/mL was performed if necessary.

(2:1) cocktail prep of antiEGFR-pMBA-MGNs to antiPDL1-DTNB-MGNs: In preparing a (2:1) mixture of the two types of antibody-labeled MGNs, a 300 mL batch of each of the respective particle was prepared. After final resuspension steps in sterile 1x PBS pH 7.4 ± 0.1, the resonance and concentration of the two antibody-labeled MGNs were determined respectively. Each solution was diluted to 6 mg/mL. Then the antiEGFR-pMBA-MGNs were mixed at an (2:1) volumetric ratio with the antiPDL1-DTNB-MGNs, assuming there was no change in the overall MGNs concentration. Plasmon resonance and concentration of the (2:1) cocktail were measured, and the particles were maintained at a concentration of 6 mg/mL in PBS, on ice at 4 °C, until retro-orbital injection time. Typical volume would be 1350 μL of antiEGFR-pMBA-MGNs + 675 μL of antiPDL1-DTNB-MGNs to create 2025 μL of (2:1) mixture, dividing into 280 μL aliquots (x7). Later, each mouse would receive 200 μL of 6 mg/mL (2:1) mixture retro-orbital injection under anesthesia (60 μg/g mouse injection).

B.3 SERS Longitudinal Assay with Portable Raman and Athymic Mice for Both Experimental and Receptor-Blocked Groups

1. A longitudinal SERS multiplex *in vivo* imaging study was performed on the immune-deficient mice subjects over 72 h time course, measuring the intensity of the two SERS tags of the functionalized MGNs
2. Using 6 mg/mL (2:1) antiEGFR-pMBA-MGNs to antiPDL1-DTNB-MGNs mixture for retro-orbital injection of the athymic mice.
3. The particle prep for (2:1) cocktail of actively targeted MGNs was completed the night before day 1 of in vivo imaging and was stored at 4 ^{0}C on ice until usage.
4. The mixture was injected at 2:1 antiEGFR-pMBA-MGNs to antiPDL1-DTNB-MGNs for the *in vivo* and *ex vivo* studies.
5. Using a portable SERS imaging system and with maneuverable handheld probe, SERS measurements on the surface of the Human xenografts (MDA MB 231) growing in the athymic mouse were recorded using a 785 nm laser diode at 80 mW power. Mice were also under isoflurane anesthesia during SERS. Since SERS acquisitions are so fast temporally, the mouse was only under for ~6 min, making the measurements easier on the subjects.
6. Note: Probe consists of glass-tubing on the inside of the chord. Thus, it must never be bent or wrapped in any way as it will cause the system to lose signal strength.
7. At the site of the tumor, non-invasive, topical measurements were acquired before and at time intervals after retro-obrital injection. While recording, mice were under heating blanket, and any signs of discomfort were monitored.
8. On day 1 of imaging experiment, 0 h time point was recorded, which showed a strong lipid peak (1440 cm^{-1}).
9. This 0 h point measurement was followed by 200 μL of 6 mg/mL (2:1) mixture retro-orbital injection under anesthesia (60 μg/g mouse injection).
10. SERS measurements were recorded at 0, 6 12, 24, 48, and 72 h, putting the mouse under anesthesia during imaging.
11. Post 72 h imaging, the mouse was euthanized, and the organs were retrieved for Ionized Coupled Plasma Mass spectroscopy (ICP-MS) to study the biodistribution of the actively targeted MGNs. Further, organ retrieval was studied for 6 h max accumulation for the experimental and additionally, 6 and 72 h for the receptor blocking control. Data not shown.
12. After background subtraction and normalizing to an endogenous peak of the tumor tissue (lipid, 1440 cm^{-1}), the SERS intensity was plotted for both the DTNB and pMBA peaks with maximum SERS intensity occurring at 6 h post retro-orbital injection.
13. A custom code was built using MATLAB software to perform smoothing and background fluorescent subtraction.
14. Truncation was performed on data sets to focus on 800-1650 cm^{-1} region of interest.
15. Smoothing and filtering were performed using Savitsky and Golay method.
16. Background subtraction of fluorescence was performed using the modified polyfit method, automated approach to iterate many times to find the proper fit for each spectra with a polynomial mathematical function of choice.

17. The software runs an iterative process fitting the selected polynomial to the data to remove background, coming as close to baseline to subtract out all fluorescence without losing any Raman peaks or jeopardizing data fidelity.
18. Further, the active targeting capabilities of the antibody coated MGNs were investigated by having a control group study that was pre-blocked with antiEGFR and antiPDL1 monoclonal antibodies through intraperitoneal injection, 2 h prior to MGN injection.
19. Through intraperitoneal injection, 400 µl of 1 mg/mL mixture of antiEGFR:antiPDL1 antibodies (20 µg/g mouse injection) was injected
20. After 2 h, time point zero was recorded, followed by 200 µL of 6 mg/mL (2:1) mixture retro-orbital injection under anesthesia (60 µg/g mouse injection).
21. SERS measurements were recorded at 0, 6 12, 24, 48, and 72 h, putting the mouse under anesthesia during imaging.
22. Followed by euthanizing and collecting organs at 6 h and 72 h for ICP-MS for the block studies. Data not shown.
23. Raman intensity for both the 1325 cm^{-1} peak for DTNB and 1580 cm^{-1} peak for pMBA were normalized to the 1440 cm^{-1} lipid peak after smoothing and background subtraction.
24. A ~30 % drop in signal is observed due to the receptor blockage on the surface of the tumor.
25. n=4 for each group subset.

B.4 Histology (H and E) and Silver Staining of *ex vivo* Tumor Sections

1. After the longitudinal study revealed the accumulation of actively targeted MGNs using 6 mg/mL (2:1) antiEGFR-pMBA-MGNs to antiPDL1-DTNB-MGNs mixture for retro-orbital injection of the athymic mice, we decided to investigate further the interaction between the functionalized MGNs and the tumor micro-environment.
2. For *ex vivo* studies, another round of *in vivo* tests with the 231 cell xenografts were carried out with 200 μL, 6 mg/mL (2:1) mixture of actively targeted MGNs injected.
3. Since we found out from the longitudinal SERS study that the maximum accumulation occurs at 6 h, we decided to investigate the tumor physiology at this time point.
4. After 6 h post retro-orbital injection, the mouse was sacrificed, and the tumor was removed through dissection.
5. The tumor was next sliced in half to form two separate hemispheres and preserved in OTC freeze, leaving the sample in a cassette over dry ice. Sample was then stored at -80 °C until processing.
6. Sample processing was handled by Vanderbilt Translational Pathology Shared Resource (TPSR).
7. The TPSR core created ultra-thin ~10 μm slices of the breast xenograft tissue in the center and periphery of the tumor for comparison.
8. Next histology stains for both (H and E) staining and silver staining were performed.
9. Haematoxylin and Eosin stains are modulated by pH, and due to the gradients in pH of different macromoleucles, one can distinguish nuclei, cytoplasm, muscles, collagen, mitochondria, and more.
10. Thus, the (H and E) stain provides necessary information about the overall physiology of the tumor tissue and how it is behaving in terms of normal physiological behavior. H and E cannot, however, tell whether there is the presence of gold nanoparticles. It can tell (if nanoparticles are known to be present) whether the particle accumulation is having a detrimental or benign effect on the cells, and if their presence is affecting the tissue morphology.
11. To determine whether there was MGN accumulation or not for the (2:1) mixture of actively targeted MGNs, a silver stain was performed on the xenograft slices as well.
12. The silver stain enhances nanoparticle contrast of the gold nanoparticles making them more apparent in brightfield imaging and easy to observed where there is localization in the tumor tissue and vasculature
13. After staining, the slides were imaged using a bright widefield microscope. In order to have the capacity to see the global image that is the whole tissue slice, a widefield microscope was required.
14. For comparison, also visualized was a control tumor slice silver stained, which had no MGNs injected to the mouse, but was removed at 6 h as well to be consistent.
15. Using a 5x objective and a zoom out setting of 8, both 231 xenografts with and without (2:1 antiEGFR-pMBA-MGNs to antiPDL1-DTNB-MGNs) mixture were recorded.
16. Side by side visualization confirmed presence of actively targeted MGNs at 6 h post injection (observed by silver stain). Additionally, vasculature and tissue morphology were not modified by MGN injection and accumulation as seen by side by side comparison of tumors both with and without actively targeted (as seen by H and E stain).

B.5 *Ex vivo* SERS Mapping of Tumor Sections

1. As performed with the histology *ex vivo* studies, the *ex vivo* SERS mapping of tumor sections required another longitudinal study to again reveal the accumulation of actively targeted MGNs at the tumor site.
2. Using 6 mg/mL (2:1) antiEGFR-pMBA-MGNs to antiPDL1-DTNB-MGNs mixture for retro-orbital injection of the athymic mice, we wanted to test the full potential of the SERS mapping by tracing MGN localization because of receptor coverage at maximum accumulation, 6 h.
3. For *ex vivo* SERS, mice with ~7 mm mammary fat pad xenografts (231 cells) were injected with 200 μL, 6 mg/mL (2:1) mixture of actively targeted MGNs injected
4. 6 h post retro-orbital injection, the mouse was sacrificed, and the tumor was removed.
5. The tumor was again sliced in half to form two separate hemispheres and preserved in OTC freeze. Storing at -80 °C in cassette. Slicing and preparation was performed by Vanderbilt TPSR.
6. Upon receiving the ~10 μm thick slice of the breast xenograft tissue
7. To minimize background fluorescence and other noise, the tissue sections were placed on Calcium Fluoride disks (CaF2, 20 x 2 mm Raman grade, Crystran Ltd.) specifically for SERS measurement.
8. The tissue samples were visualized using an inVia Raman (Renishaw) brightfield microscope. Using an 50x objective, a video montage of the 231 tissue cross-section was captured, and this resulting brightfield image provided x,y coordinates for the Raman instrument to record SERS chemical footprints of a rectangular area of ~5 mm by 5 mm.
9. Recording spectra with 50 μm steps, the invia Raman microscope took measurements of the tissue with a 785 nm wavelength laser source with 1200 lines/mm grating in high confocal mode. Static spectra (1200 cm^{-1} center) were recorded using a 50x objective at a power of 10 mW with a 10 s acquisition time.
10. Running Wire 3.4 software, SERS map was a collection of ~5 mm x 5 mm tissue cross-section. Raster acquisition was utilized, creating a dataset of ~30,000 spectra. The dataset was a matrix with (x,y) coordinates, wavenumber cm^{-1}, and Raman intensity. Using the wire 3.4 software, cosmic ray removal was performed with nearest neighbor method implemented. Next, the wire 3.4 wxd file was converted into a text file and imported into MATLAB R2016a software. Code was built using MATLAB software to perform smoothing and background fluorescent subtraction. Following the modified polyfit method, an automated approach was applied using polynomial fitting to uncover SERS peaks even at low intensity regimes.
11. Prior to implementing the modified polyfit method on the data set, truncation was performed, and data underwent smoothing and data differentiation using the Savitzsky and Golay method. The S and G filter used order of 5 and coefficient value of 61.
12. After smoothing, a 7^{th} order polynomial was utilized for fluorescent background subtraction through an iterative process with a threshold of 0.0001.
13. Direct Classical Least Squares (DCLS) component mapping of the 1325 cm^{-1} peak corresponding to DTNB of the antiPDL1-DTNB-MGNs was performed. DCLS utilizes peak geometries as parameters to determine similarity for spectra in a large dataset.
14. The analysis revealed localization of the signal on the periphery of the tumor cross section where more vasculature was concentrated when comparing to necrotic core.